

Dissertation zur Erlangung des Doktorgrades
der Fakultät für Chemie und Pharmazie
der Ludwig-Maximilians-Universität München

**Combination of X-Ray Diffraction and Electron Microscopy for
Real Structure Investigations on Luminescent Oxonitridosilicates,
Nitridogallates and Other Nitride Compounds**

Markus Armin Seibald

aus

München, Deutschland

2013

Erklärung

Diese Dissertation wurde im Sinne von § 7 der Promotionsordnung vom 28. November 2011 von Herrn Prof. Dr. W. Schnick betreut.

Eidesstattliche Versicherung

Diese Dissertation wurde eigenständig und ohne unerlaubte Hilfe erarbeitet.

München, den 01.10.2013

.....
(Markus Armin Seibald)

Dissertation eingereicht am	01.10.2013
1. Gutachter:	Prof. Dr. W. Schnick
2. Gutachter:	Prof. Dr. O. Oeckler
Mündliche Prüfung am	31.10.2013

Meiner Mutter

Acknowledgment

Ganz besonderer Dank gilt Herrn Prof. Dr. Wolfgang Schnick für die Möglichkeit meine Doktorarbeit in seiner Arbeitsgruppe anzufertigen. Die Freiheit bei der Umsetzung von Ideen, die hervorragenden Arbeitsbedingungen sowie die Unterstützung bei Problemen jeder Art waren mehr als ideale Voraussetzungen für die Erstellung dieser Arbeit. Die Gelegenheit zur Ergebnispräsentation in wissenschaftlichen Zeitschriften, auf (inter)nationalen Tagungen sowie die Aufnahme in die LED-Gruppe zeigen das Vertrauen welches Herr Prof. Dr. Wolfgang Schnick in seine Mitarbeiter setzt.

Großer Dank gilt auch Herrn Prof. Dr. Oliver Oeckler, nicht zuletzt für die Übernahme des Korreferats. Seit der ersten Strukturanalyse im Jahr 2006 war Herr Prof. Dr. Oliver Oeckler stets ein hilfsbereiter Ansprechpartner bei Problemen jeglicher Art. Erst durch seine herausragende Lehre, den vielen Besprechungen und Diskussionen sowie seiner „Hilfe zur Selbsthilfe“ Strategie war es mir möglich, mich mit derart komplexen Fragestellungen zu befassen. Für seine Überarbeitungen von Publikationen und Berichten möchte ich mich besonders herzlich bedanken.

Herrn Prof. Dr. Joost Wintterlin, Herrn Prof. Dr. Hans-Christian Böttcher, Herrn Prof. Dr. Thomas M. Klapötke und Herrn Prof. Dr. Konstantin Karaghiosoff danke ich für Ihre Bereitschaft, als Teil der Prüfungskommission am Tag der mündlichen Prüfung zur Verfügung zu stehen.

Herzlich bedanken möchte ich mich auch bei allen Beteiligten an der Kooperation mit Philips Lumileds. Besonders hervorheben möchte ich dabei Herrn Dr. Peter J. Schmidt und Herrn Dr. Andreas Tücks, die mir durch zahlreiche Lumineszenzmessungen und hochinteressante Diskussionen sehr weitergeholfen haben. Sie ermöglichten mir, auch durch die Beteiligung an aktuellen Forschungsprojekten, einen tiefen Einblick in die wunderbare Welt der LEDs.

Bei Herrn Tobias Rosenthal möchte ich mich für die Durchführung von TEM-Untersuchungen sowie der Anleitung zur Probenpräparation bzw. zur Auswertung der erhaltenen Aufnahmen bedanken. Ohne dein Engagement wäre man wohl so manchem Strukturgeheimnis der untersuchten Leuchtstoffe nicht auf die Spur gekommen.

Frau Olga Lorenz, Herrn Thomas Miller und Herrn Wolfgang Wünschheim danke ich für die Hilfe bei organisatorischen, sicherheitsrelevanten oder computertechnischen Problemen. Dank dieser Hilfe war es möglich, sich voll auf die eigene Forschung zu konzentrieren.

Bei Herrn Dr. Peter Mayer möchte ich mich für die Messung von Einkristallen bedanken. Herr Dr. Mayer war stets bereit über die Messungen selbst, aber auch über die resultierenden Ergebnisse und Probleme zu diskutieren, was bei den untersuchten Verbindungen sehr häufig der Fall war.

Herrn Christian Minke bin ich zu großem Dank für die Einführung am REM verpflichtet. Auch Herr Minke stand jederzeit für Fragen und Diskussionen zur Verfügung. In gleicher Weise trifft dies auf Herrn Steffen Schmidt zu. Ganz herzlichen Dank für die Unterstützung bei Messungen jeder Art.

Großer Dank gilt auch Herrn Dr. Florian Stadler und Frau Dr. Juliane A. Kechele. Frau Dr. Kechele danke ich für die Hilfe bei der Einarbeitung in alle gängigen Arbeitstechniken zur Synthese von nitridischen Leuchtstoffen. Herrn Dr. Stadler möchte ich für die zahlreichen Voruntersuchungen zu den Verbindungen in dieser Arbeit, für die vielen Tipps und Tricks in jeglicher Hinsicht sowie den vielen spannenden Fußballabenden danken.

Mein besonderer Dank gilt meinen (Ex-)Laborkollegen Matthias Schneider, Saskia Lupart, Frauke Thienel (geb. Hintze), Tobias Rosenthal, Thorsten Schröder und Felix Fahrnbauer aus dem schönen Labor D2.100. Es war toll euch jeden Tag um mich zu haben. Die vielen produktiven Diskussionen sowie die zahlreichen lustigen Abende möchte ich nicht missen.

Für ihre tolle Unterstützung und ihren Ehrgeiz möchte ich mich bei meinen Praktikanten Peter Käshammer, Roman Pobel, Christian Ziegler, Vinicius R. Celinski, Philipp Urban, Felix Fahrnbauer und Christian Maak vielmals bedanken.

Ich möchte mich auch bei allen weiteren Kollegen der Arbeitskreise Schnick, Oeckler, Hoch, Schmedt auf der Günne, Johrendt und Lotsch ganz herzlich für die tolle Zeit hier bedanken.

Ein Dankeschön geht auch an Herrn Dr. med. Christian Himmler für das professionelle „Zusammenbasteln“ meines Schlüsselbeinknochens.

Allergrößter Dank gilt aber meiner Mutter, meinen Großeltern sowie meiner Freundin Franziska, ohne eure Hilfe und Unterstützung wäre all dies nicht möglich gewesen.

*I do not know what I may appear to the world,
but to myself I seem to have been only like a boy playing on the sea-shore,
and diverting myself in now and then finding a smoother pebble
or a prettier shell than ordinary,
whilst the great ocean of truth lay all undiscovered before me.*

(Sir Isaac Newton)

1. Introduction	1
2. Real Structure Elucidation of Eu²⁺-Doped Layered Oxonitridosilicates ...	9
2.1 Highly Efficient pc-LED Phosphors Sr_{1-x}Ba_xSi₂O₂N₂:Eu²⁺ (0 ≤ x ≤ 1) - Crystal Structures and Luminescence Properties Revisited	9
2.1.1 <i>Introduction</i>	10
2.1.2 Crystal Structures of MSi ₂ O ₂ N ₂ (M = Sr, Ba).....	12
2.1.2.1 Crystal Structure of SrSi ₂ O ₂ N ₂	12
2.1.2.1.1 History of the Structure Determination of SrSi ₂ O ₂ N ₂	12
2.1.2.1.2 Description of the Crystal Structure of SrSi ₂ O ₂ N ₂	13
2.1.2.1.3 Critical Discussion of the Literature on SrSi ₂ O ₂ N ₂	14
2.1.2.1.4 Interpretation of Diffraction Patterns.....	16
2.1.2.2 The Crystal Structure of BaSi ₂ O ₂ N ₂	17
2.1.2.3 Crystal Structures of Mixed Sr _{1-x} Ba _x Si ₂ O ₂ N ₂ (0 ≤ x ≤ 1) Phases.....	18
2.1.2.4 Similarities and Differences in Sr _{1-x} Ba _x Si ₂ O ₂ N ₂ (0 ≤ x ≤ 1) Phases.....	19
2.1.2.5 Guidelines for the Characterization of Oxonitridosilicates.....	21
2.1.3 Synthesis of Sr _{1-x} Ba _x Si ₂ O ₂ N ₂ :Eu ²⁺	23
2.1.3.1 Overview.....	23
2.1.3.2 The Carbonate Route.....	24
2.1.3.3 The Orthosilicate Route.....	25
2.1.4 Luminescence Properties of Sr _{1-x} Ba _x Si ₂ O ₂ N ₂ :Eu ²⁺ (0 ≤ x ≤ 1).....	25
2.1.4.1 Structure-Property Relations.....	25
2.1.4.2 Critical Evaluation of the Literature.....	27
2.1.5 Summary, Conclusion and Outlook.....	28
2.1.6 <i>References</i>	30
2.2 New Polymorph of the Highly Efficient LED-Phosphor SrSi₂O₂N₂:Eu²⁺ - Polytypism of a Layered Oxonitridosilicate	35
2.2.1 <i>Introduction</i>	36
2.2.2 <i>Experimental Section</i>	37
2.2.2.1 Synthesis.....	37
2.2.2.2 X-ray Spectroscopy.....	37
2.2.2.3 Powder X-ray Diffraction.....	37
2.2.2.4 Single-Crystal X-ray Diffraction.....	38
2.2.2.5 Transmission Electron Microscopy.....	38
2.2.2.6 Luminescence.....	39
2.2.3 <i>Results and Discussion</i>	39
2.2.3.1 Synthesis and chemical analysis.....	39
2.2.3.2 Single-Crystal Structure Analysis.....	40
2.2.3.3 Lattice Energy Calculations.....	41
2.2.3.4 Rietveld Refinement.....	42
2.2.3.5 Transmission Electron Microscopy and Electron Diffraction.....	43
2.2.3.6 Luminescence.....	45

2.2.4 Conclusion.....	47
2.2.5 References	48
2.3 Real Structure and Diffuse Scattering of Sr_{0.5}Ba_{0.5}Si₂O₂N₂:Eu²⁺ - A Highly Efficient Yellow Phosphor for pc-LEDs.....	51
2.3.1 Introduction.....	52
2.3.2 Experimental Section.....	55
2.3.2.1 Synthesis.....	55
2.3.2.2 Powder X-ray Diffraction.....	55
2.3.2.3 Electron Microscopy.....	55
2.3.3 Results and Discussion.....	56
2.3.3.1 Average Structure.....	56
2.3.3.2 Lattice Energy Calculations.....	59
2.3.3.3 Luminescence.....	60
2.3.3.4 Simulation of the Diffuse Scattering.....	63
2.3.3.5 SAED Simulations.....	67
2.3.4 Conclusion.....	70
2.3.5 References	71
2.4 Unexpected Luminescence Properties of Sr_{0.25}Ba_{0.75}Si₂O₂N₂:Eu²⁺ - A Narrow Blue Emitting Oxonitridosilicate with Cation Ordering.....	74
2.4.1 Introduction.....	75
2.4.2 Results and Discussion.....	76
2.4.2.1 Synthesis and Chemical Analysis.....	76
2.4.2.2 Electron Microscopy.....	77
2.4.2.3 Single-Crystal Structure Analysis.....	80
2.4.2.4 Cation Ordering as Derived from HRTEM.....	82
2.4.2.5 Luminescence.....	84
2.4.3 Conclusion.....	85
2.4.4 Experimental Section.....	86
2.4.4.1 Synthesis and Chemical Analysis.....	86
2.4.4.2 Single-Crystal X-ray Diffraction.....	87
2.4.4.3 Transmission Electron Microscopy.....	87
2.4.5 References	88
2.5 Material Properties and Structural Characterization of M₃Si₆O₁₂N₂:Eu²⁺ (M=Ba,Sr) - A Comprehensive Study on a Promising Green Phosphor for pc-LEDs.....	90
2.5.1 Introduction.....	91
2.5.2 Results and Discussion.....	93
2.5.2.1 Synthesis.....	93
2.5.2.2 Structure Determination.....	93
2.5.2.3 Structure Description.....	96
2.5.2.4 Solid-Solution Series of Ba _{3-x} Sr _x Si ₆ O ₁₂ N ₂ :Eu ²⁺	98
2.5.2.5 High-Pressure and High-Temperature Behavior.....	99

2.5.2.6 Luminescence.....	100
2.5.2.7 Band Structure and Density of States.....	102
2.5.2.8 Band-Gap Determination Using Soft X-ray Spectra.....	104
2.5.3 <i>Conclusion</i>	108
2.5.4 <i>Experimental Section</i>	110
2.5.4.1 High-Pressure Synthesis of Ba ₃ Si ₆ O ₁₂ N ₂ and Ex-Situ High-Pressure Investigations	110
2.5.4.2 Single-Crystal Synthesis.....	110
2.5.4.3 Single-Crystal X-ray Diffraction.....	111
2.5.4.4. Powder X-ray Diffraction.....	112
2.5.4.5 In-Situ High-Pressure and High-Temperature Measurements.....	112
2.5.4.6 Luminescence.....	113
2.5.4.7 EDX Measurements.....	113
2.5.4.8 Soft X-ray Spectroscopy.....	113
2.5.5 <i>References</i>	115
3. Luminescent Gallium Compounds.....	120
3.1 <i>Preface</i>	120
3.2 Magnesium Double Nitride Mg₃GaN₃ as New Host Lattice for Eu²⁺-Doping - Synthesis, Structural Studies, Luminescence and Band-Gap Determination.....	122
3.2.1 <i>Introduction</i>	123
3.2.2 <i>Experimental Section</i>	124
3.2.3 <i>Results and Discussion</i>	126
3.2.3.1 Crystal-Structure Description.....	127
3.2.3.2 DFT Calculations and Soft X-ray Spectroscopy of Mg ₃ GaN ₃	131
3.2.3.3 Luminescence Investigations.....	134
3.2.3.4 <i>Conclusion</i>	137
3.2.3.5 <i>References</i>	138
4. Crystal-Structure Investigations of Other Nitride Compounds.....	143
4.1 High-Pressure Synthesis and Characterization of Li₂Ca₃[N₂]₃ - An Uncommon Metallic Diazenide with [N₂]²⁻ Ions.....	143
4.1.1 <i>Introduction</i>	144
4.1.2 <i>Experimental Section</i>	146
4.1.2.1 Synthesis of Li ₂ Ca ₃ [N ₂] ₃	146
4.1.2.2 Powder X-ray Diffraction (PXRD).....	147
4.1.2.3 Transmission Electron Microscopy (TEM).....	149
4.1.2.4 Computational Details.....	149
4.1.2.5 Electron Spin Resonance Spectroscopy (ESR).....	150
4.1.2.6 Fourier Transform Infrared Spectroscopy (FTIR).....	150
4.1.2.7 Magnetic and Electric Conductivity Measurements.....	151
4.1.3 <i>Results and Discussion</i>	151
4.1.3.1 Unit-Cell Metrics.....	151

4.1.3.2 Theoretical Considerations of the Hexagonal Model.....	153
4.1.3.3 Improving the Structural Model	154
4.1.3.4 Description of the Crystal Structure.....	156
4.1.3.5 Infrared Spectroscopy	160
4.1.3.6 Electron Spin Resonance (ESR) Spectroscopy	163
4.1.3.7 Magnetic and Electric Conductivity Measurements	164
4.1.4 <i>Conclusion</i>	166
4.1.5 <i>References</i>	167
5. Conclusion and Outlook	173
6. Summary	177
7. Appendix	181
7.1 Supporting information for chapter 2.5	181
7.2 Supporting information for chapter 3.2	182
7.3 Supporting information for chapter 4.1	183
8. Publications	201

1. Introduction

Pioneering technical developments like the supply of electrical energy and the use of black body radiators within incandescent lamps dramatically changed life in industrialized countries. The possibility of generating light from electrical energy is the basis for modern life, which is characterized by the isolation of the activity rhythm and daylight. However, the functional principle of incandescent lamps has not changed significantly during the last century. The major disadvantage of such lamps is their low power efficiency, which means that up to 95 % of the electrical energy is converted to heat (glowing tungsten wire).^[1] Compact Fluorescent Lamps (CFLs) exhibit much higher power efficiency as their functional principle is completely different from that of incandescent lamps. Emitted ultraviolet (UV) light of an activator (typically Hg) is absorbed and re-emitted (converted to visible light) by solid-state materials (phosphors) at low process temperatures. The European Union (EU) has initiated regulatory steps on the successive ban of low efficient incandescent lamps and their replacement by CFLs.^[2] This project requires strong efforts since already in 2006 approximately 5.1 billion incandescent lamps existed in EU households. Based on the data for 2006, referring to electric power consumption of all households in the EU, the replacement should result in saving of 39 billion kWh per year. Nevertheless, in 2011 still more than 200 million incandescent lamps were sold in the EU.^[3] This might be due to the fact that CFLs contain toxic Hg and people are skeptical to use them in their households. Also potential waste-disposal problems are frequently discussed. Phosphor-converted light-emitting diodes (pc-LEDs) are an alternative to CFLs for the replacement of incandescent lamps (see Figure 1).

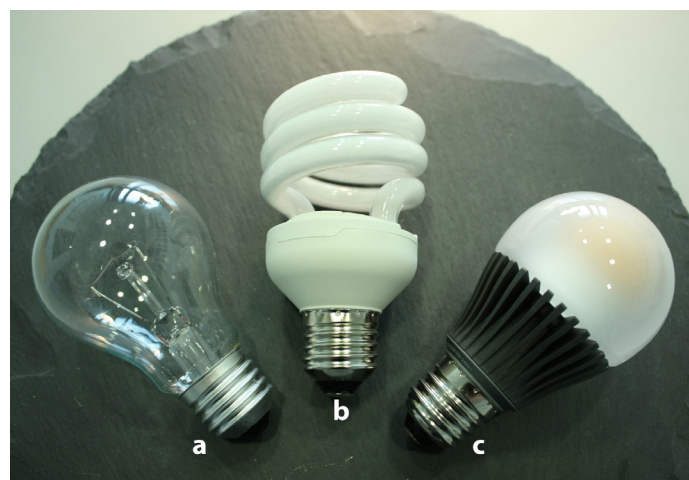


Figure 1. Incandescent lamp (a), Compact Fluorescent Lamp (CFL; b), and retrofit pc-LED bulb (c). In order to facilitate the exchange of incandescent lamps similar lamp holders (here E 27) are attached to the other devices.

These relatively new devices on the illumination market show immense economical and ecological potential and the growth of this industrial section in the last few years is very impressive. Based on a current McKinsey survey, the ratio of LEDs on the overall value of the lighting market will raise from 12 % in 2011 to over 60 % in the year 2020.^[4] The LED lighting market volume is anticipated to be around 64 billion € in 2020, which corresponds to a growth of about 700 % compared to 2011. For the company Philips Lumileds for example, the LED-based sales volume increased in the first quarter of 2013 by 38 % compared to the whole year 2012. This growth is reflected in sales of around 2 billion € during this time period, showing the great economical potential of the LED market. Since LEDs exhibit identical or even higher power efficiencies compared to CFLs and do additionally not contain toxic Hg, they are attractive candidates for the replacement of incandescent lamps also from an ecological point of view. Due to the non-toxic components, the long-life character and energy-saving potential, LEDs already find high consumer acceptance.

The discovery of efficient blue emitting GaN-LEDs by *Nakamura*^[1,5] was the basis for pc-LEDs. The functional principle of pc-LEDs is similar to that of CFLs, meaning the conversion of high-energetic radiation (here: UV to blue light from a GaN semiconductor pump LED) to light within the visible spectrum (lower energy). White light is generated by additive color mixing on top of such devices. Commercially available LEDs often contain either one yellow emitter or a combination of green-yellow and orange-red emitters (see Figure 2) for the conversion.

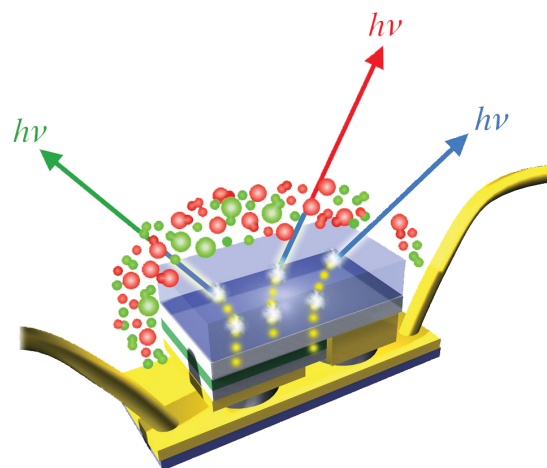


Figure 2. Schematic view on the functional principle of a 2pc-LED with green and red emitting phosphors on top of a GaN semiconductor pump LED, placed on metal substrate with electronic contacting.^[6]

The light conversion is based on the excitation of incorporated rare-earth ions (activator ions, typically Eu^{2+} , Eu^{3+} , Ce^{3+} , Tb^{3+} , or Yb^{2+}) in the solid-state material (host lattice). For e.g. Eu^{2+} , an electronic excitation transfers an electron from a 4f level to a 5d level. When relaxation to the ground state takes place, a part of the absorbed energy is re-emitted as visible light. The emission is therefore related to a parity allowed $4f^6(7F)5d^1 \rightarrow 4f^7(^8S_{7/2})$ transition. The relative position of the ground state and excited state potential mainly depends on the possibility for distortion of the excited activator ion in the crystal structure and on the coordination sphere of the activator ion itself.^[7] The difference between excitation-band maximum and emission-band maximum is called Stokes shift. As it depends on the type of chemical bonding of the activator ion to the surrounding ligands (nephelauxetic effect), this effect is most pronounced in case of highly covalent bonding. The crystal field splitting of the 5d levels as a consequence of the ligand-field strength is another impact on the relative energy-level positions (see Figure 3). Since the excitation of Eu^{2+} dramatically changes the electronic structure, a pronounced Stokes shift is observable. The probability density function exhibits maximum overlap to several energy levels, leading to a number of allowed transitions, i.e. a broad emission band. In contrast, a line emission for the parity forbidden f-f transition is observed for Eu^{3+} luminescence due to a shielding effect of noninvolved 5d levels. In this case, the electronic structure does not change significantly during the excitation process.

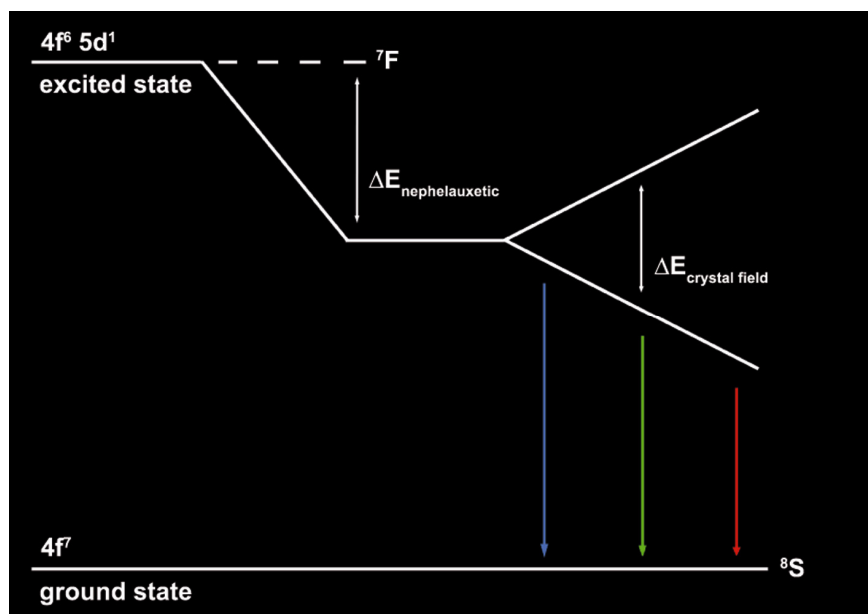


Figure 3. Schematic diagram of excitation and emission process for Eu^{2+} regarding nephelauxetic effect in dependence of Eu^{2+} -ligands in the crystal structure and splitting of 5d levels in dependence of ligand-field strength.^[8]

In addition to the desired color emission, phosphors in long-life pc-LEDs additionally have to fulfill various specifications like broadband emission, thermal and chemical stability as well as high quantum efficiency (QE).^[9,10] The latter value is often affected by thermal quenching because of strong electron-phonon coupling. This means that the absorption of a high energetic photon, followed by the electron excitation of an activator ion, does not result in the re-emission of a converted photon but just in the excitation of phonons (lattice vibrations). Such non-radiant transitions therefore decrease the conversion efficiency. Rigid host lattices often suppress this kind of quenching. (Oxo)nitridosilicates are promising host lattices for doping with rare-earth activator ions and the use in pc-LEDs, because they often comply with all requirements described. Their crystal structures are related to those of typical oxosilicates. The fundamental building units in these solids are tetrahedra on the atomic scale, where Si as central atom is coordinated by four O atoms. Liebau classified oxosilicates in dependence of the connectivity of these tetrahedra.^[11] The degree of condensation (quantified by the atomic ratio Si : O) can in principle be derived from the materials' stoichiometric formula (see Figure 4). The anion $[\text{SiO}_4]^{4-}$ represents discrete, i.e. non-condensed tetrahedra (e.g. in the orthosilicate Sr_2SiO_4). An increasing degree of condensation leads to the following anion formula units are $[\text{Si}_2\text{O}_7]^{6-}$ (group-silicates), $[\text{SiO}_3]^{2-}$ (ring- or chain-silicates), and layered silicates showing anion formula of $[\text{Si}_2\text{O}_5]^{2-}$.

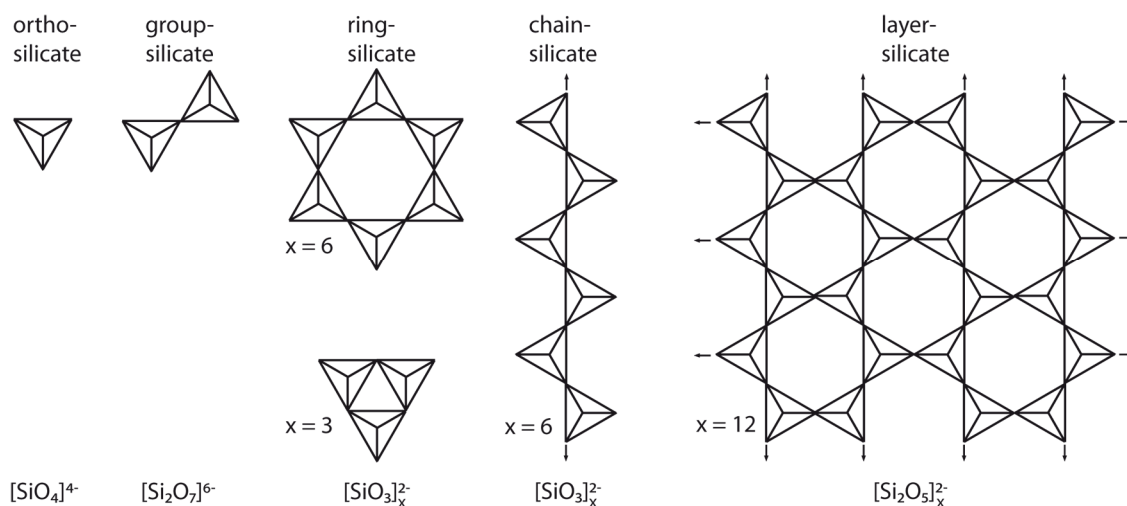


Figure 4. Schematic view on silicate substructures in oxosilicates with corresponding formula units.

If all tetrahedra are interconnected by common vertexes, a three-dimensional network is built up, e.g. in SiO_2 . Almost none of the natural silicates contain nitrogen. This is due to the fact that the Si-O bond is energetically favored compared to the analogous Si-N bond.^[12] Additionally, the nitrogen molecule ($\text{N}\equiv\text{N}$) is more stable in comparison to the oxygen

molecule ($O=O$). Dissociation of N_2 is therefore energetically unfavorable and the formation of nitridosilicates is hindered in the presence of oxygen. When silicates are synthesized under laboratory conditions in reductive atmosphere using N_2 or forming gas at high temperatures, nitride containing compounds are accessible leading to the material class of (oxo)nitridosilicates.^[10] The main difference between typical oxosilicates and (oxo)nitridosilicates is the connectivity of the tetrahedra. In oxosilicates, O atoms occupy vertex positions of the SiO_4 tetrahedra which connect up to two tetrahedra. In contrast, N atoms typically bridge up to three tetrahedra meaning that many variations of silicate substructures are possible. In e.g. $MYb[Si_4N_7]$ ($M = Eu, Sr, Ba$)^[13-15] the N atoms bridge even four tetrahedra, which leads to star-shaped units (see Figure 5).

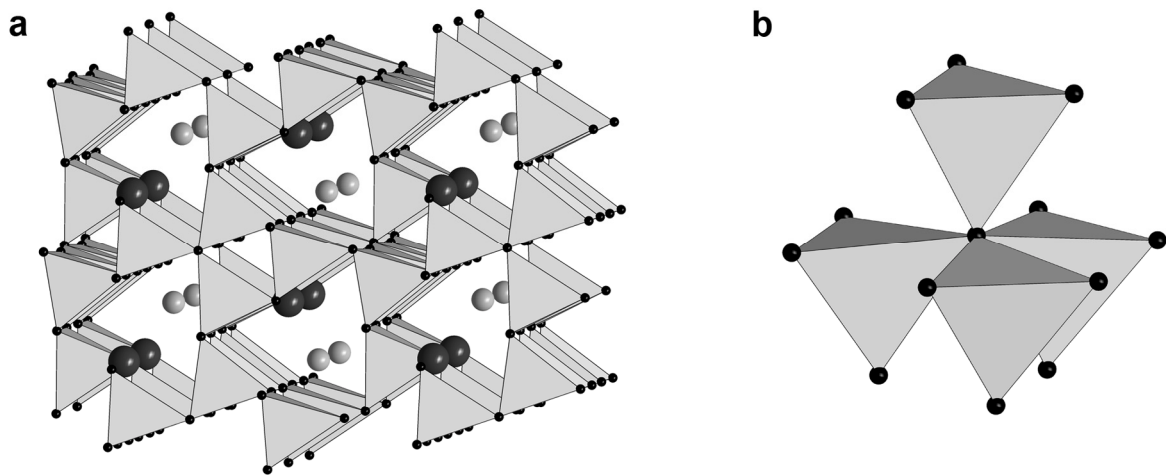


Figure 5. Crystal structure of $MYbSi_4N_7$ ($M = Eu, Sr, Ba$): a) viewed approximately along sheets of highly condensed *dreier* rings $[100]$; $[SiN_4]$ layers gray, metal ions large black and light gray spheres, nitrogen small black spheres, b) $[N(SiN_3)_4]$ building block with N^{4-} .^{[4], [10,13-15]}

Related to the structural variety within the class of (oxo)nitridosilicates and the described relationships between the material properties on the crystal structure and the composition, the emission wavelength of Eu^{2+} -doped (oxo)nitridosilicates is tunable over a wide range. High QEs can be achieved with these materials since electron-phonon coupling is suppressed in the case of a high degree of $Si(O/N)_4$ tetrahedra condensation (rigid host lattice). The most prominent representative of a Eu^{2+} -doped silicate host lattice, found in our research group, is $Sr_2Si_5N_8$.^[16] This nitridosilicate is made up of a three-dimensional network structure and is already used in commercial pc-LED applications. $Sr_2Si_5N_8:Eu^{2+}$, as well as the isotopic $Ba_2Si_5N_8:Eu^{2+}$, exhibits intense luminescence in the orange to red region of the visible spectrum while excited by UV to blue light (see Figure 6).^[17] The two crystallographic

independent Sr-sites are exclusively coordinated by N, while the coordination spheres can be described as pentagonal or hexagonal pyramids, respectively.



Figure 6. LMU written on black paper using $\text{Sr}_2\text{Si}_5\text{N}_8:\text{Eu}^{2+}$ phosphor excited by UV to blue light.^[8]

In our group, the oxonitridosilicate $\text{SrSi}_2\text{O}_2\text{N}_2$ ^[18-20] was discovered as a consequence of an oxygen contamination during the synthesis of $\text{Sr}_2\text{Si}_5\text{N}_8$ ^[16]. Today, common synthesis strategies for $\text{SrSi}_2\text{O}_2\text{N}_2$ of high purity are the carbonate and orthosilicate route.^[21] In analogy to $\text{Sr}_2\text{Si}_5\text{N}_8$, the Sr^{2+} atoms in $\text{SrSi}_2\text{O}_2\text{N}_2$ can be substituted by Eu^{2+} due to comparable ionic radii.^[22] Here Eu^{2+} is coordinated by O ions in a trigonal prismatic way. According to the less pronounced nephelauxetic effect (lower covalency of Eu-O bond compared to Eu-N), a blue shift of the emission is observed for $\text{SrSi}_2\text{O}_2\text{N}_2:\text{Eu}^{2+}$ in comparison to that of $\text{Sr}_2\text{Si}_5\text{N}_8:\text{Eu}^{2+}$.^[23,24] $\text{SrSi}_2\text{O}_2\text{N}_2:\text{Eu}^{2+}$ is therefore a phosphor with intense luminescence in the yellow to green spectral region. The combination of $\text{Sr}_2\text{Si}_5\text{N}_8:\text{Eu}^{2+}$ and $\text{SrSi}_2\text{O}_2\text{N}_2:\text{Eu}^{2+}$ as phosphors in a highly efficient warm-white pc-LED has been suggested.^[6] In addition to the pure Sr-compound, phases with composition $\text{Sr}_{1-x}\text{Ba}_x\text{Si}_2\text{O}_2\text{N}_2$ ($0 \leq x \leq 1$) are also very attractive candidates for host lattices (details on the crystal structures of $\text{Sr}_{1-x}\text{Ba}_x\text{Si}_2\text{O}_2\text{N}_2$ phases can be found in section 2.1). Eu^{2+} -doped samples show intense emission in the blue-green to green-yellow spectral region.^[25-31] Nevertheless, there are still some questions to explore concerning these phases, e.g. the determination of crystal structures, the phase pure synthesis in dependence of the synthesis route and the establishment of structure-property relations.

In this thesis, the real structures and luminescence properties of the phases $\text{Sr}_{1-x}\text{Ba}_x\text{Si}_2\text{O}_2\text{N}_2:\text{Eu}^{2+}$ ($0 \leq x \leq 1$) are investigated in detail, clarifying the question if they qualify for the use as phosphors in commercial pc-LEDs. It is discussed in detail how the deviations from an ordered crystal structure affect the luminescence properties of these

outstanding materials. Besides answering these questions, other silicate-analogous luminescent compounds are discussed with respect to the crystal structure and luminescence properties. Such materials are also of high interest because they might increase the variety of available phosphor materials for industrial applications. The investigations in this thesis help to understand in detail the impact of e.g. atomic arrangement, crystal structure, structure defects, band gap, synthesis route and composition of the host lattice on materials properties. Additionally, these investigations on highly efficient phosphors impressively show that sometimes only the complementary use of X-ray diffraction, electron microscopy, and spectroscopic methods leads to reliable structure models. These are necessary since only a comprehensible understanding of structure-property relationships enables scientists to establish strategies for the systematic improvement of the material properties.

References

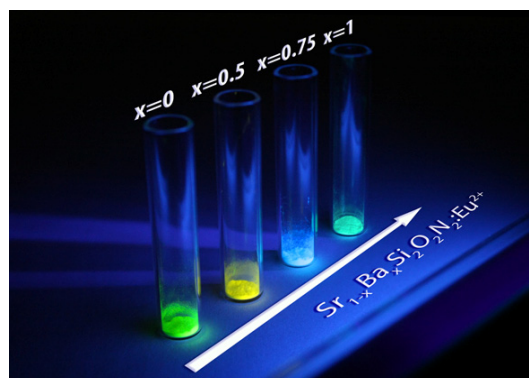
- [1] C. Feldmann, *Z. Anorg. Allg. Chem.* **2012**, *638*, 2169-2171.
- [2] http://ec.europa.eu/energy/lumen/professional/index_de.htm; visited on 31st July 2013; follow link "FAQ für Fachleute".
- [3] <http://www.zdf.de/WISO/Abschied-von-der-Gl%C3%BChbirne-23807592.html>; visited on 31st July 2013. Original text is delivered on request.
- [4] McKinsey & Company, *Lighting the way: Perspectives on the global lighting market*; second edition.
- [5] S. Nakamura, M. Senoh, T. Mukai, *Appl. Phys. Lett.* **1993**, *62*, 2390-2392.
- [6] R. Mueller-Mach, G. Mueller, M. R. Krames, H. A. Höpfe, F. Stadler, W. Schnick, T. Juestel, P. Schmidt, *Phys. Status Solidi A*, **2005**, *202*, 1727-1732 .
Copyright © 2005 WILEY-VCH Verlag GmbH & Co. KGaA, Weinheim
- [7] G. Blasse, B. C. Grabmaier, *Luminescent Materials*, edition 1, Springer Berlin Heidelberg, Germany (**1994**).
- [8] Picture originates from a collaboration of Philipp Pust, Sebastian Schmiechen, Frauke Hintze, and Markus Seibald.
- [9] P. F. Smet, A. B. Parmentier, D. Poelman, *J. Electrochem. Soc.* **2011**, *158*, R37-R57.
- [10] M. Zeuner, S. Pagano, W. Schnick, *Angew. Chem.* **2011**, *123*, 7898-7920; *Angew. Chem. Int. Ed.* **2011**, *50*, 7754-7775.
- [11] F. Liebau, *Naturwissenschaften* **1962**, *49*, 481-490.

- [12] W. Schnick, *Angew. Chem.* **1993**, *105*, 846-858; *Angew. Chem. Int. Ed. Engl.* **1993**, *32*, 806-808.
- [13] H. Huppertz, W. Schnick, *Z. Anorg. Allg. Chem.* **1997**, *623*, 212-217.
- [14] W. Schnick, H. Huppertz, *Chem. Eur. J.* **1997**, *3*, 679-683.
- [15] H. Huppertz, W. Schnick, *Acta Crystallogr., Sect. C: Cryst. Struct. Commun.* **1997**, *53*, 1751-1753.
- [16] T. Schlieper, W. Milius, W. Schnick, *Z. Anorg. Allg. Chem.* **1995**, *621*, 1380-1384.
- [17] H. A. Höpfe, H. Lutz, P. Morys, W. Schnick, A. Seilmeier, *J. Phys. Chem. Solids* **2000**, *61*, 2001-2006.
- [18] H. A. Höpfe, *Dissertation*, **2003**, LMU Munich.
- [19] O. Oeckler, F. Stadler, T. Rosenthal, W. Schnick, *Solid State Sci.* **2007**, *9*, 205-212.
- [20] M. Seibald, T. Rosenthal, O. Oeckler, C. Maak, A. Tücks, P. J. Schmidt, D. Wiechert, W. Schnick, *Chem. Mater.* **2013**, *25*, 1852-1857.
- [21] M. Seibald, T. Rosenthal, O. Oeckler, and W. Schnick, *Crit. Rev. Solid State Mater. Sci.* **2013**, (accepted).
- [22] R. D. Shannon, *Acta Crystallogr., Sect. A: Found. Crystallogr.* **1976**, *32*, 751-767.
- [23] Y. Q. Li, A. C. A. Delsing, G. de With, H. T. Hintzen, *Chem. Mater.* **2005**, *17*, 3242-3248.
- [24] V. Bachmann, C. Ronda, O. Oeckler, W. Schnick, A. Meijerink, *Chem. Mater.* **2009**, *21*, 316-325.
- [25] M. Seibald, T. Rosenthal, O. Oeckler, F. Fahrnbauer, A. Tücks, P. J. Schmidt, W. Schnick, *Chem. Eur. J.* **2012**, *18*, 13446-13452.
- [26] M. Seibald, O. Oeckler, V. R. Celinski, P. J. Schmidt, A. Tücks, W. Schnick, *Solid State Sci.* **2011**, *13*, 1769-1778.
- [27] B. Lei, K. Machida, T. Horikawa, H. Hanzawa, *Chem. Lett.* **2011**, *40*, 140-141.
- [28] I. H. Cho, G. Anoop, D. W. Suh, S. J. Lee, J. S. Yoo, *Opt. Mater. Express* **2012**, *2*, 1292-1305.
- [29] B. Y. Han, K.-S. Sohn, *Electrochem. Solid-State Lett.* **2010**, *13*, J62-J64.
- [30] B.-G. Yun, Y. Miyamoto, H. Yamamoto, *J. Electrochem. Soc.* **2007**, *154*, J320-J325.
- [31] G. Anoop, I. H. Cho, D. W. Suh, J. S. Yoo, *Phys. Status Solidi A* **2012**, *209*, 2635-2640.

2. Real Structure Elucidation of Eu^{2+} -Doped Layered Oxonitridosilicates

2.1 Highly Efficient pc-LED Phosphors $\text{Sr}_{1-x}\text{Ba}_x\text{Si}_2\text{O}_2\text{N}_2:\text{Eu}^{2+}$ ($0 \leq x \leq 1$) - Crystal Structures and Luminescence Properties Revisited

Markus Seibald, Tobias Rosenthal, Oliver Oeckler, and Wolfgang Schnick



published in: *Crit. Rev. Solid State Mater. Sci.* **2014**, Author's Accepted Manuscript.

Copyright © 2014 Taylor & Francis

Abstract

Due to their excellent luminescence properties in the blue-green to green-yellow spectral region, oxonitridosilicates $\text{Sr}_{1-x}\text{Ba}_x\text{Si}_2\text{O}_2\text{N}_2:\text{Eu}^{2+}$ ($0 \leq x \leq 1$) are promising conversion materials for application in phosphor-converted high-power LED devices. In order to understand the properties and thus to fully exploit the potential of these materials, detailed knowledge of corresponding (local) crystal structures is indispensable. Detailed insights into real structures have been achieved by combining X-ray diffraction and electron-microscopy methods. A major reason for the excellent luminescence properties of the phases $\text{Sr}_{1-x}\text{Ba}_x\text{Si}_2\text{O}_2\text{N}_2:\text{Eu}^{2+}$ ($0 \leq x \leq 1$) is the rigid silicate substructure built up of two-dimensionally condensed SiON_3 tetrahedra. The general topology of these layers is analogous for all members. However, there is no complete solid-solution series. Crystal-structure determination was frequently not straightforward because several real-structure effects had to be considered. The relative orientation of the silicate layers and the metal-atom layers inserted between them can differ without changing the chemical composition. As a consequence, polytypes are formed. The differentiation between such closely related structures was only possible by a thorough analysis of crystallographic data. The same applies for phases which

differ in their composition as all $\text{Sr}_{1-x}\text{Ba}_x\text{Si}_2\text{O}_2\text{N}_2:\text{Eu}^{2+}$ ($0 \leq x \leq 1$) phases are very similar. The literature on these compounds is critically discussed with respect to phase analysis and structure determination. Different synthesis routes are reviewed and the results of luminescence investigations are discussed in this contribution. Beyond thermal as well as chemical stability and high transparency, electron-phonon coupling is effectively suppressed in $\text{Sr}_{1-x}\text{Ba}_x\text{Si}_2\text{O}_2\text{N}_2:\text{Eu}^{2+}$ ($0 \leq x \leq 1$) phases. Therefore, primary UV to blue light (GaN based semiconductor LEDs) is efficiently converted into visible components of the spectrum. $\text{Sr}_{1-x}\text{Ba}_x\text{Si}_2\text{O}_2\text{N}_2:\text{Eu}^{2+}$ ($0 \leq x \leq 1$) phases are therefore promising oxonitridosilicate phosphors for application in LED industry.

Keywords: Structure-Property Relationships, Solid-State Lighting, Oxonitridosilicates

2.1.1 Introduction

The limited amount of primary energy resources (fossil fuels) in times of dramatic increase of worldwide energy demand is one of the major challenges of our society. Besides improvement of existing alternative energy sources (solar power, wind, etc.) and the development of new technologies, it is important to use the available energy in the most efficient way possible. It is up to science to search for new methods and materials to achieve this goal. For example, huge amounts of electric energy can be saved by replacing highly inefficient incandescent lamps by phosphor-converted light-emitting diodes (pc-LEDs). Therefore, several governments have already taken measures to ban light bulbs.^[1-6]

There are various types of pc-LEDs which mainly differ in the number, arrangement and composition of luminescent solid-state materials (phosphors).^[3,7-12] A number of phosphors emit light within the whole visible spectrum.^[4,8-10,13-18] They are used in combination with a semiconductor pump LED. For these long-life light-conversion devices, phosphors have to fulfill various specifications like broadband emission, thermal and chemical stability, as well as high quantum efficiency (QE).^[19,20] Alkaline earth (oxo)nitridosilicates are promising host lattices which often comply with all these requirements. These refractory materials have a high chemical stability, a large band gap and they show no absorption in the visible.^[20] Because of their structural variety, the emission signal is tunable over a wide range. Pc-LEDs using silicate-based phosphor materials with QE close to 100 % are therefore the most efficient way to convert electric energy to visible light. For efficient conversion of primary

UV to blue light into the yellow-green region of the visible spectrum, $\text{MSi}_2\text{O}_2\text{N}_2:\text{Eu}^{2+}$ phases (M = Ca, Sr, Ba) are specifically well suited.^[21-23]

$\text{CaSi}_2\text{O}_2\text{N}_2$ (space group $P2_1$ (no. 4), $V = 1028.3 \text{ \AA}^3$), for instance, exhibits an uncommon stoichiometric formula with respect to the fact that it is a simple layered silicate. The atomic ratio $\text{Si} : (\text{O},\text{N}) = 1 : 2$ is rather indicative for a 3D network structure of all-side vertex sharing $\text{Si}(\text{O},\text{N})_4$ tetrahedra.²⁴ However, the formula results because the N-atoms are bridging three $\text{SiO}^{[1]}\text{N}_3^{[3]}$ tetrahedra and form *dreier* rings in the silicate layers which can be described in terms of condensed *dreier* single chains (see Figure 1).

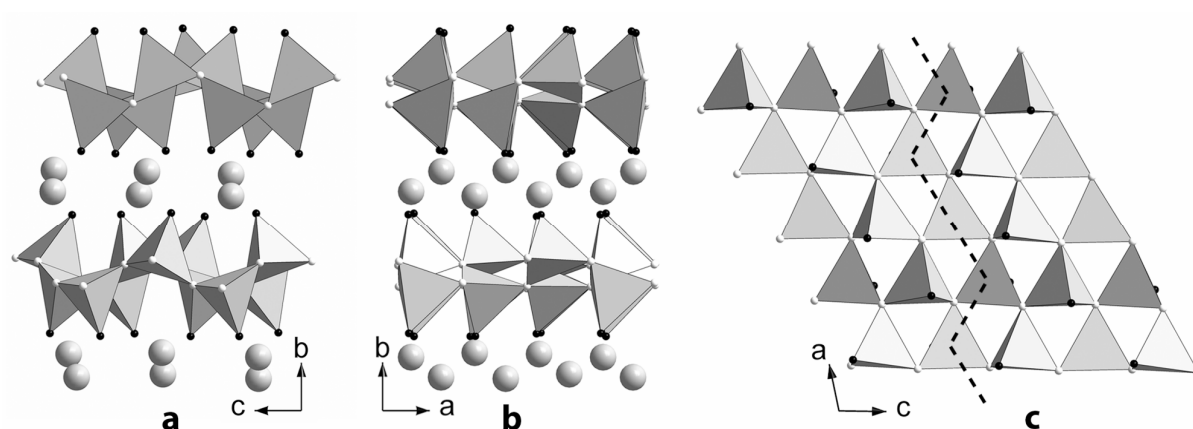


Figure 1. Crystal structure of $\text{CaSi}_2\text{O}_2\text{N}_2$ viewed along [100] (a), [001] (b, alternating orientation of silicate layers along stacking direction), and [010] (c). Tetrahedra are drawn in gray, indicating O (small black spheres) and N (small white spheres) atoms, respectively. Ca-ions between the silicate layers are shown as large gray spheres. *Dreier* single chains within the silicate layers are indicated by a dashed black line (c).

The structural motif of *dreier* rings within the silicate partial structure can be found in various (oxo)nitrido(alumo)silicate materials and might be one reason for their stability.^[25-31] The presence of O in $\text{CaSi}_2\text{O}_2\text{N}_2$ was confirmed by ^{29}Si solid-state NMR, interpretation of metal-ligand distances, electrostatic calculations and chemical analysis.^[24,32-34] As their luminescence properties are more interesting than those of $\text{CaSi}_2\text{O}_2\text{N}_2:\text{Eu}^{2+}$ (emission wavelength (λ_{em}) = 560 nm, full width at half maximum (FWHM) ~ 100 nm),^[21,22] $\text{Sr}_{1-x}\text{Ba}_x\text{Si}_2\text{O}_2\text{N}_2:\text{Eu}^{2+}$ ($0 \leq x \leq 1$) phases have been investigated in much more detail. In this contribution, a broad range of reports on $\text{Sr}_{1-x}\text{Ba}_x\text{Si}_2\text{O}_2\text{N}_2:\text{Eu}^{2+}$ are critically discussed. The focus is on crystal structure, syntheses, and the influence of the substitution of Sr^{2+} by Ba^{2+} on the luminescence properties. We attempt to sort out imprecise assumptions present in literature referring to structure-property relations and summarize the state-of-the-art knowledge about $\text{Sr}_{1-x}\text{Ba}_x\text{Si}_2\text{O}_2\text{N}_2:\text{Eu}^{2+}$ phosphors.

2.1.2 Crystal Structures of $\text{MSi}_2\text{O}_2\text{N}_2$ ($M = \text{Sr}, \text{Ba}$)

2.1.2.1 Crystal Structure of $\text{SrSi}_2\text{O}_2\text{N}_2$

2.1.2.1.1 History of the Structure Determination of $\text{SrSi}_2\text{O}_2\text{N}_2$

In 1994, Zhu et al. first reported a material with nominal composition $\text{SrSi}_2\text{O}_2\text{N}_2$.^[35] Based on diffraction data they claimed a high-temperature (X_2 ; $V = 965.3 \text{ \AA}^3$) and a low-temperature modification (X_1 ; $V = 748.3 \text{ \AA}^3$), both exhibiting orthorhombic unit cells, yet with different metrics. In the context of the structure determination of $\text{CaSi}_2\text{O}_2\text{N}_2$,^[24] $\text{SrSi}_2\text{O}_2\text{N}_2$ was reported to exhibit layers that can be viewed as a cutout of the structure of the mineral sinoite ($\text{Si}_2\text{N}_2\text{O}$). Concluding from luminescence measurements on Eu^{2+} -doped samples, the crystal structures of $\text{CaSi}_2\text{O}_2\text{N}_2$ and $\text{SrSi}_2\text{O}_2\text{N}_2$ were assumed to be closely related to each other. Apparently, Sr- as well as Ca-ions are predominantly coordinated by O-ions in the corresponding crystal structures causing an emission signal in the yellow-green spectral region. The potential application of $\text{SrSi}_2\text{O}_2\text{N}_2:\text{Eu}^{2+}$ as a green phosphor in an all-nitride pc-LED also confirms earlier results.^[36] However, the X-ray powder pattern was published later by Li et al.^[22] Latter authors assume that $\text{SrSi}_2\text{O}_2\text{N}_2$ is monoclinic and crystallizes in space group $P2_1/m$ with $V = 1234.67 \text{ \AA}^3$. The corresponding PXRD pattern was fitted using the Le Bail method without a structure model. Deviations from the nominal composition $\text{SrSi}_2\text{O}_2\text{N}_2$ have been postulated in this work (see also chapter 2.1.2.1.3). Finally, investigations on $\text{EuSi}_2\text{O}_2\text{N}_2$ shed light on the structure of $\text{SrSi}_2\text{O}_2\text{N}_2$. Because of the similar ionic radii of Eu^{2+} and Sr^{2+} ,^[37] the crystal structures are expected to be isotopic or at least very closely related. The PXRD pattern of a new “europium-silicon-oxynitride” $\text{EuSi}_2\text{O}_2\text{N}_2$ ^[38] resembled the one of $\text{SrSi}_2\text{O}_2\text{N}_2$ although different unit-cell metrics ($V = 1756.56 \text{ \AA}^3$) were reported. Additionally, a different monoclinic space group ($P2_1/a$) was deduced from reflection conditions. Later, Stadler et al. presented a single-crystal structure determination of $\text{EuSi}_2\text{O}_2\text{N}_2$ which was complemented by electron-microscopy methods.^[39] The triclinic crystal structure (space group $P1$, $V = 360.19 \text{ \AA}^3$) is similar to that of $\text{CaSi}_2\text{O}_2\text{N}_2$, representing a layered material although the stoichiometric formula is more indicative for a 3D silicate network. The crystal structure was confirmed by Rietveld refinement and simulations of high-resolution transmission electron-microscopy (HRTEM) images. The utilization of electron-microscopy methods led to the characterization of various real-structure effects like twinning, anti-phase domain boundaries and presence of intergrown domains with different orientations.

The combination of X-ray diffraction and electron-microscopy methods finally showed that the crystal structure of SrSi₂O₂N₂ ($V = 358.72 \text{ \AA}^3$) is isotypic to that of EuSi₂O₂N₂.^[40] The presence of various real-structure effects and their impact on diffraction patterns and HRTEM images is shown which also confirms the triclinic structure (space group $P1$). Later reports on a monoclinic crystal structure of SrSi₂O₂N₂ claim space group $P2_1/m$,^[41] however, lattice parameters are completely different from those reported earlier by Li et al.^[22] In further investigations these results could not be confirmed. Yet, the latest investigation on the crystal structure of SrSi₂O₂N₂^[42] revealed a monoclinic modification of SrSi₂O₂N₂ (space group $P2_1$; $V = 725.3 \text{ \AA}^3$), significantly different from the triclinic one. The structure model was derived from single-crystal data and confirmed by Rietveld refinement and simulations of electron-diffraction and HRTEM images.

2.1.2.1.2 Description of the Crystal Structure of SrSi₂O₂N₂

As various sets of lattice parameters have been reported for SrSi₂O₂N₂ (and EuSi₂O₂N₂) as described in the previous section, it is obvious that determination of unit-cell metrics is not trivial. The structural parameters from EuSi₂O₂N₂ single-crystal data, which have been confirmed by various methods,^[39] describe a consistent and reliable structure model. Although noncentrosymmetric triclinic structures are rare, it is unambiguous that EuSi₂O₂N₂ crystallizes in space group $P1$ with $a = 7.095(1)$, $b = 7.246(1)$, $c = 7.256(1) \text{ \AA}$, $\alpha = 88.69(2)$, $\beta = 84.77(2)$, $\gamma = 75.84(2)^\circ$, $V = 360.19(9) \text{ \AA}^3$. Based on this result, a comprehensive study showed that triclinic SrSi₂O₂N₂ is isotypic to EuSi₂O₂N₂ and exhibits very similar lattice parameters: $a = 7.0802(2)$, $b = 7.2306(2)$, $c = 7.2554(2) \text{ \AA}$, $\alpha = 88.767(3)$, $\beta = 84.733(2)$, $\gamma = 75.905(2)^\circ$, $V = 358.73(2) \text{ \AA}^3$.^[40] Both layered oxonitridosilicates are built up of alternating metal-ion and silicate layers stacked along $[010]^*$. The structures exhibit various real-structure effects like twinning, stacking disorder or orientated intergrowth (see section 2.1.2.1.4). The metal atoms are arranged in corrugated, pseudo-hexagonal sheets. The silicate layers consist of highly condensed SiO^[1]N₃^[3] tetrahedra forming *zweier* single chains – as opposed to *dreier* single chains in CaSi₂O₂N₂ – as a consequence of their up-down sequence (see Figure 2).

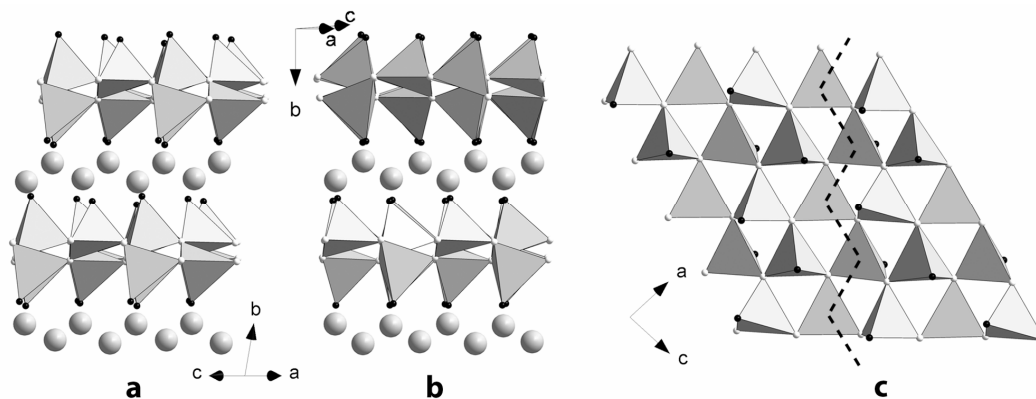


Figure 2. Crystal structure of $\text{SrSi}_2\text{O}_2\text{N}_2$ viewed along $[101]$ (a, triclinic modification, uniform silicate layer orientation in consecutive layers); $[10\bar{1}]$ (b, monoclinic modification, alternating orientation of consecutive silicate layers); $[010]$ (c). Tetrahedra are drawn in gray, indicating O (small black spheres) and N (small white spheres) atoms, respectively. Sr-ions between the silicate layers are shown as large gray spheres. *Zweier* single chains within the silicate layers are indicated by a dashed black line (c).

Oxygen and nitrogen have very similar X-ray atomic form factors. As a consequence, reliable differentiation between O and N is not trivial by structure determination on the basis of X-ray diffraction data. Accordingly, it has been accomplished by analyzing bond lengths, considering the position of luminescence emission, and following Pauling's rules. Oxygen ions favor terminal positions instead of those bridging three neighboring Si atoms. Threefold bridging N^[3]-atoms are the reason why compounds of stoichiometric formula $\text{MSi}_2\text{O}_2\text{N}_2$ ($M = \text{Ca}, \text{Sr}, \text{Eu}, \text{Ba}$) exhibit layered silicate substructures instead of a 3D network usually found for an atomic ratio $\text{Si} : (\text{O}/\text{N}) = 1 : 2$. Recently, a further monoclinic modification of $\text{SrSi}_2\text{O}_2\text{N}_2$ (space group $P2_1$, see Figure 2) was published with lattice parameters of $a = 7.1036(14)$, $b = 14.078(3)$, $c = 7.2833(15)$ Å, $\beta = 95.23(3)^\circ$, and $V = 725.3(3)$ Å³.^[42] The corresponding unit cell is enlarged by a factor of approximately 2 along the stacking direction $[010]^*$ in comparison to the triclinic phase (see also section 2.1.2.4).

2.1.2.1.3 Critical Discussion of the Literature on $\text{SrSi}_2\text{O}_2\text{N}_2$

The experimental positions of characteristic reflections in the PXRD pattern of the high-temperature phase X_2 of a sample $\text{SrO}:\text{Si}_2\text{N}_2\text{O}$, as reported by Zhu et al.^[35] (X_2 ; $d_{200} = 7.04$, $d_{400} = 3.520$, $d_{022} = 2.826$ Å), can be assigned to typical reflections of triclinic $\text{SrSi}_2\text{O}_2\text{N}_2$ as reported by Oeckler et al.^[40] ($d_{010} = 7.02$, $d_{020} = 3.513$, $d_{210} = 2.821$, $d_{220} = 2.820$ Å). The unit-cell volume according to the orthorhombic indexing by Zhu et al. differs by a factor of 2.7 from the value reported by Oeckler et al.^[35,40] The monoclinic indexing of Li et al.^[22] results in a huge amount of theoretical reflection positions. Most of them are not observed in

the experiment, while the presented PXRD pattern is analogous to the one shown by Oeckler et al.^[40] Thus, the samples are comparable, but monoclinic indexing of PXRD pattern with large lattice parameters is not significant in this case. Variations of the chemical composition depending on the synthesis strategy have been assumed; distinguishing oxygen- ($\delta = 0$) and nitrogen-rich ($\delta = 1$) samples according to formula $\text{SrSi}_2\text{O}_{2-\delta}\text{N}_{2+2/3\delta}$.^[22] This was deduced from reflection intensities in the corresponding PXRD patterns. Yet, samples with different δ exhibit very similar PXRD patterns. The intensity differences are limited to just two reflections ($d_{040} = 3.53 \text{ \AA}$ ($25.35^\circ 2\theta$) and $d_{400} = 2.83 \text{ \AA}$ ($31.69^\circ 2\theta$)). However, the atom form factors of O and N are similar and contribute little to the scattered intensity, which is dominated by Si and Sr atoms. Furthermore, nitrogen-rich compounds $\text{SrSi}_2\text{O}_{2-\delta}\text{N}_{2+2/3\delta}$ (e.g., with $\delta = 1$) would contain fewer anions and therefore require deviations from the present silicate substructure.^[39,40,42] In electroneutral $\text{SrSi}_2\text{O}_2\text{N}_2$ ($\delta = 0$) four anions per formula unit are required for the layered structure described above. Electroneutral nitrogen-rich $\text{SrSi}_2\text{ON}_{2+2/3}$ formally contains $11/3$ anions per formula unit instead of $12/3 = 4$. This means that in every third tetrahedron one corner would be absent which is inconsistent with the refined structure model.^[39,40,42] The intensity variation observed in PXRD patterns is more likely to be due to preferred orientation of the crystallites (texture) as suggested by the indices of the respective reflections. They can be correlated to the stacking direction of metal-atom and silicate layers.^[43] The PXRD pattern was claimed to be close to that of the X_1 -phase (low-temperature phase); however, the positions of the strongest observed reflections resemble those of the X_2 -phase (high-temperature phase). Additionally, characteristic $d_{020} = 7.08 \text{ \AA}$ is also similar to reported values, therefore all three authors (Zhu, Li and Oeckler) investigated the same phase.^[22,35,40] An atomic ratio $\text{O} : \text{N} > 1$ in the silicate substructure as reported by Anoop et al.^[44] would require cation vacancies, for which no experimental evidence was reported. In contrast to “nitrogen-rich samples” such compounds would contain more than 4 anions per sum formula.

In principle, similar assumptions have been made for $\text{EuSi}_2\text{O}_2\text{N}_2$, whose PXRD pattern was also indexed with a large monoclinic unit cell.^[38] Unit-cell volume is about 5 times that derived from single-crystal data.^[39] In contrast to $\text{SrSi}_2\text{O}_2\text{N}_2$ ($P2_1/m$)^[22] the space group was determined to be $P2_1/a$; however, e.g., reflection 30-5 with $I/I_0 = 20 \%$ should then be absent. In the PXRD pattern, preferred orientation can be observed unequivocally regarding relative intensity of the first reflection.^[43]

2.1.2.1.4 Interpretation of Diffraction Patterns

Structure investigations on $\text{Sr}/\text{EuSi}_2\text{O}_2\text{N}_2$ need to consider a variety of effects. Reflections are not single indexed due to pronounced overlap problems as a consequence of triclinic unit-cell metrics. Therefore, the determination of lattice parameters from the strongest reflections in PXRD data is ambiguous. Techniques which take into account 3D reciprocal space, such as single-crystal X-ray diffraction or selected-area electron diffraction (SAED) are reliable in such cases. Yet, the analysis of such diffraction patterns is complicated by the fact that triclinic $\text{SrSi}_2\text{O}_2\text{N}_2$ (also $\text{EuSi}_2\text{O}_2\text{N}_2$) tends to form twin domains which involve overlapping reflections.^[39,40] Due to the special values of lattice parameters, α^* is close to 90° so that reflections with $h = 2n$ overlap completely whereas reflections with $h = 2n + 1$ show additional reflections from the other twin individual. If this is not recognized, a larger unit cell of higher symmetry is found. Additionally, diffuse streaks in rows where reflections of both twin individuals do not overlap are frequently observed indicating stacking disorder. Structure determination was therefore accomplished using crystals with large twin domains and thus negligible diffuse scattering. Twinning which corresponds to a 180° rotation around $[010]^*$ (twin law $(-100, -\frac{1}{2}10, 00-1)$) was taken into account. The twinning is due to the higher symmetry of the metal-ion and silicate layers, respectively. Rotated metal-ion layers fit into silicate layers in the same way as the original ones. Diffuse scattering results from a large number of parallel twin and / or anti-phase boundaries which can be viewed as stacking faults. The average crystal structure of $\text{SrSi}_2\text{O}_2\text{N}_2$ derived from Rietveld refinement exhibits disordered metal-atom positions while the alternative set of cation positions is occupied with a probability of 20 %.^[40] This affects the diffracted intensities significantly so that phase analysis should involve the refinement of structure data. Preferred orientation can be recognized by comparing the relative intensities of 010, 020 and $-210 / 220$ (overlap) reflections and should be included in Rietveld refinements. The interpretation of SEAD patterns can be problematic if oriented intergrowth is present and, e.g., zone axis orientations $[001]$ and $[100]$ superimpose. Such intergrowth is possible due to a pseudotetragonal arrangement of O-ions in the silicate substructure so that metal ions fit onto silicate layers in different ways. If powder samples contain triclinic and monoclinic $\text{SrSi}_2\text{O}_2\text{N}_2$ polytypes, some reflections in PXRD patterns ($14.0, 17.8, 20.9, 22.7, \text{ and } 29.4^\circ 2\theta$, Cu- $K_{\alpha 1}$ radiation) can exclusively be assigned to monoclinic $\text{SrSi}_2\text{O}_2\text{N}_2$.^[42] In single-crystal X-ray and SAED patterns, both polytypes can clearly be distinguished based on their translation periods along

the stacking direction $[010]^*$. The platelet-shape morphology occasionally requires embedding the powder for TEM investigations in order to avoid preferred orientation.

2.1.2.2 The Crystal Structure of $\text{BaSi}_2\text{O}_2\text{N}_2$

A closer look at $\text{BaSi}_2\text{O}_2\text{N}_2$ is helpful to understand the structure of mixed $\text{Sr}_{1-x}\text{Ba}_x\text{Si}_2\text{O}_2\text{N}_2$ ($0 \leq x \leq 1$) phases (see section 2.1.2.3). $\text{BaSi}_2\text{O}_2\text{N}_2$ was first characterized by indexing a PXRD pattern using the strongest reflections.^[22] A unit cell with monoclinic metrics ($a = 14.070(4)$, $b = 7.276(2)$, $c = 13.181(3)$ Å, $\beta = 107.74(6)^\circ$, $V = 1285.23$ Å³) was assumed. However, the crystal structure of $\text{BaSi}_2\text{O}_2\text{N}_2$ as determined using X-ray diffraction and electron-microscopy methods combined with neutron powder diffraction^[45] was described with an orthorhombic unit cell with $a = 14.3902(3)$, $b = 5.3433(1)$, $c = 4.8325(1)$ Å, $V = 371.58(1)$ Å³. The volume differs by a factor of about 3.5 from the one reported earlier. X-ray data yielded a structure model with disordered tetrahedra in the silicate layers (space group $Cmcm$). Two ordered models can be derived as maximum-degree-of-order polytypes in $Pbcn$ and $Cmc2_1$, respectively. Neutron data indicate that the one in $Pbcn$ is dominant; however, electron diffraction indicates stacking disorder. These results were also confirmed by theoretical investigations.^[46] Some additional reflections in PXRD pattern of supposedly pure $\text{BaSi}_2\text{O}_2\text{N}_2$, that are not expected assuming this structure,^[47] could not be explained by an improved model. It would be interesting if, similarly to $\text{SrSi}_2\text{O}_2\text{N}_2$, they originate from real-structure effects or have to be attributed to a possibly unknown impurity. Investigations on Eu-doped $\text{BaSi}_2\text{O}_2\text{N}_2$ for sensor applications^[48] concluded that a significant fraction of domains crystallize in space group $Cmc2_1$ which exhibits the polar axis required for mechanoluminescence. Surface and interface effects might also account for this effect. In analogy to $\text{SrSi}_2\text{O}_2\text{N}_2$ and $\text{EuSi}_2\text{O}_2\text{N}_2$, $\text{BaSi}_2\text{O}_2\text{N}_2$ ^[45] also represents a layered oxonitridosilicate with alternating metal-ion and silicate layers (see Figure 3). The metal-ion layers are planar in contrast to the corrugated ones in the Sr- and Eu-phases, which explains the higher symmetry of the Ba-phase. The silicate layers show the same tetrahedra topology to those found in $\text{SrSi}_2\text{O}_2\text{N}_2$ and $\text{EuSi}_2\text{O}_2\text{N}_2$.

2.1.2.3 Crystal Structures of Mixed $\text{Sr}_{1-x}\text{Ba}_x\text{Si}_2\text{O}_2\text{N}_2$ ($0 \leq x \leq 1$) Phases

The structures of mixed $\text{Sr}_{1-x}\text{Ba}_x\text{Si}_2\text{O}_2\text{N}_2$ ($0 \leq x \leq 1$) phases are intriguing since no complete solid-solution series can be present due to the different structures of the “end members”. The structure determination needs to take into account real-structure effects mentioned above like twinning, intergrowth or stacking disorder which may result in diffuse scattering. Consistent with literature, domains with the structure of triclinic $\text{SrSi}_2\text{O}_2\text{N}_2$ are present in $\text{Sr}_{1-x}\text{Ba}_x\text{Si}_2\text{O}_2\text{N}_2$ phases even for samples with high Ba^{2+} -content.^[21,23,44,49-51] Ba-containing solid-solutions are corroborated by reflections that are shifted to smaller angles when larger Ba^{2+} is integrated into the crystal structure.^[37] For $\text{Sr}_{0.5}\text{Ba}_{0.5}\text{Si}_2\text{O}_2\text{N}_2$ the largest relative increase of lattice parameters has been observed for b ($\sim [010]^*$),^[43] i.e., along the stacking direction which is typical for layered structures. The interpretation of details in PXRD patterns becomes more complicated if Ba^{2+} is integrated into the structure. The probability of anti-phase boundaries increases from 20 % in $\text{SrSi}_2\text{O}_2\text{N}_2$ to a value close to 50 % in $\text{Sr}_{0.5}\text{Ba}_{0.5}\text{Si}_2\text{O}_2\text{N}_2$ which, of course, significantly affects diffraction patterns. The pseudo- B -centered superposition structure means that reflections with $h + l = 2n + 1$ are weakened, depending on the degree of disorder which varies for different crystals in the powder sample. As a consequence of preferred orientation, the shifted reflections and the changed overlap of reflections due to the anisotropic behavior of lattice parameters upon Ba doping, PXRD patterns can look completely different for isotypic compounds. The increasing amount of 2D extended anti-phase boundaries does not only affect Bragg reflection intensities. The pronounced short-range order also leads to diffuse streaks interconnecting Bragg reflections in SAED patterns. In PXRD patterns, they appear as asymmetric maxima. Small twin domains (coherent interference of scattered waves) require a complex layer disorder model to adequately describe the stacking sequence statistics in powder samples. If the Ba content in $\text{Sr}_{1-x}\text{Ba}_x\text{Si}_2\text{O}_2\text{N}_2$ approaches $x = 0.75$, phase separation into Sr-rich and Ba-rich compounds is observed.^[52] Due to the solid-solution series $\text{Sr}_{1-x}\text{Eu}_x\text{Si}_2\text{O}_2\text{N}_2$ ($0 \leq x \leq 1$), the maximum Ba content of 75 mol% must be related to the overall metal content in Eu-doped samples, not only to the Sr-content.⁵⁰ Whereas Sr-rich compounds (Ba amount <75 mol%) crystallize in the triclinic $\text{SrSi}_2\text{O}_2\text{N}_2$ structure type, the Ba-rich compound $\text{Sr}_{0.25}\text{Ba}_{0.75}\text{Si}_2\text{O}_2\text{N}_2$ adopts a distorted variation of the $\text{BaSi}_2\text{O}_2\text{N}_2$ structure type.^[52] Such domains show orientated intergrowth, the directions $[001]$ of the distorted $\text{BaSi}_2\text{O}_2\text{N}_2$ structure type and $[10 \bar{1}]$ of the triclinic $\text{SrSi}_2\text{O}_2\text{N}_2$ structure type coincide. The crystal structure of $\text{Sr}_{0.25}\text{Ba}_{0.75}\text{Si}_2\text{O}_2\text{N}_2$ combines the unit-cell metrics of the $\text{BaSi}_2\text{O}_2\text{N}_2$ type with corrugated metal-ion layers, found

in the $\text{SrSi}_2\text{O}_2\text{N}_2$ type. “Single” crystals show an intergrown domain structure. Distinguishing reflections that exhibit contributions from both crystal-structure types, the crystal structure of $\text{Sr}_{0.25}\text{Ba}_{0.75}\text{Si}_2\text{O}_2\text{N}_2$ could be refined in the orthorhombic space group $Pna2_1$ with $a = 5.470(2)$, $b = 14.277(3)$, $c = 4.791(1)$ Å, $V = 374.2(2)$ Å³ with Sr/Ba sharing the metal-ion position. In contrast to $\text{Sr}_{1-x}\text{Ba}_x\text{Si}_2\text{O}_2\text{N}_2$ phases that exhibit the triclinic $\text{SrSi}_2\text{O}_2\text{N}_2$ structure type, HRTEM images and simulations thereof indicate the presence of short-range cation ordering in $\text{Sr}_{0.25}\text{Ba}_{0.75}\text{Si}_2\text{O}_2\text{N}_2$, implying symmetry reduction to $P1$. In contrast to these detailed investigations, Ba doping of monoclinic $\text{SrSi}_2\text{O}_2\text{N}_2$ has not been reported so far.

2.1.2.4 Similarities and Differences in $\text{Sr}_{1-x}\text{Ba}_x\text{Si}_2\text{O}_2\text{N}_2$ ($0 \leq x \leq 1$) Phases

Based on the detailed knowledge of the crystal structures of $\text{Sr}_{1-x}\text{Ba}_x\text{Si}_2\text{O}_2\text{N}_2$ phases ($0 \leq x \leq 1$) the corresponding structures can be compared taking into account the increasing Ba^{2+} -content (see Figure 3).

The triclinic polymorph of $\text{SrSi}_2\text{O}_2\text{N}_2$ exhibits disordered corrugated metal-ion layers between silicate layers with uniform orientation.^[40] This is not the case for monoclinic $\text{SrSi}_2\text{O}_2\text{N}_2$ where consecutive silicate layers are rotated by 180° against each other.^[42] This situation can be viewed as a “chemically twinned” form of triclinic $\text{SrSi}_2\text{O}_2\text{N}_2$. Each other layer is rotated whereas twin boundaries in $\text{SrSi}_2\text{O}_2\text{N}_2$ occur approximately every 100 nm. Nevertheless, metal-ion as well as silicate layers are similar in both modifications, the difference concerns their relative arrangement. The $\text{SrSi}_2\text{O}_2\text{N}_2$ structure with corrugated metal-ion layers dominates up to a Ba-content of 50 % according to diffraction data; however, HRTEM in combination with TEM-EDX analysis revealed the presence of this structure type also for higher Ba-contents (< 75 mol%).^[43,52] At 75 mol% Ba the distorted variant of the $\text{BaSi}_2\text{O}_2\text{N}_2$ structure type appears besides the triclinic $\text{SrSi}_2\text{O}_2\text{N}_2$ structure type.^[43] The average structure of $\text{Sr}_{0.25}\text{Ba}_{0.75}\text{Si}_2\text{O}_2\text{N}_2$ with disordered metal ions exhibits orthorhombic lattice parameters similar to $\text{BaSi}_2\text{O}_2\text{N}_2$. $\text{Sr}_{0.25}\text{Ba}_{0.75}\text{Si}_2\text{O}_2\text{N}_2$ may therefore be regarded as a “transition state” between the $\text{SrSi}_2\text{O}_2\text{N}_2$ and $\text{BaSi}_2\text{O}_2\text{N}_2$ structure types as it combines corrugated metal-ion layers (like in the $\text{SrSi}_2\text{O}_2\text{N}_2$ type) with unit-cell metrics of the $\text{BaSi}_2\text{O}_2\text{N}_2$ type.

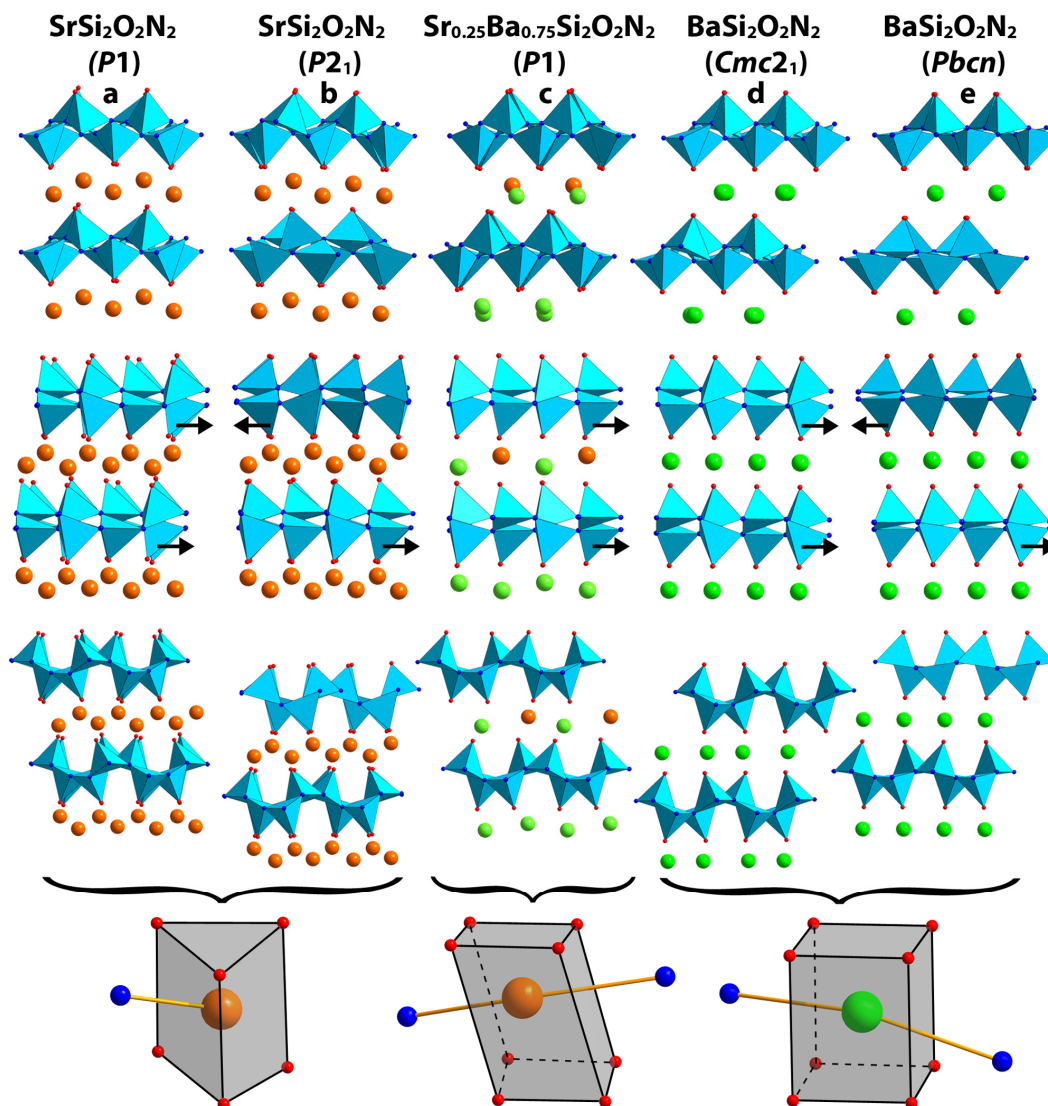


Figure 3. Crystal structures of: (a) triclinic $\text{SrSi}_2\text{O}_2\text{N}_2$ (top: along $[100]$, middle: along $[10\bar{1}]$, bottom: along $[10\bar{1}]$); (b) monoclinic $\text{SrSi}_2\text{O}_2\text{N}_2$ (top: along $[100]$, middle: along $[10\bar{1}]$, bottom: along $[101]$); (c) $\text{Sr}_{0.25}\text{Ba}_{0.75}\text{Si}_2\text{O}_2\text{N}_2$ (top: along $[1\bar{1}0]$, middle: along $[100]$, bottom: along $[010]$); (d) $\text{BaSi}_2\text{O}_2\text{N}_2$ (space group $Cmc2_1$, top: along $[0\bar{1}1]$, middle: along $[010]$, bottom: along $[00\bar{1}]$); (e) $\text{BaSi}_2\text{O}_2\text{N}_2$ (space group $Pbcn$, top: along $[01\bar{1}]$, middle: along $[010]$, bottom: along $[00\bar{1}]$). Tetrahedra are drawn in light blue, O (small red spheres) and N (small blue spheres) atoms are indicated. Sr-ions between the silicate layers are shown as large orange spheres, Ba-ions as large green spheres. The orientation of silicate layers is shown using black arrows. The coordination polyhedra of metal ions are depicted in gray (below the structures).

The degree of corrugation of the metal-ion layers decreases with increasing Ba^{2+} -content until coplanar layers result for pure $\text{BaSi}_2\text{O}_2\text{N}_2$.^[45] For the latter compound, two polytypes with either uniform or alternating silicate-layer orientations – similar to triclinic and monoclinic $\text{SrSi}_2\text{O}_2\text{N}_2$, respectively – were assumed. Their presence is derived from a superposition structure with disordered silicate layers. According to neutron data, the alternating sequence predominates (see above).

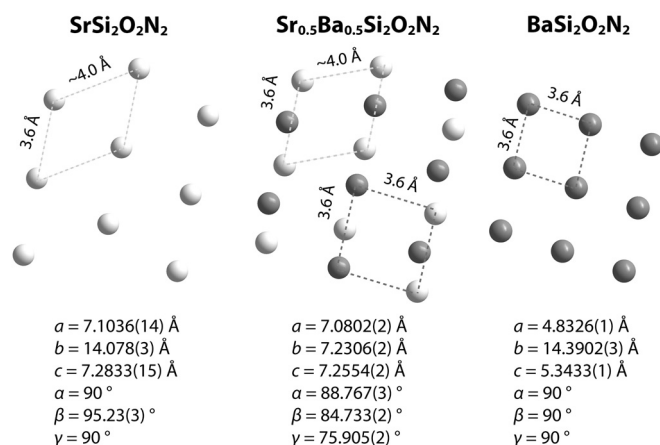


Figure 4. Top view on metal-ion layers and lattice parameters of monoclinic $\text{SrSi}_2\text{O}_2\text{N}_2$ (left, space group $P2_1$), $\text{Sr}_{0.5}\text{Ba}_{0.5}\text{Si}_2\text{O}_2\text{N}_2$ (middle, triclinic $\text{SrSi}_2\text{O}_2\text{N}_2$ structure type, space group $P1$), and $\text{BaSi}_2\text{O}_2\text{N}_2$ (right, space group $Pbcn$). In two-colored sheets positions of the same color are occupied with 50 % probability each.

Figure 4 shows the similarities between the $\text{Sr}_{1-x}\text{Ba}_x\text{Si}_2\text{O}_2\text{N}_2$ structure types with respect to the metal-ion layers. If sets of positions marked with different colors are occupied with almost 50 % probability each, the unit-cell determination can be problematic. Otherwise, the situation corresponds to a structure with ordered cations and the determination of lattice parameters is unambiguous. Sequences and distances between the positions in average structures determined from X-ray data may, of course, not be present in reality.

The distances between the metal ions remain nearly unchanged when Sr^{2+} is increasingly substituted by larger Ba^{2+} . This is probably due to the rigidity of the silicate substructure which is the key for the excellent luminescence properties as described below.

2.1.2.5 Guidelines for the Characterization of Oxonitridosilicates

The numerous effects that occur in the crystal chemistry of oxonitridosilicates often require combined approaches for an unambiguous characterization. The appreciation of “correctness” of unit-cell metrics of $\text{Sr}_{1-x}\text{Ba}_x\text{Si}_2\text{O}_2\text{N}_2$ ($0 \leq x \leq 1$) phases, after indexing the strongest or otherwise selected reflections using a large unit cell with low symmetry, can be very misleading especially when Le Bail method is used. This is due to the fact, that no structure model is required in this case for the fitting of integral intensities in PXRD patterns. Deducing the product’s composition from the weighted starting materials, i.e., neglecting chemical analysis, is another source of misleading assumptions especially regarding materials properties (see also section synthesis and luminescence). For $\text{Sr}_{1-x}\text{Ba}_x\text{Si}_2\text{O}_2\text{N}_2$ ($0 \leq x \leq 1$) phases, more details have to be kept in mind. The corresponding metal-ion and silicate layers

exhibit a higher individual symmetry than the overall crystal structure. This leads to structures with pronounced pseudo-symmetry, which differ in their diffraction intensities (and properties as well). Figure 5 gives an overview of typical real-structure effects found for layered oxonitridosilicates $\text{Sr}_{1-x}\text{Ba}_x\text{Si}_2\text{O}_2\text{N}_2$ ($0 \leq x \leq 1$). Twinning leads to higher reflection density of some rows in diffraction patterns. Combined with stacking disorder such rows can show more or less pronounced diffuse scattering. Intergrowth is detectable in diffraction patterns as well as in HRTEM images. Domains of the same structure type with different orientations can be involved as well as domains of different composition and crystal structure.

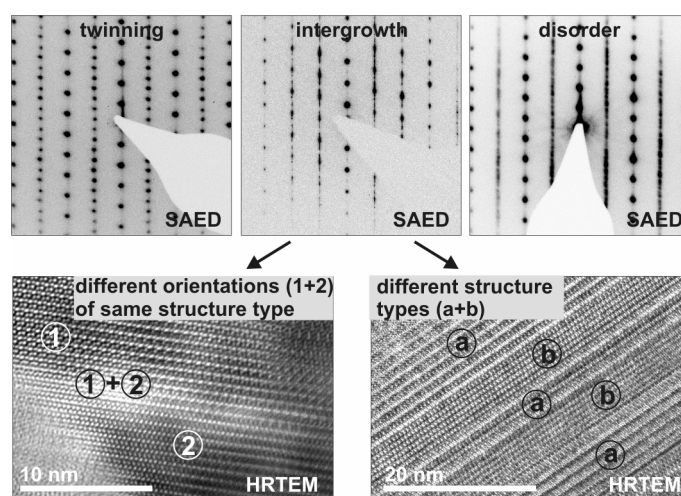


Figure 5. Typical real-structure effects for layered oxonitridosilicates (examples: twinning in $\text{SrSi}_2\text{O}_2\text{N}_2$ (SAED, zone axis $[10\bar{1}]$, upper left); disorder in $\text{SrSi}_2\text{O}_2\text{N}_2$ (SAED, zone axis $[10\bar{1}]$, upper right); intergrowth in $\text{Sr}_{0.25}\text{Ba}_{0.75}\text{Si}_2\text{O}_2\text{N}_2$ (SAED, upper middle); oriented intergrowth of $\text{SrSi}_2\text{O}_2\text{N}_2$ domains of zone axes $[001]$ (1) and $[100]$ (2); oriented intergrowth of domains in distorted $\text{BaSi}_2\text{O}_2\text{N}_2$ structure type (zone axis $[001]$, (a)) and domains in $\text{SrSi}_2\text{O}_2\text{N}_2$ structure type (zone axis $[10\bar{1}]$, (b)).

The phase purity of $\text{Sr}_{1-x}\text{Ba}_x\text{Si}_2\text{O}_2\text{N}_2$ ($0 \leq x \leq 1$) samples as well as their composition were frequently discussed in literature based on visual comparison of PXRD patterns.^[41,47,49,51,53-55] This is not very reliable when polymorphs may be present. In order to confirm a phase pure synthesis, HRTEM investigations on several crystallites are helpful because some domain structures show domain thicknesses of only a few unit cells. Thus, there are probably no phase-pure samples of $\text{Sr}_{1-x}\text{Ba}_x\text{Si}_2\text{O}_2\text{N}_2$ ($0 \leq x \leq 1$) in a strict sense as even “single crystals” usually contain several domains. However, even minor impurities, whether detectable in PXRD patterns or not, might have decisive influence on the performance of phosphor materials. Although, for instance, a structure model for $\text{SrSi}_2\text{O}_2\text{N}_2$ is well established,^[40] phase analysis was often done by visual comparison of PXRD patterns instead of Rietveld refinements. For $\text{Sr}_{1-x}\text{Ba}_x\text{Si}_2\text{O}_2\text{N}_2$ ($0 \leq x \leq 1$) phases, a verification of diffraction intensities using Rietveld method is more important than for most other phosphor materials. Variations

in the Bragg intensities compared to simulated PXRD patterns of published (average) crystal structures must be determined, since they indicate a deviation in the stacking sequence that might result in different luminescence properties.

Concerning $\text{Sr}_{1-x}\text{Ba}_x\text{Si}_2\text{O}_2\text{N}_2$ ($0 \leq x \leq 1$) many authors were primarily interested in properties and applications, but not in the crystal structures. However, even small deviations from ideal crystal structure may have an impact on material properties. Therefore, it is important to analyze the crystal structure thoroughly in order to understand the luminescence properties. A combination of X-ray diffraction and electron-microscopy methods is effective in this case, as resulting domains extend on different length scales. For $\text{MSi}_2\text{O}_2\text{N}_2$ ($M = \text{Sr}, \text{Ba}$) no significant deviation from the ideal composition $[\text{Si}_2\text{O}_2\text{N}_2]^{2-}$ of the anionic substructure has been proved, which would also seem unlikely (see above). Differences in diffraction patterns thus mean changes of the crystal structure or may be attributed to preferred orientation. As O and N cannot be differentiated by X-ray diffraction, other methods are required. The interpretation of bond lengths coupled with knowledge of similar crystal structures give hints for correct assignment of O and N. The position of the emission band in correlation to activator-ligand distances is also significant for O and N, respectively. An immense support for the “correct” assignment of O and N might provide neutron diffraction experiments. Nevertheless, this method is also not trivial and straightforward at all. Future investigations should optimally include chemical analysis of the products and at least Rietveld refinement in order to reveal unknown impurities in PXRD patterns. Such reflections should be assigned to impurity phases unless they can be explained by modified structure models of $\text{Sr}_{1-x}\text{Ba}_x\text{Si}_2\text{O}_2\text{N}_2$ ($0 \leq x \leq 1$) phases. Samples showing unknown reflections in PXRD patterns should ideally not be used for investigations of structure-property relations as the observed properties might not correspond to the desired product (see section 4).

2.1.3 Synthesis of $\text{Sr}_{1-x}\text{Ba}_x\text{Si}_2\text{O}_2\text{N}_2:\text{Eu}^{2+}$

2.1.3.1 Overview

Various strategies to synthesize $\text{MSi}_2\text{O}_2\text{N}_2$ have been described. The standard procedure is the reaction of corresponding carbonates (SrCO_3 / BaCO_3) or (mixed) *ortho*-silicates ($\text{Sr}_{2-x}\text{Ba}_x\text{SiO}_4$) with SiO_2 and Si_3N_4 . Less usual methods are spray pyrolysis,^[56] microwave syntheses,^[57] precursor syntheses with silicon diimide^[39] or syntheses within an arc.^[51] All

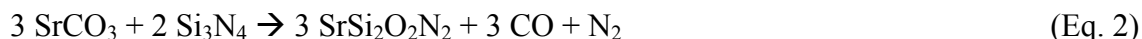
methods require high temperatures at the end of the temperature program, e.g., 1300 – 1700 °C for carbonate route and 1300 – 1500 °C for *ortho*-silicate route. This is a disadvantage for this kind of phosphor materials from an economical point of view. Additionally, phase pure synthesis and upscaling to industrially relevant amounts is challenging.^[17] For both standard reactions, nitrogen or forming gas is suitable as reaction gas. In addition also the use of various fluxes is described in literature.^[50,58-62]

2.1.3.2 The Carbonate Route

At first glance, the direct reaction of MCO_3 with Si_3N_4 to $\text{MSi}_2\text{O}_2\text{N}_2$ requires stoichiometric amounts of SiO_2 according to equation 1.

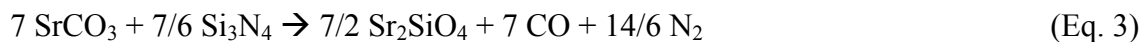


Nevertheless, the investigations of Zhu et al. already showed that X_2 -phase (except of remaining starting material) is only present in absence of SiO_2 .^[35] The formation of $\text{MSi}_2\text{O}_2\text{N}_2$ using SiO_2 -free synthesis was also observed and reported by Li et al.^[22] and therefore transferred to later investigations. A possible equation for reaction of SrCO_3 with Si_3N_4 is:



“Unknown” reflections were observed in PXRD pattern for the synthesis route according to equation 1 in case of $\text{SrSi}_2\text{O}_2\text{N}_2$.^[35,50,59] The firing temperatures are 200 - 300 °C lower than those for the carbonate route. The position of the strongest reflection of X_1 -phase or impurity phase, respectively, corresponds to that of $\text{M}_3\text{Si}_6\text{O}_9\text{N}_4$.^[63,64] The formation of this oxygen rich phase is also in agreement with the reported synthesis temperature of 1370 °C and with increased O-content compared to $\text{MSi}_2\text{O}_2\text{N}_2$ (additional SiO_2 related to equation 2).

Since M_2SiO_4 often occurs as an impurity phase,^[35] this might be an intermediate state on the way to $\text{MSi}_2\text{O}_2\text{N}_2$. The following fictive reaction scheme is based on typical weighted samples ($\text{MCO}_3:\text{Si}_3\text{N}_4 \approx 3:2$, see equation 5) where $\text{MSi}_2\text{O}_2\text{N}_2$ was obtained with high purity rate and precisely analyzed.^[39,40,45]



2.1.3.3 The Orthosilicate Route

The thesis that M_2SiO_4 might be an intermediate state towards $\text{MSi}_2\text{O}_2\text{N}_2$ is supported by the fact that M_2SiO_4 is an excellent starting material for the synthesis of $\text{MSi}_2\text{O}_2\text{N}_2$ phases. As mentioned above the *ortho*-silicate route is frequently used and leads to a higher purity of final products (equation 6). A variation of the synthesis conditions leads to the formation of polytypes; however, this is not investigated in detail in the literature.



For this synthesis route impurities are observed if the O/N ratio is not strictly controlled. A deviation from the 1:1 ratio might occur for high Eu-doping levels using Eu_2O_3 as a starting material. The “substitution” of SrCO_3 ($\text{SrO} + \text{CO}_2$) by Eu_2O_3 for the synthesis of M_2SiO_4 precursors does not result in a single-phase material because metal/oxygen ratio does not match. This may be the reason for samples that contain an O-rich phase corresponding to the $\text{M}_3\text{Si}_6\text{O}_9\text{N}_4$ structure type based on the interpretation of PXRD patterns shown.^[59] This would be in good agreement to the measured O/N content which is inconsistent with the one expected for $\text{MSi}_2\text{O}_2\text{N}_2$ composition.

2.1.4 Luminescence Properties of $\text{Sr}_{1-x}\text{Ba}_x\text{Si}_2\text{O}_2\text{N}_2:\text{Eu}^{2+}$ ($0 \leq x \leq 1$)

2.1.4.1 Structure-Property Relations

The results of luminescence investigations of Eu-doped $\text{Sr}_{1-x}\text{Ba}_x\text{Si}_2\text{O}_2\text{N}_2$ phases in the literature are much more consistent than corresponding structure investigations. $\text{SrSi}_2\text{O}_2\text{N}_2:\text{Eu}^{2+}$ emits light within the green spectral region when excited by UV to blue light (see Figure 6).

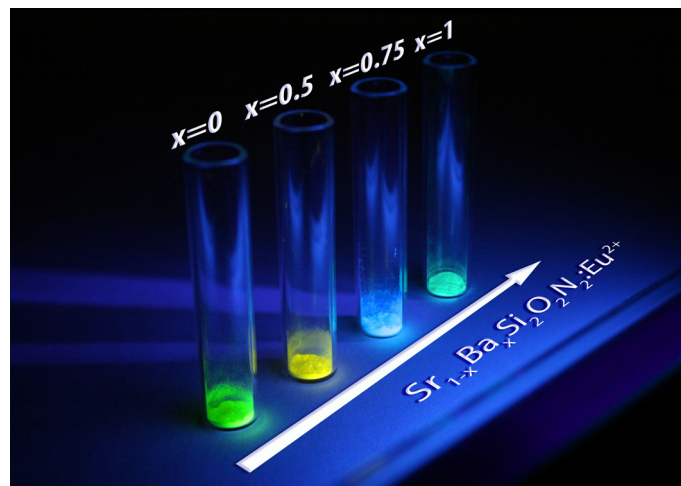


Figure 6. Luminescence colors of $\text{Sr}_{1-x}\text{Ba}_x\text{Si}_2\text{O}_2\text{N}_2:\text{Eu}^{2+}$ phases with increasing Ba^{2+} -content x .

The maximum wavelength of the emission peaks at $\sim 537\text{-}540$ nm for the triclinic modification of $\text{SrSi}_2\text{O}_2\text{N}_2:\text{Eu}^{2+}$,^[11,36,41,44,55,65-70] at 532 nm for the corresponding monoclinic one,^[42] and mixtures of both phases emit between these values.^[60,71-75] For a doping level of 2 mol% Eu^{2+} , the quantum efficiency (QE) of the triclinic modification was reported to be approximately 90 %, even for temperatures around 200 °C.^[21,36,66] Co-doping with various cations and/or a partial or complete substitution of the activator ion are common ways to tune the luminescence properties.^[41,61,66,69-71,74,76-83] When the Ba-content is increased, the emission wavelength is continuously shifted to lower energies.^[21,43,44,49-51,62] This behavior is observed for the mixed $\text{Sr}_{1-x}\text{Ba}_x\text{Si}_2\text{O}_2\text{N}_2$ phases as long as the $\text{SrSi}_2\text{O}_2\text{N}_2$ structure type is built up.^[43] In that case, the corresponding emission is shifted to the yellow-green spectral region (see Figure 6). For a Ba-content of 75 mol% (related on overall metal content), a change of the crystal structure towards a distorted variant of the $\text{BaSi}_2\text{O}_2\text{N}_2$ structure type is observed. This leads to a shift of the emission into the blue spectral region ($\lambda_{\text{em}} = 472$ nm, Figure 6).^[52] The emission band exhibits a FWHM of only 37 nm which is the smallest value found for blue emitters of that material class. If the Ba-content is further increased, the emission color reaches the blue-green spectral region which was reported for $\text{BaSi}_2\text{O}_2\text{N}_2:\text{Eu}^{2+}$ ($\lambda_{\text{em}} \sim 500$ nm; see Figure 6).^[21,47,48,84-87]

In addition, the FWHM of the emission band depends on the number of crystallographically independent metal-atom positions (i.e., positions occupied by Eu^{2+}) for $\text{Sr}_{1-x}\text{Ba}_x\text{Si}_2\text{O}_2\text{N}_2:\text{Eu}^{2+}$ phases. In the crystal structures of both, triclinic and monoclinic $\text{SrSi}_2\text{O}_2\text{N}_2$,^[40,42] four different metal-atom sites are present and FWHM is about 70-80 nm.^[21,22] For $\text{BaSi}_2\text{O}_2\text{N}_2:\text{Eu}^{2+}$ ^[45] one metal site is present and the FWHM is <40 nm.^[21,22] Additionally, the $\text{Sr}_{1-x}\text{Ba}_x\text{Si}_2\text{O}_2\text{N}_2:\text{Eu}^{2+}$ phases exhibit adequate stability in the case of thermal stress next to a

primary GaN-based pump LED chip (approximately 120-150 °C)^[49]. For $\text{SrSi}_2\text{O}_2\text{N}_2:\text{Eu}^{2+}$, the emission intensity at 170-200 °C is at least 80 % of the intensity at room temperature.^[21,44,47,49,50,54,58,61,65,66,75,82] This thermal behavior is comparable to that of industrially used nitride phosphor $\text{Sr}_2\text{Si}_5\text{N}_8:\text{Eu}^{2+}$ ^[36,88] and significantly improved compared to the frequently used phosphor YAG:Ce³⁺^[50,58]. Also $\text{BaSi}_2\text{O}_2\text{N}_2:\text{Eu}^{2+}$ exhibits over 80 % of the room temperature emission intensity at 150 °C.^[89] Nevertheless, for mixed $\text{Sr}_{1-x}\text{Ba}_x\text{Si}_2\text{O}_2\text{N}_2:\text{Eu}^{2+}$ phases some problems concerning the long-life stability were reported, meaning that there is still a demand for improvements.^[10,49] Summarizing, the phases $\text{Sr}_{1-x}\text{Ba}_x\text{Si}_2\text{O}_2\text{N}_2:\text{Eu}^{2+}$ are promising phosphor materials in the blue-green to green-yellow spectral region for commercial applications in pc-LEDs. Such devices might soon replace incandescent lamps, because they exhibit a more efficient conversion of electric energy to visible light.

2.1.4.2 Critical Evaluation of the Literature

Like phase analyses (see section 2.1.2.1.2), luminescence investigations also require thoroughness in order to ensure that measured properties really correspond to the desired product which was investigated. For instance, Gu et al.^[86] found that $\text{BaSi}_2\text{O}_2\text{N}_2:\text{Eu}^{2+}$ formed from core-shell nanoparticles exhibits a shift of the emission wavelength to lower energies with increasing firing temperature under NH_3 -atmosphere. The emission wavelength (λ_{em}) can apparently be tuned in a range of 490 – 530 nm. Compared to the emission band for $\text{BaSi}_2\text{O}_2\text{N}_2:\text{Eu}^{2+}$ (FWHM ~40 nm), the samples with the highest λ_{em} exhibit approximately twice that FWHM and the shape of excitation band is completely different. The measured luminescence signals (excitation and emission) resemble those of $\text{Ba}_3\text{Si}_6\text{O}_{12}\text{N}_2:\text{Eu}^{2+}$ ^[90-92] which can easily be obtained from $\text{BaSi}_2\text{O}_2\text{N}_2$ at high temperature. As the PXRD patterns of the samples which show remarkably different luminescence properties^[86] in comparison to $\text{BaSi}_2\text{O}_2\text{N}_2:\text{Eu}^{2+}$ are not shown, it remains an open question whether in fact another phase (namely $\text{Ba}_3\text{Si}_6\text{O}_{12}\text{N}_2:\text{Eu}^{2+}$) was investigated. It seems unlikely that one can conclude that an increasing N-content in $\text{BaSi}_2\text{O}_2\text{N}_2:\text{Eu}^{2+}$ is the reason for the observed changes in emission signals.

Zhang et al. describe luminescence properties of a compound $\text{BaSi}_2\text{SN}_{2.67}:\text{Eu}^{2+}$, including a comparison with $\text{BaSi}_2\text{O}_2\text{N}_2:\text{Eu}^{2+}$.^[93] $\text{BaSi}_2\text{SN}_{2.67}$ would be the first thionitridosilicates with $\text{Si}(\text{S},\text{N})_4$ tetrahedra in the crystal structure. This material class would also be very interesting

with respect to phosphor materials for LED applications. Sulfide anions are softer than oxide anions, which increases the nephelauxetic effect. This might yield new phosphor materials which emit visible light in the orange-red spectral region by excitation with UV to blue light. However, the published data (symmetry, lattice parameters, PXRD pattern, excitation / emission spectrum) resemble those of $\text{Ba}_3\text{Si}_6\text{O}_{12}\text{N}_2:\text{Eu}^{2+}$.^[90-92] Although sulfur is present during the reaction, the sulfur content of the product was not confirmed by chemical analysis or by spectroscopy. Regarding lattice parameters and position of the emission band it seems unlikely that a significant amount of sulfur is present in the crystal structure.

Apparently, phases belonging to the $\text{M}_3\text{Si}_6\text{O}_9\text{N}_4$ and $\text{M}_3\text{Si}_6\text{O}_{12}\text{N}_2$ structure type are often present if the parameters for the synthesis of $\text{MSi}_2\text{O}_2\text{N}_2$ are not strictly controlled.^[62] This is probably due to the similar atomic ratio M : Si of all these phases. The crystal structures are defect variants or otherwise similar to the one with the highest degree of condensation, i.e., $\text{MSi}_2\text{O}_2\text{N}_2$. Figure 7 shows the change of the silicate partial structure with increasing O-content.

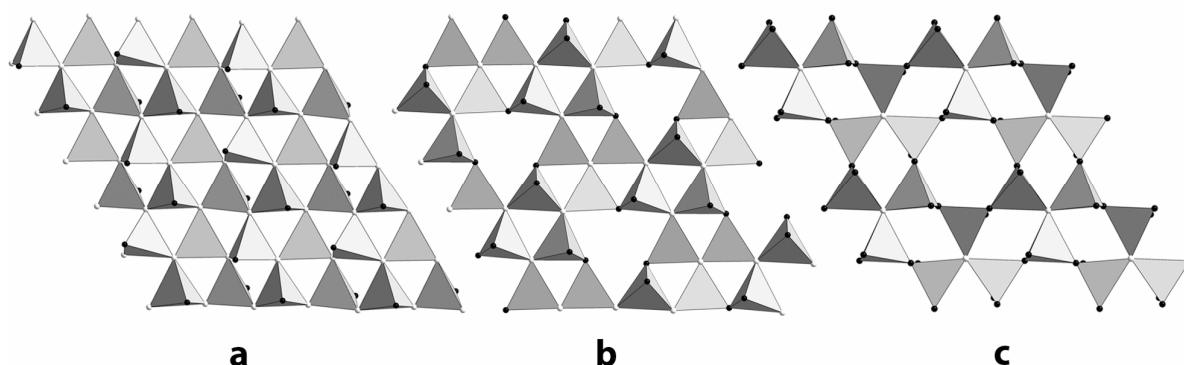


Figure 7. Top view on silicate layers in the structures of $\text{MSi}_2\text{O}_2\text{N}_2$ (a), $\text{M}_3\text{Si}_6\text{O}_9\text{N}_4$ (b), $\text{M}_3\text{Si}_6\text{O}_{12}\text{N}_2$ (c). Tetrahedra are drawn in gray with O (small black spheres) and N (small white spheres).

Summarizing, reliable luminescence investigations require an overall, detailed analysis of the material which ideally should be single-phase. Synthesis methods may significantly affect the composition so that chemical analysis is mandatory if slight changes are to be correlated to changes of properties.

2.1.5 Summary, Conclusion and Outlook

$\text{Sr}_{1-x}\text{Ba}_x\text{Si}_2\text{O}_2\text{N}_2:\text{Eu}^{2+}$ phases are very interesting materials, because of their intriguing applications in high-power LEDs due to their excellent luminescence properties. They are

also textbook examples for complicated crystallographic investigations from the point of view of fundamental science. Various real-structure effects render structure determination difficult and often have an almost unpredictable influence on diffraction patterns. This is especially true when pronounced short-range order leads to intense diffuse scattering. Even the determination of the unit-cell metrics can become ambiguous and almost impossible from PXRD data alone. The combination of X-ray diffraction and electron-microscopy methods turned out to be a suitable tool for a detailed determination of atomic arrangement in the corresponding crystal structures. Based on this knowledge, correlations between crystal structure and luminescence properties of corresponding Eu-doped samples can be formulated. Both triclinic and monoclinic modifications of $\text{SrSi}_2\text{O}_2\text{N}_2:\text{Eu}^{2+}$ exhibit extraordinary chemical and thermal stability, high quantum efficiency ($> 90\%$), and an emission wavelength close to 530 nm (FWHM ~ 75 nm) which is the ideal value for green emitting light sources. The origin of these properties is the highly covalent, rigid layered silicate substructure consisting of condensed $\text{SiO}^{[1]}\text{N}^{[3]}_3$ tetrahedra. The alkaline-earth ions are coordinated by oxygen; however, the interatomic distances are longer than the sum of the ionic radii. Thus, for an incorporation of Eu^{2+} onto the cation positions, the lattice is pre-strained and weak electron-phonon coupling is present in the case of excited Eu^{2+} . Although this is also true for $\text{BaSi}_2\text{O}_2\text{N}_2:\text{Eu}^{2+}$, the overall performance of this phosphor is inferior, compared to $\text{SrSi}_2\text{O}_2\text{N}_2:\text{Eu}^{2+}$, because of the color point in the blue-green spectral region and a lower quantum efficiency. Due to the highly symmetric coordination of Ba^{2+} , the FWHM is only half of that in $\text{SrSi}_2\text{O}_2\text{N}_2:\text{Eu}^{2+}$. It is yet not possible to shift the emission wavelength of $\text{BaSi}_2\text{O}_2\text{N}_2:\text{Eu}^{2+}$ towards 530 nm by chemical substitution in order to obtain the “ideal green phosphor” for solid-state lighting. Table 1 summarizes available information regarding luminescence properties of $\text{Sr}_{1-x}\text{Ba}_x\text{Si}_2\text{O}_2\text{N}_2:\text{Eu}^{2+}$ ($0 \leq x \leq 1$) phases.

Table 1. Luminescence data of $\text{MSi}_2\text{O}_2\text{N}_2:\text{Eu}^{2+}$ phases (M = Ca, Sr, Ba).

Compound (2% Eu^{2+})	λ_{em} (max) [nm]	λ_{exc} [nm]	FWHM [nm]	QE [%]	x	y	Ref.
$\text{CaSi}_2\text{O}_2\text{N}_2$	560 ^[a]	450 ^[a] , 400 ^[b]	~ 100	76 ^[a]	0.419	0.556	21,22
$\text{SrSi}_2\text{O}_2\text{N}_2$ (triclinic)	537 – 540 ^[c]	450 ^[a] , 400 ^[b]	< 80	> 90	0.337	0.619	21,22,36,66
$\text{SrSi}_2\text{O}_2\text{N}_2$ (monoclinic)	532	420	< 80	-	0.314	0.621	42
$\text{Sr}_{0.5}\text{Ba}_{0.5}\text{Si}_2\text{O}_2\text{N}_2$	~ 560	450 ^[d]	~ 90	> 90 ^[a]	0.441	0.544	21,43,51
$\text{Sr}_{0.25}\text{Ba}_{0.75}\text{Si}_2\text{O}_2\text{N}_2$	472	400	~ 37	-	0.140	0.163	52
$\text{BaSi}_2\text{O}_2\text{N}_2$	< 500 ^[c]	450 ^[a] , 440 ^[b]	~ 35	71 ^[a]	0.076	0.440	21,22

[a] according to Bachmann et al.²¹; [b] according to Li et al.²²; [c] see text; [d] according to Seibald et al.⁴³

The crystal structures of $\text{SrSi}_2\text{O}_2\text{N}_2$ and $\text{BaSi}_2\text{O}_2\text{N}_2$ are closely related but differ concerning the arrangement of metal ions and in the relative orientation of consecutive silicate layers which mainly has an influence on the coordination sphere of the cations. In crystals of $\text{Sr}_{1-x}\text{Ba}_x\text{Si}_2\text{O}_2\text{N}_2$, disordered stacking sequences are sometimes formed owing to the intergrowth of domains, either with the same individual stacking sequence of metal-ion and silicate layers or with different ones. Such effects may be relevant for the analysis of structure-property relations. Caution is required to ensure that the measured luminescence properties characterize the investigated compound and are not affected by impurity phases. The discussion of properties of samples with unknown reflection in PXRD patterns can be misleading. Polytypes exhibit slightly different properties as shown, e.g., for $\text{SrSi}_2\text{O}_2\text{N}_2:\text{Eu}^{2+}$. Future projects might focus on controlling the properties by optimizing the synthesis conditions, i.e., the “tuning” of luminescence properties by controlling the stacking sequence, domain formation, polytype stabilization etc. This might lead to color points which are not accessible via cation substitution as the properties do not only depend on the composition.^[94] After a decade of investigations on $\text{Sr}_{1-x}\text{Ba}_x\text{Si}_2\text{O}_2\text{N}_2:\text{Eu}^{2+}$ phases by various scientists, there is still a demand for further work since not all questions concerning these highly interesting and outstanding materials have been answered yet (e.g., the change of the thermal behavior and the band gap in dependence of the Ba-content). Still, this class of materials represents intriguing oxonitridosilicate phosphors for LED applications.

2.1.6 References

- [1] C. Feldmann, *Z. Anorg. Allg. Chem.* **2012**, 638, 2169-2171.
- [2] M. Mikami, H. Watanabe, K. Uheda, S. Shimooka, Y. Shimomura, T. Kurushima, N. Kijima, *IOP Conf. Ser.: Mater. Sci. Eng.* **2009**, 1, 012002 (1-10).
- [3] S. Ye, F. Xiao, Y. X. Pan, Y. Y. Ma, Q. Y. Zhang, *Mater. Sci. Eng., R* **2010**, 71, 1-34.
- [4] C. C. Lin, R.-S. Liu, *J. Phys. Chem. Lett.* **2011**, 2, 1268-1277.
- [5] J. M. Phillips, M. E. Coltrin, M. H. Crawford, A. J. Fischer, M. R. Krames, R. Mueller-Mach, G. O. Mueller, Y. Ohno, L. E. S. Rohwer, J. A. Simmons, J. Y. Tsao, *Laser & Photon. Rev.* **2007**, 1, 307-333.
- [6] C. Sommer, P. Hartmann, P. Pachler, H. Hoschopf, F. P. Wenzl, *J. Alloys Compd.* **2012**, 520, 146-152.
- [7] R.-J. Xie, N. Hirosaki, Y. Li, T. Takeda, *Materials* **2010**, 3, 3777-3793.

- [8] D. P. Dutta, A. K. Tyagi, *Solid State Phenomena* **2009**, 155, 113-143.
- [9] R.-J. Xie, N. Hirosaki, *Sci. Technol. Adv. Mater.* **2007**, 8, 588-600.
- [10] R.-J. Xie, N. Hirosaki, T. Takeda, T. Suehiro, *ECS J. Solid State Sci. Technol.* **2013**, 2, R3031-R3040.
- [11] C.-C. Yang, C.-M. Lin, Y.-J. Chen, Y.-T. Wu, S.-R. Chuang, *Appl. Phys. Lett.* **2007**, 90, 123503 (1-3).
- [12] R.-J. Xie, N. Hirosaki, T. Takeda, *J. Korean Ceram. Soc.* **2012**, 49, 375-379.
- [13] H. A. Höpfe, *Angew. Chem.* **2009**, 121, 3626-3636; *Angew. Chem. Int. Ed.* **2009**, 48, 3572-3582.
- [14] X.-H. He, N. Lian, J.-H. Sun, M.-Y. Guan, *J. Mater. Sci.* **2009**, 44, 4763-4775.
- [15] R.-J. Xie, H. T. (Bert) Hintzen, *J. Am. Ceram. Soc.* **2013**, 96, 665-687.
- [16] G. Blasse and B. C. Grabmaier, *Luminescent Materials*, edition 1, Springer Berlin Heidelberg, Germany (**1994**).
- [17] C. R. Ronda, *Luminescence*, edition 1, Wiley-VCH Verlag GmbH & Co. KGaA, Weinheim, Germany (**2007**).
- [18] R.-J. Xie, Y. Q. Li, N. Hirosaki and H. Yamamoto, *Nitride phosphors and solid-state lighting*, Taylor & Francis Inc., Boca Raton, Florida, USA (**2011**).
- [19] P. F. Smet, A. B. Parmentier, D. Poelman, *J. Electrochem. Soc.* **2011**, 158, R37-R54.
- [20] M. Zeuner, S. Pagano, W. Schnick, *Angew. Chem.* **2011**, 123, 7898-7920; *Angew. Chem. Int. Ed.* **2011**, 50, 7754-7775.
- [21] V. Bachmann, C. Ronda, O. Oeckler, W. Schnick, A. Meijerink, *Chem. Mater.* **2009**, 21, 316-325.
- [22] Y. Q. Li, A. C. A. Delsing, G. de With, H. T. Hintzen, *Chem. Mater.* **2005**, 17, 3242-3248.
- [23] B. Y. Han, K.-S. Sohn, *Electrochem. Solid-State Lett.* **2010**, 13, J62-J64.
- [24] H. A. Höpfe, F. Stadler, O. Oeckler, W. Schnick, *Angew. Chem.* **2004**, 116, 5656-5659; *Angew. Chem. Int. Ed.* **2004**, 43, 5540-5542.
- [25] G. Pilet, H. A. Höpfe, W. Schnick, S. Esmaeilzadeh, *Solid State Sci.* **2005**, 7, 391-396.
- [26] J. Grins, Z. Shen, S. Esmaeilzadeh, P. Berastegui, *J. Mater. Chem.* **2001**, 11, 2358-2362.
- [27] J. A. Kechele, O. Oeckler, P. J. Schmidt, W. Schnick, *Eur. J. Inorg. Chem.* **2009**, 3326-3332.
- [28] C. Hecht, F. Stadler, P. J. Schmidt, J. Schmedt auf der Günne, V. Baumann, W. Schnick, *Chem. Mater.* **2009**, 21, 1595-1601.

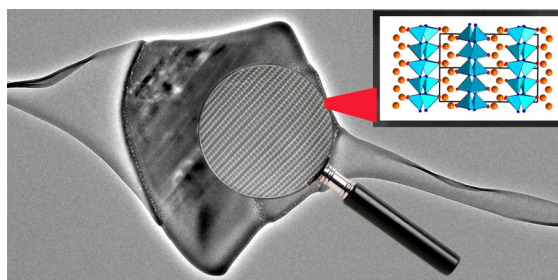
- [29] J. A. Kechele, C. Hecht, O. Oeckler, J. Schmedt auf der Günne, P. J. Schmidt, W. Schnick, *Chem. Mater.* **2009**, *21*, 1288-1295.
- [30] O. Oeckler, J. A. Kechele, H. Koss, P. J. Schmidt, W. Schnick, *Chem. Eur. J.* **2009**, *15*, 5311-5319.
- [31] H. Yamane, S. Shimooka, K. Uheda, *J. Solid State Chem.* **2012**, *190*, 264-270.
- [32] Hübenthal, R. *Madlung Part of Lattice Energy*, version 4, **1993**, University of Gießen (Germany).
- [33] R. Hoppe, *Angew. Chem.* **1966**, *78*, 52-63; *Angew. Chem. Int. Ed.* **1966**, *5*, 95-106.
- [34] R. Hoppe, *Angew. Chem.* **1970**, *82*, 7-16; *Angew. Chem. Int. Ed.* **1970**, *9*, 25-34.
- [35] W. H. Zhu, P. L. Wang, W. Y. Sun, D. S. Yan, *J. Mater. Sci. Lett.* **1994**, *13*, 560-562.
- [36] R. Mueller-Mach, G. Mueller, M. R. Krames, H. A. Höpfe, F. Stadler, W. Schnick, T. Juestel, P. Schmidt, *Phys. Status Solidi A*, **2005**, *202*, 1727-1732.
- [37] R. D. Shannon, *Acta Crystallogr., Sect. A: Found. Crystallogr.* **1976**, *32*, 751-767.
- [38] Y. Q. Li, K. V. Ramanujachary, S. E. Lofland, G. de With, H. T. Hintzen, *J. Mater. Res.* **2006**, *21*, 396-401.
- [39] F. Stadler, O. Oeckler, H. A. Höpfe, M. H. Möller, R. Pöttgen, B. D. Mosel, P. Schmidt, V. Duppel, A. Simon, W. Schnick, *Chem. Eur. J.* **2006**, *12*, 6984-6990.
- [40] O. Oeckler, F. Stadler, T. Rosenthal, W. Schnick, *Solid State Sci.* **2007**, *9*, 205-212.
- [41] R.-S. Liu, Y.-H. Liu, N. C. Bagkar, S.-F. Hu, *Appl. Phys. Lett.* **2007**, *91*, 061119 (1-3).
- [42] M. Seibald, T. Rosenthal, O. Oeckler, C. Maak, A. Tücks, P. J. Schmidt, D. Wiechert, W. Schnick, *Chem. Mater.* **2013**, *25*, 1852-1857.
- [43] M. Seibald, O. Oeckler, V. R. Celinski, P. J. Schmidt, A. Tücks, W. Schnick, *Solid State Sci.* **2011**, *13*, 1769-1778.
- [44] G. Anoop, I. H. Cho, D. W. Suh, J. S. Yoo, *Phys. Status Solidi A* **2012**, *209*, 2635-2640.
- [45] J. A. Kechele, O. Oeckler, F. Stadler, W. Schnick, *Solid State Sci.* **2009**, *11*, 537-543.
- [46] L. Wang, H. Ni, Q. Zhang, F. Xiao, *J. Alloys Compd.* **2011**, *509*, 10203-10206.
- [47] B.-G. Yun, T. Horikawa, H. Hanzawa, K. Machida, *J. Electrochem. Soc.* **2010**, *157*, J364-J370.
- [48] J. Botterman, K. Van den Eeckhout, I. de Baere, D. Poelman, P. F. Smet, *Acta Mater.* **2012**, *60*, 5494-5500.
- [49] I. H. Cho, G. Anoop, D. W. Suh, S. J. Lee, J. S. Yoo, *Opt. Mater. Express* **2012**, *2*, 1292-1305.
- [50] B.-G. Yun, Y. Miyamoto, H. Yamamoto, *J. Electrochem. Soc.* **2007**, *154*, J320-J325.

- [51] B. Lei, K. Machida, T. Horikawa, H. Hanzawa, *Chem. Lett.* **2011**, *40*, 140-141.
- [52] M. Seibald, T. Rosenthal, O. Oeckler, F. Fahrnbauer, A. Tücks, P. J. Schmidt, W. Schnick, *Chem. Eur. J.* **2012**, *18*, 13446-13452.
- [53] B.-G. Yun, T. Horikawa, H. Hanzawa, K. Machida, *J. Electrochem. Soc.* **2010**, *157*, J97-J101.
- [54] S. D. Jee, K. S. Choi, J. S. Kim, *Met. Mater. Int.* **2011**, *17*, 655-660.
- [55] X. Yang, H. Song, L. Yang, X. Xu, *J. Am. Ceram. Soc.* **2011**, *94*, 28-35.
- [56] K. Y. Jung, J. H. Seo, *Electrochem. Solid-State Lett.* **2008**, *11*, J64-J67.
- [57] Y. Zhang, X. Liu, B. Lei, H. Wang, Q. Sun, *Energy Procedia* **2012**, *16*, 391-396.
- [58] K. Machida, *IOP Conf. Ser.: Mater. Sci. Eng.* **2011**, *18*, 052001 (1-4).
- [59] B.-G. Yun, K. Machida, H. Yamamoto, *J. Ceram. Soc. Jpn.* **2007**, *115*, 619-622.
- [60] X.-K. Meng, J. Tan, T. Lei, W. Zhang, W. Yan, C.-M. Li, X.-W. Sun, *Chinese J. Inorg. Chem.* **2012**, *28*, 893-897.
- [61] J. Ruan, R.-J. Xie, N. Hirosaki, T. Takeda, *J. Electrochem. Soc.* **2012**, *159*, H66-H71.
- [62] H. Yamamoto, M. Yamauchi, J. Iizuka, B. G. Yun, K. Machida, N. Kijima, *ECS Trans.* **2011**, *33*, 109-114.
- [63] F. Stadler, W. Schnick, *Z. Anorg. Allg. Chem.* **2006**, *632*, 949-954.
- [64] F. Stadler, *doctoral thesis*, LMU Munich (**2006**).
- [65] M. Zhang, J. Wang, Z. Zhang, Q. Zhang, Q. Su, *Appl. Phys. B: Lasers Opt.* **2008**, *93*, 829-835.
- [66] V. Bachmann, T. Jüstel, A. Meijerink, C. Ronda, P. J. Schmidt, *J. Lumin.* **2006**, *121*, 441-449.
- [67] J.-Y. Tang, X.-F. Yang, C. Zhan, L.-Y. Hao, X. Xu, W.-H. Zhang, *J. Mater. Chem.* **2012**, *22*, 488-494.
- [68] J. Botterman, K. Van den Eeckhout, A. J. J. Bos, P. Dorenbos, P. F. Smet, *Opt. Mater. Express* **2012**, *2*, 341-349.
- [69] C.-W. Yeh, Y. Li, J. Wang, R.-S. Liu, *Opt. Express* **2012**, *20*, 18031-18043.
- [70] A. Kirakosyan, A. Mnayan, S. H. Cheong, G. Y. Lee, D. Y. Jeon, *ECS J. Solid State Sci. Technol.* **2013**, *2*, R5-R8.
- [71] X. Song, R. Fu, S. Agathopoulos, H. He, X. Zhao, R. Li, *J. Electrochem. Soc.* **2010**, *157*, J34-J38.
- [72] Y. Song, X. Xu, H. Zou, Y. Sheng, H. You, *J. Alloys Compd.* **2012**, *513*, 86-90.
- [73] X. Song, H. He, R. Fu, D. Wang, X. Zhao, Z. Pan, *J. Phys. D: Appl. Phys.* **2009**, *42*, 065409-065414.

- [74] X. Song, R. Fu, S. Agathopoulos, H. He, X. Zhao, J. Zeng, *Mater. Sci. Eng., B* **2009**, *164*, 12-15.
- [75] Y.-C. Fang, P.-C. Kao, Y.-C. Yang, S.-Y. Chu, *J. Electrochem. Soc.* **2011**, *158*, J246-J249.
- [76] H. Ju, X. Su, B. Wang, D. Deng, S. Zhao, S. Xu, *J. Rare Earth* **2012**, *30*, 97-99.
- [77] X. Xu, K. Fu, L. Hu, Z. Lu, X. Zhang, C. Tang, *Advanced Materials Research* **2012**, *430-432*, 315-318.
- [78] C.-H. Hsu, C.-H. Lu, *J. Mater. Chem.* **2011**, *21*, 2932-2939.
- [79] Q.-N. Fei, Y.-H. Liu, T.-C. Gu, D.-J. Wang, *J. Lumin.* **2011**, *131*, 960-964.
- [80] R. Li, R. Fu, X. Song, H. He, X. Yu, B. He, Z. Shi, *J. Phys. Chem. Solids* **2011**, *72*, 233-235.
- [81] C.-H. Hsu, B.-M. Cheng, C.-H. Lu, *J. Am. Ceram. Soc.* **2011**, *94*, 3256-3260.
- [82] S.-H. Lee, K.-B. Kim, J.-M. Kim, Y.-K. Jeong, J.-G. Kang, *Phys. Status Solidi A*, **2013**, *210*, 1093-1097.
- [83] Y. Q. Li, G. de With, H. T. Hintzen, *J. Mater. Chem.* **2005**, *15*, 4492-4496.
- [84] L. Wang, H. Ni, Q. Zhang, *Chinese Journal of Luminescence* **2012**, *33*, 465-469.
- [85] M. Wang, X. Zhang, Z. Hao, X. Ren, Y. Luo, H. Zhao, X. Wang, J. Zhang, *J. Electrochem. Soc.* **2010**, *157*, H178-H181.
- [86] Y. Gu, Q. Zhang, Y. Li, H. Wang, *J. Mater. Chem.* **2010**, *20*, 6050-6056.
- [87] X. Song, R. Fu, S. Agathopoulos, H. He, X. Zhao, X. Yu, *J. Am. Ceram. Soc.* **2011**, *94*, 501-507.
- [88] R.-J. Xie, N. Hirosaki, N. Kimura, K. Sakuma, M. Mitomo, *Appl. Phys. Lett.* **2007**, *90*, 191101 (1-3).
- [89] R.-J. Xie, N. Hirosaki, K. Sakuma, and N. Kimura, *J. Phys. D: Appl. Phys.* **2008**, *41*, 144013 (1-5).
- [90] M. Mikami, S. Shimooka, K. Uheda, H. Imura, N. Kijima, *Key Eng. Mater.* **2009**, *403*, 11-14.
- [91] S. Shimooka, K. Uheda, M. Mikami, N. Kijima, H. Imura, K. Horibe, *PCT Int. Appl.* **2007**, WO088966, A1.
- [92] C. Braun, M. Seibald, S. L. Börger, O. Oeckler, T. D. Boyko, A. Moewes, G. Mieke, A. Tücks, W. Schnick, *Chem. Eur. J.* **2010**, *16*, 9646-9657.
- [93] Z. Zhang, J. Wang, Y. Yin, J. Zhou, S. Zhou, Y. Pan, *Opt. Mater.* **2013**, *35*, 1273-1275.
- [94] M. Mikami, N. Kijima, *Opt. Mater.* **2010**, *33*, 145-148.

2.2 New Polymorph of the Highly Efficient LED-Phosphor $\text{SrSi}_2\text{O}_2\text{N}_2:\text{Eu}^{2+}$ – Polytypism of a Layered Oxonitridosilicate

Markus Seibald, Tobias Rosenthal, Oliver Oeckler, Christian Maak, Andreas Tücks, Peter J. Schmidt, Detlef Wiechert, and Wolfgang Schnick



published in: *Chem. Mater.* **2013**, 25, 1852-1857; DOI: 10.1021/cm400461v

Copyright © 2013 American Chemical Society

Abstract

$\text{SrSi}_2\text{O}_2\text{N}_2:\text{Eu}^{2+}$ is an outstanding yellow emitting phosphor material with practical relevance for application in high power phosphor-converted light-emitting diodes. The triclinic compound exhibits high thermal and chemical stability and quantum efficiency above 90 % and can be excited by GaN-based UV to blue LEDs efficiently. We have now discovered a hitherto unknown monoclinic polymorph of $\text{SrSi}_2\text{O}_2\text{N}_2$, synthesized by solid-state reaction, which is characterized by an alternating stacking sequence of silicate layers made up of condensed SiON_3 tetrahedra and metal-ion layers. As proven by single-crystal X-ray diffraction, the arrangement of the silicate layers is significantly different from the triclinic polymorph. The translation period along the stacking direction is doubled in the monoclinic modification ($P2_1$, $Z = 8$, $a = 7.1036(14)$, $b = 14.078(3)$, $c = 7.2833(15)$ Å, $\beta = 95.23(3)^\circ$, $V = 725.3(3)$ Å³). TEM investigations in combination with HRTEM-image simulations confirm the structure model. The powder X-ray diffraction pattern shows that the volume fractions of the monoclinic and triclinic modifications are approximately equal in the corresponding powder sample. The emission wavelength of 532 nm (fwhm ~ 2600 cm⁻¹) as determined by single-crystal luminescence measurements of the monoclinic phase exhibits a shift to smaller wavelengths by ~ 5 nm compared to the triclinic polymorph. Differences of the luminescence properties between the monoclinic and triclinic phase are interpreted with respect to the differing coordination of Eu^{2+} in both phases. The new monoclinic

$\text{SrSi}_2\text{O}_2\text{N}_2\text{:Eu}^{2+}$ polymorph is a very attractive phosphor material for enhancement of color rendition of white-light pc-LEDs.

Keywords: Oxonitridosilicate, Structure Determination, TEM, Luminescence

2.2.1 Introduction

Phosphor-converted light-emitting diodes (pc-LEDs) are attractive candidates to replace incandescent light bulbs because of their much more efficient conversion of electric energy to visible light.^[1-4] In order to improve the performance and energy-saving potential of pc-LEDs, there is a huge demand for novel efficient phosphors as well as for improvement of the properties of existing materials.^[5,6] Various luminescent solid-state materials with emission from the blue to the red spectral region have been described.^[2,6-14] Analysis of their properties in relation to composition and crystal structure of the host material has revealed general requirements for phosphors to be used for pc-LED applications.^[12] The detailed knowledge of the crystal structure is a prerequisite as properties of such optical materials cannot be fully predicted from the material's composition alone.^[15]

According to these specifications, the material class of (oxo)nitridosilicates is well suited for application as host lattices because high quantum efficiencies (> 90%) can be achieved, a small Stokes shift is possible due to the rigidity of silicate substructures and pronounced thermal and chemical stability is present.^[16] $\text{SrSi}_2\text{O}_2\text{N}_2$ is a host lattice showing excellent luminescence properties when doped with Eu^{2+} . $\text{SrSi}_2\text{O}_2\text{N}_2\text{:Eu}^{2+}$ exhibits intense broad-band emission in the yellow-green spectral region due to the parity allowed $4f^6(7F)5d^1 \rightarrow 4f^7(8S_{7/2})$ transition when excited by UV to blue light.^[4,10,17-35] The disordered crystal structure consists of alternating metal-ion and silicate layers. Both the idealized ordered structure as well as the average structure of the disordered variant are triclinic ($a = 7.0802(2)$, $b = 7.2306(2)$, $c = 7.2554(2)$ Å, $\alpha = 88.767(3)$, $\beta = 84.733(2)$, $\gamma = 75.905(2)^\circ$, $V = 358.73(2)$ Å³, space group $P1$). The metal-ion layers are strongly affected by disorder phenomena, i.e. polysynthetic twinning, antiphase boundaries, or oriented intergrowth. The silicate layers are built up of vertex-sharing $\text{SiO}^{[1]}\text{N}^{[3]}_3$ tetrahedra forming *dreier* rings perpendicular to $[010]^*$.^[36] The reflection positions in powder X-ray diffraction (PXRD) patterns, in principle, resemble those reported by Zhu (X_2 -phase)^[37] and Hintzen^[28] although these authors have proposed different metrics. However, some powder patterns of our samples and also those in the literature show

a number of reflections that are inconsistent with the triclinic structure model of SrSi₂O₂N₂ discussed in literature.^[20,29,31,35,38-41] Surprisingly, samples with such "impurity phases" exhibit excellent overall luminescence properties. Whenever peak emission wavelengths of SrSi₂O₂N₂:Eu²⁺ powder samples are reported to be significantly smaller than 537 nm the corresponding PXRD patterns show unknown, additional reflections.^[20,29,31,35,38,39] In this contribution, we clarify the nature of the additional phase that leads to these reflections and further investigate its impact on luminescence properties.

2.2.2 Experimental Section

2.2.2.1 Synthesis

SrSi₂O₂N₂:Eu²⁺ (2 mol% Eu) was prepared by heating a stoichiometric mixture of Sr₂SiO₄:Eu²⁺ and Si₃N₄ (UBE, > 98%) for 16 h to 1540 °C in forming gas atmosphere (N₂:H₂ = 95:5) according to eq. 1. The starting materials were placed on tungsten foil within a molybdenum crucible and heated to the final temperature with 300 °C/h (T < 1000 °C) and 150 °C/h (T > 1000 °C), respectively.



2.2.2.2 X-ray Spectroscopy

The chemical composition of several crystallites was analyzed by energy dispersive X-ray (EDX) spectroscopy using a JSM-6500F scanning electron microscope (SEM, Jeol) with a Si/Li EDX detector (Oxford Instruments, model 7418). The SEM was also used to collect images of particles to study their morphology. Further analyses were performed using the EDX system (TEM Tops 30, Edax) of the transmission electron microscope mentioned below.

2.2.2.3 Powder X-ray Diffraction

PXRD data were collected on a STOE STADI P diffractometer (Cu-K_{α1} radiation, Ge(111) monochromator, position sensitive detector) in transmission geometry using a flat sample

holder with thin film of investigated powder material. Rietveld refinement was carried out using the TOPAS package.^[42]

2.2.2.4 Single-Crystal X-ray Diffraction

Selected green luminescent single crystals of $\text{SrSi}_2\text{O}_2\text{N}_2:\text{Eu}^{2+}$ were mounted on glass fibers and checked for quality on a Buerger precession camera. Intensity data were collected on a Nonius Kappa-CCD diffractometer with graded multilayer X-ray optics (Mo- K_α radiation, $\lambda = 0.71093 \text{ \AA}$). The structure was solved by direct methods and refined by full-matrix least-squares methods.^[43] Further details of the crystal structure investigation may be obtained from Fachinformationszentrum Karlsruhe, 76344 Eggenstein-Leopoldshafen, Germany (fax, (+49)7247-808-666; e-mail, crysdata@fiz-karlsruhe.de, http://www.fiz-karlsruhe.de/request_for_deposited_data.html) on quoting the depository number CSD-425649.

2.2.2.5 Transmission Electron Microscopy

Selected area electron diffraction (SAED) patterns and high-resolution (HR) images were recorded on a Fei Titan 80-300 (acceleration voltage 300 kV) transmission electron microscope (TEM). Tilt series of diffraction patterns were obtained using a double-tilt sample holder with a maximum tilt angle of $\pm 30^\circ$. For preliminary experiments, ground powder samples were dispersed in ethanol and drop cast on copper grids coated with a holey carbon film. Since such samples showed pronounced preferred orientation, the powder was mixed with a two-component glue, placed between silicon wafers and glass panels, and then fixed in brass tubes (inner diameter 2 mm). These were cut into slices perpendicular to the tube elongation (thickness approx. 200 μm) and polished to 80-90 μm using different SiC coated sand papers (grain size: 40–5 μm). Finally, the thickness in the middle of the disk was reduced to approximately 10 μm using a dimple grinder (type 650, Gatan) and diamond polishing paste (Electron Microscopy Science). Subsequently, a hole in the glue matrix was fabricated using a precision ion polishing system (type 691, Gatan). Crystallites at the perimeter of the hole (partially free of glue) were randomly oriented and suitable for TEM investigations. For simulations of SAED patterns and HRTEM images EMS program was used.^[44] In order to ensure comparability to results from single-crystal and powder investigations, the same sample was used for TEM analysis.

2.2.2.6 Luminescence

Luminescence investigations were done using a luminescence microscope consisting of a HORIBA Fluoromax4 spectrofluorimeter system attached to an Olympus BX51 microscope via fiber optical bundles. The samples were measured inside a glass capillary (outer diameter approx. 0.2 mm). The excitation wavelength was chosen to 420 nm with a spectral width of 10 nm. The emission spectra were collected in the wavelength range between 450 nm and 750 nm with 2 nm step size. This range was also used for color-point calculations.

2.2.3 Results and Discussion

2.2.3.1 Synthesis and chemical analysis

In powder samples of $\text{SrSi}_2\text{O}_2\text{N}_2:\text{Eu}^{2+}$ (2 mol% Eu) prepared by the above-mentioned synthesis, which exhibit additional reflections in PXRD patterns (referring to triclinic structure model), two different types of particle morphology can be found in SEM images. Particles of type 1 (Figure 1, left) are built up of stacked platelet-like crystals. Due to the well-known real-structure effects,^[36] such morphology seems to be reasonable for the triclinic $\text{SrSi}_2\text{O}_2\text{N}_2$ structure type. Particles of type 2 (Figure 1, right) show crystals with approximately isometric polyhedral shape with diameters of $> 10 \mu\text{m}$ as required for X-ray structure analysis, which is surprising for $\text{SrSi}_2\text{O}_2\text{N}_2$. EDX yields an average composition (7 measurements), normalized according to the overall metal content, of $\text{Sr}_{0.98}\text{Eu}_{0.02}\text{Si}_{2.35(3)}\text{O}_{2.6(2)}\text{N}_{2.3(6)}$ for crystals of type 2. This is in accordance with the nominal composition $\text{SrSi}_2\text{O}_2\text{N}_2$ taking into account the typical uncertainty intervals (Sr/Si signal overlap).

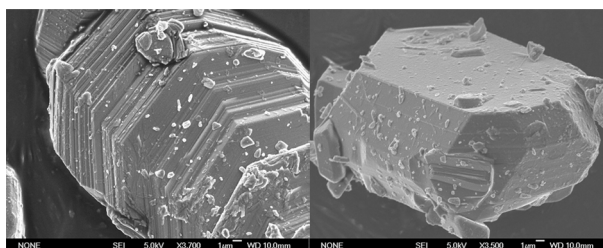


Figure 1. SEM images of two typical $\text{SrSi}_2\text{O}_2\text{N}_2:\text{Eu}^{2+}$ particles in the powder sample. Stacked platelet-like crystals (left) and polyhedral single crystals (right) can clearly be distinguished.

2.2.3.2 Single-Crystal Structure Analysis

Diffraction data of a green luminescent polyhedral crystal (type 2) were collected and the corresponding crystal structure of monoclinic $\text{SrSi}_2\text{O}_2\text{N}_2\cdot\text{Eu}^{2+}$ was refined in space group $P2_1$.^[43] The Eu^{2+} content (2 mol%) was neglected because of its insignificant contribution to the scattering density. A separate scale factor was used for the broadened reflections with $h = 2n + 1$, and inversion twinning was taken into account. Crystallographic data are summarized in Table 1. Similar to triclinic $\text{SrSi}_2\text{O}_2\text{N}_2$, the crystal structure exhibits alternating metal-ion and silicate layers, the latter ones built up from highly condensed $\text{SiO}^{[1]}\text{N}^{[3]}_3$ tetrahedra forming *dreier* rings.^[36,45-48] In contrast to the triclinic structure, the tetrahedra orientation changes in consecutive silicate layer, which are rotated against each other by 180° , consistent with a 2_1 screw axis and the doubled translation period along the $[010]^*$ stacking direction compared to the triclinic structure (Figure 2).^[36] The cations are coordinated in a trigonal prismatic way by O atoms, similar to the triclinic model.

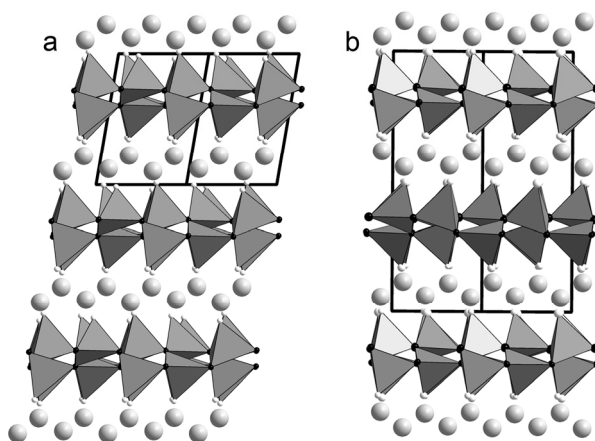


Figure 2. Crystal structures (metal atoms: gray spheres, unit-cells outlined) of (a) triclinic $\text{SrSi}_2\text{O}_2\text{N}_2$ (projection along $[101]$) and (b) monoclinic $\text{SrSi}_2\text{O}_2\text{N}_2$ (projection along $[10\bar{1}]$). The orientation of consecutive silicate layers (SiON_3 tetrahedra: gray, oxygen: white spheres, nitrogen: black spheres) differs in both models.

The 180° rotation of two consecutive silicate layers corresponds to the structure of twin boundaries as they are present in the real structure of $\text{Sr}_{0.5}\text{Ba}_{0.5}\text{Si}_2\text{O}_2\text{N}_2$, which is isotopic to triclinic $\text{SrSi}_2\text{O}_2\text{N}_2$.^[47] There, such twin boundaries occur approximately every 100 nm. Significantly smaller twin domains dramatically change the PXRD pattern as they involve a different average structure. Monoclinic $\text{SrSi}_2\text{O}_2\text{N}_2$, however, can be regarded as a maximally twinned form of the triclinic modification with “domains” of just one layer thickness in an ordered stacking sequence. This yields higher symmetry and different unit-cell metrics.

Table 1. Crystallographic data for SrSi₂O₂N₂.

Crystal system	monoclinic
Space group	<i>P2</i> ₁ (no. 4)
Lattice parameters [Å]	<i>a</i> = 7.1036(14) <i>b</i> = 14.078(3) <i>c</i> = 7.2833(15) <i>β</i> = 95.23(3) ^o
Cell volume [Å ³]	725.3(3)
<i>Z</i>	8
Formula weight [g mol ⁻¹]	203.82
ρ_{calcd} [g cm ⁻³]	3.733
Absorption coefficient μ [mm ⁻¹]	15.358
<i>F</i> (000)	768
2 θ range [°]	3.16 – 26.00
Radiation λ [Å]	0.71073 (Mo- <i>K</i> _α)
Reflections (total)	5572
Independent reflections	1468
Observed reflections	1145
Goodness of fit	1.077
<i>R</i> 1 / <i>wR</i> 2 (all reflections)	0.0850 / 0.1743
<i>R</i> 1 / <i>wR</i> 2 ($F_o^2 \geq 2\sigma(F_o^2)$)	0.0633 / 0.1573
min / max residual electron density [eÅ ⁻³]	- 1.58 / 2.74

2.2.3.3 Lattice Energy Calculations

The consistency of the structure model is corroborated by lattice energy calculations (MAPLE, Madelung part of lattice energy).^[49-52] The assignment of O and N atoms was done in analogy to other Sr_{1-x}Ba_xSi₂O₂N₂ phases with the same silicate layer topology.^[36,45-48] This is confirmed by the calculated values listed in Table 2 which are close to typical partial MAPLE values.^[16] The comparison between the calculated total MAPLE value and the sum of MAPLE values corresponding to the reference reaction equation, starting from the respective binaries, shows a difference of only 0.06 %. This is in good agreement to the value calculated for EuSi₂O₂N₂ also based on single crystal data ($\Delta = 0.1$ %).

Table 2. Results of MAPLE Calculations (in kJ/mol) for Monoclinic SrSi₂O₂N₂: Partial MAPLE Values, Total MAPLE Sum and Difference to Theoretical Total MAPLE Value Corresponding to a Reference Equation^a

Sr ²⁺	Si ⁴⁺	O ^{[1]2-}	N ^{[3]3-}	Total MAPLE	Δ
1929-2070	9373-9617	2227-2432	6093-6268	37923	0.06 %
Total MAPLE (SrO + 0.5 SiO ₂ + 0.5 Si ₃ N ₄): 37946					

^aTypical MAPLE values (in kJ/mol): Sr²⁺: 1500-2100; Si⁴⁺: 9000-10200; O^{[1]2-}: 2000-2800; N^{[3]3-}: 5000-6200.

2.2.3.4 Rietveld Refinement

In order to evaluate the proportion of monoclinic $\text{SrSi}_2\text{O}_2\text{N}_2$ in the powder sample, a two-phase Rietveld refinement using TOPAS^[42] was done (Figure 3). Weighted distance restraints for Si-O/N tetrahedra in monoclinic $\text{SrSi}_2\text{O}_2\text{N}_2$ were used to ensure comparability to other $\text{Sr}_{1-x}\text{Ba}_x\text{Si}_2\text{O}_2\text{N}_2$ phases with the same kind of silicate layers.^[36,45-48] Thereby all atomic coordinates could be refined. The remaining misfit was significantly reduced after adding the triclinic structure of $\text{SrSi}_2\text{O}_2\text{N}_2$ as a second phase. For the latter, only Sr and Si atom positions were refined.^[36] Some 2θ regions were excluded because they are strongly affected by diffuse scattering as a consequence of real-structure effects in triclinic $\text{SrSi}_2\text{O}_2\text{N}_2$ ^[47] (stacking disorder) which cannot be described by the Rietveld method. The degree of cation disorder, i.e. value of antiphase transitions in %, was refined to 40 % using split positions as described for the triclinic average structure.^[36,47] As expected, both diffraction patterns are rather similar since basically only the N positions in every second silicate layer are different in the two structure models. Nevertheless, the patterns can clearly be distinguished by reflections at 14.0 , 17.8 , 20.9 , 22.7 , and especially at $29.4^\circ 2\theta$ because there are no contributions from the triclinic structure (see Figure 3). The results confirm that the described stacking sequence in monoclinic $\text{SrSi}_2\text{O}_2\text{N}_2$ is present in a significant portion of the powder particles. The amounts of both modifications are approximately equal, and no further unexplained reflections occur in PXRD pattern.

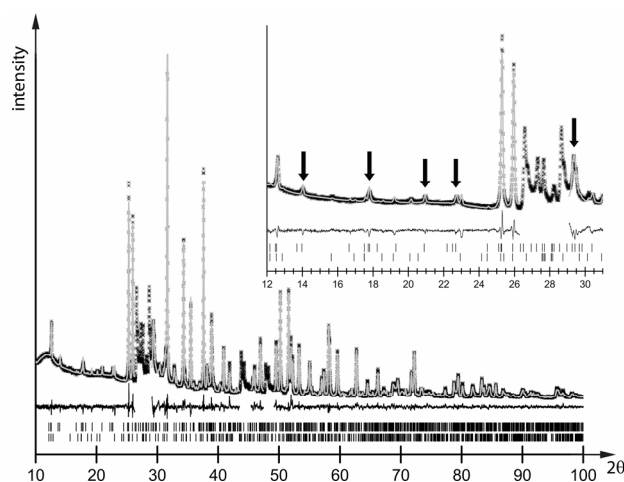


Figure 3. Two-phase Rietveld fit ($R_p = 0.041$, $wR_p = 0.055$; 8367 data points) of the PXRD pattern of $\text{SrSi}_2\text{O}_2\text{N}_2\cdot\text{Eu}^{2+}$ with measured histogram (black crosses), calculated pattern (gray solid line), difference curve (black solid line) and positions of reflections (bars): top monoclinic $\text{SrSi}_2\text{O}_2\text{N}_2$ (48 %, $\rho_{\text{calcd}} [\text{g cm}^{-3}] = 3.7083(5)$), bottom triclinic $\text{SrSi}_2\text{O}_2\text{N}_2$ (52 %, $\rho_{\text{calcd}} [\text{g cm}^{-3}] = 3.7043(2)$). The excluded regions (no difference curve) correspond to maxima due to diffuse scattering. Selected reflections exclusively belonging to monoclinic phase are marked by black arrows in enlarged pattern (upper right).

2.2.3.5 Transmission Electron Microscopy and Electron Diffraction

In TEM samples prepared by dispersing powder on Cu grids with carbon film, all plate-like crystallites exhibited approximately the same orientation of the stacking direction, perpendicular to the grid, as it is typical for layered compounds. This, of course, impedes the determination of the stacking periodicities. Such texture effects are not significant if the powder is embedded in glue, where crystallites with a translation period of ~ 14 Å, typical for monoclinic SrSi₂O₂N₂, could easily be found. TEM-EDX yielded an average formula of Sr_{0.98}Eu_{0.02}Si_{2.01(8)}O_{2.3(5)}N_{1.6(3)} for the crystallites investigated. Traces of SrSiO₃ were found, although the corresponding reflections cannot be observed in PXRD data. Various SAED patterns showing translation periods of 14 Å can be simulated based on the results from single-crystal analysis. Calculated tilt angles between different zone axes correspond to the expected ones (Figure 4).^[44] Experimental SAEDs contain $0k0$ reflections with $k = 2n + 1$ (kinematically absent for $2_1 \parallel [010]$) because of dynamic effects.

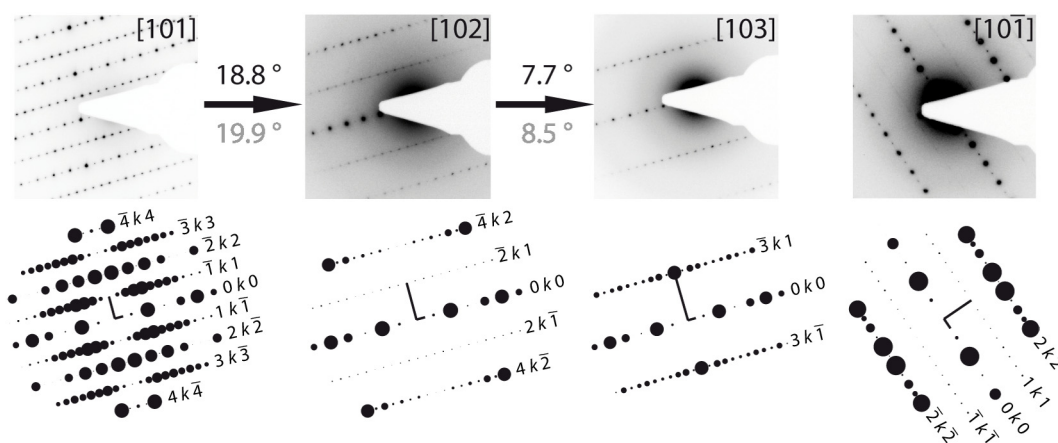


Figure 4. Experimental SAED patterns (top) of monoclinic SrSi₂O₂N₂:Eu²⁺ with the corresponding zone axes and simulated ones (bottom, calculated from single-crystal data). Experimental tilt angles (black) between zone axes match calculated ones (gray). The [10 $\bar{1}$] pattern was recorded using another crystallite due to the limited tilt range of the sample holder.

Although the monoclinic model for SrSi₂O₂N₂ is appropriate to simulate experimental SAED images, the local stacking sequence might differ since the beam diameter for SAED patterns ($\varnothing = 100$ nm) is significantly larger than the smallest area (10 unit cells ≈ 10 nm) that may be described by an ordered structure model. Figure 5 shows an HRTEM image of a crystallite fringe. As the Fourier transform (FT) of the marked area (diagonal 10 nm) corresponds to the SAED pattern, this area is representative for the whole area contributing to SAED patterns; no or few defects are expected.

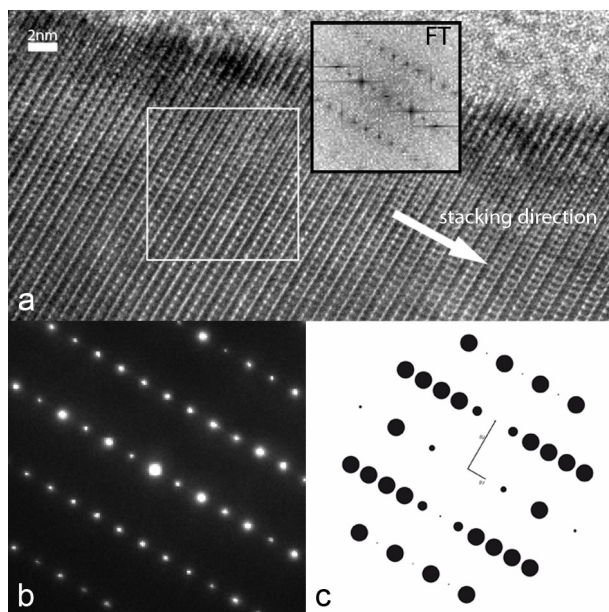


Figure 5. (a) HRTEM image of monoclinic $\text{SrSi}_2\text{O}_2\text{N}_2:\text{Eu}^{2+}$ (zone axis $[101]$); approximately 10 unit cells (~ 10 nm) along stacking direction (white frame), the corresponding FT is shown (black frame); (b) experimental SAED pattern (beam diameter ~ 100 nm); (c) SAED pattern simulated using $\text{SrSi}_2\text{O}_2\text{N}_2$ (monoclinic) single-crystal data.

HRTEM image simulations using the multislice method correlate the structure model to experimental images of a defocus series, passing the Scherzer defocus.^[44] The defocus value in Figure 6a (zone axis $[10\bar{1}]$) is -52 nm, i.e. close to the Scherzer defocus so that contrasts can directly be correlated to atom positions.

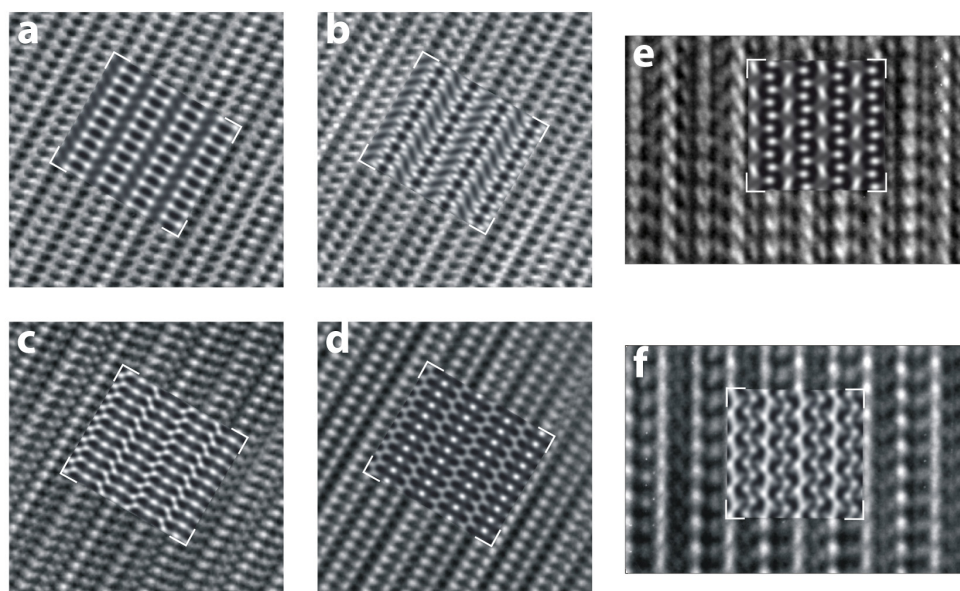


Figure 6. HRTEM (accelerating voltage = 300 kV) images of monoclinic $\text{SrSi}_2\text{O}_2\text{N}_2:\text{Eu}^{2+}$ crystallites of zone axis $[101]$ (a-d) and $[10\bar{1}]$ (e,f) with inserted image simulations (a: $\Delta f = -52$ nm; b: $\Delta f = -72$ nm; c: $\Delta f = -92$ nm; d: $\Delta f = -112$ nm; e: $\Delta f = +19$ nm; f: $\Delta f = +40$ nm; for all simulations: aperture diameter = 20 nm^{-1} , $c_s = 1.2$ mm, spread of focus = 2.14 nm, beam semi-convergence = 0.60 mrad, layer thickness approx. 4 nm).

The simulation fits all features of the experimental image quite well, which is also true for the other HRTEM simulations in Figure 6. In summary, the results of TEM investigations confirm the existence of the monoclinic stacking variant of SrSi₂O₂N₂ derived from single-crystal X-ray diffraction analysis.

2.2.3.6 Luminescence

The emission wavelength of green (presumably) triclinic SrSi₂O₂N₂:Eu²⁺ (no additional reflections in PXRD pattern belonging to monoclinic modification) was reported in a range of ~537-540 nm for doping with 2 mol% Eu,^[4,17,21,24,27,53,54] which leads to high quantum efficiency (QE > 90%).²⁴ Regarding the enhancement of color rendition of white-light pc-LEDs that make use of mixtures of green and red emitting phosphors, a shift of the peak emission wavelength towards shorter wavelengths (~ 530 nm) would be desirable.^[14] The color point of “triclinic” SrSi₂O₂N₂:Eu²⁺ can be changed by variation of the Eu-doping level^[19,26,28-30,34] or substitution of Sr by Ca or Ba.^[11,23,24,26,34,55-57] Nevertheless, all changes of the host-lattice composition shift the emission wavelength towards smaller energies. For Sr_{1-x}Ba_xSi₂O₂N₂:Eu²⁺ with x ≥ 0.75, a shift to higher energies can be achieved; however, its emission spectrum is located in the blue-green spectral region due to the different structure type.^[28,46] The determination of luminescence properties of monoclinic SrSi₂O₂N₂:Eu²⁺ cannot be done using powder samples because all obtained samples were inhomogeneous (see section: Rietveld refinement). In order to avoid averaging of emission signals of both modifications, the emission spectrum of the single crystal, which was already used for structure analysis, was measured (Figure 7).

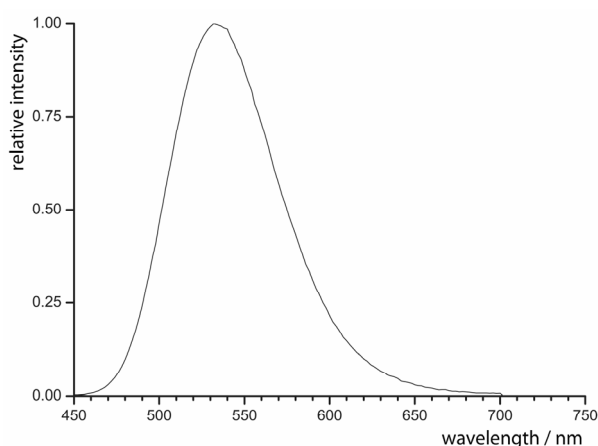


Figure 7. Emission spectrum of the SrSi₂O₂N₂:Eu²⁺ (2 mol% Eu) single crystal ($\lambda_{\text{exc}} = 420$ nm, $\lambda_{\text{em}} = 532$ nm, fwhm ~2600 cm⁻¹); CIE color coordinates: x = 0.314, y = 0.621.

The peak position was determined at $\lambda_{\text{em}} = 532 \text{ nm}$ by exciting with UV to blue radiation. This means that the emission wavelength of the single crystal of monoclinic $\text{SrSi}_2\text{O}_2\text{N}_2:\text{Eu}^{2+}$ is shifted at least 5 nm towards smaller wavelengths in comparison to powder material of $\text{SrSi}_2\text{O}_2\text{N}_2:\text{Eu}^{2+}$ which do not show additional reflections in PXRD pattern belonging to monoclinic modification. In order to prove whether this fact is intrinsic or caused by reabsorption of emitted high-energetic radiation in the powder sample (i.e. excitation of another Eu^{2+} -ion by re-emitted photons due to overlap of absorption and emission band), various crystallites (independent of crystal symmetry) with anisotropic morphology were investigated. If the emission wavelength is affected by the length of the radiation pathway through a crystal (i.e. number of activator centers along the pathway, maximal for macroscopic powder sample) different values for λ_{em} are expected for varying orientations of crystallites. The more centers are involved, the more the macroscopically composed emission signal gets shifted to smaller energies. In the present case, λ_{em} was constant for various orientations of three investigated anisotropic crystallites with different sizes. Thus, the red-shifted emission wavelength of $\text{SrSi}_2\text{O}_2\text{N}_2:\text{Eu}^{2+}$ powder samples (“triclinic” modification, i.e. no additional reflections in PXRD patterns belonging to monoclinic modification), compared to $\text{SrSi}_2\text{O}_2\text{N}_2:\text{Eu}^{2+}$ single crystal (monoclinic modification), is not caused by reabsorption effects. Therefore, the observed differences in measured λ_{em} -values for $\text{SrSi}_2\text{O}_2\text{N}_2:\text{Eu}^{2+}$ (single crystal, monoclinic) and $\text{SrSi}_2\text{O}_2\text{N}_2:\text{Eu}^{2+}$ (powder, no additional reflections in PXRD pattern belonging to monoclinic modification) are significant. In order to draft a possible reason for the shift on the basis of the crystal structures, we focus on lattice parameters of triclinic and monoclinic modification. In contrast to the triclinic phase, monoclinic $\text{SrSi}_2\text{O}_2\text{N}_2$ has larger a and c lattice parameters which represent the periodicity of silicate layers because corresponding settings are equal for both crystal structures. As a direct consequence, interatomic distances increase which corresponds to less corrugated chains of condensed SiON_3 tetrahedra. Furthermore, Sr-O distances are also increased which should lead to a decreased 5d-orbital splitting in case of substitution of Sr by an Eu activator ion and an increase of the energetic separation of the $4f^75d^0$ and $4f^65d^1$ states, equivalent to a blue-shifted maximum of the emission band for monoclinic $\text{SrSi}_2\text{O}_2\text{N}_2:\text{Eu}^{2+}$ compared to the triclinic modification. For both modifications, average activator-ligand distances are slightly longer than the sum of the ionic radii.^[52] This hardly leads to lattice relaxation in the case of excited Eu^{2+} . As a consequence, less electron-phonon coupling may result in reduced Stokes shift and narrower fwhm, which decreases thermal quenching of luminescence.^[58] Luminescence properties of the above-mentioned $\text{SrSi}_2\text{O}_2\text{N}_2:\text{Eu}^{2+}$ powder (mixture of triclinic and

monoclinic phase) were also measured while reabsorption effects for the powder were minimized by extrapolating the emission properties of a dilution series (silicone suspensions) to zero phosphor concentration, in order to ensure comparability of single-crystal and powder data. An emission wavelength of $\lambda_{\text{em}} = 535$ nm was determined supporting the thesis that the emission band of the monoclinic modification is blue-shifted in comparison to samples without additional reflections in the PXRD pattern (537-540 nm).

2.2.4 Conclusion

A new monoclinic modification of $\text{SrSi}_2\text{O}_2\text{N}_2$ has been characterized applying a combination of X-ray diffraction and electron-microscopy methods. For the first time, single-crystal data could be obtained for samples with this composition. The triclinic and monoclinic modifications are, in fact, polytypes. Phase formation might therefore be controlled by kinetics. Polytypism was occasionally discussed for layered $\text{M}^{\text{II}}\text{Si}_2\text{O}_2\text{N}_2$ ($\text{M} = \text{Ca}, \text{Sr}, \text{Ba}$) phases; now we have described two distinct maximum degree of order (MDO) polytypes. The emission wavelength of a single crystal of the Eu-doped monoclinic modification is shifted by ~ 5 nm towards smaller wavelengths ($\lambda_{\text{em}} = 532$ nm) compared to that of triclinic $\text{SrSi}_2\text{O}_2\text{N}_2:\text{Eu}^{2+}$ (2 mol%) whose emission wavelength cannot be tuned to that value by host-lattice modification because substitution of Sr by Ca as well as Ba always leads to red-shifted emission bands. The triclinic and monoclinic polytypes only differ by the orientation of consecutive symmetrically equivalent silicate layers. A dependence of luminescence properties on layer orientation in polytypes has not yet been discussed for phosphor materials in the literature. As the triclinic and monoclinic modifications are so closely related, it is not clear if phase pure samples of any $\text{SrSi}_2\text{O}_2\text{N}_2$ modification can be prepared. The results from our contribution complement the understanding of structure-property relationships for frequently used phosphor material $\text{SrSi}_2\text{O}_2\text{N}_2:\text{Eu}^{2+}$.

Acknowledgment

The authors thank Dr. Peter Mayer for collecting single-crystal data and Dr. Florian Stadler for preliminary work (both LMU Munich) as well as Petra Huppertz (LDCA Aachen) for single-crystal luminescence measurements. Financial support by the Fonds der Chemischen Industrie (FCI) is gratefully acknowledged.

2.2.5 References

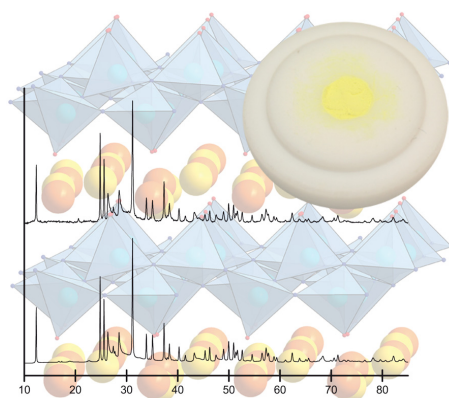
- [1] M. Mikami, H. Watanabe, K. Uheda, S. Shimooka, Y. Shimomura, T. Kurushima, N. Kijima, *IOP Conf. Ser.: Mater. Sci. Eng.* **2009**, *1*, 012002 (1-10).
- [2] S. Ye, F. Xiao, Y. X. Pan, Y. Y. Ma, Q. Y. Zhang, *Mater. Sci. Eng., R* **2010**, *71*, 1-34.
- [3] C. C. Lin, R.-S. Liu, *J. Phys. Chem. Lett.* **2011**, *2*, 1268-1277.
- [4] R. Mueller-Mach, G. Mueller, M. R. Krames, H. A. Höpfe, F. Stadler, W. Schnick, T. Juestel, P. Schmidt, *Phys. Status Solidi A* **2005**, *202*, 1727-1732.
- [5] A. A. Setlur, *Electrochem. Soc. Interface* **2009**, *18*, 32-36.
- [6] R.-J. Xie, N. Hirosaki, T. Takeda, T. Suehiro, *ECS J. Solid State Sci. Technol.* **2013**, *2*, R3031-R3040.
- [7] R.-J. Xie, N. Hirosaki, Y. Li, T. Takeda, *Materials* **2010**, *3*, 3777-3793.
- [8] X.-H. He, N. Lian, J.-H. Sun, M.-Y. Guan, *J. Mater. Sci.* **2009**, *44*, 4763-4775.
- [9] R.-J. Xie, N. Hirosaki, T. Takeda, *J. Korean Ceram. Soc.* **2012**, *49*, 375-379.
- [10] R.-J. Xie, N. Hirosaki, *Sci. Technol. Adv. Mater.* **2007**, *8*, 588-600.
- [11] D. P. Dutta, A. K. Tyagi, *Solid State Phenomena* **2009**, *155*, 113-143.
- [12] P. F. Smet, A. B. Parmentier, D. Poelman, *J. Electrochem. Soc.* **2011**, *158*, R37-R54.
- [13] H. A. Höpfe, *Angew. Chem.* **2009**, *121*, 3626-3636; *Angew. Chem. Int. Ed.* **2009**, *48*, 3572-3582.
- [14] J. M. Phillips, M. E. Coltrin, M. H. Crawford, A. J. Fischer, M. R. Krames, R. Mueller-Mach, G. O. Mueller, Y. Ohno, L. E. S. Rohwer, J. A. Simmons, J. Y. Tsao, *Laser & Photon. Rev.* **2007**, *1*, 307-333.
- [15] M. Mikami, N. Kijima, *Optical Materials* **2010**, *33*, 145-148.
- [16] M. Zeuner, S. Pagano, W. Schnick, *Angew. Chem.* **2011**, *123*, 7898-7920; *Angew. Chem. Int. Ed.* **2011**, *50*, 7754-7775.
- [17] J. Botterman, K. Van den Eeckhout, A. J. J. Bos, P. Dorenbos, P. F. Smet, *Opt. Mater. Express* **2012**, *2*, 341-349.
- [18] K. Machida, *IOP Conf. Ser.: Mater. Sci. Eng.* **2011**, *18*, 052001 (1-4).
- [19] Y. H. Song, W. J. Park, D. H. Yoon, *J. Phys. Chem. Solids* **2010**, *71*, 473-475.
- [20] X. Song, H. He, R. Fu, D. Wang, X. Zhao, Z. Pan, *J. Phys. D: Appl. Phys.* **2009**, *42*, 065409-065414.
- [21] C.-C. Yang, C.-M. Lin, Y.-J. Chen, Y.-T. Wu, S.-R. Chuang, *Appl. Phys. Lett.* **2007**, *90*, 123503 (1-3).
- [22] Y. Zhang, X. Liu, B. Lei, H. Wang, Q. Sun, *Energy Procedia* **2012**, *16*, 391-396.

- [23] B. Y. Han, K.-S. Sohn, *Electrochem. Solid-State Lett.* **2010**, *13*, J62-J64.
- [24] V. Bachmann, C. Ronda, O. Oeckler, W. Schnick, A. Meijerink, *Chem. Mater.* **2009**, *21*, 316-325.
- [25] M. Zhang, J. Wang, Z. Zhang, Q. Zhang, Q. Su, *Appl. Phys. B: Lasers Opt.* **2008**, *93*, 829-835.
- [26] B.-G. Yun, Y. Miyamoto, H. Yamamoto, *J. Electrochem. Soc.* **2007**, *154*, J320-J325.
- [27] X. Yang, H. Song, L. Yang, X. Xu, *J. Am. Ceram. Soc.* **2011**, *94*, 28-35.
- [28] Y. Q. Li, A. C. A. Delsing, G. De With, H. T. Hintzen, *Chem. Mater.* **2005**, *17*, 3242-3248.
- [29] Y. Song, X. Xu, H. Zou, Y. Sheng, H. You, *J. Alloys Compd.* **2012**, *513*, 86-90.
- [30] B.-G. Yun, K. Machida, H. Yamamoto, *J. Ceram. Soc. Jpn.* **2007**, *115*, 619-622.
- [31] Y.-C. Fang, P.-C. Kao, Y.-C. Yang, S.-Y. Chu, *J. Electrochem. Soc.* **2011**, *158*, J246-J249.
- [32] K. Y. Jung, J. H. Seo, *Electrochem. Solid-State Lett.* **2008**, *11*, J64-J67.
- [33] S. D. Jee, K. S. Choi, J. S. Kim, *Met. Mater. Int.* **2011**, *17*, 655-660.
- [34] G. Anoop, I. H. Cho, D. W. Suh, J. S. Yoo, *Phys. Status Solidi A* **2012**, *209*, 2635-2640.
- [35] X.-K. Meng, J. Tan, T. Lei, W. Zhang, W. Yan, C.-M. Li, X.-W. Sun, *Chinese J. Inorg. Chem.* **2012**, *28*, 893-897.
- [36] O. Oeckler, F. Stadler, T. Rosenthal, W. Schnick, *Solid State Sci.* **2007**, *9*, 205-212.
- [37] W. H. Zhu, P. L. Wang, W. Y. Sun, D. S. Yan, *J. Mater. Sci. Lett.* **1994**, *13*, 560-562.
- [38] X. Song, R. Fu, S. Agathopoulos, H. He, X. Zhao, R. Li, *J. Electrochem. Soc.* **2010**, *157*, J34-J38.
- [39] X. Song, R. Fu, S. Agathopoulos, H. He, X. Zhao, J. Zeng, *Mater. Sci. Eng., B* **2009**, *164*, 12-15.
- [40] J.-Y. Tang, X.-F. Yang, C. Zhan, L.-Y. Hao, X. Xu, W.-H. Zhang, *J. Mater. Chem.* **2012**, *22*, 488-494.
- [41] J. Ruan, R.-J. Xie, N. Hirosaki, T. Takeda, *J. Electrochem. Soc.* **2012**, *159*, H66-H71.
- [42] A. Coelho, *TOPAS – Academic* **2007**, Brisbane: Coelho Software.
- [43] G. M. Sheldrick, *Acta Crystallogr., Sect. A: Found. Crystallogr.* **2008**, *64*, 112-122.
- [44] P. A. Stadelmann, *Ultramicroscopy* **1987**, *21*, 131-146.
- [45] J. A. Kechele, O. Oeckler, F. Stadler, W. Schnick, *Solid State Sci.* **2009**, *11*, 537-543.
- [46] M. Seibald, T. Rosenthal, O. Oeckler, F. Fahrnbauer, A. Tücks, P. J. Schmidt, W. Schnick, *Chem.–Eur. J.* **2012**, *18*, 13446-13452.

- [47] M. Seibald, O. Oeckler, V. R. Celinski, P. J. Schmidt, A. Tücks, W. Schnick, *Solid State Sci.* **2011**, *13*, 1769-1778.
- [48] F. Stadler, O. Oeckler, H. A. Höppe, M. H. Möller, R. Pöttgen, B. D. Mosel, P. Schmidt, V. Duppel, A. Simon, W. Schnick, *Chem.–Eur. J.* **2006**, *12*, 6984-6990.
- [49] R. Hoppe, *Angew. Chem.* **1966**, *78*, 52-63; *Angew. Chem. Int. Ed.* **1966**, *5*, 95-106.
- [50] R. Hoppe, *Angew. Chem.* **1970**, *82*, 7-16; *Angew. Chem. Int. Ed.* **1970**, *9*, 25-34.
- [51] R. Hübenthal, *Madlung Part of Lattice Energy*, version 4, **1993**, University of Gießen (Germany).
- [52] R. D. Shannon, *Acta Crystallogr., Sect. A: Found. Crystallogr.* **1976**, *32*, 751-767.
- [53] V. Bachmann, T. Juestel, A. Meijerink, C. Ronda, P. J. Schmidt, *J. Lumin.* **2006**, *121*, 441-449.
- [54] C.-W. Yeh, Y. Li, J. Wang, R.-S. Liu, *Opt. Express* **2012**, *20*, 18031-18043.
- [55] H. Yamamoto, M. Yamauchi, J. Iizuka, B. G. Yun, K. Machida, N. Kijima, *ECS Trans.* **2011**, *33*, 109-114.
- [56] B. Lei, K. Machida, T. Horikawa, H. Hanzawa, *Chem. Lett.* **2011**, *40*, 140-141.
- [57] I. H. Cho, G. Anoop, D. W. Suh, S. J. Lee, J. S. Yoo, *Opt. Mater. Express* **2012**, *2*, 1292-1305.
- [58] G. Blasse, B. C. Grabmaier, *Luminescent Materials*; Springer: Berlin, **1994**.

2.3 Real Structure and Diffuse Scattering of $\text{Sr}_{0.5}\text{Ba}_{0.5}\text{Si}_2\text{O}_2\text{N}_2:\text{Eu}^{2+}$ - A Highly Efficient Yellow Phosphor for pc-LEDs

Markus Seibald, Oliver Oeckler, Vinicius R. Celinski, Peter J. Schmidt, Andreas Tücks, Wolfgang Schnick



published in: *Solid State Sci.* **2011**, *13*, 1769-1778.

Copyright © 2011 Elsevier

Abstract

$\text{Sr}_{0.5}\text{Ba}_{0.5}\text{Si}_2\text{O}_2\text{N}_2:\text{Eu}^{2+}$ is a promising new phosphor for white light phosphor converted (pc)-LEDs. The material shows broad-band emission due to parity allowed $4f^6(^7F)5d \rightarrow 4f^7(^8S_{7/2})$ transition in the yellow spectral range ($\lambda_{\text{em}} \approx 560$ nm) while excited with UV to blue radiation. The X-ray powder diffraction pattern shows noticeable intensity maxima indicative for diffuse scattering from planar defects and also “missing” reflections compared to $\text{SrSi}_2\text{O}_2\text{N}_2:\text{Eu}^{2+}$. Rietveld refinement reveals an average structure of $\text{Sr}_{0.5}\text{Ba}_{0.5}\text{Si}_2\text{O}_2\text{N}_2:\text{Eu}^{2+}$ which is isotypic to that of $\text{SrSi}_2\text{O}_2\text{N}_2:\text{Eu}^{2+}$, with the latter representing a twinned layered oxonitridosilicate with disordered metal atoms. The average structure of $\text{Sr}_{0.5}\text{Ba}_{0.5}\text{Si}_2\text{O}_2\text{N}_2:\text{Eu}^{2+}$ was refined in space group $P1$ (no. 1) resulting in lattice parameters $a = 7.2059(2)$, $b = 7.3887(3)$, $c = 7.3340(2)$ Å, $\alpha = 88.524(4)$, $\beta = 84.454(3)$, $\gamma = 75.980(4)^\circ$ and $V = 377.07(2)$ Å³. Based on the crystallographic results and considering lattice relaxation behavior as a consequence of lattice expansion, the observed unexpectedly large Stokes shift (as compared to $\text{SrSi}_2\text{O}_2\text{N}_2:\text{Eu}^{2+}$; 3573 vs. 3285 cm^{-1}) can be explained using a least square fit of the emission spectra. With almost identical chromaticity coordinates with respect to the most frequently used commercial LED phosphor $\text{YAG}:\text{Ce}^{3+}$ but significantly higher luminous

efficacy ($\text{LE} = 495 \text{ lm/W}$), $\text{Sr}_{0.5}\text{Ba}_{0.5}\text{Si}_2\text{O}_2\text{N}_2:\text{Eu}^{2+}$ is a promising material for outdoor lighting, e.g. in cool-white pc-LEDs. To elucidate the real structure, powder XRD simulations have been recorded compiling a disorder model taking into account all permutations of metal ion sets and silicate layer orientations. Experimental diffraction data were well reproduced including the diffuse intensities observed in powder XRD and also in SAED patterns. These simulations show that crystallites of $\text{Sr}_{0.5}\text{Ba}_{0.5}\text{Si}_2\text{O}_2\text{N}_2:\text{Eu}^{2+}$ are built up of small anti-phase domains within larger twin domains.

Keywords: Oxonitridosilicate; Diffuse Scattering; Structure Elucidation; Luminescence

2.3.1 Introduction

Various promising luminescent materials for application in phosphor converted light emitting diodes ((pc)-LEDs) have been reported during the last few years.^[1,2] Most notably, Eu^{2+} -doped (oxo)nitridosilicates show remarkable materials properties, e.g. high thermal and chemical stability, large band gaps as well as high quantum (QE) and luminous efficiency (LE) for parity allowed $4f^6(^7F)5d \rightarrow 4f^7(^8S_{7/2})$ transition.^[3-8] Important examples for these materials are e.g. the $\text{M}^{\text{II}}\text{Si}_2\text{O}_2\text{N}_2:\text{Eu}^{2+}$ phases (with $\text{M}^{\text{II}} = \text{Ca}, \text{Sr}, \text{Ba}$). However, synthesis of phase pure samples of these compounds remained problematic and detailed crystal structure determination proved to be challenging. Important parameters like Stokes shift, luminous efficacy or stability against degradation can be varied either by substitution or by changing the dopant concentration and/or the dopant itself or by optimizing the synthesis conditions.^[9-21] For $\text{SrSi}_2\text{O}_2\text{N}_2:\text{Eu}^{2+}$, remarkable values of $\text{QE} = 0.95$ and $\text{LE} = 537 \text{ lm/W}$, both measured at room temperature, have been reported.^[22] Although a number of LED phosphors have been thoroughly studied by X-ray methods and the luminescence properties have been analyzed in detail, only a few more general structure-property relations have been yet established.^[23] An accurate quantitative prediction of the luminescence properties based solely on crystal structures is not possible as yet. This might be due to the fact that average crystal structures do not always appropriately describe the local atomic arrangement of the activator ion in a phosphor material. To consider stacking disorder, intergrowth phenomena, vacancy ordering and related effects, a real-structure description is desirable which should be representative for the entire sample. The quantitative evaluation of experimental powder X-ray diffraction (PXRD) patterns in combination with other crystallographic methods like

transmission electron microscopy (TEM) promises to be an appropriate experimental approach. Although less pronounced than in single-crystal diffraction patterns, powder patterns are inherently containing information concerning real-structure effects. The latter ones may be visible as increased background intensity and/or as broadened reflections corresponding to diffuse scattering. A number of real-structure effects on different length scales have been reported for (oxo)nitridosilicate based LED phosphors.^[10,11,24] Solely if the real structures can be elucidated, the effect of short-range ordering on the performance of LED phosphors may be properly understood and controlled. The triclinic compound $\text{EuSi}_2\text{O}_2\text{N}_2$ ^[25] is a layered oxonitridosilicate that exhibits characteristic twinning by reticular pseudomerohedry which is due to the fact that silicate layers rotated by 180° can coordinate the cations that are located between consecutive layers in almost the same fashion as non-rotated silicate layers because of the pseudo-symmetry of the Si/O partial structure. The highly condensed silicate layers are built up of vertex-sharing SiON_3 tetrahedra of Q^3 -type (superscript number specifies connectedness: number of directly connected polyhedra) in which O atoms are terminally bound and each N atom bridges three Si atoms, respectively. If the twin domains are larger than the X-ray's length of coherence, the twinning does not affect X-ray powder diffraction patterns significantly. However, if the size of ordered domains is smaller, intensities in PXRD patterns may be affected and single-crystal like twin refinements on data from twinned crystals become impossible.

Based on these results, the structure of the isotopic compound $\text{SrSi}_2\text{O}_2\text{N}_2$ was investigated.^[10] Upon doping with Eu^{2+} , this compound shows efficient green to yellow luminescence ($\lambda_{\text{em}} \approx 540$ nm) when excited by blue radiation ($\lambda_{\text{exc}} \approx 450$ nm) rendering this material a possible phosphor for pc-LEDs.^[12,13,15,22] In the Rietveld refinement, a reasonable fit could only be obtained assuming two sets of four metal atom positions each in the unit cell which constitute two alternatives of the cation distribution in different domains. The resulting average crystal structure is illustrated in Figure 1 (illustrating the structure of $\text{Sr}_{0.5}\text{Ba}_{0.5}\text{Si}_2\text{O}_2\text{N}_2:\text{Eu}^{2+}$ as well).

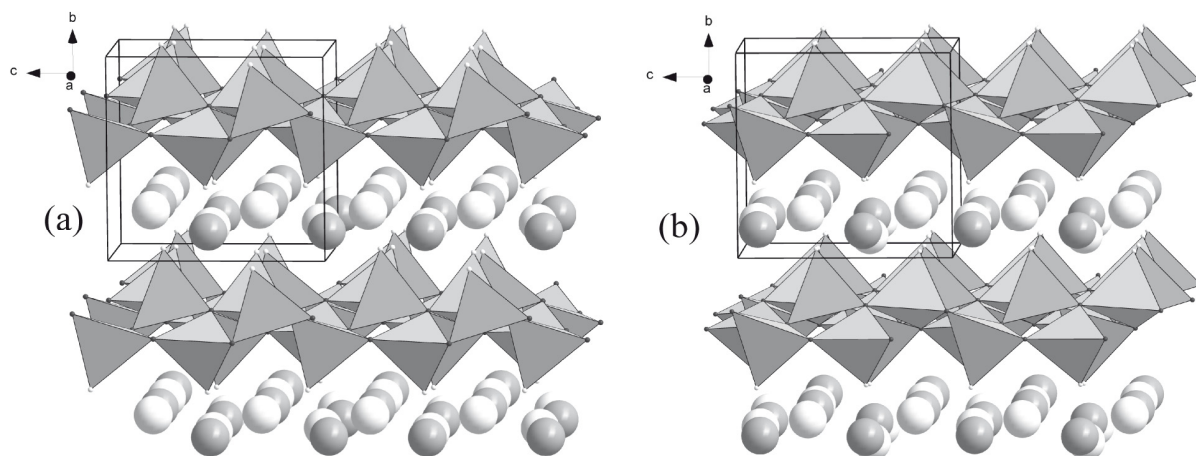


Figure 1. Side view (approximately along [100]) on the average structure of (a) $\text{SrSi}_2\text{O}_2\text{N}_2$ and (b) $\text{Sr}_{0.5}\text{Ba}_{0.5}\text{Si}_2\text{O}_2\text{N}_2$ (2 mol% Eu doped; SiON_3 polyhedra gray; O atoms: small white spheres; N atoms: small black spheres) with alternative sets of cation positions (set A white spheres; set B gray spheres). The unit cell is indicated by black solid lines.

Selected area electron diffraction (SAED) patterns of this material exhibit frequently diffuse streaks interconnecting the Bragg reflections. The presence of small domains consequently yielded a disordered average structure with significant intensity changes in PXRD patterns as compared to the fully ordered structural model. The fact that no crystals with sufficient size for single-crystal diffraction could be synthesized is probably due to such disorder phenomena. Because disorder occurs along the stacking direction this is disadvantageous for the growth of single crystals along this direction resulting in a plate-like morphology.

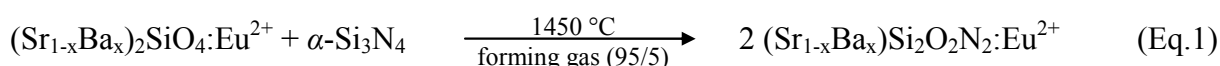
In this contribution, investigations on the real structure of $\text{Sr}_{0.5}\text{Ba}_{0.5}\text{Si}_2\text{O}_2\text{N}_2:\text{Eu}^{2+}$ based on powder pattern simulations are described. With respect to high impact on the development of novel LED-phosphors, Eu^{2+} -doped $\text{Sr}_{1-x}\text{Ba}_x\text{Si}_2\text{O}_2\text{N}_2$ phases have already been investigated in the past.^[12,15,20] However, only preliminary results have been published leaving a number of important questions unanswered (e.g. comprehensive phase analysis, structural description, chemical analysis, phase purity, influence of unknown impurities). Reported luminescence investigations are inconsistent but, nevertheless, revealed an unexpected red shift for increasing Ba^{2+} content in all cases. The impact of Ba substitution in $\text{SrSi}_2\text{O}_2\text{N}_2$ on the crystal structure and the thus provoked lattice deformation due to incorporation of larger Ba^{2+} ions are ambiguous and were therefore not correlated with the luminescence properties so far. In the PXRD pattern of $\text{Sr}_{0.5}\text{Ba}_{0.5}\text{Si}_2\text{O}_2\text{N}_2:\text{Eu}^{2+}$, there are both asymmetric broadened maxima as well as sharp Bragg reflections and apparently, both of them belong to one and the same phase. Additionally, reflections are missing compared to the powder pattern of $\text{SrSi}_2\text{O}_2\text{N}_2$. In this contribution, we present a thorough structural characterization including one-dimensional

stacking disorder using the Hendricks & Teller algorithm ^[26] and detailed luminescence investigations of Eu^{2+} -doped $\text{Sr}_{1-x}\text{Ba}_x\text{Si}_2\text{O}_2\text{N}_2$ phases in respect to structure-property relations.

2.3.2 Experimental Section

2.3.2.1 Synthesis

$\text{Sr}_{0.5}\text{Ba}_{0.5}\text{Si}_2\text{O}_2\text{N}_2:\text{Eu}^{2+}$ (2 mole% Eu) was prepared by heating a stoichiometric mixture of $(\text{Sr}_{1-x}\text{Ba}_x)_2\text{SiO}_4:\text{Eu}^{2+}$ ($x = 0.5$) and $\alpha\text{-Si}_3\text{N}_4$ (UBE, >95 %) for 5 h to 1375 °C in a stream of forming gas ($\text{N}_2:\text{H}_2 = 95:5$; equation 1). The product was ground and reheated to 1450 °C for 5 h under forming gas. The sample was then washed with diluted HCl and water to remove remaining oxosilicate byproducts.



2.3.2.2 Powder X-ray Diffraction

Powder diffraction data were collected on a STOE STADI P diffractometer (Cu- $\text{K}_{\alpha 1}$ radiation, Ge(111) monochromator, position sensitive detector) in transmission geometry. Simulations of Bragg data were performed using the WinXPOW program package.^[27] Rietveld refinement was carried out using the TOPAS package.^[28] Powder patterns and SAED diagrams of disordered polytypes including diffuse scattering were calculated using DIFFaX.^[29,30]

2.3.2.3 Electron Microscopy

The chemical composition of several crystallites was analyzed by energy dispersive X-ray spectroscopy (EDX) using a JSM-6500F scanning electron microscope (Joel) with a Si/Li EDX detector (Oxford Instruments, model 7418). The composition of the starting material $(\text{Sr}_{1-x}\text{Ba}_x)_2\text{SiO}_4:\text{Eu}^{2+}$ was verified by EDX analysis specifying the value $x = 0.50(2)$. For the product $(\text{Sr}_{1-x}\text{Ba}_x)\text{Si}_2\text{O}_2\text{N}_2:\text{Eu}^{2+}$, the value of x was analyzed to be $0.53(2)$. Accordingly, the overall value of $x = 0.5$ (within experimental standard deviation) is corroborated by EDX measurements. Electron diffraction patterns (SAD, selected area diffraction) and high-

resolution images were recorded on transmission electron microscopes (Philips CM30/ST, 300 kV or Fei Titan 80-300, 300 kV respectively).

2.3.3 Results and Discussion

2.3.3.1 Average Structure

The average structure of $\text{SrSi}_2\text{O}_2\text{N}_2$ was described as a layered silicate structure with triclinic metrics and lattice parameters $a = 7.0802(2)$, $b = 7.2306(2)$, $c = 7.2554(2)$ Å, $\alpha = 88.767(3)$, $\beta = 84.733(2)$, $\gamma = 75.905(2)$ ° and $V = 358.73(2)$ Å³.^[10] Calculated powder patterns based on the ordered structure of $\text{EuSi}_2\text{O}_2\text{N}_2$ ^[25] showed a significant misfit of some reflections compared to the experimental ones. Introducing an alternative set B of metal atom positions, occupied with a probability of 20 %, significantly improved the fit. Structures with exclusively set A or set B, respectively, are congruent due to additional translational symmetry of the silicate layer. Increasing the occupation of the alternative sets of positions up to 50 % each causes a continuous decrease of some intensities in calculated powder patterns (see Figure 2).

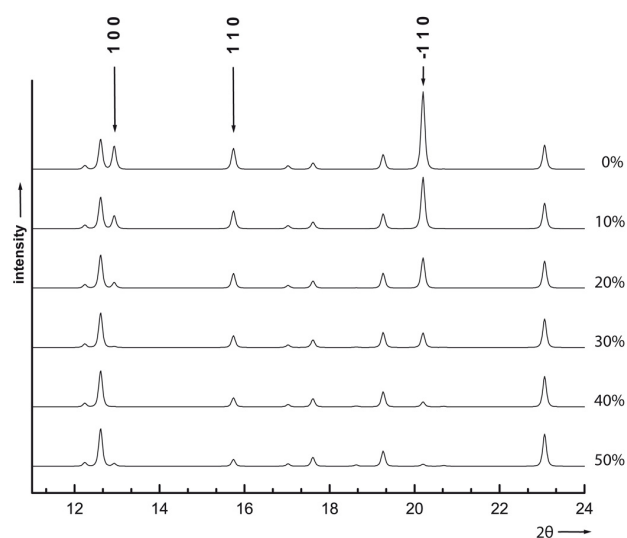


Figure 2. Simulated powder XRD patterns for the average structure of $\text{SrSi}_2\text{O}_2\text{N}_2$ with increasing occupation of set B positions (0, 10, 20, 30, 40, 50 %). The intensity weakening is indicated for three reflections (which would be extinct in case of *B*-centering).

This corresponds to a real structure with rather small domains, *i.e.* a high concentration of domain boundaries between undisturbed areas. If the occupancy of set A equals that of set B,

the disordered structure can be described by a subcell with triclinic metrics ($a = 4.8306(1)$, $b = 5.2962(1)$, $c = 7.2306(2)$ Å, $\alpha = 100.225(2)$, $\beta = 99.341(2)$, $\gamma = 91.406(1)$ °). However, for the sake of easier comparison with isotopic $\text{SrSi}_2\text{O}_2\text{N}_2$ the cell is better described in a non-standard setting with the original lattice parameters, but with additional B -centering. In refinements using space group $P1$, this would mean that atoms placed on x, y, z are doubled by equivalent ones with $x + 0.5, y, z + 0.5$. The powder sample contains crystallites with different degree of disorder as observed in electron diffraction patterns (see below), many of them exhibiting reflections not consistent with extinction rules for B -centering. However, although not extinct, reflections with $h + l = 2n + 1$ are predominantly affected by the intensity weakening described above. Therefore, the B -centering was not taken into account in the refinement of the structure of $\text{Sr}_{0.5}\text{Ba}_{0.5}\text{Si}_2\text{O}_2\text{N}_2:\text{Eu}^{2+}$.

For Rietveld refinement (see Figure 3) of the average structure of $\text{Sr}_{0.5}\text{Ba}_{0.5}\text{Si}_2\text{O}_2\text{N}_2:\text{Eu}^{2+}$, the structure parameters of $\text{SrSi}_2\text{O}_2\text{N}_2$ were used as a starting model.

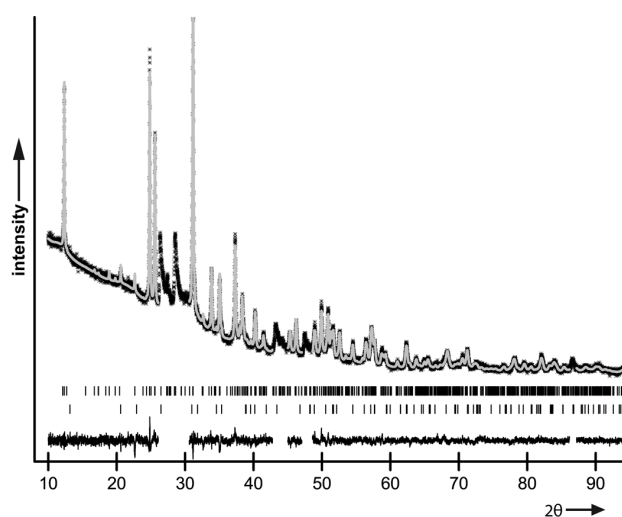


Figure 3. Rietveld fit of the powder diffraction pattern of $\text{Sr}_{0.5}\text{Ba}_{0.5}\text{Si}_2\text{O}_2\text{N}_2$ (2 mol% Eu doped) with measured histogram (black), calculated pattern (gray solid line), difference curve and positions of reflections (bars; top: $\text{Sr}_{0.5}\text{Ba}_{0.5}\text{Si}_2\text{O}_2\text{N}_2$, bottom $\alpha\text{-Si}_3\text{N}_4$ (2.84 wt%)). The excluded regions correspond to maxima due to diffuse scattering.

On both sets A and B, the molar ratio Sr/Ba was not refined, however, the positional parameters and occupancy factors for each set were refined. The occupancy of set A and B, respectively, was refined to a ratio 0.48(2)/0.52(2) indicating approximately equal occupation of both sets of cation positions A and B within accuracy of the method. This can also be deduced by comparing the experimental pattern with Figure 2. The small amount of Eu^{2+} was not taken into account because of the insignificant scattering intensity. As a consequence of the limited information present in the powder pattern of such a triclinic compound, bond-lengths restraints combined with a penalty weighting were applied for the interatomic

distances within the silicate layer. The target values for bond lengths (Si/N)-(O/N) were set to those refined from single-crystal data of $\text{EuSi}_2\text{O}_2\text{N}_2$.^[25] Overall isotropic displacement parameters were refined for both metal atoms and light atoms (Si/O/N), respectively. Reflections that apparently do not result from Bragg scattering were excluded during refinement, they are discussed below. Taking into account the non-luminescent impurity phase $\alpha\text{-Si}_3\text{N}_4$, this model explains the observed Bragg intensities quite well. Although the morphology of the crystallites is anisotropic, taking into account preferred orientation did not yield any improvement and was neglected in the final refinement. Due to larger size of Ba^{2+} , the cell parameters increase compared to $\text{SrSi}_2\text{O}_2\text{N}_2$, leading to a unit cell with $a = 7.2059(2)$, $b = 7.3887(3)$, $c = 7.3340(2)$ Å, $\alpha = 88.525(4)$, $\beta = 84.454(3)$, $\gamma = 75.979(4)^\circ$ and $V = 377.07(2)$ Å³. The largest relative increase can be observed for b which approximately corresponds to the stacking direction of the layered structure (layers \perp $[010]^*$). The change of lattice parameters leads to a non-standard setting of the triclinic unit cell which was not changed in order to emphasize the analogies with the isotypic compounds $\text{EuSi}_2\text{O}_2\text{N}_2$ and $\text{SrSi}_2\text{O}_2\text{N}_2$. Crystal data and details concerning the Rietveld refinement are summarized in Table 1. Further details of the crystal structure investigation may be obtained from Fachinformationszentrum Karlsruhe, 76344 Eggenstein-Leopoldshafen, Germany (fax: (+49)7247-808-666; e-mail, crysdata@fiz-karlsruhe.de, http://www.fiz-karlsruhe.de/request_for_deposited_data.html) on quoting the depository number CSD-422238 ($\text{Sr}_{0.5}\text{Ba}_{0.5}\text{Si}_2\text{O}_2\text{N}_2$).

Table 1. Crystal data and Rietveld structure refinement of $\text{Sr}_{0.5}\text{Ba}_{0.5}\text{Si}_2\text{O}_2\text{N}_2:\text{Eu}^{2+}$ (the presence of Eu was neglected because of insignificant scattering intensity).

Crystal system	Triclinic
Space group	$P1$ (no.1)
Lattice parameters	$a = 7.2059(2)$ Å, $b = 7.3887(3)$ Å, $c = 7.3340(2)$ Å, $\alpha = 88.526(4)^\circ$, $\beta = 84.454(3)^\circ$, $\gamma = 75.980(4)^\circ$
Cell volume	$377.07(2)$ Å ³
Z	4
Formula weight	228.66 g mol ⁻¹
Total number of reflections	1130
Refined parameters/restraints	158/80
Diffractometer	STOE STADI P
Radiation	Cu-K α_1 ($\lambda = 1.54056$ Å)
Increment	0.01°
2θ range	$10^\circ - 120^\circ$
Excluded regions	5 ($\Sigma\Delta 2\theta = 10.45^\circ$)
Data points	9931
Background function	Shifted Chebyshev (42 parameters)
R values	$R_p = 0.0241$, $wR_p = 0.0316$, $R(F^2) = 0.0651$

Samples with composition $\text{Sr}_{1-x}\text{Ba}_x\text{Si}_2\text{O}_2\text{N}_2:\text{Eu}^{2+}$ ($0.45 \leq x \leq 0.55$), but synthesized at a much higher temperature of 1650 °C (compared to 1450 °C in this study), have been reported to show yellow luminescence upon excitation with UV to blue radiation in a patent application.^[31] The powder XRD pattern depicted there cannot be explained assuming single-phase material. The main phase corresponds to the $\text{BaSi}_6\text{N}_8\text{O}$ type of structure^[32] which is not consistent with the metrics given for a hypothetical new phase in the $\text{MSi}_2\text{O}_2\text{N}_2$ ($M = \text{Ba}, \text{Sr}$) system. As $\text{BaSi}_6\text{N}_8\text{O}:\text{Eu}^{2+}$ shows a blue to cyan emission, the observed yellow luminescence (a few nm red-shifted compared to $\text{SrSi}_2\text{O}_2\text{N}_2:\text{Eu}^{2+}$, see section Luminescence) probably originates from $(\text{Sr}, \text{Ba})\text{Si}_2\text{O}_2\text{N}_2:\text{Eu}^{2+}$, which apparently was an impurity phase there. Identification of more than one phase is not easy because obviously the PXRD pattern is strongly affected by texture effects. This can be inferred from the increased relative intensity of the 010 reflection corresponding to platelet crystallites extended in the (010) plane that are preferentially oriented perpendicular to the diffraction vector.

2.3.3.2 Lattice Energy Calculations

Based on the refined structure parameters, lattice energy calculations (MAPLE, Madelung part of lattice energy) were performed.^[33-36] Because oxygen and nitrogen positions cannot be distinguished by X-ray diffraction, O and N were assigned in analogy to isotypic $\text{EuSi}_2\text{O}_2\text{N}_2$ for which single-crystal data have been reported.^[25] Accordingly, oxygen atoms are bound terminally ($\text{O}^{[1]}$) and all nitrogen atoms are of $\text{N}^{[3]}$ -type. Only one set of metal atom positions was taken into account. All relevant values are listed in Table 2 and are very close to typical ranges of partial MAPLE values.

Table 2. Results of MAPLE calculations (in kJ/mol) for $\text{Sr}_{0.5}\text{Ba}_{0.5}\text{Si}_2\text{O}_2\text{N}_2$ and increment calculations: partial MAPLE values, total MAPLE sum and difference to theoretical total MAPLE value.

$(\text{Sr}/\text{Ba})^{2+}$	Si^{4+}	$\text{O}^{[1]2-}$	$\text{N}^{[3]3-}$	Total MAPLE	Δ
1838-2045	9023-9581	1945-2565	5907-6430	37713	0.30%
Total MAPLE (0.5 SrO + 0.5 BaO + 0.5 SiO ₂ + 0.5 Si ₃ N ₄): 37828					
Typical MAPLE values (in kJ/mol): Ba ²⁺ : 1500-2000; Sr ²⁺ : 1500-2100; Si ⁴⁺ : 9000-10200; O ^{[1]2-} : 2000-2800; N ^{[3]3-} : 5000-6200. ^[8]					

Small differences might be a result of less precise light atom position refinement based on powder diffraction data. A comparison between the calculated total MAPLE value and a theoretical reference reaction equation starting from the respective binaries show a small difference of 0.30%.

2.3.3.3 Luminescence

This study complements preliminary investigations of the substitutional series $\text{Sr}_{1-x}\text{Ba}_x\text{Si}_2\text{O}_2\text{N}_2:\text{Eu}^{2+}$.^[12,15,20] Due to the improved synthesis, a phosphor material containing only one luminescent phase was obtained. For the first time a complex two phase Rietveld refinement for such a sample was done considering all atoms in the unit cell. Unlike prior investigations, such samples, fully characterised by electron- and X-ray methods, with no unknown impurities yield more significant, *i.e.* intrinsic values because of unaffected, sharp emission spectra. The discrepancy regarding emission band positions and shape, related to the given compositions in $\text{Sr}_{1-x}\text{Ba}_x\text{Si}_2\text{O}_2\text{N}_2:\text{Eu}^{2+}$ phases in the literature, could therefore be ascribed to insufficient phase analysis. Prediction of crystal structure or phase purity only by comparing PXRD data (highly affected by texture effects and/or diffuse scattering *e.g.* background) without any refinement and/or chemical analysis is deficient in such a case. Although the crystal structures are highly disordered, these phases are highly relevant for pc-LED applications. The present luminescence study on $\text{Sr}_{0.5}\text{Ba}_{0.5}\text{Si}_2\text{O}_2\text{N}_2:\text{Eu}^{2+}$ provides a convincing explanation for unexpected red-shifted luminescence based on refined structural data.

Substitution of Sr^{2+} by Ba^{2+} in $\text{SrSi}_2\text{O}_2\text{N}_2:\text{Eu}^{2+}$ leads to a continuous red shift of the emission band while the edge position of the lowest lying absorption band is similar for both compositions (see Figure 4).

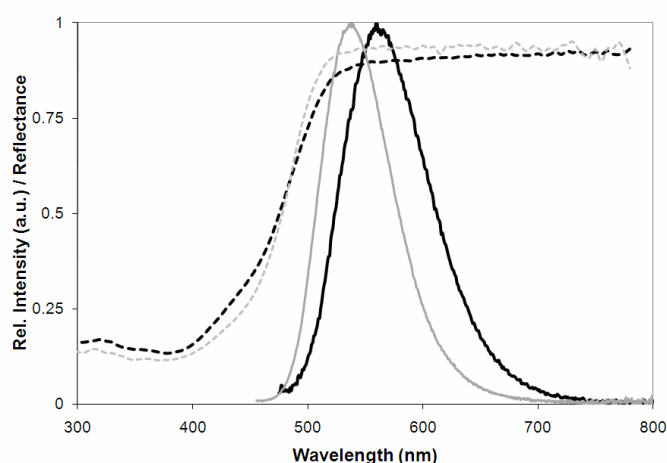


Figure 4. Absorption (dashed) and emission spectra ($\lambda_{\text{exc}} = 450 \text{ nm}$) of powder samples of $(\text{Ba}_{0.5}\text{Sr}_{0.5})_{0.98}\text{Si}_2\text{O}_2\text{N}_2:\text{Eu}_{0.02}$ (black curves) and $\text{Sr}_{0.98}\text{Si}_2\text{O}_2\text{N}_2:\text{Eu}_{0.02}$ (gray curves).

The larger Ba^{2+} ions cause a lattice expansion which usually involves increased Eu-(O/N) bond lengths. Because the structure type remains unchanged, the change in covalent activator-

ligand interaction (nephelauxetic effect) should be small and lowering of the Eu^{2+} 5d-orbital splitting is expected to lead to blue-shifted absorption and emission bands. However, as for the case of $\text{CaSi}_2\text{O}_2\text{N}_2:\text{Eu}^{2+}$ [9,22] nearly no absorption band shift is observed but a red shift and broadening of the emission band is detected caused by a larger Stokes shift of the yellow emitting $(\text{Ba}_{0.5}\text{Sr}_{0.5})_{0.98}\text{Si}_2\text{O}_2\text{N}_2:\text{Eu}_{0.02}$. The emission band width (full width at half maximum, FWHM) increases from $\sim 2450 \text{ cm}^{-1}$ to $\sim 2744 \text{ cm}^{-1}$ for $\text{Sr}_{0.98}\text{Si}_2\text{O}_2\text{N}_2:\text{Eu}_{0.02}$ and $(\text{Ba}_{0.5}\text{Sr}_{0.5})_{0.98}\text{Si}_2\text{O}_2\text{N}_2:\text{Eu}_{0.02}$, respectively.

In order to gain more insight into the differing spectroscopic properties of the isotopic phases $\text{Sr}_{0.98}\text{Si}_2\text{O}_2\text{N}_2:\text{Eu}_{0.02}$ and $(\text{Ba}_{0.5}\text{Sr}_{0.5})_{0.98}\text{Si}_2\text{O}_2\text{N}_2:\text{Eu}_{0.02}$, a least squares fit of the respective emission bands to calculated optical transition probabilities has been carried out assuming a configuration coordinate model with identical curvature of ground and excited state parabola for $T = 298 \text{ K}$. [37,38] Because of the very similar coordination spheres of the various cation lattice sites that can be substituted by Eu^{2+} , a fit procedure for single-site optical transitions is considered as being appropriate to study the optical transition properties of the layered SiON phases. Figure 5 shows the fitted emission spectra for $\text{Sr}_{0.98}\text{Si}_2\text{O}_2\text{N}_2:\text{Eu}_{0.02}$ and $(\text{Ba}_{0.5}\text{Sr}_{0.5})_{0.98}\text{Si}_2\text{O}_2\text{N}_2:\text{Eu}_{0.02}$ and the derived configurational diagram with the zero phonon emission transitions indicated as arrows.

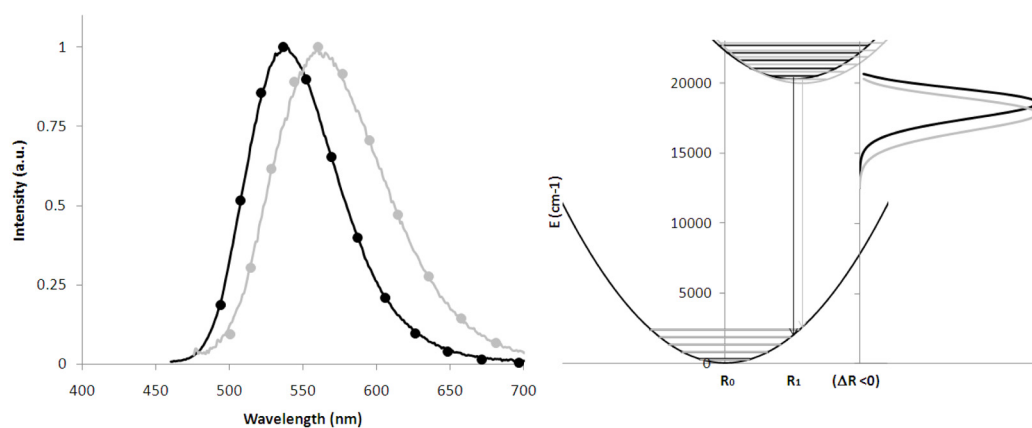


Figure 5. Emission spectra for 450 nm excitation (lines) and fitted optical transition probabilities (points) for $\text{Sr}_{0.98}\text{Si}_2\text{O}_2\text{N}_2:\text{Eu}_{0.02}$ (black curve) and $(\text{Ba}_{0.5}\text{Sr}_{0.5})_{0.98}\text{Si}_2\text{O}_2\text{N}_2:\text{Eu}_{0.02}$ (gray curve; left side) and the derived configurational coordinate diagram for Eu^{2+} in the respective host lattices (identical color codes; right side). Huang-Rhys coupling parameters S of 3.7 and 4.8 and phonon frequencies $\hbar\omega$ of 535 and 528 cm^{-1} have been obtained for $\text{Sr}_{0.98}\text{Si}_2\text{O}_2\text{N}_2:\text{Eu}_{0.02}$ and $(\text{Ba}_{0.5}\text{Sr}_{0.5})_{0.98}\text{Si}_2\text{O}_2\text{N}_2:\text{Eu}_{0.02}$, respectively.

The fit results indicate that the zero phonon energies are comparable on a wavelength scale for both compositions with values of 494 nm and 501 nm for $\text{Sr}_{0.98}\text{Si}_2\text{O}_2\text{N}_2:\text{Eu}_{0.02}$ and $(\text{Ba}_{0.5}\text{Sr}_{0.5})_{0.98}\text{Si}_2\text{O}_2\text{N}_2:\text{Eu}_{0.02}$, respectively, and correlate with the very similar low energy absorption band edges for both compounds (see Figure 4).

A stronger electron-phonon coupling for $\text{Ba}_{0.5}\text{Sr}_{0.5}\text{Si}_2\text{O}_2\text{N}_2:\text{Eu}^{2+}$ as indicated by the fit results should in principle be related to similar structural differences as discussed for $\text{CaSi}_2\text{O}_2\text{N}_2:\text{Eu}^{2+}$ vs. $\text{SrSi}_2\text{O}_2\text{N}_2:\text{Eu}^{2+}$.^[22] The relative size of the substitutional lattice site has a large impact on the magnitude of lattice relaxation of the local surroundings of Eu^{2+} in its excited $4f^65d$ state. A larger site for Eu^{2+} frequently leads to a more restricted relaxation and has been explained based on a configurational coordinate diagram for Eu^{2+} in which $\Delta r < 0$.^[39,40]

According to the Rietveld refinement, the coordination spheres of all metal atoms in $\text{Ba}_{0.5}\text{Sr}_{0.5}\text{Si}_2\text{O}_2\text{N}_2:\text{Eu}^{2+}$ are comparable to the corresponding ones in $\text{SrSi}_2\text{O}_2\text{N}_2:\text{Eu}^{2+}$. As a consequence of expanding lattice parameters, the silicate layer is stretched and becomes less corrugated. The terminal oxygen atoms ($\text{O}^{[1]}$) approach each other, simultaneously generating a more symmetric trigonal prismatic coordination around each metal site. A possible explanation for this aberrant behavior in $\text{Sr}_{1-x}\text{Ba}_x\text{Si}_2\text{O}_2\text{N}_2:\text{Eu}^{2+}$ may be established by regarding average metal oxygen bond lengths in comparison with ionic-radii sum,^[36] because the sixfold coordination of metal atoms by terminal oxygen atoms might be the predominant factor that determines the spectral position of absorption and emission bands of Eu^{2+} located at the respective sites. For $\text{SrSi}_2\text{O}_2\text{N}_2:\text{Eu}^{2+}$, the average metal-oxygen bond length is 2.62 Å whereas the ionic radii sum for sixfold coordinated Sr^{2+} and fourfold coordinated O^{2-} is only 2.56 Å. This means that the O^{2-} ions do not approach the centers of the polyhedra as close as possible, resulting in non maximal shortened Eu-O bond length. In the mixed compound $\text{Sr}_{0.5}\text{Ba}_{0.5}\text{Si}_2\text{O}_2\text{N}_2:\text{Eu}^{2+}$ the average metal-oxygen bond length was determined to 2.68 Å. Calculations for ionic-radii sum for sixfold coordinated Sr^{2+} and equally frequent Ba^{2+} , respectively, and again fourfold coordinated O^{2-} ions leads to 2.65 Å which resembles the value given by Rietveld refinement. As a consequence Sr-O as well as Ba-O bond length are close to the respective ionic radii sum (Sr-O: 2.56 Å; Ba-O: 2.73 Å) which finally means that in this case Sr-O distances are obviously shorter than in $\text{SrSi}_2\text{O}_2\text{N}_2:\text{Eu}^{2+}$ in spite of unit cell enlargement. Furthermore, if Eu^{2+} ions prefer occupation of Sr sites in $\text{Sr}_{0.5}\text{Ba}_{0.5}\text{Si}_2\text{O}_2\text{N}_2:\text{Eu}^{2+}$, a stronger structural relaxation can be expected compared to $\text{SrSi}_2\text{O}_2\text{N}_2:\text{Eu}^{2+}$ which should lead to a larger Stokes shift and a broadened emission band. These results support the assumption that a local lattice deformation as a consequence of Ba^{2+} integration might be responsible for shorter interatomic distances within neighboring coordination polyhedra containing smaller Eu^{2+} in its excited state.^[12] Therefore, the unexpected emission shift to longer wavelength can be explained by a less restricted local lattice relaxation at the Eu^{2+} sites resulting in a larger Stokes shift compared to $\text{SrSi}_2\text{O}_2\text{N}_2:\text{Eu}^{2+}$ in accordance with the fitting results presented above (3573 vs. 3285 cm^{-1}).

The chromaticity coordinates of $\text{Sr}_{0.5}\text{Ba}_{0.5}\text{Si}_2\text{O}_2\text{N}_2:\text{Eu}^{2+}$ (yellow emission; CIE $x, y = 0.441, 0.544$) makes it a very attractive candidate material for white phosphor converted LEDs.

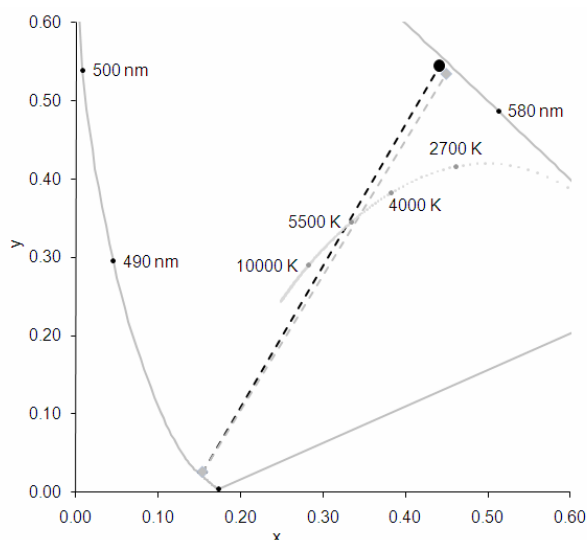


Figure 6. CIE 1931 chromaticity diagram showing the color coordinates of $\text{Sr}_{0.5}\text{Ba}_{0.5}\text{Si}_2\text{O}_2\text{N}_2:\text{Eu}^{2+}$ (black circle) and $\text{Y}_3\text{Al}_5\text{O}_{12}:\text{Ce}^{3+}$ (gray diamond) that are close together and are positioned in the yellow spectral range. Combination with a 450 nm emitting InGaN LED yields white phosphor converted LEDs with the respective load lines (dashed lines) crossing the black body curve at correlated color temperatures of ~ 5500 K (cool white).

Figure 6 shows a comparison of the color coordinates and resulting white points in a pc-LED with data for $\text{Y}_3\text{Al}_5\text{O}_{12}:\text{Ce}^{3+}$ (YAG), the most widely used commercial phosphor for highly efficient cool white pc-LEDs. Because the emission of $\text{Sr}_{0.5}\text{Ba}_{0.5}\text{Si}_2\text{O}_2\text{N}_2:\text{Eu}^{2+}$ is narrower than the Ce^{3+} emission of YAG, pc-LEDs with a higher luminous efficacy can be fabricated (LE of $\text{Sr}_{0.5}\text{Ba}_{0.5}\text{Si}_2\text{O}_2\text{N}_2:\text{Eu}^{2+}$ ($\text{Y}_3\text{Al}_5\text{O}_{12}:\text{Ce}^{3+}$) = 495 (441) $\text{lm}/\text{W}_{\text{opt}}$). Such LED lamps may find application e.g. for outdoor lighting.

2.3.3.4 Simulation of the Diffuse Scattering

The average structure of $\text{Sr}_{0.5}\text{Ba}_{0.5}\text{Si}_2\text{O}_2\text{N}_2:\text{Eu}^{2+}$ comprises disordered metal atom positions. Although it yields a convincing fit of the observed intensities, the model offers no information about the real structure. However, the asymmetric intensity maxima excluded during refinement result from real-structure effects. The profile of these broadened maxima is typical for diffuse scattering from planar defects. For layered structures, the presence of planar defects is due to the fact that perfect two-dimensional periodicity can be combined with different kinds of polytypic modifications with identical layer distances and almost the same lattice energy.^[41]

For the simulation of diffuse intensities, the triclinic unit cell was transformed into a setting with monoclinic metrics using the matrix $(1\ 0\ 0, -0.24817\ 1\ -0.00238, 0\ 0\ 1)$, thus the new basis vector b' is perpendicular to the layers. The vectors a and c which are parallel to the silicate layers were kept unchanged. The absolute value of b' corresponds to the y -component of the original b axis. The unit cell volume is thus fixed to the refined value. In order to describe the real structure, all permutations of the metal atom sets A and B (equals shifted A) combined with silicate layers, both “normal” and rotated by 180° around $[010]^*$ (due to twinning by a twofold axis), were taken into account. Additionally, two different stacking vectors $0.24817\ 1\ 0.00238$ or $-0.24817\ 1\ -0.00238$ were employed, they correspond to twinning by a mirror operation. This leads to a complex model with $2^3 = 8$ different possibilities combining layers to a real structure (see Table 3).

Table 3. Characteristics of all ($2^3 = 8$) possible layer transitions which have been taken into account: shift, rotation and reflection (+ = yes; - = no).

Stacking mode	shifted metal position, <i>i.e.</i> anti-phase boundary	180° rotation (around $[010]^*$)	Stacking along $-0.24817\ 1\ -0.00238$, <i>i.e.</i> mirror operation	Probability in final model (in %)
1	-	-	-	50.45
2	+	-	-	31.00
3	-	-	+	8.00
4	+	-	+	10.00
5	+	+	-	0.08
6	-	+	-	0.03
7	+	+	+	0.12
8	-	+	+	0.32
				$\Sigma\ 100$

With related stacking probabilities between defined layers (metal atoms combined with silicate layers) a 3D-structure can be built up. To optimize the fit of experimental data, transition probabilities (sum: 100 %) between the different types of layers were varied arbitrarily, taking care not to change Bragg intensities of the average structure. Instrumental broadening was taken into account by a pseudo-Voigt function ($u = 0.15$; $v = -0.02$; $w = 0.015$; $\sigma = 0.4$) to offer a reasonable fit at all diffraction angles. Whenever a rotated silicate layer follows a non-rotated one, a twin-like boundary is created. If rotated layers are stacked along the ideal stacking vector (see stacking mode 5 and 6 in Table 3) an alternative structure is built up based on pseudosymmetry. In order to simulate SAED patterns, layers corresponding to rotational twinning (in a narrower sense; see stacking mode 7 and 8 in Table 3) are important although they are not essential for powder XRD simulations as it turned out that their frequency is low and thus the intensities from rotation-twin domains

superimpose incoherently. Non-rotated layers, stacked along $-0.24817 \ 1 \ -0.00238$, describe mirror twinning (see stacking mode 3 and 4 in Table 3). Taking into account typical rotation-twin domain sizes of about 100 nm as reported for $\text{SrSi}_2\text{O}_2\text{N}_2$, the stacking probabilities were chosen in such a way (0.44 %) that rotation-twin boundaries occur roughly every hundred nm. Rotational twinning in the real structure is illustrated in Figure 7 (see stacking mode 8 in Table 3): A silicate layer with metal atoms of set A (black unit cell) is followed by an identical one (stacking vector of the idealized structure), both being part of a domain which is followed by another two (darker shading, with corresponding metal atoms gray), generated from the first layers by 180° rotation around $[010]^*$ (indicated by a gray unit cell). The unit-cell orientation is changed because of the triclinic metrics. At the twin boundary a rotated silicate layer follows a non-rotated one. Both cation sets of the average structure are shown at the rotation-twin boundary, but in the real structure only one set is present. Both atom sets yield identical models for the described boundary.

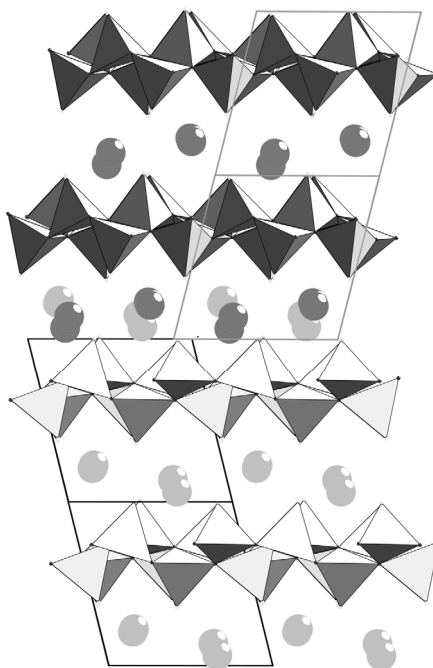


Figure 7. Side view (along $[001]$) on a sequence of silicate layers with corresponding metal atoms (light gray and gray spheres for set A and B, respectively); bottom: two silicate layers with set A metal atom positions (black unit cell edges); top: layers rotated by 180° around $[010]^*$ (unit cell edges gray, metal atoms gray); due to the pseudo-symmetry of the O atom positions (see Figure. 8), rotated and non-rotated layers can coordinate both cation sets in a similar way, which corresponds to the local structure of a twin boundary. Overlap of both orientations (average structure) leads to the superposition of the two sets of metal atom positions.

Within such twin domains, most layers correspond to the ideal stacking sequence, (50.45 %; see Table 3) while other layers contain the alternative metal atom set without a change of the

stacking vector (31.00 %; see Table 3). In both cases, the unit-cell orientation and also the silicate layer sequence remain unchanged, but metal atoms are either placed on “ideal” positions (set A, as in $\text{EuSi}_2\text{O}_2\text{N}_2$) or, less likely, placed on alternative positions (set B). This means that small anti-phase domains (translation vector approx. $0.5\ 0\ 0.5$, see Figure 8) of few nm of size are built up.

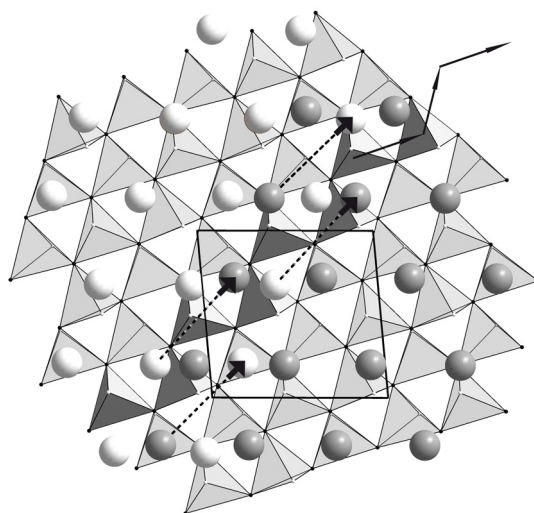


Figure 8. Top view (along $[010]^*$) on a silicate layer of $\text{Sr}_{0.5}\text{Ba}_{0.5}\text{Si}_2\text{O}_2\text{N}_2$ (doped with 2 mol% Eu; SiON_3 polyhedra, gray; O atoms small white spheres; N atoms small black spheres) with corresponding Sr/Ba atoms (set A white spheres; set B gray spheres). The two sets of metal atom positions are shown in the upper left and lower right parts, respectively, overlapping in the central part of the figure. The silicate layer is built up of condensed *zweier* single chains (one of them is highlighted by darker tetrahedra) with “zig-zag” conformation (indicated by solid black arrows). Anti-phase boundaries are formed by displacing one set of metal atoms by one translation period of the single chains, corresponding to a shift from set A to set B, or vice versa (dashed arrows), this shift maps the silicate layer onto itself (translational symmetry of the silicate substructure).

Apparently, the mixed occupation of the cation position also leads to a higher degree of stacking disorder. The displacement equals one translation period of the condensed single chains building up the silicate layer. In Figure 8 this is shown by mapping set A metal positions onto set B when moving the structure by one translation period of the silicate layer. The intensity weakening of reflections in Figure 2 corresponds to approaching the *B*-centered structure that results in case of equal probabilities for both atom sets.

As a consequence, anti-phase boundaries seem to be energetically more favorable than twin boundaries. With this complex model, mainly containing small anti-phase domains within larger twin domains, the PXRD pattern could be reproduced very well (see Figure 9).

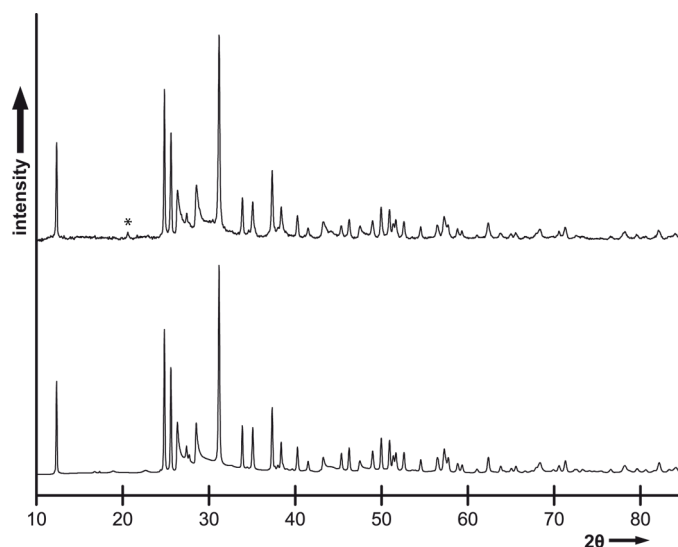


Figure 9. Experimental powder pattern of a sample of $\text{Sr}_{0.5}\text{Ba}_{0.5}\text{Si}_2\text{O}_2\text{N}_2:\text{Eu}^{2+}$ (top, manual background correction) and a simulation based on the final real-structure model (bottom). Reflections of the impurity phase $\alpha\text{-Si}_3\text{N}_4$ are labeled by asterisks.

In general, both anti-phase boundaries as well as twin boundaries lead to diffuse intensities and Bragg intensity weakening. However, both possibilities can be clearly distinguished. As the silicate layers have no rotational symmetry along $[010]^*$, rotation twinning leads to a change of the average structure in the case of small twin domains and thus to a significant change of Bragg intensities. Since powder methods, in general, average over the whole sample whereas X-ray methods average only over coherently scattering volumes, the averaging present in the structure model is slightly biased as not all crystallites exhibit the same diffraction patterns as shown by SAED (see below). However, the convincing fit of the experimental data indicates that the majority of the crystallites are very similar and they are well described by the model discussed above.

2.3.3.5 SAED Simulations

Concluding from the average structure, $\text{Sr}_{0.5}\text{Ba}_{0.5}\text{Si}_2\text{O}_2\text{N}_2:\text{Eu}^{2+}$ is a highly disordered layered oxonitridosilicate. The simulation of diffuse scattering in the powder pattern using a disorder model supports this thesis. Another approach is HRTEM (Figure 10).

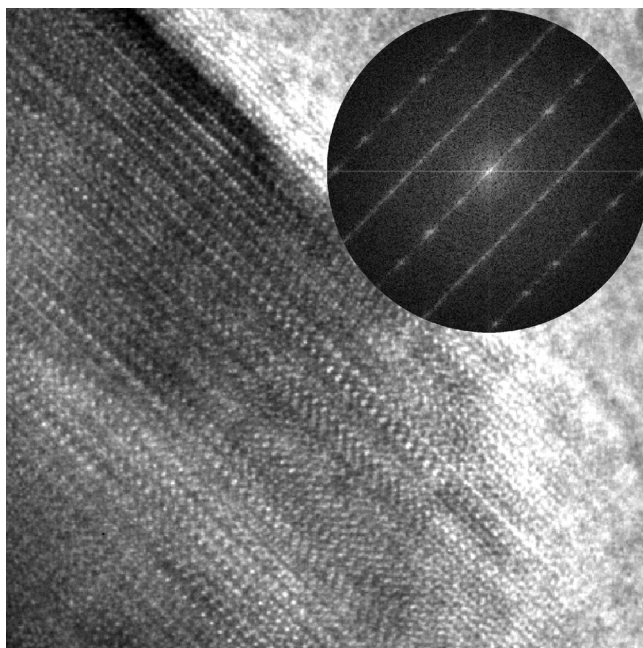


Figure 10: HRTEM image (Fei Titan 80-300) of a $\text{Sr}_{0.5}\text{Ba}_{0.5}\text{Si}_2\text{O}_2\text{N}_2:\text{Eu}^{2+}$ crystallite showing one-dimensional disorder. In the FT (inset), there are diffuse streaks perpendicular to the layer plane that either interconnect Bragg reflections or appear in between rows of Bragg reflections.

The Fourier transformation (FT) of a high-resolution micrograph of a crystallite of $\text{Sr}_{0.5}\text{Ba}_{0.5}\text{Si}_2\text{O}_2\text{N}_2:\text{Eu}^{2+}$ shows sharp Bragg reflections interconnected by diffuse streaks and additional strong diffuse streaks in between as a consequence of many domain boundaries per area. To demonstrate the performance of the disorder model described above and also to illustrate the impact of domain size variation on diffraction patterns, SAED patterns were simulated, in dependence on the model compiled for $\text{Sr}_{0.5}\text{Ba}_{0.5}\text{Si}_2\text{O}_2\text{N}_2:\text{Eu}^{2+}$, and compared to experimental ones of $\text{SrSi}_2\text{O}_2\text{N}_2$ (varying degree of disorder, Figure 11). In contrast to $\text{Sr}_{0.5}\text{Ba}_{0.5}\text{Si}_2\text{O}_2\text{N}_2:\text{Eu}^{2+}$, the domain sizes in the pure Sr compound vary more significantly. It also contains larger domains, however, all diffraction patterns can be simulated with the same disorder model assuming slightly different transition probabilities for the stacking possibilities.

For crystallites of $\text{SrSi}_2\text{O}_2\text{N}_2$ the occurrence and intensity distribution of diffuse streaks varies due to varying domain sizes. To simulate such effects in $\text{SrSi}_2\text{O}_2\text{N}_2$, the stacking probabilities in a stacking model were slightly changed towards more extreme values. Both rotation-twin (stacking mode 7 and 8; see Table 3) as well as anti-phase domain sizes (stacking mode 2; see Table 3) were varied in order to simulate more or less diffuse intensities while the other transition probabilities were kept on fixed values. In Figure 11, simulated SAED patterns with different stacking probabilities are compared to experimental ones (hkh layer, *i.e.* zone axis $[10\bar{1}]$). Corresponding to the chosen values, the appearance of doubled number of reflections

(due to twinning) in every second row and/or intense diffuse streaks connecting the Bragg reflections, respectively, can be observed as a consequence of varying domain sizes.

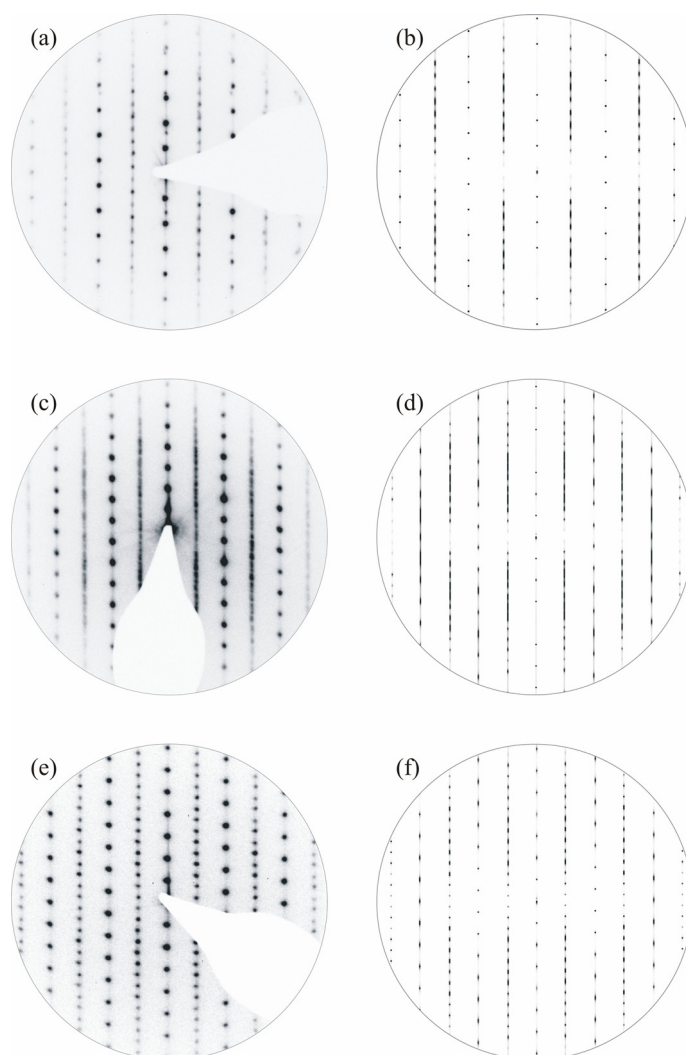


Figure 11. Comparison of electron diffraction patterns of $\text{SrSi}_2\text{O}_2\text{N}_2$ (left: a, c, e (experimental, CM30/ST); right: b, d, f (simulations)). Top: calculation with the same stacking sequence used for PXRD simulation (weak parasitic reflections); middle: smaller sizes for anti-phase and rotation-twin domains (see text); bottom: larger sizes for anti-phase and rotation-twin domains (see text).

For SAED simulation (b) the values reported in section “Simulation of the diffuse scattering” were chosen. As a consequence, sharp Bragg reflections are interconnected by diffuse streaks primarily for rows with $h = 2n + 1$. For the SAED simulation (d) both rotation-twin and anti-phase domain sizes were reduced. Rotation-twin boundaries are now calculated with 10 % probability (domains size about 10 nm) and the occupation probabilities for set A and B positions equals each other (average domain size about few nm). Diffuse streaks are more clearly visible while doubled reflections due to twinning are about to disappear. SAED simulation (f) is contrary because domain sizes are enlarged. In detail rotation-twin boundaries occur with overall 0.1 % probability leading to domains with $\approx 1 \mu\text{m}$ of size. Anti-

phase boundaries were also reduced meaning that layers with metal atoms on alternative positions are positioned on each other with a probability of only 24 %. Diffuse streaks are therefore rather weak. The observed diffraction pattern resembles that of the ideal structure ($\text{EuSi}_2\text{O}_2\text{N}_2$) with large twin domains.

2.3.4 Conclusion

A promising way of a systematic optimization of luminescent materials with defined properties is based on the detailed knowledge of the atomic structure and its influence on the luminescence parameters. Understanding and analyzing effects like stacking disorder in layered materials is therefore of great interest. To characterize samples with respect to such effects, the simulation of diffuse scattering in powder XRD patterns is a promising way because the degree of disorder in selected crystals may differ strongly. Thus, “best” crystals used for structural studies might not be representative for macroscopic samples.

Although average structure models for disordered systems do not contain information about the local structure, they are necessary to show e.g. isotypism to other structures. Furthermore, the uncommon red-shifted luminescence of $\text{Sr}_{0.5}\text{Ba}_{0.5}\text{Si}_2\text{O}_2\text{N}_2:\text{Eu}^{2+}$, compared to $\text{SrSi}_2\text{O}_2\text{N}_2:\text{Eu}^{2+}$, could be explained on the basis of the average structure model. The shift to longer wavelength can be explained by a less restricted local lattice relaxation at the Eu^{2+} sites because of shorter Eu-O bond length compared to $\text{SrSi}_2\text{O}_2\text{N}_2:\text{Eu}^{2+}$. The present luminescence investigation and also the reported structural data are significantly more reliable than prior results because of fully characterised samples. As shown by Rietveld refinement, the average structure of $\text{Sr}_{0.5}\text{Ba}_{0.5}\text{Si}_2\text{O}_2\text{N}_2:\text{Eu}^{2+}$ is isotypic to that of $\text{SrSi}_2\text{O}_2\text{N}_2$, however, the real structures of the compounds differ significantly. Simulations of the powder pattern of $\text{Sr}_{0.5}\text{Ba}_{0.5}\text{Si}_2\text{O}_2\text{N}_2:\text{Eu}^{2+}$ prove a disorder model with many anti-phase and few twin boundaries, however more twin boundaries are present than reported for $\text{SrSi}_2\text{O}_2\text{N}_2$. Because of the pseudo-symmetry of both the metal atom layers as well as the silicate layers, the presence of anti-phase domains does not change the metal coordination significantly. Moreover, disorder might influence luminescence properties noticeable, although in the present case this was not observed because of the pronounced pseudosymmetry. Not much is known about such effects. The results derived by detailed fitting of XRD patterns in this work encourage comparable investigations for other layered luminescence materials.

Acknowledgements

The authors thank Viola Duppel (MPI FKF Stuttgart) and Markus Döblinger (LMU Munich) for TEM investigations, Christian Minke for EDX measurements as well as Tobias Rosenthal and Florian Stadler (all at LMU Munich) for preliminary work. Financial support by the Fonds der Chemischen Industrie (FCI), Germany, and Philips Lumileds Lighting Company is gratefully acknowledged.

2.3.5 References

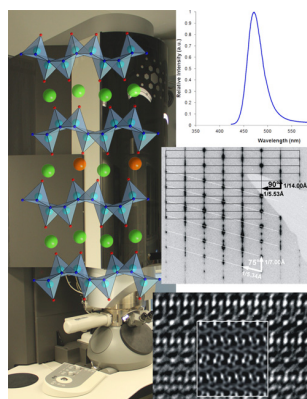
- [1] S. Ye, F. Xiao, Y. X. Pan, Y. Y. Ma, Q. Y. Zhang, *Mater. Sci. Eng., R* **2010**, *71*, 1-34.
- [2] X.-H. He, N. Lian, J.-H. Sun, M.-Y. Guan, *J. Mater. Sci.* **2009**, *44*, 4763-4775.
- [3] C. Braun, M. Seibald, S. L. Börger, O. Oeckler, T. D. Boyko, A. Moewes, G. Miehe, A. Tücks, W. Schnick, *Chem. Eur. J.* **2010**, *16*, 9646-9657.
- [4] J. A. Kechele, C. Hecht, O. Oeckler, J. Schmedt auf der Günne, P. J. Schmidt, W. Schnick, *Chem. Mater.* **2009**, *21*, 1288-1295.
- [5] R. Mueller-Mach, G. Mueller, M. R. Krames, H. A. Höpfe, F. Stadler, W. Schnick, T. Juestel, P. Schmidt, *Phys. Status Solidi A* **2005**, *202*, 1727-1732.
- [6] W. Schnick, *Phys. Status Solidi RRL* **2009**, *3*, A113-A114.
- [7] H. A. Höpfe, *Angew. Chem.* **2009**, *121*, 3626-3636; *Angew. Chem. Int. Ed.* **2009**, *48*, 3572-3582.
- [8] M. Zeuner, S. Pagano, W. Schnick, *Angew. Chem.* **2011**, *123*, 7898-7920; *Angew. Chem. Int. Ed.* **2011**, *50*, 7754-7775.
- [9] H. A. Höpfe, F. Stadler, O. Oeckler, W. Schnick, *Angew. Chem.* **2004**, *116*, 5656-5659; *Angew. Chem. Int. Ed.* **2004**, *43*, 5540-5542.
- [10] O. Oeckler, F. Stadler, T. Rosenthal, W. Schnick, *Solid State Sci.* **2007**, *9*, 205-212.
- [11] J. A. Kechele, O. Oeckler, F. Stadler, W. Schnick, *Solid State Sci.* **2009**, *11*, 537-543.
- [12] V. Bachmann, C. Ronda, O. Oeckler, W. Schnick, A. Meijerink, *Chem. Mater.* **2009**, *21*, 316-325.
- [13] Y. Q. Li, A. C. A. Delsing, G. de With, H. T. Hintzen, *Chem. Mater.* **2005**, *17*, 3242-3248.
- [14] R.-J. Xie, N. Hirotsaki, K. Sakuma, N. Kimura, *J. Phys. D: Appl. Phys.* **2008**, *41*, 144013-144017.
- [15] B.-G. Yun, Y. Miyamoto, H. Yamamoto, *J. Electrochem. Soc.* **2007**, *154*, J320-J325.

- [16] B. Y. Han, K.-S. Sohn, *J. Electrochem. Soc.* **2010**, *13*, J62-J64.
- [17] X. Song, H. He, R. Fu, D. Wang, X. Zhao, Z. Pan, *J. Phys. D: Appl. Phys.* **2009**, *42*, 065409-065414.
- [18] Y. H. Song, W. J. Park, D. H. Yoon, *J. Phys. Chem. Solids* **2010**, *71*, 473-475.
- [19] B.-G. Yun, T. Horikawa, H. Hanzawa, K. Machida, *J. Electrochem. Soc.* **2010**, *157*, J364-J370.
- [20] B. Lei, K. Machida, T. Horikawa, H. Hanzawa, *Chem. Lett.* **2011**, *40*, 140-141.
- [21] V. Bachmann, T. Jüstel, A. Meijerink, C. Ronda, P. J. Schmidt, *J. Lumin.* **2006**, *121*, 441-449.
- [22] P. Schmidt, A. Tuecks, H. Bechtel, D. Wiechert, R. Mueller-Mach, G. Mueller and W. Schnick, *Proc. SPIE-Int. Soc. Opt. Eng.* **2008**, *7058*, 70580L (Eighth International Conference on Solid State Lighting, **2008**).
- [23] P. Schmidt, A. Tuecks, J. Meyer, H. Bechtel, D. Wiechert, R. Mueller-Mach, G. Mueller and W. Schnick, *Proc. SPIE-Int. Soc. Opt. Eng.* **2007**, *6669*, 66690P (Seventh International Conference on Solid State Lighting, **2007**).
- [24] O. Oeckler, J. A. Kechele, H. Koss, P. J. Schmidt, W. Schnick, *Chem. Eur. J.* **2009**, *15*, 5311-5319.
- [25] F. Stadler, O. Oeckler, H. A. Höpfe, M. H. Möller, R. Pöttgen, B. D. Mosel, P. Schmidt, V. Duppel, A. Simon, W. Schnick, *Chem. Eur. J.* **2006**, *12*, 6984-6990.
- [26] S. Hendricks, E. Teller, *J. Chem. Phys.* **1942**, *10*, 147-167.
- [27] Stoe & Cie GmbH WINXPOW -Program for powder data handling, **2005**, Darmstadt, Germany.
- [28] A. Coelho, *TOPAS –Academic* **2007**, Brisbane: Coelho Software.
- [29] M. M. J Treacy, *DIFFAx* **2005**, version 1.812.
- [30] M. M. J Treacy, J. M. Newsam, M. W. Deem, *Proc. R. Soc. London Ser. A* **1991**, *433*, 499-520.
- [31] D. Becker, T. Fiedler, W. Hempel, F. Jermann, Patent-Treuhand-Gesellschaft für elektrische Glühlampen mbH, München, Deutschland, DE102006008300, A1, **2007**.
- [32] F. Stadler, R. Kraut, O. Oeckler, S. Schmid, W. Schnick, *Z. Anorg. Allg. Chem.* **2005**, *631*, 1773-1778.
- [33] R. Hoppe, *Angew. Chem.* **1966**, *78*, 52-63; *Angew. Chem. Int. Ed.* **1966**, *5*, 95-106.
- [34] R. Hoppe, *Angew. Chem.* **1970**, *82*, 7-16; *Angew. Chem. Int. Ed.* **1970**, *9*, 25-34.
- [35] R. Hübenthal, Programm zur Berechnung des Madelunganteils der Gitterenergie, **1993**, version 4, University of Gießen, Germany.

- [36] R. D. Shannon, *Acta Crystallogr., Sect. A: Found. Crystallogr.* **1976**, *32*, 751-767.
- [37] B. Henderson, G. F. Imbusch, *Optical Spectroscopy of Inorganic Solids*, Clarendon Press, Oxford, **1989**.
- [38] M. Nazarov, B. Tsukerblat, D. Y. Noh, *J. Phys. Chem. Solids* **2008**, *69*, 2605-2612.
- [39] A. Meijerink, G. Blasse, *J. Lumin.* **1989**, *43*, 283-289.
- [40] G. Blasse, A. Bril, *Philips Techn. Mag.* **1970**, *10*, 314.
- [41] W. Seidl, A. Stoll, J. Breu, *Z. Anorg. Allg. Chem.* **2003**, *629*, 503-515.

2.4 Unexpected Luminescence Properties of $\text{Sr}_{0.25}\text{Ba}_{0.75}\text{Si}_2\text{O}_2\text{N}_2:\text{Eu}^{2+}$ - A Narrow Blue Emitting Oxonitridosilicate with Cation Ordering

Markus Seibald, Tobias Rosenthal, Oliver Oeckler, Felix Fahrnbauer, Andreas Tücks, Peter J. Schmidt, and Wolfgang Schnick



published in: *Chem. Eur. J.* **2012**, *18*, 13446-13452; DOI: 10.1002/chem.201201953

Copyright © 2012 WILEY-VCH Verlag GmbH & Co. KGaA, Weinheim

Abstract

Due to parity allowed $4f^6(^7F)5d^1 \rightarrow 4f^7(^8S_{7/2})$ transition, powders of the nominal composition $\text{Sr}_{0.25}\text{Ba}_{0.75}\text{Si}_2\text{O}_2\text{N}_2:\text{Eu}^{2+}$ (2 mol % Eu^{2+}) show surprising intense blue emission ($\lambda_{\text{em}} = 472$ nm) when excited by UV to blue radiation. Similarly to other phases in the system $\text{Sr}_{1-x}\text{Ba}_x\text{Si}_2\text{O}_2\text{N}_2:\text{Eu}^{2+}$, the described compound is a promising phosphor material for pc-LED applications as well. The FWHM of the emission band is 37 nm, representing the smallest value found for blue emitting (oxo)nitridosilicates so far. A combination of electron and X-ray diffraction methods was used to determine the crystal structure of $\text{Sr}_{0.25}\text{Ba}_{0.75}\text{Si}_2\text{O}_2\text{N}_2:\text{Eu}^{2+}$. HRTEM images reveal the intergrowth of nanodomains with $\text{SrSi}_2\text{O}_2\text{N}_2$ and $\text{BaSi}_2\text{O}_2\text{N}_2$ -type structures, which leads to pronounced diffuse scattering. Taking into account the intergrowth, the structure of the $\text{BaSi}_2\text{O}_2\text{N}_2$ -type domains was refined on single-crystal diffraction data. In contrast to coplanar metal atom layers which are located between layers of condensed SiON_3 -tetrahedra in pure $\text{BaSi}_2\text{O}_2\text{N}_2$, in $\text{Sr}_{0.25}\text{Ba}_{0.75}\text{Si}_2\text{O}_2\text{N}_2:\text{Eu}^{2+}$ corrugated metal atom layers occur. HRTEM image simulations indicate cation ordering in the final structure model, which, in combination with the corrugated metal atom layers, explains the unexpected and excellent luminescence properties.

Keywords: Crystal-Structure Determination, Luminescence, Electron Diffraction, HRTEM, Oxonitridosilicate

2.4.1 Introduction

In times of economic crises, shortage of resources and increased sensibility of people to their environment, there is a huge demand for new materials or improved applications to enhance energy and cost efficiency together with environmental compatibility. One possible strategy is the replacement of conventional incandescent bulbs and fluorescent lamps by phosphor converted (pc)-LED applications that leads to energy saving and positive environment effects.^[1-5] White light can be generated by pc-LEDs employing the combination of a blue pump LED with yellow-green and orange-red solid-state luminescent materials (phosphors) for light conversion. Therefore, the interest and research on host lattices for rare earth activators rapidly increased during the last few years. Beside oxidic garnet phosphors especially (oxo)nitrido(alumo)silicates are being investigated in this respect.^[1-7] Their crystal structures show higher variability compared to pure oxosilicates, because N atoms can bridge up to four tetrahedra leading to a higher degree of condensation.^[7] As a consequence, emission variable within the entire visible optical spectrum can be achieved with these materials. The oxonitridosilicate phases $\text{Sr}_{1-x}\text{Ba}_x\text{Si}_2\text{O}_2\text{N}_2$ (examples of so called 1-2-2-2 phases) are promising host lattices since excellent luminescence properties in the yellow-green spectral region are observed upon doping with Eu^{2+} ions.^[8-17] For instance, $\text{SrSi}_2\text{O}_2\text{N}_2:\text{Eu}^{2+}$ can be used in white high power pc-LED applications achieving a high luminous efficiency, excellent color quality and high color stability.^[18] The corresponding crystal structures exhibit various real-structure effects on different length scales, e.g. intergrowth, microtwinning and stacking disorder.^[8,15,19] Single crystals for structure elucidation could only be obtained for $\text{EuSi}_2\text{O}_2\text{N}_2$ (isotypic to $\text{SrSi}_2\text{O}_2\text{N}_2$).^[20] As a consequence, routine strategies for structure determination could not be used for the related Sr and Ba compounds as well as the respective mixed phases.^[8,15,19] The compounds $\text{Sr}_{1-x}\text{Ba}_x\text{Si}_2\text{O}_2\text{N}_2:\text{Eu}^{2+}$ exhibit outstanding luminescence properties. They show an unexpected red-shifted luminescence for increasing Ba^{2+} content.^[10,11] Usually, substitution of Sr^{2+} by larger Ba^{2+} ions causes a shift to shorter emission wavelengths due to lower Eu^{2+} 5d-orbital splitting when Eu^{2+} randomly occupies the metal positions. Rietveld refinement on powder X-ray diffraction (PXRD) data in combination with transmission electron microscopy (TEM) showed that $\text{Sr}_{0.5}\text{Ba}_{0.5}\text{Si}_2\text{O}_2\text{N}_2:\text{Eu}^{2+}$ is highly disordered and multiply twinned.^[15] Its crystal structure is very similar to that of $\text{SrSi}_2\text{O}_2\text{N}_2:\text{Eu}^{2+}$, which exhibits a lower degree of disorder. Substitution of Sr^{2+} by Ba^{2+} leads to a deformation of the layered crystal structure. The Sr-O distances in the pure Sr phase are larger than the sum of the ionic radii, however, Ba

integration leads to shorter Sr-O distances in the mixed phase compared to non-substituted $\text{SrSi}_2\text{O}_2\text{N}_2:\text{Eu}^{2+}$. The dopant Eu^{2+} preferably occupies these Sr positions, resulting in more pronounced structural relaxation and a larger Stokes shift.^[15] Preferred occupation of Sr sites, i.e. sites with shorter metal-ligand distances, by Eu^{2+} was also reported for $\text{Ba}_{3-x}\text{Sr}_x\text{Si}_6\text{O}_{12}\text{N}_2:\text{Eu}^{2+}$ where the unexpected small FWHM of the emission band was explained by a favored occupation of one of the two independent alkaline earth sites.^[21] The detailed knowledge of the crystal structure thus allows to explain the luminescence properties, which appear surprising at first glance. Apparently, the impact of cation substitution on the deformation of the crystal structure is difficult to predict, so that the luminescence properties may be unexpected. This is most pronounced for systems which do not form solid solutions with a broad compositional range (e.g. $\text{SrSi}_2\text{O}_2\text{N}_2$ and $\text{BaSi}_2\text{O}_2\text{N}_2$). As shown for $\text{Sr}_{0.5}\text{Ba}_{0.5}\text{Si}_2\text{O}_2\text{N}_2:\text{Eu}^{2+}$, PXRD patterns of very similar structures may look significantly different; both additional and “missing” intensities do result from real structure effects. The coherent interference of scattered waves can change the pattern dramatically if nanodomains are present.^[15] Therefore, nanotwinning may affect the intensities in powder diffraction patterns whereas “classical” twinning (domain sizes larger than the X-ray’s length of coherence) has no influence. Here, we present the structure of $\text{Sr}_{1-x}\text{Ba}_x\text{Si}_2\text{O}_2\text{N}_2:\text{Eu}^{2+}$ ($x = 0.75$) which was elucidated by combining X-ray and electron diffraction and high-resolution TEM (HRTEM). The material exhibits complex real structure effects as well as excellent luminescence properties.

2.4.2 Results and Discussion

2.4.2.1 Synthesis and Chemical Analysis

Two different approaches for sample synthesis have been applied: (1) Powder samples of $\text{Sr}_{1-x}\text{Ba}_x\text{Si}_2\text{O}_2\text{N}_2:\text{Eu}^{2+}$ ($x = 0.75$) suitable for TEM investigations were prepared by heating a stoichiometric mixture (1:3; ball milled) of $(\text{Sr}_{0.25}\text{Ba}_{0.75})_2\text{SiO}_4:\text{Eu}^{2+}$ and Si powder (Cerac, 99.999%) at maximum temperatures of 1400 °C in a stream of forming gas ($\text{N}_2:\text{H}_2 = 95:5$) using a molybdenum crucible.

(2) Samples with crystals suitable for single-crystal analysis were obtained by heating a stoichiometric mixture of $(\text{Sr}_{0.25}\text{Ba}_{0.75})_2\text{SiO}_4:\text{Eu}^{2+}$ and $\alpha\text{-Si}_3\text{N}_4$ (UBE, >95 %) at maximum

temperatures of 1400 °C using a tungsten crucible positioned in a radio-frequency (RF) furnace^[22] with stationary forming gas ($\text{N}_2:\text{H}_2 = 95:5$) atmosphere (equation 1).



EDX analysis of the $\text{Sr}_{1-x}\text{Ba}_x\text{Si}_2\text{O}_2\text{N}_2:\text{Eu}^{2+}$ powder, obtained in a forming gas stream, yielded $x = 0.74(1)$ (average of seven measurements of crystallites with typical platelet morphology) as expected. For single crystals (RF furnace synthesis), x was determined to be $0.75(1)$ as an average of five measurements. From TEM-EDX, $x = 0.73(2)$ was obtained as an average of eight measurements on crystallites with typical morphology. Accordingly, the value of $x = 0.75$ (within experimental standard deviation 2 - 4 at. %) is confirmed by EDX measurements so that results from electron and X-ray diffraction data are comparable. A minor impurity phase with $\text{BaSi}_6\text{N}_8\text{O}$ structure type^[23] was detected, which is typical for thermal decomposition of 1-2-2-2 phases.^[15]

2.4.2.2 Electron Microscopy

In samples prepared by dispersing powder on Cu grids with carbon film, all crystallites with the expected composition exhibited approximately the same orientation due to the platelet particle morphology typical for layered compounds. This impedes the determination of lattice parameters. Although in general tilting the sample changes the diffraction pattern significantly, in this case tilting (overall up to 48 °) did not result in a variation of the zone axis visible in selected area electron diffraction (SAED) patterns. However, the intensity of the “reflections” varies (Figure 1).

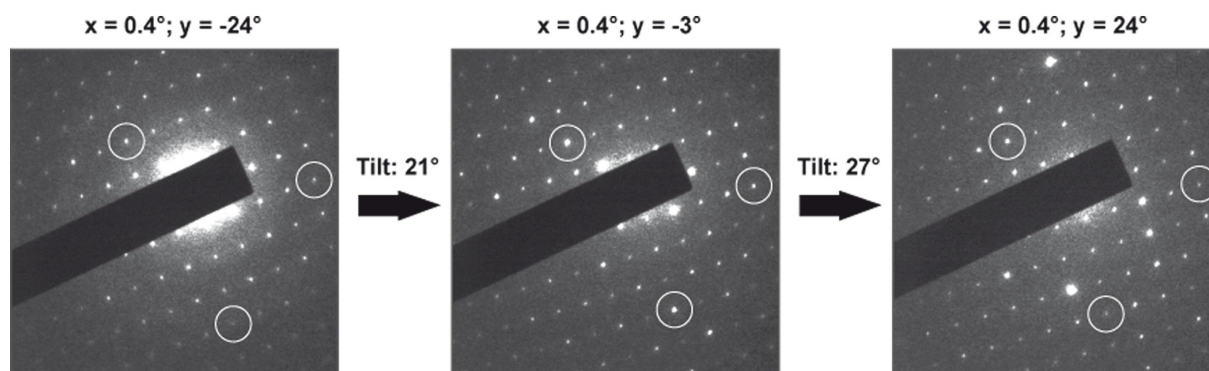


Figure 1. SAED patterns of a tilt series (along y ; overall 48° tilt angle; x and y are absolute tilt angles of the TEM sample holder). Exemplary “reflections” with changing intensities are marked by white circles.

This effect can be explained by assuming continuous diffuse streaks interconnecting the Bragg positions along the viewing direction. The maximum of the measured (real) lattice spacing during the tilt is $d = 5.46$ and 4.80 \AA , respectively, which is close to d values determined by single-crystal analysis (*next section*) and include an angle of 90.5° , corresponding to the unit mesh dimension within the silicate layer (Figure 2).

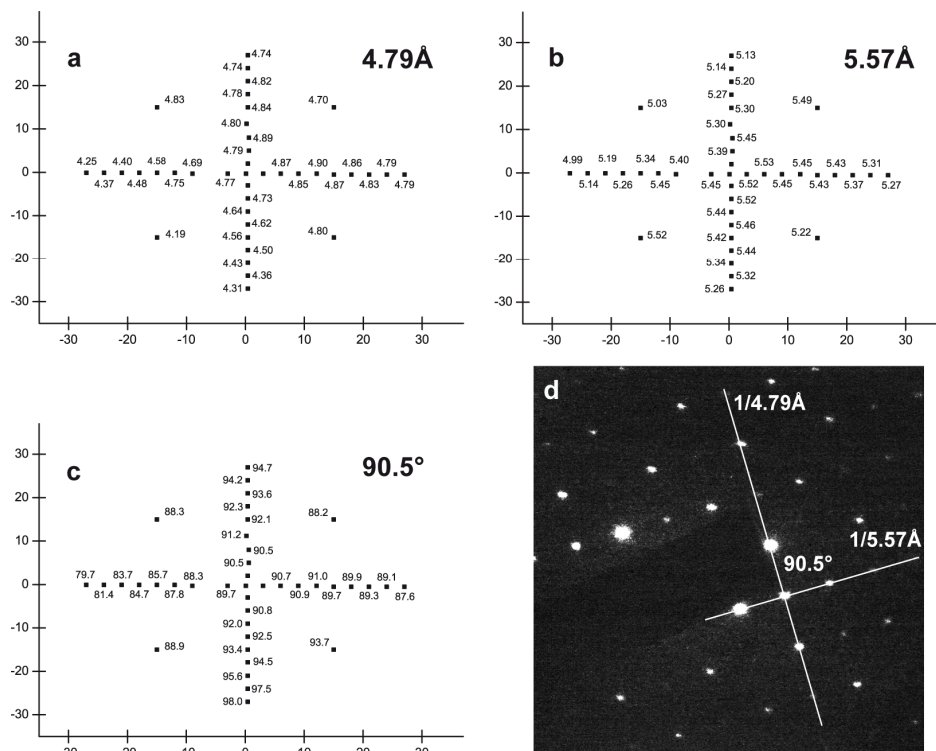


Figure 2. "Pseudo" lattice spacing (a, b) and corresponding angle (c) of $\text{Sr}_{0.25}\text{Ba}_{0.75}\text{Si}_2\text{O}_2\text{N}_2:\text{Eu}^{2+}$ dependent on tilt angle of TEM sample holder (axes of coordinate systems). Due to platelet morphology of crystallites, the tilt angles of the sample holder are approx. 0° in both directions for the maximal d values. Typical SAED pattern (d) close to 0° tilt angle of sample holder.

To diminish texture effects (to accomplish more statistical distribution of particles) and directly observe diffuse streaks, powder samples, embedded in two-component glue, were used. Intense diffuse streaks interconnecting Bragg reflections were observed. The lattice spacing along the streaks correspond to the unit cell dimension of $\text{BaSi}_2\text{O}_2\text{N}_2$.

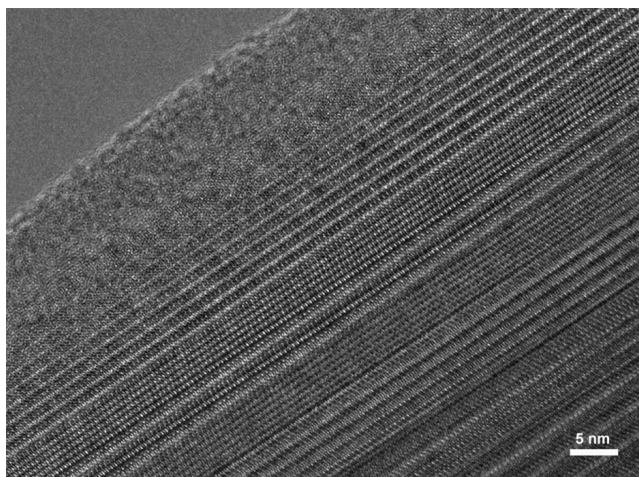


Figure 3. Typical HRTEM image of $\text{Sr}_{0.25}\text{Ba}_{0.75}\text{Si}_2\text{O}_2\text{N}_2:\text{Eu}^{2+}$ with layered domain structure.

In HRTEM images, a domain structure can be observed (Figure 3). The metrics of the crystal structure of both domain types were determined using SAED patterns (Figure 4). A subset of the reflections can be described by the metrics of the $\text{BaSi}_2\text{O}_2\text{N}_2$ type. The elongated maxima between these Bragg reflections cannot be indexed by this lattice; they require a second lattice, resembling that of $\text{SrSi}_2\text{O}_2\text{N}_2$. Results of TEM-EDX analyses corroborate the presence of domains with higher Sr content which can be expected to exhibit the $\text{SrSi}_2\text{O}_2\text{N}_2$ structure type. This variation of the Sr distribution cannot be detected in SEM-EDX measurements because the domain sizes are much smaller than the area investigated. Both lattices share one direction: d_{010} of the $\text{BaSi}_2\text{O}_2\text{N}_2$ type (14.00 Å; 14.28 Å from single-crystal data; black unit cell) is twice d_{010} of the $\text{Sr}_{0.5}\text{Ba}_{0.5}\text{Si}_2\text{O}_2\text{N}_2$ type (7.00 Å; 7.17 Å from PXRD,^[15] white unit cell). Both lattice vectors are parallel and correspond to the stacking direction of silicate layers. The second smallest spacing of each lattice corresponds to d_{100} of $\text{BaSi}_2\text{O}_2\text{N}_2$ type (5.53 Å; 5.47 Å from single-crystal analysis,) and d_{101} of $\text{Sr}_{0.5}\text{Ba}_{0.5}\text{Si}_2\text{O}_2\text{N}_2$ type (5.34 Å; 5.29 Å from PXRD,^[15] respectively. The corresponding angles ($\text{BaSi}_2\text{O}_2\text{N}_2$ type: 90°; single crystal orthorhombic; $\text{Sr}_{0.5}\text{Ba}_{0.5}\text{Si}_2\text{O}_2\text{N}_2$ type: 75°; 76° from PXRD)^[15] also match well. The deviations between lattice parameters from electron and X-ray diffraction data are consistent within experimental errors of both methods.

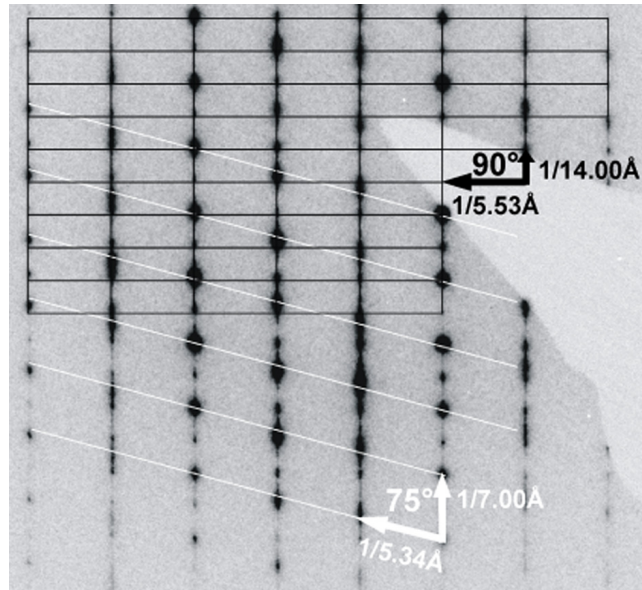


Figure 4. SAED pattern representing a superposition (middle) of the $[001]$ zone axis of the $\text{BaSi}_2\text{O}_2\text{N}_2$ type (black, top) and the $[10\bar{1}]$ zone axis of the $\text{SrSi}_2\text{O}_2\text{N}_2$ type (white, bottom). For both, d values and corresponding angles are shown. In every third vertical row, some Bragg reflections of both compounds overlap completely. Diffuse streaks interconnect the reflections.

Some reflections of $\text{SrSi}_2\text{O}_2\text{N}_2$ and $\text{BaSi}_2\text{O}_2\text{N}_2$ lattice types overlap completely and therefore the intensity of affected sharp Bragg reflections (in every third row) is the sum of two contributions and thus contains information from both systems. Therefore, diffraction patterns do not show orthorhombic Laue symmetry (see $\text{BaSi}_2\text{O}_2\text{N}_2$ ^[8] structure type). The $\text{SrSi}_2\text{O}_2\text{N}_2$ structure type ^[19] is triclinic (space group $P1$) and the superposition with any other pattern yields overall triclinic Laue symmetry.

2.4.2.3 Single-Crystal Structure Analysis

As shown in Figure 3, $\text{Sr}_{0.25}\text{Ba}_{0.75}\text{Si}_2\text{O}_2\text{N}_2:\text{Eu}^{2+}$ exhibits a domain structure with 2D extended domains, which are only a few nanometers thick. Single crystals show pronounced diffuse scattering in reciprocal lattice sections. Because the domains are very thin, the scattered waves superimpose coherently which means that overlapping intensities contain information on both domain types (see Figure 4). These overlapping reflections were discarded for the refinement of the structure of the blue emitting material (based on $\text{BaSi}_2\text{O}_2\text{N}_2$ lattice parameters). The relative orientation of both domain types does not change, so “single crystal” methods can be used for such crystals when reflections with contributions from different domain types are neglected. The scheme in Figure 5, which was derived from

different reciprocal lattice sections, shows that all rows along $[010]$ with exclusively sharp reflections (see Figure 4) are involved. This corresponds to 1/3 of all reflections.

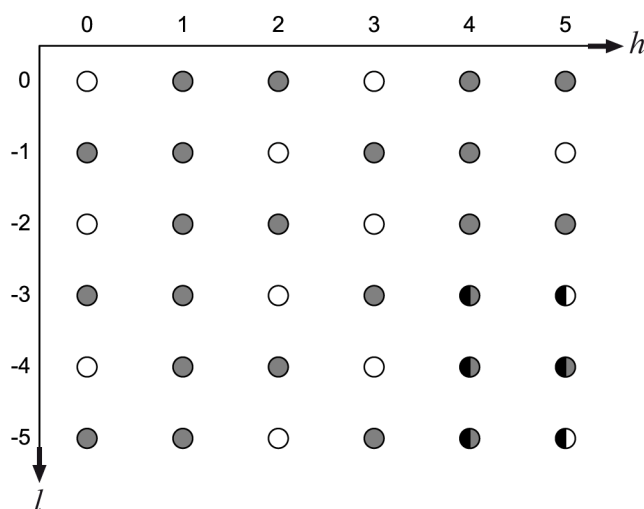


Figure 5. Schematic view of the overlap of the reciprocal lattice of $\text{BaSi}_2\text{O}_2\text{N}_2$ with that of the $\text{SrSi}_2\text{O}_2\text{N}_2$ structure type. As derived from reciprocal lattice sections, rows along $[010]$ of the $\text{BaSi}_2\text{O}_2\text{N}_2$ type show either exclusively sharp reflections or elongated, diffuse intensities. Referring to Figure 4, rows with only sharp reflections overlap for both lattice types (white spheres) while the others exclusively belong to the $\text{BaSi}_2\text{O}_2\text{N}_2$ lattice type (gray spheres). As the resolution of the reciprocal lattice sections available was limited, some rows (black-gray spheres, black-white spheres) were extrapolated.

The crystal structure of $\text{Sr}_{0.25}\text{Ba}_{0.75}\text{Si}_2\text{O}_2\text{N}_2:\text{Eu}^{2+}$ was refined in space group $Pna2_1$ (no. 33) with $a = 5.470(2)$, $b = 14.277(3)$, $c = 4.791(1)$ Å and $V = 374.2(2)$ Å³ (see Figure 7). Refinement converged finally to $R1 = 0.0924$. Comparable refinements in $Pnma$ show disordered silicate layers as described for $\text{BaSi}_2\text{O}_2\text{N}_2$ [8] but with significantly higher R -values. The absence of disorder in the crystal structure is corroborated by the Fourier transforms of individual domains in HRTEM images, which exhibit no diffuse intensities. In the refined structure model, the silicate layers are built up of vertex sharing SiON_3 -tetrahedra and shifted against each other along the stacking direction $[010]$. The metal atom layers in between them are corrugated instead of being coplanar as in $\text{BaSi}_2\text{O}_2\text{N}_2$. [8] As the Bragg reflections used for the structure refinement are located on diffuse streaks, their absolute intensities are biased. Mixed occupation of the metal atom position was set to an atomic ratio Sr:Ba = 1:3 as suggested by the EDX analysis. The doping with 2 mol% Eu was neglected during refinement. Distance restraints for the SiON_3 -tetrahedra were implemented in order to ensure their comparability to the values in $\text{SrSi}_2\text{O}_2\text{N}_2$ and $\text{BaSi}_2\text{O}_2\text{N}_2$. The similarity of tetrahedra topology within the silicate layers is the reason for the intergrowth of $\text{Sr}_{0.25}\text{Ba}_{0.75}\text{Si}_2\text{O}_2\text{N}_2$ domains in zone axis orientation $[001]$ with $\text{SrSi}_2\text{O}_2\text{N}_2$ structure type domains in $[10\bar{1}]$ respectively, as determined from superimposed diffraction patterns like the

one in Figure 4. Related anionic substructures can for example also be observed in $(\text{Sr}_{0.94}\text{Eu}_{0.06})(\text{Al}_{0.3}\text{Si}_{0.7})_4(\text{N}_{0.8}\text{O}_{0.2})_6$, an aluminosilicate with stacking faults.^[24]

2.4.2.4 Cation Ordering as Derived from HRTEM

HRTEM image simulations^[25] were compared to experimental images (Figure 6). They show that a structure model with one mixed occupied metal atom position ($Pna2_1$) does not well describe all significant features of the HRTEM images (Figure 6b).

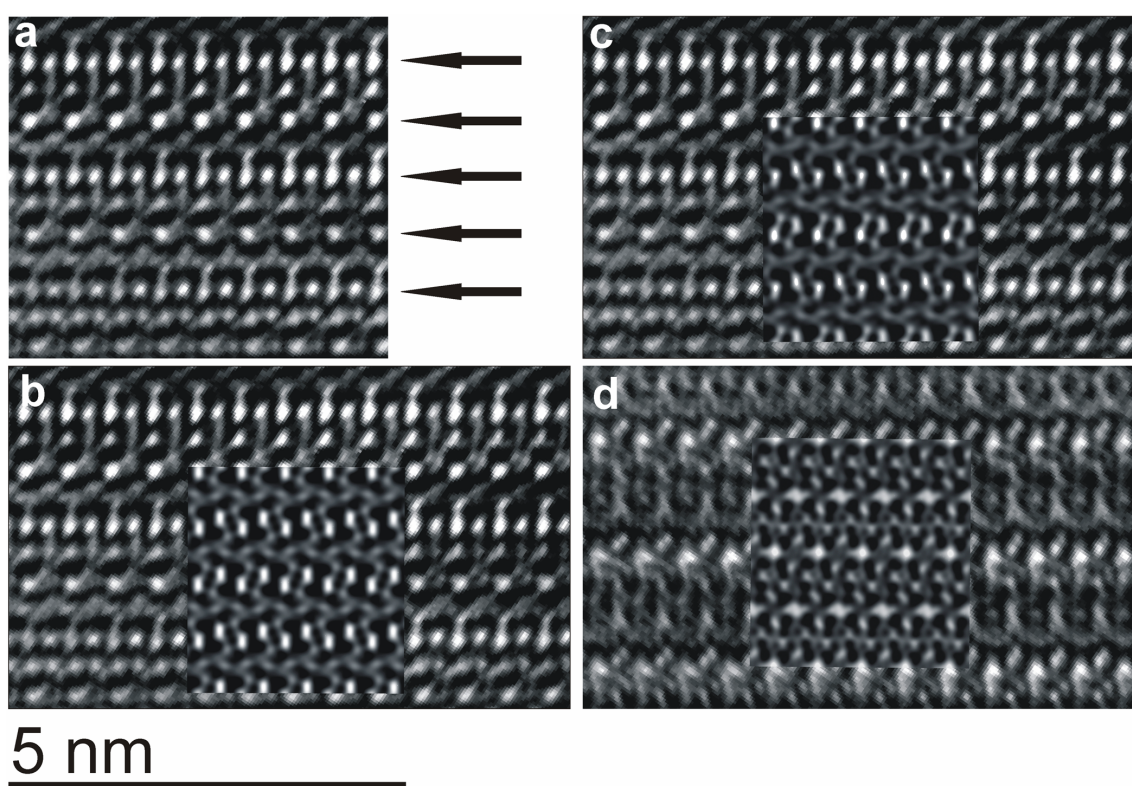


Figure 6. HRTEM images of $\text{Sr}_{0.25}\text{Ba}_{0.75}\text{Si}_2\text{O}_2\text{N}_2:\text{Eu}^{2+}$ with: black arrows indicating horizontal contrasts mainly affected by metal atom layers (a), simulation for the refined structure in space group $Pna2_1$ (b, defocus value -81 nm), simulation for structure in space group $P1$ (c, cation ordering, defocus value -81 nm) and simulation for structure in $P1$ (d, cation ordering, defocus value -119 nm). For all simulations the following values were used: accelerating voltage = 300 kV, aperture diameter = 20 nm^{-1} , $c_s = 1.2$ mm, spread of focus = 2.14 nm, beam semi-convergence = 0.60 mrad, layer thickness approx. 4 nm (8 unit cells in corresponding viewing direction).

Horizontal rows with bright white contrasts (indicated by black arrows, Figure 6a) are strongly affected by the metal atom positions so that the periodic varying contrast in every second of these rows indicates deviations from space group $Pna2_1$ as it is not consistent with mirror planes and mixed occupation of a single metal atom position. A convincing fit was obtained employing space group $P1$ and full occupation of one of the four resulting metal atom positions with Sr, which is consistent with the chemical composition Sr:Ba = 1:3

(Figure 6c, 6d). Additionally, the position of the metal atoms was slightly shifted, because of different ionic radii and consequently different coordination spheres of Sr and Ba (compare trigonal prismatic in $\text{SrSi}_2\text{O}_2\text{N}_2$ vs. cuboid in $\text{BaSi}_2\text{O}_2\text{N}_2$). This means that rows exclusively occupied by Ba atoms are less corrugated than rows containing alternating Ba and Sr atoms and Ba-Sr bond lengths are shorter than the Ba-Ba bond lengths (Figure 7). The relaxation of surrounding light atoms was neglected because it affects only slightly the simulated images. Simulated images for two defocus values reproduce the main features (Figure 6c, 6d) quite well.

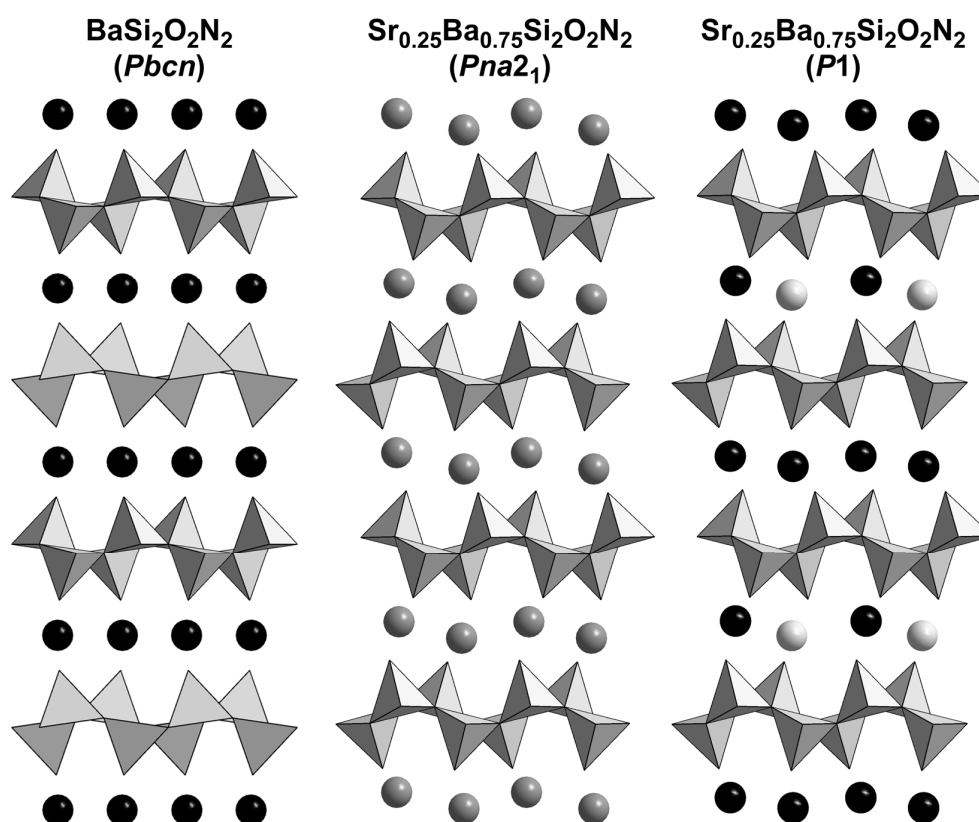


Figure 7. Projections of the crystal structures of $\text{BaSi}_2\text{O}_2\text{N}_2$ (left),^[8] $\text{Sr}_{0.25}\text{Ba}_{0.75}\text{Si}_2\text{O}_2\text{N}_2$ (“average” structure from single-crystal data, middle) and $\text{Sr}_{0.25}\text{Ba}_{0.75}\text{Si}_2\text{O}_2\text{N}_2$ (local cation ordering according to TEM, right) perpendicular to stacking direction. Silicate layers of condensed SiON_3 -tetrahedra are illustrated gray, Ba atoms black, Sr/Ba mixed occupied positions dark gray and Sr atoms light gray.

The consistency of the structure model is corroborated by lattice energy calculations (MAPLE, Madelung part of lattice energy).^[26-29] The assignment of O and N atoms was done in analogy to other $\text{Sr}_{1-x}\text{Ba}_x\text{Si}_2\text{O}_2\text{N}_2$ phases with the same silicate layer topology.^[8,15,19] The calculated values listed in Table 1 are close to typical partial MAPLE values.^[7] The total MAPLE values calculated for the refined structure and the structure model containing ordered cations are compared to that of a theoretical reference reaction equation starting from the

respective binary compounds. The deviation is almost half the value for the structure model with cation ordering compared to the structure model refined on X-ray data.

Table 1. Results of MAPLE calculations (in kJ/mol) for $\text{Sr}_{0.25}\text{Ba}_{0.75}\text{Si}_2\text{O}_2\text{N}_2$ and increment calculations: partial MAPLE values, total MAPLE sum and difference to theoretical total MAPLE value.^[a]

	Sr^{2+}	Ba^{2+}	Si^{4+}	$\text{O}^{11}2^-$	$\text{N}^{13}3^-$	Total MAPLE	Δ
<i>Pna2</i> ₁	1896 (mixed)		9408-9566	2219-2276	6174-6206	37745	0.064 %
<i>P1</i>	1916	1871-1900	9249-9755	2144-2386	6051-6331	37755	0.037 %
Total MAPLE (0.25 SrO + 0.75 BaO + 0.5 SiO ₂ + 0.5 Si ₃ N ₄): 37769							

[a] Typical MAPLE values (in kJ/mol): Ba^{2+} : 1500-2000; Sr^{2+} : 1500-2100; Si^{4+} : 9000-10200; $\text{O}^{11}2^-$: 2000-2800; $\text{N}^{13}3^-$: 5000-6200.^[7]...

2.4.2.5 Luminescence

Eu^{2+} -doped samples of $\text{Sr}_{0.25}\text{Ba}_{0.75}\text{Si}_2\text{O}_2\text{N}_2$ show unexpected intense narrow band blue emission when excited with UV to blue radiation as a consequence of the parity allowed $4f^6(^7F)5d^1 \rightarrow 4f^7(^8S_{7/2})$ transition.

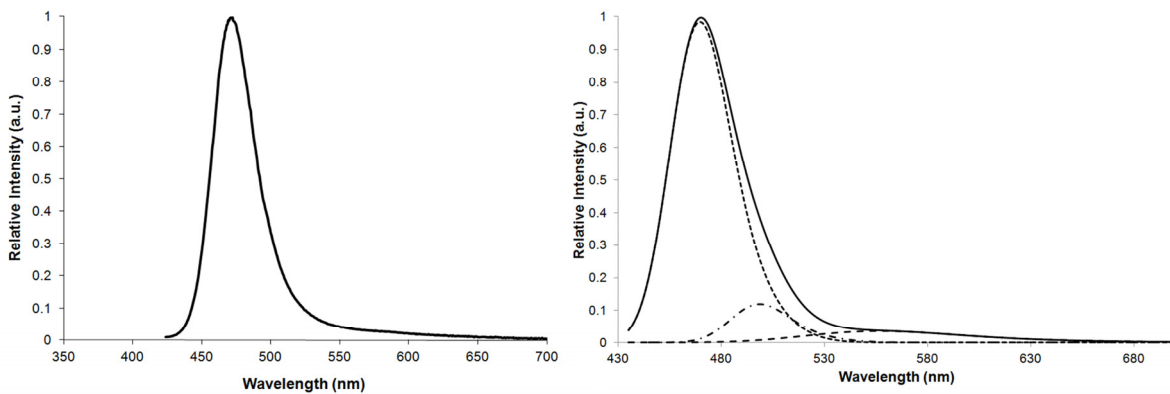


Figure 8 Left: emission spectrum of $\text{Sr}_{0.25}\text{Ba}_{0.75}\text{Si}_2\text{O}_2\text{N}_2:\text{Eu}^{2+}$ (2 mol %) powder sample ($\lambda_{\text{exc}} = 400$ nm, $\lambda_{\text{em}} = 472$ nm, FWHM = 37 nm). Right: Least-square refinement of measured emission spectrum (black solid line) with three individual curves (1: $\lambda_{\text{em}} = 469$ nm, FWHM = 36 nm, line: dashed; 2: $\lambda_{\text{em}} = 498$ nm, FWHM = 35 nm, line: dashed and dotted; 3: $\lambda_{\text{em}} = 555$ nm, FWHM = 90 nm, line: dashed).

As shown for the $\text{SrSi}_2\text{O}_2\text{N}_2$ structure type, the substitution of Sr by Ba leads to an unexpected increase of the Stokes shift (i.e. a shift of emission wavelength from green to yellow spectral region), e.g. for $\text{Sr}_{0.5}\text{Ba}_{0.5}\text{Si}_2\text{O}_2\text{N}_2:\text{Eu}^{2+}$.^[15] $\text{Sr}_{0.25}\text{Ba}_{0.75}\text{Si}_2\text{O}_2\text{N}_2:\text{Eu}^{2+}$ is supposed to show an even larger Stokes shift,^[10,11] which, at first glance, seems obvious because of the increasing amount of Ba. For this composition, however, the structure changes towards the $\text{BaSi}_2\text{O}_2\text{N}_2$ structure type as mentioned above. In relation to $\text{BaSi}_2\text{O}_2\text{N}_2:\text{Eu}^{2+}$, a larger Stokes shift is expected for $\text{Sr}_{0.25}\text{Ba}_{0.75}\text{Si}_2\text{O}_2\text{N}_2:\text{Eu}^{2+}$ due to more pronounced local

structure relaxation of Eu^{2+} sites in the excited state in case of increasing Sr content. However, a comparable Stokes shift is observed, leading to an overall emission wavelength of 472 nm and a shifted lowest lying absorption band towards higher energies for this material. The explanation for this behavior is based on structure deformation. In the crystal structure of $\text{Sr}_{0.25}\text{Ba}_{0.75}\text{Si}_2\text{O}_2\text{N}_2$ there are corrugated metal atom layers while they are coplanar in $\text{BaSi}_2\text{O}_2\text{N}_2$. Additionally, the silicate layers are slightly shifted against each other perpendicular to stacking direction. As a consequence, there are longer Eu-O (also Eu-N) distances than in $\text{BaSi}_2\text{O}_2\text{N}_2:\text{Eu}^{2+}$ because of distorted cuboid metal atom coordination. The overall Eu^{2+} coordination explains the shift of absorption and emission bands towards higher energies. The similarity of the ionic radii results obviously in a preferred occupation of Eu^{2+} on the single Sr^{2+} site, causing the narrow band width of only 37 nm. This is the smallest value found so far for blue emitters of this material class. A second emission band can be assigned to the yellow conversion of primary radiation by domains with $\text{SrSi}_2\text{O}_2\text{N}_2:\text{Eu}^{2+}$ structure type with its typical broad band emission (see Figure 8). To improve the refinement of measured values, a sharp profile according to Eu^{2+} emission in $\text{BaSi}_2\text{O}_2\text{N}_2$ host lattice was included (see Figure 8). $\text{BaSi}_6\text{N}_8\text{O}:\text{Eu}^{2+}$ is not present in this case, because there is no quantitative excitation at 400 nm.^[30]

2.4.3 Conclusion

Within the series of $\text{Sr}_{1-x}\text{Ba}_x\text{Si}_2\text{O}_2\text{N}_2:\text{Eu}^{2+}$ phosphor materials, $\text{Sr}_{0.25}\text{Ba}_{0.75}\text{Si}_2\text{O}_2\text{N}_2:\text{Eu}^{2+}$ is a remarkable example that complex analytic methods are required to determine the crystal structure when dealing with real structure effects. Only detailed knowledge of atomic arrangement qualifies to describe reliable structure-property relations. Integration of Ba^{2+} in $\text{Sr}_{1-x}\text{Ba}_x\text{Si}_2\text{O}_2\text{N}_2$ leads to an intergrowth of domains of the $\text{SrSi}_2\text{O}_2\text{N}_2$ and $\text{BaSi}_2\text{O}_2\text{N}_2$ structure type, respectively, for $x = 0.75$, as there is no solid solution series. Fourier transforms of individual domains in HRTEM images do not show diffuse streaks. Therefore, the diffuse scattering in electron diffraction patterns presumably results from this intergrowth. Based on HRTEM image simulations, there is only one crystallographic site exclusively occupied by Sr^{2+} ions in the final structure model of $\text{Sr}_{0.25}\text{Ba}_{0.75}\text{Si}_2\text{O}_2\text{N}_2:\text{Eu}^{2+}$. According to very similar ionic radii, also preferred single-site occupation for the Eu^{2+} ions can be expected. In accordance with the results observed for $\text{SrSi}_6\text{N}_8:\text{Eu}^{2+}$ ^[31] and $\text{BaSi}_2\text{O}_2\text{N}_2:\text{Eu}^{2+}$, occupation of only one site with Eu^{2+} is obviously a main reason for a very sharp emission band in phosphor

materials. $\text{Sr}_{0.25}\text{Ba}_{0.75}\text{Si}_2\text{O}_2\text{N}_2:\text{Eu}^{2+}$ exhibits the smallest value for FWHM (37 nm) known so far for blue emitters of this material class. The narrow band emission in the blue spectral region qualifies this material for applications in pc-LEDs, e.g. white LEDs with high color rendering index, blue LEDs (UV irradiation) or blue pump-LEDs closing the cyan spectral gap. Layered $\text{Sr}_{1-x}\text{Ba}_x\text{Si}_2\text{O}_2\text{N}_2:\text{Eu}^{2+}$ phases are good examples how conformation and arrangement of metal atoms and the Si-O/N partial structure affect luminescence properties.

2.4.4 Experimental Section

2.4.4.1 Synthesis and Chemical Analysis

Powder samples of $\text{Sr}_{1-x}\text{Ba}_x\text{Si}_2\text{O}_2\text{N}_2:\text{Eu}^{2+}$ ($x = 0.75$) suitable for TEM investigations were prepared by heating a stoichiometric mixture (1:3; ball milled) of $(\text{Sr}_{0.25}\text{Ba}_{0.75})_2\text{SiO}_4:\text{Eu}^{2+}$ and Si powder (Cerac, 99.999%) for 5 h to 1350 °C in a stream of forming gas ($\text{N}_2:\text{H}_2 = 95:5$) using a molybdenum crucible. The product was ground (ball milled using agate balls in cyclohexane) and reheated to 1400 °C for another 5 h under forming gas and ground again. The final product was washed with diluted HCl and ethanol to remove remaining oxosilicate byproducts. Samples with crystals suitable for single-crystal analysis were obtained by heating a stoichiometric mixture of $(\text{Sr}_{0.25}\text{Ba}_{0.75})_2\text{SiO}_4:\text{Eu}^{2+}$ and $\alpha\text{-Si}_3\text{N}_4$ (UBE, >95 %) using a tungsten crucible positioned in a radio-frequency (RF) furnace^[22] with stationary forming gas ($\text{N}_2:\text{H}_2 = 95:5$) atmosphere. The temperature was increased to 1350 °C (22 °C/ min) and held for 3 h. After heating to 1400 °C (10 °C/ min) and keeping this temperature for 3 h, the temperature was reduced to 650 °C (1.1 °C/ min). The starting material $(\text{Sr}_{0.25}\text{Ba}_{0.75})_2\text{SiO}_4:\text{Eu}^{2+}$ was synthesized by heating a mixture (ball milled) of SrCO_3 (Solvay, SL300), BaCO_3 (Solvay, L500), SiO_2 (Evonik, Aerosil OX 50) and Eu_2O_3 (Rhodia, 99,99 %, dopant, 2 mol %) for 2 h in a stream of forming gas ($\text{N}_2:\text{H}_2 = 95:5$). The chemical composition of the crystalline product was analyzed by energy dispersive X-ray spectroscopy (EDX) using a JSM-6500F scanning electron microscope (SEM, Joel) with a Si/Li EDX detector (model 7418, Oxford Instruments).

2.4.4.2 Single-Crystal X-ray Diffraction

Blue luminescent crystals obtained by RF furnace synthesis were mounted on glass fibers and checked for quality on a Buerger precession camera. Intensity data were collected on a Nonius Kappa-CCD diffractometer with graded multilayer X-ray optics ($\lambda = 0.71093 \text{ \AA}$). The structure was solved by direct methods^[32] and refined by full-matrix least-squares method using anisotropic displacement parameters for the metal atoms.^[33] Due to intergrowth with $\text{SrSi}_2\text{O}_2\text{N}_2$ intensity data were corrected (*section single-crystal structure analysis*).^[34]

2.4.4.3 Transmission Electron Microscopy

For preliminary experiments, ground powder samples were dispersed in ethanol in order to deposit them on copper grids coated with a holey carbon film. Since such samples showed preferred orientation, the powder was mixed with two-component glue, placed between silicon wafers and glass panels, and then fixed in brass tubes (inner diameter 2 mm). These were cut into slices perpendicular to the tube elongation (thickness approx. 200 μm) and polished to 80-90 μm using different SiC coated sand papers (grain size: 40 – 5 μm). Finally, the thickness in the middle of the disk was reduced to approx. 20 μm using a dimple grinder (type 650, Gatan) and diamond grind (Electron Microscopy Science). Subsequently, a hole within the glue matrix samples was fabricated using an argon ion precision ion polishing system (type 691, Gatan). Crystallites near the hole, which are partially free of glue, are suitable for TEM investigations. SAED patterns and/or high-resolution images were recorded on transmission electron microscopes Jeol JEM-2011 (200 kV) and Fei Titan 80-300 (300 kV), respectively. The latter one was equipped with an EDX system (TEM Tops 30, Edax). Tilt series of diffraction patterns were obtained using a double tilt sample holder with maximum tilt angle of $\pm 30^\circ$.

Acknowledgements

The authors thank Dr. Peter Mayer (LMU Munich) for collection of single-crystal data, Dr. Markus Döblinger (LMU Munich) for support concerning TEM investigations as well as Peter Käshammer and Roman Pobel (both LMU Munich) for preliminary work. Financial support by the Fonds der Chemischen Industrie (FCI), Germany, is gratefully acknowledged.

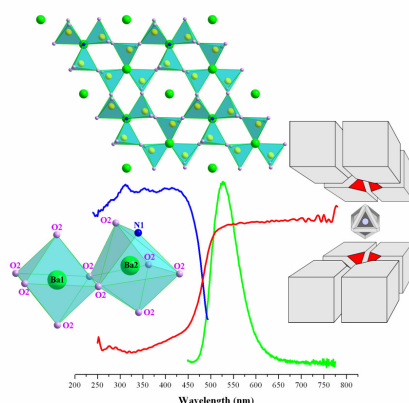
2.4.5 References

- [1] R.-J. Xie, N. Hirosaki, *Sci. Technol. Adv. Mater.* **2007**, *8*, 588-600.
- [2] X.-H. He, N. Lian, J.-H. Sun, M.-Y. Guan, *J. Mater. Sci.* **2009**, *44*, 4763-4775.
- [3] S. Ye, F. Xiao, Y. X. Pan, Y. Y. Ma, Q. Y. Zhang, *Mater. Sci. Eng., R* **2010**, *71*, 1-34.
- [4] P. F. Smet, A. B. Parmentier, D. Poelman, *J. Electrochem. Soc.* **2011**, *158*, R37-R54.
- [5] C. C. Lin, R.-S. Liu, *J. Phys. Chem. Lett.* **2011**, *2*, 1268-1277.
- [6] R.-J. Xie, N. Hirosaki, K. Sakuma, N. Kimura, *J. Phys. D: Appl. Phys.* **2008**, *41*, 144013-144017.
- [7] M. Zeuner, S. Pagano, W. Schnick, *Angew. Chem.* **2011**, *123*, 7898-7920; *Angew. Chem. Int. Ed.* **2011**, *50*, 7754-7775.
- [8] J. A. Kechele, O. Oeckler, F. Stadler, W. Schnick, *Solid State Sci.* **2009**, *11*, 537-543.
- [9] Y. Q. Li, A. C. A. Delsing, G. de With, H. T. Hintzen, *Chem. Mater.* **2005**, *17*, 3242-3248.
- [10] V. Bachmann, C. Ronda, O. Oeckler, W. Schnick, A. Meijerink, *Chem. Mater.* **2009**, *21*, 316-325.
- [11] B.-G. Yun, Y. Miyamoto, H. Yamamoto, *J. Electrochem. Soc.* **2007**, *154*, J320-J325.
- [12] B. Lei, K. Machida, T. Horikawa, H. Hanzawa, *Chem. Lett.* **2011**, *40*, 140-141.
- [13] Y. H. Song, W. J. Park, D. H. Yoon, *J. Phys. Chem. Solids* **2010**, *71*, 473-475.
- [14] X. Song, H. He, R. Fu, D. Wang, X. Zhao, Z. Pan, *J. Phys. D: Appl. Phys.* **2009**, *42*, 065409-065414.
- [15] M. Seibald, O. Oeckler, V. R. Celinski, P. J. Schmidt, A. Tücks, W. Schnick, *Solid State Sci.* **2011**, *13*, 1769-1778.
- [16] V. Bachmann, T. Jüstel, A. Meijerink, C. Ronda, P. J. Schmidt, *J. Lumin.* **2006**, *121*, 441-449.
- [17] P. Schmidt, A. Tücks, H. Bechtel, D. Wiechert, R. Mueller-Mach, G. Mueller, W. Schnick, *Proc. SPIE-Int. Soc. Opt. Eng.* **2008**, *7058*, 70580L (Eighth International Conference on Solid State Lighting, 2008).
- [18] R. Mueller-Mach, G. Mueller, M. R. Krames, H. A. Höpfe, F. Stadler, W. Schnick, T. Jüstel, P. Schmidt, *Phys. Status Solidi A* **2005**, *202*, 1727-1732.
- [19] O. Oeckler, F. Stadler, T. Rosenthal, W. Schnick, *Solid State Sci.* **2007**, *9*, 205-212.
- [20] F. Stadler, O. Oeckler, H. A. Höpfe, M. H. Möller, R. Pöttgen, B. D. Mosel, P. Schmidt, V. Duppel, A. Simon, W. Schnick, *Chem. Eur. J.* **2006**, *12*, 6984-6990.

- [21] C. Braun, M. Seibald, S. L. Börger, O. Oeckler, T. D. Boyko, A. Moewes, G. Miede, A. Tücks, W. Schnick, *Chem. Eur. J.* **2010**, *16*, 9646-9657.
- [22] W. Schnick, H. Huppertz, R. Lauterbach, *J. Mater. Chem.* **1999**, *9*, 289-296.
- [23] F. Stadler, R. Kraut, O. Oeckler, S. Schmid, W. Schnick, *Z. Anorg. Allg. Chem.* **2005**, *631*, 1773-1778.
- [24] H. Yamane, S. Shimooka, K. Uheda, *J. Solid State Chem.* **2012**, *190*, 264-270.
- [25] P. A. Stadelmann, *Ultramicroscopy* **1987**, *21*, 131-146.
- [26] R. Hoppe, *Angew. Chem.* **1966**, *78*, 52-63; *Angew. Chem. Int. Ed.* **1966**, *5*, 95-106.
- [27] R. Hoppe, *Angew. Chem.* **1970**, *82*, 7-16; *Angew. Chem. Int. Ed.* **1970**, *9*, 25-34.
- [28] R. Hübenthal, Madlung Part of Lattice Energy (Program), version 4, University of Gießen (Germany), **1993**.
- [29] R. D. Shannon, *Acta Crystallogr., Sect. A:* **1976**, *32*, 751-767.
- [30] R.-J. Xie, N. Hirosaki, Y. Li, T. Takeda, *J. Lumin.* **2010**, *130*, 266-269.
- [31] K. Shioi, N. Hirosaki, R.-J. Xie, T. Takeda, Y. Li, *J. Mater. Sci.* **2008**, *43*, 5659-5661.
- [32] M. C. Burla, M. Camalli, B. Carrozzini, G. L. Casciarano, C. Giacovazzo, G. Polidori, R. Spagna, *J. Appl. Crystallogr.* **2003**, *36*, 1103-1103.
- [33] G. M. Sheldrick, *Acta Crystallogr., Sect. A: Found. Crystallogr.* **2008**, *64*, 112-122.
- [34] Further details of the crystal structure investigation may be obtained from Fachinformationszentrum Karlsruhe, 76344 Eggenstein-Leopoldshafen, Germany (fax: (+49)7247-808-666; e-mail, crysdata@fiz-karlsruhe.de, http://www.fiz-karlsruhe.de/request_for_deposited_data.html) on quoting the depository number CSD-424289 ($\text{Sr}_{0.25}\text{Ba}_{0.75}\text{Si}_2\text{O}_2\text{N}_2$).

2.5 Material Properties and Structural Characterization of $M_3Si_6O_{12}N_2:Eu^{2+}$ (M=Ba, Sr) - A Comprehensive Study on a Promising Green Phosphor for pc-LEDs

Cordula Braun, Markus Seibald, Saskia L. Börger, Oliver Oeckler, Teak D. Boyko, Alexander Moewes, Gerhard Miehe, Andreas Tücks, and Wolfgang Schnick



published in: *Chem. Eur. J.* **2010**, *16*, 9646-9657; DOI: 10.1002/chem.201000660

Copyright © 2010 WILEY-VCH Verlag GmbH & Co. KGaA, Weinheim

Abstract

The efficient green phosphor $Ba_3Si_6O_{12}N_2:Eu^{2+}$ and its solid-solution series $Ba_{3-x}Sr_xSi_6O_{12}N_2$ (with $x \sim 0.4$ and 1) were synthesized in a radio-frequency furnace under nitrogen atmosphere at temperatures up to 1425 °C. The crystal structure ($Ba_3Si_6O_{12}N_2$, space group $P\bar{3}$ (no. 147), $a = 7.5218(1)$ Å, $c = 6.4684(1)$ Å, $wR2 = 0.048$, $Z=1$) has been solved and refined on the basis of both single-crystal and powder X-ray diffraction data. $Ba_3Si_6O_{12}N_2:Eu^{2+}$ is a layer-like oxonitridosilicate and consists of vertex-sharing SiO_3N -tetrahedra forming 6er- and 4er-rings as fundamental building units (FBU). The nitrogen atoms are connected to three silicon atoms ($N^{[3]}$), while the oxygen atoms are either terminally bound ($O^{[1]}$) or bridge two silicon atoms ($O^{[2]}$) (numbers in superscripted square brackets after atoms indicate the coordination number of the atom in question). Two crystallographically independent Ba^{2+} -sites are situated between the silicate layers. Luminescence investigations have shown that $Ba_3Si_6O_{12}N_2:Eu^{2+}$ exhibits excellent luminescence properties (emission maximum at ≈ 527 nm, FWHM of ≈ 65 nm, low thermal quenching) which provides potential for industrial application in phosphor-converted light-emitting diodes (pc-LEDs). In-situ high-pressure and high-temperature investigations with synchrotron X-ray diffraction indicate decomposition of

$Ba_3Si_6O_{12}N_2$ under these conditions. The band gap of $Ba_3Si_6O_{12}N_2:Eu^{2+}$ was measured to be 7.05 ± 0.25 eV by means of X-ray emission spectroscopy (XES) and X-ray absorption near edge spectroscopy (XANES). This agrees well with calculated band gap of 6.93 eV using the mBJ-GGA potential. Bonding to the Ba atoms is highly ionic with only the $4p_{3/2}$ orbitals participating in covalent bonds. The valence band consists primarily of N and O p states and the conduction band contains primarily Ba d and f states with a small contribution from the N and O p states.

Keywords: Density-Functional Calculations, High-pressure chemistry, Luminescence, Oxonitridosilicates, X-Ray Absorption Spectroscopy

2.5.1 Introduction

Nitrido- and oxonitridosilicates as well as binary silicon nitride (e.g. Si_3N_4 ,^[1-3] $SiAlONs$,^[4] $Sr_2Si_5N_8:Eu^{2+}$,^[5-7] $Eu_2Si_5N_8$ ^[8,9]) are known to exhibit interesting physical^[10,11] and luminescence properties.^[12-16] During the last ten years, Eu^{2+} -doped nitrido- and oxonitridosilicates emerged as promising materials applicable for phosphor-converted light-emitting diodes (pc-LEDs) owing to their high chemical and physical stability, their extraordinary quantum efficiency of the luminescence process (up to $\approx 95\%$), and their very low thermal quenching. Namely $M_2Si_5N_8:Eu^{2+}$ ^[6,7,12,17-19] and $MSi_2O_2N_2:Eu^{2+}$ (M=alkaline earth metal)^[20-24] are excellent examples for highly effective red-orange (2-5-8) and yellow-green (1-2-2-2) phosphors, respectively.^[25] Thereby, the first warm white all-nitride pc-LED has been realized, exhibiting unprecedented color quality and stability with temperature and drive.^[12] Another important red phosphor is the nitridoaluminosilicate $CaAlSiN_3:Eu^{2+}$ ^[26,27] and its derivatives. As the quest for higher energy efficiency represents one of the most fundamental and exigent challenges to be solved by modern science and technology, it becomes apparent that the search for novel and ecologically acceptable energy sources is indispensable. Addressing this challenge, LEDs become more and more important due to their ongoing improved efficiency, their remarkable durability as well as their environmentally friendly production process and waste disposal. Nowadays AlGaInP-based LEDs are accessible emitting in the red to yellow range of the spectrum. It was not before the pioneering work of Nakamura in the 1990s that the technological access to efficient blue LEDs was provided.^[28,29] Further band-gap engineering has made AlGaInN-based LEDs

accessible emitting in the UV to green range of the spectrum. The concept of down conversion of blue light from InGaN LEDs by suitable color converters (i.e., phosphors) is appropriate for efficient lighting^[30] and provides monochrome light of high color purity, especially in the wavelength range in which direct emitting LEDs are relatively inefficient ("yellow gap"). The spectral position of the emission of these down-conversion phosphors doped with rare-earth ions (e.g. Ce^{3+} or Eu^{2+}) depends very much on the ligand field of the rare-earth ions in the host lattice, with stronger covalent interactions driving the emission into the red region of the spectrum (nephelauxetic effect).

The new green-emitting phosphor $Ba_3Si_6O_{12}N_2:Eu^{2+}$ has been discovered recently,^[31,32] and its luminescence properties emerged to be promising^[31,32] due to a small Stokes shift and a narrow emission band. However, no detailed crystallographic description based on single-crystal structure determination has been reported for $Ba_3Si_6O_{12}N_2:Eu^{2+}$ nor for the related solid solutions with Sr as yet.

As phosphor materials may show phase transitions at elevated temperatures and/or pressures, in-situ investigations of these solids can decisively contribute to a better understanding and optimization of their manufacturing process. In addition, from a more fundamental point of view, new modifications with different luminescence properties (e.g., due to higher symmetry or a lower number of cation sites) may be revealed by applying non-ambient reaction conditions. These aspects are addressed in this work by a systematic investigation of the high-pressure and high-temperature behavior of $Ba_3Si_6O_{12}N_2:Eu^{2+}$.

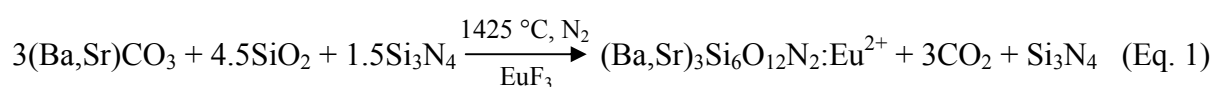
Furthermore, important material properties (e.g., conductivity, optical absorption, chemical bonding, energy gap) are determined by the electronic structure. For example, the band gap of efficient phosphors must be large enough to avoid the lowest Eu d states being too close to the conduction band, which can result in thermal ionization of the photoexcited 5d-electron of Eu^{2+} . Therefore, the local partial density of states (LPDOS) of $Ba_3Si_6O_{12}N_2:Eu^{2+}$ has been probed by soft X-ray spectroscopy (SXS) utilizing synchrotron radiation, namely by X-ray absorption near edge spectroscopy (XANES) and X-ray emission spectroscopy (XES), and is compared to our theoretical calculations within the density functional theory (DFT) framework.

2.5.2 Results and Discussion

2.5.2.1 Synthesis

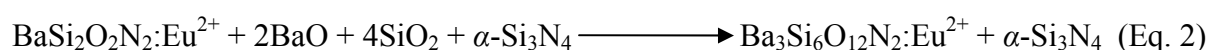
Two different methods for sample synthesis have been applied:

1) Mixtures of MCO_3 (M=Ba,Sr), SiO_2 and an excess of $\alpha-Si_3N_4$ were heated in a radio-frequency (RF) furnace^[33] at maximum temperatures of 1425 °C under nitrogen atmosphere according to the reaction below (equation 1).



During synthesis EuF_3 was used as a dopant. The reaction product was inhomogeneous, but contained single-crystals of $(Ba,Sr)_3Si_6O_{12}N_2:Eu^{2+}$, suitable for X-ray structure analysis.

2) A more homogeneous bulk product of highly crystalline material (in this case without europium) was obtained from $BaSi_2O_2N_2$ ^[23] (synthesis with small impurities of different Ba oxosilicates and $\alpha-Si_3N_4$ according to reference [23]) by high-pressure/high-temperature (HP/HT) synthesis employing the multianvil press technique^[34-36] at a pressure of 14 GPa and 1200 °C according to the reaction below (equation 2).



The atomic ratio M:Si:O:N = 3:6:12:2 of $Ba_3Si_6O_{12}N_2$ was confirmed by EDX measurements (see Experimental Section). However, samples obtained by high-pressure synthesis did not contain single-crystals suitable for X-ray diffraction analysis.

2.5.2.2 Structure Determination

The crystal structure of $Ba_3Si_6O_{12}N_2:Eu^{2+}$ and its solid-solution series $Ba_{3-x}Sr_xSi_6O_{12}N_2$ (with $x \approx 0.4$ and 1) was solved by direct methods^[37] and refined^[38] in space group $P\bar{3}$ (no. 147) by using anisotropic displacement parameters for all atoms. The atomic parameters for Ba and Sr occupying the same site in the solid solution were constrained to be equal. However, the site

occupancies were refined and the presence of Eu^{2+} in the structure (2 mol%) was neglected in these refinements. The details of the single-crystal structure refinement are listed in Table 1.

Table 1. Crystallographic data for $Ba_3Si_6O_{12}N_2$, $Ba_{2.56}Sr_{0.44}Si_6O_{12}N_2$ and $Ba_2SrSi_6O_{12}N_2$.^[a]

Formula	$Ba_3Si_6O_{12}N_2$	$Ba_{2.56}Sr_{0.44}Si_6O_{12}N_2$	$Ba_2SrSi_6O_{12}N_2$
M_r [$g\text{mol}^{-1}$]	800.58	778.70	750.86
Crystal system	trigonal	trigonal	trigonal
Space group	$P\bar{3}$ (no. 147)	$P\bar{3}$ (no. 147)	$P\bar{3}$ (no. 147)
a [\AA]	7.5218(1)	7.4830(6)	7.4624(2)
c [\AA]	6.4684(1)	6.4513(5)	6.4234(2)
V [\AA^3]	316.935(8)	312.84(4)	309.78(9)
Z	1	1	1
ρ_{calcd} [$g\text{cm}^{-3}$]	4.195	4.133	4.025
μ [mm^{-1}]	9.857	10.474	11.230
F(000)	362	355	344
Crystal size [mm^3]	0.07 x 0.05 x 0.03	0.01 x 0.01 x 0.02	0.04 x 0.04 x 0.02
T [K]	293(2)	293(2)	293(2)
2θ range [$^\circ$]	6.28 – 60.78	6.28 – 54.80	6.30 – 67.52
Total reflns	3294	1423	4591
Independent reflns	625	479	838
Observed reflns	482	338	757
Parameters	36	38	38
GOF	0.921	0.919	1.072
R -values [$I > 2\sigma(I)$]	$R1 = 0.0256$ $wR2 = 0.0479$	$R1 = 0.0389$ $wR2 = 0.0609$	$R1 = 0.0165$ $wR2 = 0.0327$
R -values (all data)	$R1 = 0.0406$ $wR2 = 0.0506$	$R1 = 0.0764$ $wR2 = 0.0718$	$R1 = 0.0210$ $wR2 = 0.0340$
max. / min. residual electron density [$e \text{\AA}^{-3}$]	1.660 / -1.146	1.422 / -1.138	0.678 / -0.558

[a] Lattice parameters for $Ba_3Si_6O_{12}N_2$ were taken from the Rietveld refinement based on powder diffraction data. The refined compositions for the solid-solution series are: $Ba_{2.56(2)}Sr_{0.44(2)}Si_6O_{12}N_2$ and $Ba_{2.01(2)}Sr_{0.99(2)}Si_6O_{12}N_2$.

Occupied Wyckoff sites and refined atomic coordinates from the single-crystal diffraction data are shown in the Supporting Information (Table S1). The interatomic distances and angles are within the typical range, selected data are given in Table 2.

Table 2. Selected bond lengths [in Å] and angles [in °] of $Ba_3Si_6O_{12}N_2$, $Ba_{2.56}Sr_{0.44}Si_6O_{12}N_2$ and $Ba_2SrSi_6O_{12}N_2$ derived from single-crystal data (standard deviations in parentheses).

	$Ba_3Si_6O_{12}N_2$	$Ba_{2.56}Sr_{0.44}Si_6O_{12}N_2$	$Ba_2SrSi_6O_{12}N_2$
Ba1-O2 (6x)	2.744(3)	2.687(5)	2.660(2)
Ba2-O2 (3x)	2.819(3)	2.815(5)	2.819(2)
Ba2-O2 (3x)	2.902(3)	2.902(6)	2.884(2)
Ba2-N1 (2x)	2.997(6) / 3.471(6)	3.02(2) / 3.44 (2)	3.017(3) / 3.407(3)
Si1-O2 (1x)	1.587(3)	1.582(6)	1.586(2)
Si1-O1 (2x)	1.649(3) / 1.650(4)	1.635(5) / 1.651(6)	1.644(2) / 1.647(2)
Si1-N1 (1x)	1.735(2)	1.737(3)	1.7311(6)
O2-O1-O1	134.6(5)	133.9(3)	133.2(8)
O2-N1-O2	86.3(4)	87.0(2)	87.7(5)
O1-N1-O1	160.1(5)	158.8(2)	158.0(5)

The refined crystal structure of $Ba_3Si_6O_{12}N_2$ solved by single-crystal diffraction was confirmed by X-ray powder diffraction on a sample obtained from HP/HT synthesis. Crystallographic data and details of the Rietveld refinement^[39] are listed in Table 3 and in the Experimental section.

Table 3. Crystallographic data of $Ba_3Si_6O_{12}N_2$ derived from Rietveld refinement.

Formula	$Ba_3Si_6O_{12}N_2$
M_r [g mol ⁻¹]	780.54
Crystal system	trigonal
Space group	$P\bar{3}$ (no.147)
a [Å]	7.5218(1)
c [Å]	6.4684(1)
V Å ³	316.935(8)
Z	1
T [K]	293
Data range , step width	$5^\circ \leq 2\theta \leq 60^\circ$, 0.01°
Background treatment	18 fixed background points
Profile function	pseudo-Voigt (no. 7)
R_{Bragg}	1.56
GoF	1.6
Reduced χ^2	2.66

The observed and calculated X-ray powder diffraction patterns as well as their difference curve after Rietveld refinement are shown in Figure 1.

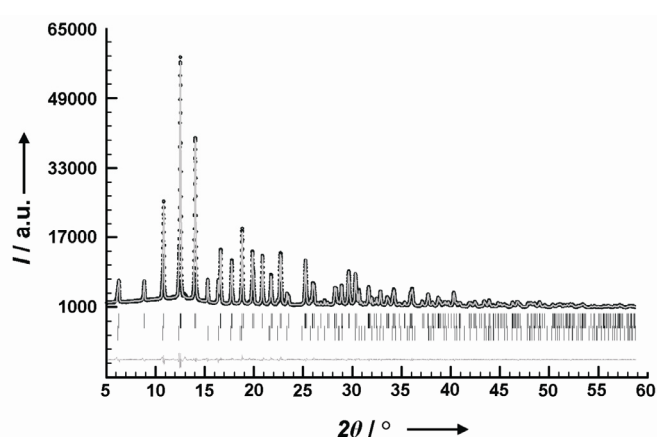


Figure 1. Observed (circles) and calculated (line) X-ray powder diffraction pattern together with their difference curve after Rietveld refinement ($\lambda = 0.709026 \text{ \AA}$). The upper row of reflection marks corresponds to $Ba_3Si_6O_{12}N_2$ and the lower one to $\beta\text{-Si}_3N_4$ (25% w/w).

2.5.2.3 Structure Description

A detailed insight into the crystal structure of $Ba_3Si_6O_{12}N_2$ is required to understand its luminescent properties. Here a comprehensive crystallographic structure description is presented, which is based on the structure refinements described above. The structural parameters given by Mikami et al. are basically correct.^[31,32]

The structure of $Ba_3Si_6O_{12}N_2$ consists of layers of vertex-sharing SiO_3N tetrahedra of Q^3 -type, building 6er- and 4er-rings as fundamental building units (FBU),^[40] which leads to a degree of condensation of $\kappa = n(\text{Si}) : n(\text{O},\text{N}) = 0.43$ for the $[Si_6O_{12}N_2]^{6-}$ substructure.

According to Pauling's rule^[41] and $\{uB, 3, 1_{\infty 2}\} [(Si_6^{[4]}O_6^{[1]}O_6^{[2]}N_{4/2}^{[3]})_6]^{6-}$ ^[42,43] the O atoms bridge two Si-atoms ($O^{[2]}$) or are terminally bound ($O^{[1]}$), respectively, whereas the N atoms connect three silicon tetrahedral centers ($N^{[3]}$; see Figure 2; numbers in superscripted square brackets beside atoms indicate the coordination number of the atom in question).

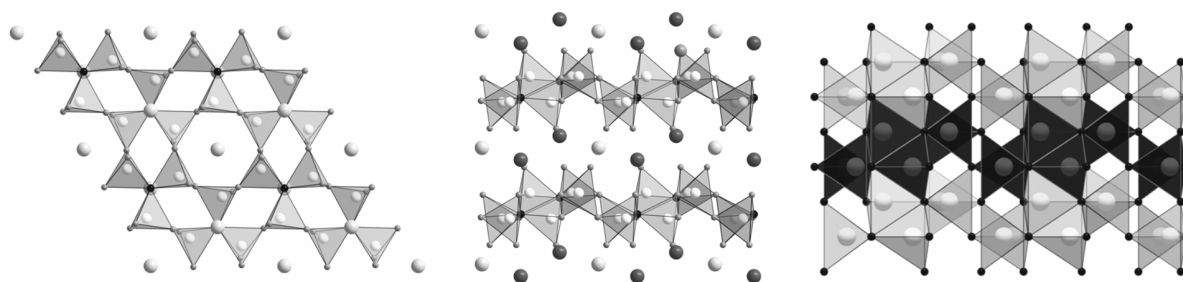


Figure 2. Comparison of $Ba_3Si_6O_{12}N_2$ and $\beta\text{-Si}_3N_4$: $Ba_3Si_6O_{12}N_2$ view along $[001]$ (left), view along $[010]$ (middle), and $\beta\text{-Si}_3N_4$ for comparison (right, view along $[010]$), removing every second Si-atom layer (black) and substituting the emerging terminal N-atoms by O-atoms results in layers, topologically similar to those in $Ba_3Si_6O_{12}N_2$ (Si atoms white, N black, Ba1 light gray, Ba2 dark gray and O gray).

According to lattice energy calculations (Madelung part of lattice energy, MAPLE)^[44-46] there is a clear assignment of N/O.^[32,41] As expected the MAPLE of $Ba_3Si_6O_{12}N_2$ is almost identical with the sum of the respective MAPLE values of the constituting binary components BaO, SiO_2 and $\alpha-Si_3N_4$ (see Table 4).

Table 4. Madelung part of lattice energy (MAPLE) values for $Ba_3Si_6O_{12}N_2$ (values given in kJ mol^{-1}).^[a]

	$Ba_3Si_6O_{12}N_2$	BaO	SiO_2	$\alpha-Si_3N_4$
MAPLE	105684.75	3527.40	15347.60	53017.53
atom ^[a]	Ba1 ²⁺	Ba2 ²⁺	Si ⁴⁺	(O1 ^[2]) ²⁻ (O2 ^[1]) ²⁻ (N ^[3]) ³⁻
MAPLE	1916.15	1890.63	9254.26	2987.00 2303.67 6358.86
total MAPLE ($Ba_3Si_6O_{12}N_2$) exptl.				105684.75
total MAPLE (3x BaO + 4.5x SiO_2 + 0.5x $\alpha-Si_3N_4$)				106155.17
difference Δ / %				0.44

[a] Typical partial MAPLE values [kJ mol^{-1}]: Ba²⁺:1500-2000, Sr²⁺:1500-2000, Si⁴⁺:9000-10200, (O^[2])²⁻:2400-2900, (O^[1])²⁻:2050-2800, N^[3]:5200-6300.^[72]

The two crystallographically independent Ba²⁺ ions occupy the Wyckoff sites 1a and 2d. They are situated between the silicate layers and are six- or sevenfold coordinated by (O,N) atoms, respectively (see Figure 3).

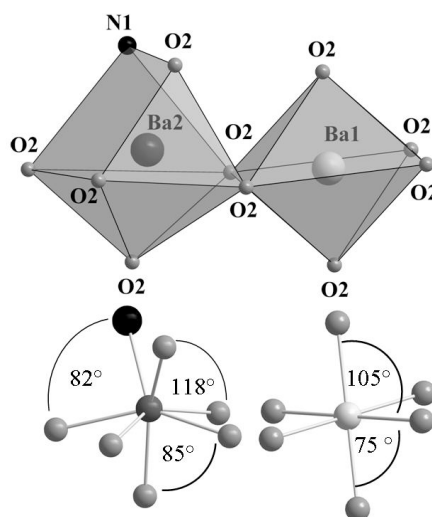


Figure 3. Coordination polyhedra and the corresponding angles of the two different Ba sites in $Ba_3Si_6O_{12}N_2$ (N atoms black, Ba1 light gray, Ba2 dark gray and O gray).

The crystal structure of $Ba_3Si_6O_{12}N_2$, which is isotypic with recently discovered $Sr_3P_6O_6N_8$,^[47] can be derived from the structure of $\beta-Si_3N_4$.^[48] The isosteric Si_6N_{14} layers in $\beta-Si_3N_4$ are linked in the third dimension through SiN_4 tetrahedra. A formal derivation of the structure of $Ba_3Si_6O_{12}N_2/Sr_3P_6O_6N_8$ from $\beta-Si_3N_4$ can be achieved by a separation of the Si_6N_{14} layers in $\beta-Si_3N_4$ and intercalating Ba²⁺ ions (see Figure 2). Similar layered

arrangements of Si/O/N-tetrahedra with different degrees of condensation can be found in other Ba oxonitridosilicates as well, namely $Ba_3Si_6O_9N_4$ ^[49] and $BaSi_2O_2N_2$.^[23]

While in $BaSi_2O_2N_2$ only 3er-rings can be found, $Ba_3Si_6O_9N_4$ ^[49] exhibits a structure related to $Ba_3Si_6O_{12}N_2$, which however contains different 6er-rings and additional 3er-rings.^[50]

The bond lengths Si-O/N in $Ba_3Si_6O_{12}N_2$ are in the typical range with 1.59 - 1.73 Å ($Ba_3Si_6O_9N_4$: Si-O/N = 1.60 - 1.75 Å,^[49] $BaSi_2O_2N_2$: Si-O/N = 1.66 - 1.73 Å).^[23] The distances Si-O^[1] and Si-O^[2] range between 1.59 Å for O^[1] and 1.61 - 1.71 Å for O^[2] and are therefore comparable with related Ba oxonitridosilicates (e.g. $Ba_3Si_6O_9N_4$: Si-O^[1]: 1.60 Å, Si-O^[2]: 1.65 Å,^[49] $BaSi_2O_2N_2$: Si-O^[1]: 1.66 Å).^[23] Within the tetrahedra, the Si-N^[3] distance is, as expected, the longest one with 1.73 Å ($Ba_3Si_6O_9N_4$: Si-N^[3] = 1.73 - 1.75 Å,^[49] $BaSi_2O_2N_2$: Si-N^[3] 1.72 - 1.73 Å).^[23] The (O,N)-Si-(O,N) angles range from 103 - 116° and correspond well with other Ba oxonitridosilicates ($Ba_3Si_6O_9N_4$: 103 - 114°,^[49] $BaSi_2O_2N_2$: 99 - 118°).^[23] Compared to other Ba oxonitridosilicates the Si-N^[3]-Si angle in $Ba_3Si_6O_{12}N_2$ (118°) is in the same range as in $Ba_3Si_6O_9N_4$ (118 - 120°)^[49] and $BaSi_2O_2N_2$ (116 - 121°).^[23] Cation coordination polyhedra in $Ba_3Si_6O_9N_4$ and $Ba_3Si_6O_{12}N_2$ are very similar as well.

In $Ba_3Si_6O_{12}N_2$ the oxygen atoms in the coordination sphere of Ba1 form a trigonal antiprism, which can be described as well as a distorted octahedron with six equal distances (Ba1^[6]-O = 2.74 Å), but some angles (see Figure 3) deviating from 90° ($Ba_3Si_6O_9N_4$: Ba1^[6]-O = 2.69 - 2.82 Å).^[49] The coordination polyhedron around Ba2 can be described for $Ba_3Si_6O_{12}N_2$ as well as for $Ba_3Si_6O_9N_4$ as a capped distorted octahedron ($Ba_3Si_6O_{12}N_2$: Ba2^[7]-O/N = 2.82 - 3.00 Å, $Ba_3Si_6O_9N_4$: Ba2^[7]-O/N = 2.70 - 3.16 Å).^[49]

In contrast to $Ba_3Si_6O_9N_4$, $Ba_3Si_6O_{12}N_2$ features excellent luminescence properties. Mikami^[32] has suggested that this may be due to the longer Ba-N distances and a lower energy host absorption band of $Ba_3Si_6O_9N_4$ in comparison to $Ba_3Si_6O_{12}N_2$.

2.5.2.4 Solid-Solution Series of $Ba_{3-x}Sr_xSi_6O_{12}N_2:Eu^{2+}$

The influence of the Ba²⁺ substitution by Sr²⁺ in the solid-solution series $Ba_{3-x}Sr_xSi_6O_{12}N_2:Eu^{2+}$ (with $x \approx 0.4$ and 1) has been studied. In $Ba_{3-x}Sr_xSi_6O_{12}N_2:Eu^{2+}$ a substitution of Ba²⁺ by smaller Sr²⁺ mainly affects the Ba1 site (see Figure 3) which might be due to the smaller coordination number of this site. The substitution of Ba²⁺ by Sr²⁺ significantly influences the bond length Ba1/Sr1-O2, which decreases with increasing amount of Sr²⁺ ($Ba_3Si_6O_{12}N_2$: 2.74 Å, $(Ba_2Sr)Si_6O_{12}N_2$: 2.66 Å) as the silicate layers approach along

[001] upon substitution. Thereby, the curvature of the corrugated layers increases as well, especially around the Ba1/Sr1-sites. Table 2 shows the interatomic distances of selected atoms for $Ba_3Si_6O_{12}N_2$, $Ba_{2.56}Sr_{0.44}Si_6O_{12}N_2$ and $Ba_2SrSi_6O_{12}N_2$, respectively.

2.5.2.5 High-Pressure and High-Temperature Behavior

In-situ high-pressure and high-temperature studies of luminescent materials were shown to be useful in optimizing the manufacturing process of several (oxo-)nitridosilicate phosphors. Therefore, ex-situ and in-situ investigations of $Ba_3Si_6O_{12}N_2$ have been performed from 0.15 to 18 GPa and temperatures ranging from 100 to 1500 °C in order to evaluate the stability. This should be representative for the Ba/Sr solid-solution series as well. Ex-situ investigations at ambient conditions on HP/HT treated samples in the range from 9 to 18 GPa and at temperatures from 800 to 1200 °C using a Walker-type multianvil press were carried out. Formation of small amounts of β - Si_3N_4 besides $Ba_3Si_6O_{12}N_2$ indicate that $Ba_3Si_6O_{12}N_2$ might not be stable above 14 GPa. In-situ high-pressure X-ray diffraction investigations at the synchrotron (MAX80, Beamline F2.1 Desy/HASYLAB Hamburg) confirmed the instability of $Ba_3Si_6O_{12}N_2$ and elucidated the underlying mechanism. Above 0.15 GPa decomposition into the related Ba oxonitridosilicate $BaSi_4O_6N_2$ ^[51] was identified already at room temperature. This suggests that the formation of at least one amorphous phase is likely, since no other crystalline phase could be observed, particularly no Si_3N_4 . The quantity of crystalline $BaSi_4O_6N_2$ increased in comparison to the remaining $Ba_3Si_6O_{12}N_2$ as the pressure was increased. At 9 GPa the sample showed distinct signs of amorphization, which are reversible after pressure release. Again at ambient pressure the powder pattern indicates mainly $Ba_3Si_6O_{12}N_2$, however slight traces of $BaSi_4O_6N_2$ still could be detected. Therefore, the pressure-induced transformation from $Ba_3Si_6O_{12}N_2$ into $BaSi_4O_6N_2$ is mostly reversible. The same transformation is also observed at elevated temperatures (\approx 0.15 GPa) and the relative amount of $BaSi_4O_6N_2$ increases from 100 to 1500 °C successively. Furthermore, above 1200 °C two other decomposition products emerge: $BaSi_2O_2N_2$ ^[23] and β - Si_3N_4 .^[48]

The temperature- and pressure-induced transformations of $Ba_3Si_6O_{12}N_2$, as observed under in-situ conditions, mainly agree with the final products detected ex-situ after HP/HT treatment. The formation of β - Si_3N_4 results from excursion to high temperatures above about 1200 °C (or at high pressures already at lower temperatures), either as a result of the instability of

$Ba_3Si_6O_{12}N_2$ or from crystallization of initially amorphous and therefore in XRD not detectable Si_3N_4 .

2.5.2.6 Luminescence

Samples of $Ba_3Si_6O_{12}N_2$ were doped with 2 mol% Eu^{2+} in order to study photoluminescence. $Ba_3Si_6O_{12}N_2:Eu^{2+}$ exhibits an intense green body color due to $4f^7(^8S_{7/2}) \rightarrow 4f^65d$ absorption of Eu^{2+} in the blue to green spectral range. Under near-UV to blue light irradiation a saturated green emission band with a peak wavelength of ≈ 527 nm is observed (full width at half maximum (FWHM) ≈ 65 nm). The broad excitation band enables efficient excitation at wavelengths below 450 nm.

The excitation (PLE) and emission (PE) spectra of several samples of $Ba_{3-x}Sr_xSi_6O_{12}N_2:Eu^{2+}$ are shown in Figure 4 and Figure 5.

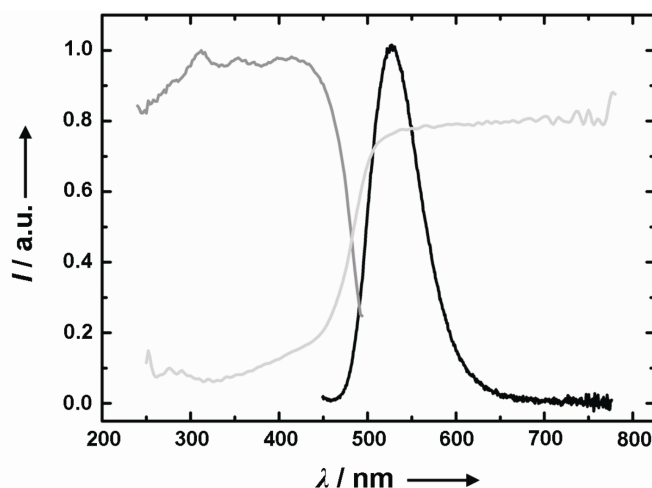


Figure 4. Excitation (gray), reflectance (light gray) and emission (black) spectra of $Ba_3Si_6O_{12}N_2:Eu^{2+}$ (2 mol% Eu^{2+}).

For $x = 0$ the broad emission band almost matches the spectrum of Eu^{2+} activated $BaSrSiO_4:Eu^{2+}$ phosphors^[52] and resembles typical Eu^{2+} spectra observed for other oxonitridosilicate compounds (e.g., $MSi_2O_2N_2:Eu^{2+}$).^[53] For 11 % Sr the emission spectrum nearly coincides with that of $SrSi_2O_2N_2:Eu^{2+}$. The spectral half-width of 2310 cm^{-1} (0 % Sr) lies between the values observed for $BaSi_2O_2N_2:Eu^{2+}$ (1340 cm^{-1}) and $SrSi_2O_2N_2:Eu^{2+}$ (2423 cm^{-1}).^[53] The former exhibits an exceptionally small FWHM value that corresponds to direct emitting cyan-green LEDs and can be attributed to the presence of only one very symmetrical crystallographic M^{2+} site as well as a small Stokes shift.

$Ba_3Si_6O_{12}N_2:Eu^{2+}$ has a Stokes shift of $\approx 2600\text{ cm}^{-1}$ which is higher than the values for $BaSi_2O_2N_2:Eu^{2+}$ (1030 cm^{-1}), but significantly lower than the Stokes shift of $SrSi_2O_2N_2:Eu^{2+}$ (4740 cm^{-1}).^[53] Partial substitution of Ba by Sr causes a noticeable red-shift and broadening of the emission band (see Table 5).

Table 5. Peak emission wavelength and spectral half-width of $Ba_{3-x}Sr_xSi_6O_{12}N_2$, depending on the partial substitution of Ba by Sr. (Eu^{2+} content 2%)

Sr concentration [%]	λ_{\max} [nm]	FWHM [cm^{-1}]
0	523	2310
11	532	2360
34	549	2510

As expected, the unit cell contracts with increasing amounts of Sr^{2+} (see crystallographic data, Table 1). Typically, such a unit-cell contraction involves decreasing interatomic distances between Eu^{2+} and its ligands and thus results in a larger crystal field strength at the activator site, leading to a red-shift of the emission band.

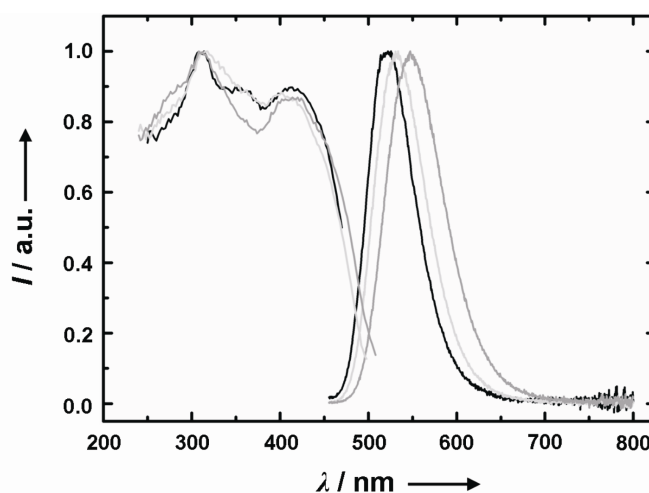


Figure 5. Excitation (PLE) and emission (PE) spectra of $Ba_{3-x}Sr_xSi_6O_{12}N_2:Eu^{2+}$ (several samples) with varying Sr contents. Excitation and emission spectra with 0 % Sr are depicted in black, with 11 % Sr in light gray, with 34 % Sr in dark gray.

Another factor that may affect the spectral shift and half-width is the presence of two different crystallographic sites, Ba1 and Ba2, which exhibit slightly different coordination (see Figure 3) and interatomic distances (see Table 2).

Due to their smaller but very similar ionic radii, Sr^{2+} as well as Eu^{2+} (compared to Ba^{2+}) should both preferentially occupy the distorted octahedral Ba1-site. Unless more than 1/3 of Ba is substituted by Sr and Eu, Eu^{2+} can always compete with the larger Ba^{2+} for the smaller Ba1-site. The spectral shift in the Ba/Sr-mixed compound is mainly caused by a unit-cell

contraction. The increase in spectral width at higher Sr concentration can be attributed to an increasing Stokes shift. However, Mikami et al. suggested emission from Eu^{2+} primarily occupying the Ba2 site.^[32]

2.5.2.7 Band Structure and Density of States

The band structure calculations (Figure 6) indicate that the material has an indirect band gap of 4.80 eV (using GGA), which is in good agreement with the previously reported value of 4.63 eV^[32] using GGA.

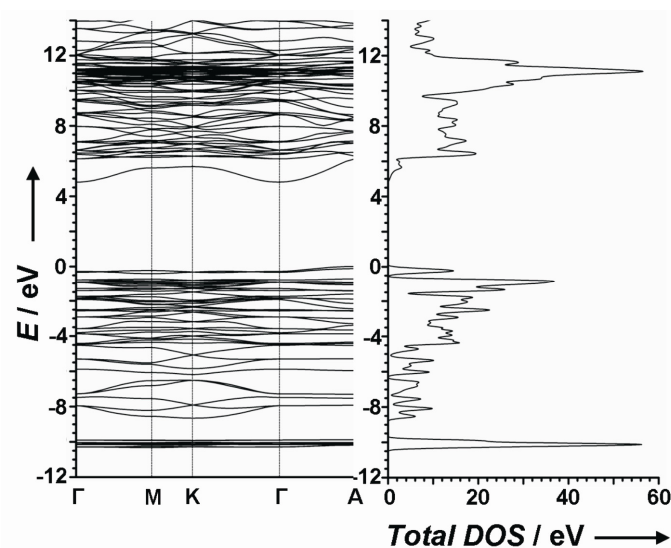


Figure 6. The total density of states (right, measured in states/eV-unit cell) and the band structure (left) of $Ba_3Si_6O_{12}N_2:Eu^{2+}$ show the calculated direct (5.08 eV) and indirect (4.80 eV, A- Γ) band gap values. The density of states (DOS) is broadened by a Gaussian function with a FWHM of 0.1 eV to aid in visual analysis.

The band gap calculated using a modified Becke-Johnson potential with GGA (mBJ-GGA)^[54] is 6.93 eV and accounts for the typical underestimation of the band gap. The modified potential is a semi-local exchange potential that allows for the correct calculation of the band gap in insulators and semiconductors. This potential is ab initio and requires no further input during the calculation. The total density of states (DOS) and partial DOS is derived from integrating momentum space and is shown for all atomic sites in Figure 6 and 7, respectively.

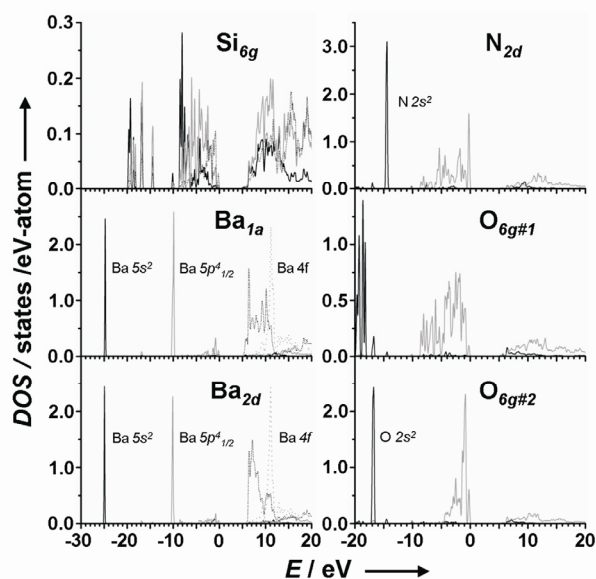


Figure 7. The Density of States (DOS) is split into atomic site and electron symmetry contributions. The panels are labelled according to their Wyckoff site, furthermore the $O_{6g\#1}$ site refers to the site that forms bridging bonds to silicon. The s states are displayed black (solid), p states gray (solid), d states black (dotted) and f states gray (dotted). The DOS were broadened with a constant Gaussian of 0.1 eV FWHM and displayed in energy scale such that 0 eV corresponds to top of the valence band (i.e., the filled states). The large intensity peaks have been scaled; the Ba_{1a} 5s states (reduced by 80%), 5p_{1/2} states (reduced by 80%), 4f states (reduced by 80%), and the Ba_{2d} 5s states (reduced by 85%), 5p_{1/2} states (reduced by 88%), 4f states (reduced by 80%).

The DOS shows that $Ba_3Si_6O_{12}N_2$ exhibits a mixture of ionic bonding and weak covalent contributions. The Ba 5s electrons are highly localized and exhibit orbital-like behavior with no bonding. There is no indication of any Ba 6s states, thus the respective electrons of Ba are fully transferred to the N and O anion sites. The Ba 5p states are split by total angular momentum; the $j=1/2$ are highly localized and non-bonding, while the $j=3/2$ participate largely in the valence band (VB) covalent bonds with a small degree of participation in the conduction band (CB). The Ba 4f states play a key role in the formation of the CB, exhibiting a large peak (localized concentration of states) buried 5 eV into the CB. The CB states that are situated below 10 eV are primarily unfilled Ba 5d states. The Si s,p,d states show a large degree of hybridization with the O and N sites in conjunction with a large amount of charge transfer to the anion sites. The N and O sites suggest weak covalent bonds to the Si atoms; the N_{2d} and $O_{6g\#2}$ 2s states are highly localized with little or no bonding, but the N and O p states have a large degree of hybridization. The $O_{6g\#1}$ 2s states, however, show an affinity to form covalent bonds with Si, extending further to the $O_{6g\#1}$ 2p band as well. The N and O 2p states make of the majority of the VB with modest contribution to the CB.

2.5.2.8 Band-Gap Determination Using Soft X-ray Spectra

The participation of the N and O p states in both the VB and CB makes studying the K-edge spectra of these elements an excellent probe for the electronic structure properties in general and the band gap in particular. We will first focus on the oxygen spectra.

Figure 8 shows the O K-edge soft X-ray spectroscopy measurements; this includes the O K α X-ray emission spectra (XES) and O 1s X-ray absorption near edge spectra (XANES). There are three distinct features labelled d-g (see Figure 8) in the $Ba_3Si_6O_{12}N_2:Eu^{2+}$ O 1s XANES spectrum.

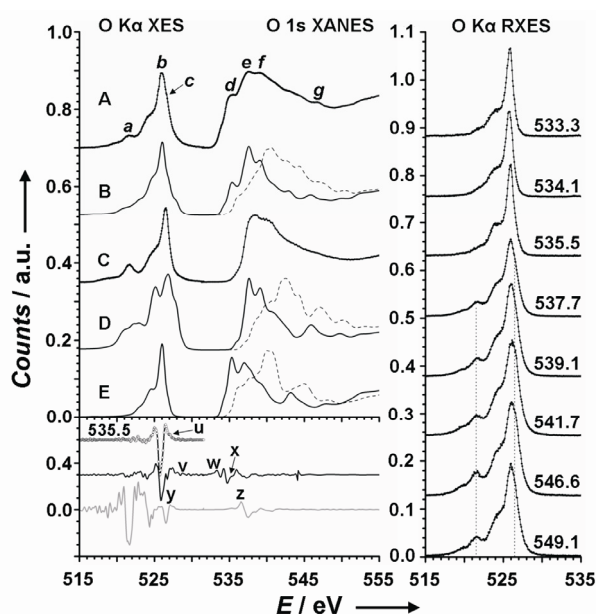


Figure 8. Non-resonant O K α XES and O 1s XANES (left), and resonant O K α XES (right) of A) measured $Ba_3Si_6O_{12}N_2:Eu^{2+}$, B) total calculated $Ba_3Si_6O_{12}N_2:Eu^{2+}$, C) measured SiO_2 , D) calculated $O_{6g\#1}$ site, and E) calculated $O_{6g\#2}$ site are shown. The main features in the O K α XES and O 1s XANES spectra for $Ba_3Si_6O_{12}N_2:Eu^{2+}$ are marked a-g. The right panel shows the resonant excitation energy of O K α XES with the excitation energy indicated above each spectrum. The dashed lines indicate the contribution from SiO_2 . The effect of the core hole is demonstrated with the simulated XANES spectra without the inclusion of the core hole, this is displayed as the dashed line plot in the left panel. The second derivatives of the experimental spectra are displayed in the lower left panel. The valence band (E_v) and conduction band (E_c) edges are indicated on the scatter line (the resonant XES spectra with the excitation energy indicated above, $u = O_{6g\#2}:E_v$), the solid black line (the experimental $Ba_3Si_6O_{12}N_2:Eu^{2+}$ spectra, $v = O_{6g\#1}:E_v$, $w = O_{6g\#1}:E_c$, $x = O_{6g\#1}:E_c$) and the gray line plots (the experiment SiO_2 spectra, $y = SiO_2:E_v$, $z = SiO_2:E_c$).

The calculated O 1s XANES spectrum reproduces all the marked features and the general shape of the experimental spectrum very well. The true XANES spectrum consists of a summation of two spectra from the two non-equivalent O sites. These O 1s binding energies differ by 1.92 eV, owing to the different local symmetry (bridging bonds and tetrahedral bonds), which was determined with density functional theory (DFT) calculations. However, the energy separation seen in the measured XANES spectra is 1.76 eV, owing to the effect of

an O 1s core hole. There is a small disagreement between the calculated and measured spectrum, mainly feature f (see Figure 8) is more intense in the measured spectrum than in the calculated spectrum. The added intensity is due to a third contributing spectrum, which is most likely from SiO₂ contamination. One of the starting materials for synthesis of Ba₃Si₆O₁₂N₂:Eu²⁺ is α-Si₃N₄, and there are significant amounts left after synthesis. Also, this material forms a surface SiO₂ layer under atmosphere readily, which will provide a spectral contribution to the O 1s XANES spectrum. This contamination and the two non-equivalent O sites were explored further with resonant XES. In the O Kα XES spectrum of Ba₃Si₆O₁₂N₂:Eu²⁺ three spectral features can be found. Feature c (see Figure 8) is very subtle and is a high-energy shoulder that has been increased in intensity due to SiO₂ contamination. The low energy peak a (see Figure 8) not seen in the simulated spectrum is also due to SiO₂. The two non-equivalent O sites are shifted by the difference in the 1s binding energy mentioned above (and not corrected for core hole effect since it is not present in the XES final state). In these spectra the excitation energy is tuned to resonant features of the XANES spectra. This allows the excitation of specific atomic sites within the lattice. Feature a in the O Kα resonant XES increases in intensity with excitation energies of 555.1 to 541.7 eV. The 541.7 eV excitation corresponds to the maximum absorption cross section in SiO₂, which is why the SiO₂ feature is the most intense. Feature c (see Figure 8) also increases in intensity, which is due to SiO₂ and confirms that SiO₂ is present on the surface. Tuning the excitation to even lower energy reduces the contributions of these peaks.

At an excitation energy of 535.5 eV, the emission spectrum changes drastically showing no signs of the O_{6g#1} site or the features of the SiO₂ contamination. The emission stems now purely from the O_{6g#2} p states and matches the calculated spectrum perfectly.

The lower energy resonant XES spectra are the same except that there are contributions from the other O atoms in the material; these are more apparent since the absorption cross sections of all the O atom sites are very low. These results suggest that the calculated spectrum for XES and XANES are correct if we properly consider the SiO₂ contamination.

The use of XES and XANES spectra to determine the top of the valence and bottom of the conduction band is not trivial due to the inherent experimental broadening mechanisms, difficulties in energy calibration and the effect of the core hole on the absorption spectra. The energy positions of the conduction and valence band edges are determined by taking the second derivative of the experimental spectra (see Figure 8) and the first peak (above the level of noise) in the second derivative is used as the edge location.^[55] The comparison of the SiO₂ second derivative to the non-resonant Ba₃Si₆O₁₂N₂: Eu²⁺ shows that the SiO₂ valence band

edge is located somewhere between the two edges of the oxygen non-equivalent sites. The conduction band edge of SiO_2 is much higher in energy than $Ba_3Si_6O_{12}N_2:Eu^{2+}$ (this is due to the very large band gap) and should present no problem for determining the bottom of the conduction band of $Ba_3Si_6O_{12}N_2:Eu^{2+}$ with O 1s XANES. The top of the valence band, however, can be more accurately determined by using resonant XES. Since the valence band edge of the $O_{6g\#1}$ site is very close to SiO_2 , we determined the edge of the $O_{6g\#2}$ site. The O $K\alpha$ XES spectrum with excitation energy of 535.5 eV is used to determine the $O_{6g\#2}$ site valence band edge; this was shown earlier to resemble the calculated spectrum best for that site. The edge locations of the $O_{6g\#1}$ are determined from the site splitting that is calculated, which makes the band gaps identical. The determined band gap for this site is 7.10 ± 0.20 eV and the corresponding VB and CB edge values are listed in Table 6. The details of the band-gap determination are further discussed in the experimental section.

Table 6. Band-gap determination using data from XES and XANES spectra in conjunction with DFT results. The sites are labelled according to their Wyckoff sites. The measured valence band and conduction edge locations are presented. The core hole effect has been rounded to the nearest 0.05 eV, and the final value of the band gap is average of the two independent determined values of the O K-edge and N K-edge. The measured band gap is compared to the values using GGA-PBE and mBJ-GGA.

	N_{2d}	$O_{6g\#1}$	$O_{6g\#2}$
Valence band edge [eV]	394.75 ± 0.15	528.85 ± 0.15	526.95 ± 0.15
Conduction band edge [eV]	401.20 ± 0.15	535.10 ± 0.15	533.35 ± 0.15
Core hole shift [eV]	0.25	0.45	0.30
Site band gap [eV]	7.00 ± 0.20	7.10 ± 0.20	7.10 ± 0.20
Average measured band gap [eV]	7.05 ± 0.25		
Calculated band gap (GGA-PBE) [eV]	4.80		
Calculated band gap (mBJ-GGA) [eV]	6.93		

We now turn to the discussion of the nitrogen spectra. The N 1s XANES spectrum of $Ba_3Si_6O_{12}N_2:Eu^{2+}$ exhibits three features k-m (see Figure 9) which are reproduced well in the calculated $Ba_3Si_6O_{12}N_2:Eu^{2+}$ N 1s XANES spectrum.

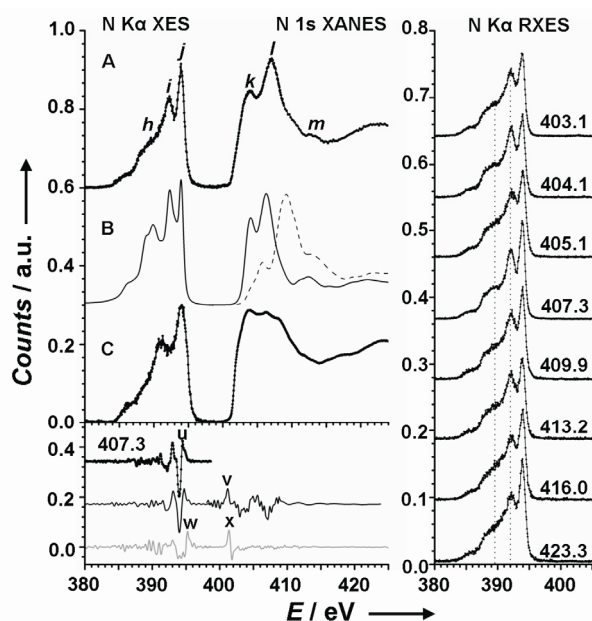


Figure 9. Non-resonant N K α XES and N 1s XANES (left), and resonant N K α XES (right) of A) measured $Ba_3Si_6O_{12}N_2:Eu^{2+}$, B) total calculated $Ba_3Si_6O_{12}N_2:Eu^{2+}$, and C) measured $\alpha-Si_3N_4$ are shown. The main features in the N K α XES and N 1s XANES spectra for $Ba_3Si_6O_{12}N_2:Eu^{2+}$ are denoted h-m. The panel on the right hand side shows the resonant N K α XES with the excitation energy indicated above each spectrum. The dashed lines indicate the peaks that result from the remaining $\alpha-Si_3N_4$. The effect of the core hole is demonstrated with the simulated XANES spectra without the inclusion of the core hole, this is displayed as the dashed line plot. The second derivatives of the experimental spectra are displayed in the lower left panel. The valence band (E_v) and conduction band (E_c) edges are indicated on the scatter line (the resonant XES spectra with the excitation energy indicated above, u = $N_{2d}:E_v$), the solid black line (the experimental $Ba_3Si_6O_{12}N_2:Eu^{2+}$ spectra, v = $N_{2d}:E_c$) and the gray line plots (the experiment $\alpha-Si_3N_4$ spectra, w = $Si_3N_4:E_v$, x = $Si_3N_4:E_c$).

The position of feature l is slightly distorted, because of the presence of $\alpha-Si_3N_4$ (as discussed previously). The addition of this spectrum increases the spacing between the features k and l in the experiment with comparison to the calculated N 1s XANES spectrum. Feature m remains relatively unchanged because the $\alpha-Si_3N_4$ N 1s XANES spectrum is very smooth in this region. The effect of this impurity is readily seen in the N K α XES spectra. The non-resonant N K α XES spectrum displays the features h-j, which are reproduced in the calculated spectrum as well (see Figure 9) There remains still moderate agreement between features i and j in experiment, however feature h (Figure 9) is overestimated in the calculated spectrum. This can be explained with the consideration of $\alpha-Si_3N_4$ contribution to the measured spectrum. Feature h is present in the calculated spectrum and appears not to be present in the measured spectrum. However, this feature is present and has been removed due to the summation of $Ba_3Si_6O_{12}N_2:Eu^{2+}$ and $\beta-Si_3N_4$. Furthermore, it is enhanced with selective excitation as seen in the resonant XES spectra. Many of the resonant N K α XES spectra look very similar except for the two excited at 404.4 and 407.3 eV. In these spectra features h and i are enhanced and provide better agreement with the calculated spectrum. These spectra are the result of exciting on the two resonant features k and l in the N 1s XANES spectrum,

which are attributed to $Ba_3Si_6O_{12}N_2:Eu^{2+}$. This shows that the calculated spectrum is a very reasonable representation of the material with the consideration of $\alpha-Si_3N_4$ that is present in the sample. The band gap has also been determined using the N sites. The DOS results show that 1) both the N and O electron states contribute to the band gap and 2) that the band gaps determined from the N and O site should be identical. The same method used for the oxygen sites and explained above is applied to the nitrogen sites; resonant XES again is used to preferentially excite the nitrogen atoms that are part of the $Ba_3Si_6O_{12}N_2:Eu^{2+}$ matrix. The second derivative of $\alpha-Si_3N_4$ has a valence band edge that is higher in energy than $Ba_3Si_6O_{12}N_2:Eu^{2+}$ and the conduction band edge is higher in energy as well. The band gaps of these materials are predicted to be very similar^[32,56] and the offset in the spectra is due to the differences in the nitrogen-bonding environment (the N 1s binding energy is slightly different). The $\alpha-Si_3N_4$ contribution to the N K α XES spectrum is removed as much as possible through resonant XES to obtain the best determination of the N valence band edge. The excitation energy of 407.3 eV of the resonant XES spectrum is used to determine the valence band edge. The band gap obtained is identical to the one obtained for the O K-edge 7.00 ± 0.2 eV and the corresponding VB and CB edge values are summarized in Table 6. To summarize, the band gap obtained from both oxygen and nitrogen sites is 7.05 ± 0.25 eV. These agree with each other within the experimental precision (± 0.25 eV), and are determined from the experimental spectra with a small correction derived in our calculations to account for the presence of the core hole and non-equivalent sites.

2.5.3 Conclusion

The high color purity, the small thermal quenching^[57] at elevated temperatures, and the intense green color with a broadband emission spectrum peaking at ≈ 527 nm and a FWHM of ≈ 65 nm renders $Ba_3Si_6O_{12}N_2:Eu^{2+}$ a promising phosphor for pc-LED based general illumination and display applications.^[12,31,32,52,58,59]

Especially important for the luminescence properties is the band gap being large enough to avoid the lowest Eu d states being too close to the conduction band and the thermal ionization of the photoexcited 5d electrons of Eu^{2+} .^[32] In the case of $Ba_3Si_6O_9N_4:Eu^{2+}$ this effect becomes very apparent; the narrower band gap and a smaller crystal field splitting provide quite different optical properties compared to $Ba_3Si_6O_{12}N_2:Eu^{2+}$. Although the crystal

structure and chemical formula of $Ba_3Si_6O_9N_4$ ^[49] appear rather similar to the one of $Ba_3Si_6O_{12}N_2$, its luminescence properties render it inapplicable for use in pc-LEDs.

Structural studies at high-pressure and high-temperature reveal a decomposition of $Ba_3Si_6O_{12}N_2$, mainly into $BaSi_4O_6N_2$, and can explain the sintering behavior of this material. The band gap is an important parameter for the luminescent properties. Synchrotron-based soft X-ray emission and absorption spectra were measured and are compared to the respective density functional theory calculations. The calculated band gap from these calculations is 4.80 eV (indirect) using GGA-PBE; however, this method strongly underestimates the band gap. The XES and XANES spectra were calculated and show excellent agreement with the experimental ones when the presence of the core hole is taken into account. The calculations were also used to discuss and determine energy shifts due to the presence of the core hole and site splitting in the two non-equivalent oxygen sites. These considerations allow a reliable experimental determination of the band gap of $Ba_3Si_6O_{12}N_2:Eu^{2+}$, which is found to be 7.05 ± 0.25 eV for both the N and O K-edge measurements. This value agrees with the calculated band gap of 6.93 eV (mBJ-GGA) within experimental error. Furthermore, the valence band is shown to be primarily made up of N and O p states and the conduction band of primarily Ba d and f states, with a small contribution from the N and O p states. The bonding of the Ba atoms is highly ionic with only the $4p_{3/2}$ participating in covalent bonds, which makes this material ideal for cation substitution.

As a consequence of this, our future research will focus on in-situ investigations of material properties to intentionally access new compounds with respect to the specific requirements for efficient phosphors.

Acknowledgements

The authors gratefully acknowledge financial support from the Fonds der Chemischen Industrie and the Deutsche Forschungsgemeinschaft (priority program SPP 1236, project SCHN 377/13), Germany. We further would like to thank Anke Großer (LMU München) for experimental help, Christian Lathe (Geoforschungszentrum Potsdam) for his help at the Beamline F2.1 of the Hamburger Synchrotronstrahlungslabor at the Deutsches Elektronen Synchrotron (DESY) and for the provided beamtime, Christian Minke (LMU München) for the EDX measurements and Thomas Miller and Dr. Peter Mayer (LMU München) for X-ray single-crystal data collection. Furthermore, we gratefully acknowledge the Natural Sciences and Engineering Research Council of Canada (NSERC) and the Canada Research Chair

program for their support in this research. We also thank the Advanced Light Source and Canadian Light Source along with their staff and support for helping us conduct this research.

2.5.4 Experimental Section

2.5.4.1 High-Pressure Synthesis of $Ba_3Si_6O_{12}N_2$ and Ex-Situ High-Pressure Investigations

The high-pressure synthesis of $Ba_3Si_6O_{12}N_2$ was carried out using the multianvil technique^[34-36] with a hydraulic press (Voggenreiter, Mainleus). Cr_2O_3 -doped MgO-octahedra (Ceramic Substrates & Components, Isle of Wight) with an edge length of 10 mm were used. Eight truncated tungsten carbide cubes separated by pyrophyllite gaskets served as anvils for the compression of the octahedra. The truncation edge length was 5 mm. Powder of ambient-pressure $BaSi_2O_2N_2$ ^[23] was loaded into a cylindrical capsule of hexagonal boron nitride (Henze, Kempten) with a capacity of 4 mm³ and sealed with a BN cap. The capsule was centered within two nested graphite tubes, which acted as an electrical resistance furnace. The remaining volume at both ends of the sample capsule was filled out with two cylindrical pieces of magnesium oxide. The arrangement was placed into a zirconia tube and then transferred into a pierced MgO octahedron. Two plates of molybdenum provided electrical contact for the graphite tubes. The assembly was compressed up to 14 GPa at room temperature within 2.5 h and then heated up to 1000 °C within 12 min. Under these conditions, the sample was held for 12 minutes and cooled down to 600 °C within 30 minutes. The sample was then quenched to room temperature, followed by decompression over 9.6 h. By this procedure about 5 mg of $Ba_3Si_6O_{12}N_2$ were obtained as a dark gray substance. The temperature was calculated from the electrical power applied to the furnace which was determined on the basis of calibration curves from measurements with $W_{97}Re_3W_{75}Re_{25}$ thermocouples, as described in ref.^[60] Ex-situ high-pressure measurements were performed at 9, 12, 14, 16 and 18 GPa, respectively.

2.5.4.2 Single-Crystal Synthesis

To synthesize single crystals of $Ba_3Si_6O_{12}N_2$, $BaCO_3$ (0.49 mmol, powder, Alfa Aesar, 98 %), SiO_2 (0.75 mmol, Aerosil[®] A380 nano-powder, Degussa, ≥ 99.8 %), crystalline α - Si_3N_4 (0.25 mmol, excess, powder, UBE Industries, 98 %) and EuF_3 (0.01 mmol, powder, Aldrich

Chemical, 99.99 %) were mixed together, ground in an agate mortar, and placed into a tungsten crucible inside a glovebox under Ar atmosphere (Unilab, Fa. Braun, Garching, $O_2 < 1$ ppm, $H_2O < 1$ ppm). The crucible was then heated inductively in the water cooled quartz reactor of a radio-frequency furnace (typ TIG 10/100, frequency: 100 kHz, max. electrical output: 10 kV, Huettinger, Freiburg) under N_2 atmosphere (purified by passing columns of silica gel (Merck), KOH (Merck, ≥ 85 %), molecular sieve (Merck, 4 Å) and P_4O_{10} (Roth, Granulopent[®]) to 1150 °C with a rate of about 23 °C min^{-1} . The temperature was then increased to 1350 °C during 9 h, kept at this temperature for 1 h, and was then again increased to 1400 °C over a period of 20 h. After another temperature enhancement to 1425 °C over a period of 1 h, the sample was cooled down to 650 °C with a rate of about 0.33 °C min^{-1} to offer best conditions for good crystallinity. $Ba_3Si_6O_{12}N_2$ showing green luminescence when excited with UV-light was obtained in the shape of a hard and flat ingot coated with a transparent Matrix of glassy like α - Si_3N_4 which has to be removed to achieve single crystals. To get samples of the solid-solution series $SrCO_3$ (powder, Alfa Aeser, 98 %) was used beside the other reactants.

2.5.4.3 Single-Crystal X-ray Diffraction

Mechanically isolated green luminescent ($Ba_3Si_6O_{12}N_2:Eu^{2+}$) and yellow greenish ($(Ba,Sr)_3Si_6O_{12}N_2:Eu^{2+}$) single crystals obtained by RF-furnace synthesis were mounted on glass fibres and checked for quality by Laue photographs on a Buerger precession camera. Intensity data were collected on a STOE IPDS-I diffractometer with imaging plate detector and graphite monochromator ($Ba_3Si_6O_{12}N_2$) or on a Nonius Kappa-CCD diffractometer with graded multilayer X-ray optics ($Ba_{2.56}Sr_{0.44}Si_6O_{12}N_2$ and $Ba_2SrSi_6O_{12}N_2$), both using $Mo_{K\alpha}$ radiation ($\lambda = 0.71093$ Å). Semiempirical absorption corrections based on equivalent reflections were applied^[61] before the structures were solved by direct methods in space group $P\bar{3}$ (no. 147).^[37] Full-matrix least-squares refinements of models developed from the initial solutions were executed with SHELXL^[38] with anisotropic displacement parameters for all atoms. Further details of the crystal structure investigations may be obtained from Fachinformationszentrum Karlsruhe, 76344 Eggenstein-Leopoldshafen, Germany (fax, (+49)7247-808-666; e-mail, crysdata@fiz-karlsruhe.de, http://www.fiz-karlsruhe.de/request_for_deposited_data.html) on quoting the depository numbers CSD-421322 ($Ba_3Si_6O_{12}N_2$), CSD-421323 ($Ba_2SrSi_6O_{12}N_2$), and CSD-421324 ($Ba_{2.56}Sr_{0.44}Si_6O_{12}N_2$).

2.5.4.4. Powder X-ray Diffraction

X-ray diffraction experiments on powder samples of $Ba_3Si_6O_{12}N_2$ were performed on a STOE STADI P powder diffractometer in Debye-Scherrer geometry with Ge(111)-monochromatized $Mo_{K\alpha 1}$ radiation ($\lambda = 0.70926 \text{ \AA}$). The sample was enclosed in a glass capillary with 0.1 mm diameter. A Rietveld refinement was carried out using the program package Fullprof.^[39] Estimated standard deviations were calculated in agreement with reference [62]. The atomic parameters agreed with the single crystal data within the standard deviations (2σ). $\beta\text{-Si}_3\text{N}_4$ ^[48] was included as a second phase (24.5 % w/w) (see Figure 1).

2.5.4.5 In-Situ High-Pressure and High-Temperature Measurements

In-situ high-pressure measurements were performed with the multianvil high-pressure apparatus MAX80 (NRD Tsukuba, Japan), which is located at the Hamburger Synchrotronstrahlungslabor (HASYLAB, Beamline F.2.1) for in-situ high-pressure and high-temperature X-ray diffraction investigations. Energy-dispersive diffraction patterns were recorded by using white X-rays from the storage ring DORIS III. The pressure was measured by using the high-pressure equation of state for admixed NaCl by Decker.^[63] The beamline was equipped with a Ge solid-state detector, situated at the press frame and tracking the adjustment of the whole apparatus in relation to the X-ray beam.

The multianvil apparatus was equipped with six tungsten carbide anvils that were driven by a 2.500 N uniaxial hydraulic ram. The top and bottom anvil are driven directly, the lateral anvils by two load frames and four reaction bolsters. The maximum pressure for the 8 mm cube set-up is approximately 9 GPa with temperatures up to 1600 °C, which were produced by an internal graphite heater. The high-pressure cell consists of a cube made of boron epoxy resin and the gaskets between the anvils are formed from the boron epoxy cube's material during the runs. The high-pressure cell is filled with the ground sample, the graphite heater, the pressure standard (NaCl) and the thermocouple, which is insulated by boron nitride. The sample was surrounded by rings made from pyrophyllite for electrical insulation and as a quasi-hydrostatic pressure transmitting medium. Copper rings contacted the heater at the top and bottom anvils.

2.5.4.6 Luminescence

Photoluminescence measurements were carried out with a spectrofluorimeter, equipped with a 150 W Xe lamp, two 500 mm Czerny-Turner-monochromators, 1800 1 mm lattices and 250/500 nm lamps, providing a spectral range from 230-820 nm.

2.5.4.7 EDX Measurements

The carbon coated sample was examined with a scanning electron microscope (SEM) JSM-6500F (Joel, Japan, maximum acceleration voltage 30 kV). Qualitative and semi-quantitative elemental analyses were carried out using an energy dispersive spectrometer (Model 7418, Oxford Instruments, United Kingdom).

2.5.4.8 Soft X-ray Spectroscopy

The XANES measurements were performed at the SGM^[64] beamline of the Canadian Light Source, Saskatoon, Saskatchewan, Canada. The XANES measurements were taken in total fluorescence yield mode with an experimental resolving power $E/\Delta E$ of approximately 5000. The XES measurements were performed with the soft X-ray fluorescence spectrometer at Beamline 8.0.1^[65] of the Advanced Light Source, Berkeley, California (USA). The resolving power in the emission experiments was approximately 700. All measurements were taken with the sample orientated 30° from normal with respect to the incoming beam. A powder sample was pressed into freshly scraped indium foil in order to minimize background contributions from oxygen during the measurements. The measured spectra were calibrated with reference spectra from well-characterized samples. The N K-edge spectra were calibrated using hexagonal BN, using the peaks near the band gap with assigned values 392.6 eV for XES and 394.4 eV for XANES, respectively. The O K-edge spectra were calibrated with BGO ($Bi_4Ge_3O_{12}$) with peak values near to the band gap assigned as 526.4 eV and 532.7 eV for XES and XANES spectra, respectively. The ab initio density functional theory (DFT) calculations employed the commercially available WIEN2k DFT software.^[66] This code uses Kohn-Sham methodology with spherical wave functions to model core orbitals, linearized augmented plane waves (LAPW), semi-core, and valence states.^[67,68] The exchange interactions used were the generalized gradient approximation (GGA) of Perdew-Burke-Ernzerhof^[69] and the modified Becke-Johnson potential within GGA (mBJ-GGa).^[54]

We note that this approximation is known to strongly underestimate the band gap, but can provide good agreement with the shape of the valence and conduction bands and therefore the measured soft X-ray spectra. The proper simulation of the XES and XANES measurements requires that one considers the final state of the system during the measurement. The final state of the XES measurement can be approximated as the ground state of the system; all of the core electrons are present. The simulation of this measurement requires no modification of the system. The final state after a XANES measurement included a missing core electron. The effects from this core hole were modelled in the current work by including a single core hole inside of a supercell. This supercell was a larger cell made by replicating the unit cell along its common axes approximating the core hole density that is seen in experimental measurements. The only input to the calculation was the crystal structure as determined by X-ray diffraction. The ground-state calculations were carried out on the unit cell with a 1000 k-point mesh. The sphere sizes used to define the core electrons were 2.400, 1.800, 1.4810, and 1.1590 Bohr for Ba, Si, N, and O, respectively, and the energy cut off was set to -6.0 Ryd. The size of the supercell used was 2 x 1 x 1 of the unit cell (46 atoms) with a 100 k-point mesh. Normally a larger supercell would be used, but due the large interstitial space between the Ba cations and the N or O anions extensive memory resources (≈ 6 GB memory per k-point) was required for the plane wave expansion, and so the size of the supercell had to be limited in order to achieve convergence in a reasonable time frame without limiting the plane wave basis size. The simulated spectra were broadened to facilitate comparison with the experiments. A combination of Lorentzian and Gaussian functions was used to emulate the core-hole lifetime broadening^[70] ($\Delta E = 0.10$ eV for oxygen and $\Delta E = 0.09$ eV for nitrogen), final state lifetime broadening^[71] (this is variable broadening and scales with the energy squared from the central point being the conduction band edge) with a scaling factor of 0.30 for N and 0.20 for O, instrumental broadening with a scaling factor of 0.30 for N and 0.20 for O, and instrumental broadening (this is resolution of the beamline and spectrometer) with a FWHM of 0.40 eV at 400 eV and 0.40 eV and 520 eV for the spectrometer, respectively, and 0.80 eV at 400 eV and 0.80 eV at 520 eV for the monochromator, respectively.

The band-gap determination used a combination of experimentally measured and calculated results. There were three key considerations in this study used when determining the band gap. 1) The VB and CB edge locations were determined by using the second derivative, which has been previously successful.^[55] 2) The site splitting, which occurs because of non-equivalent core electron binding energy in non-equivalent sites was determined from DFT results. 3) The XANES measurements were strongly affected by the core hole present in the

final state; again DFT calculations provide an estimate in the shift of the CB that is caused by the core hole. These three effects were added numerically to the initially determined band gap and provide a reliable estimate of the actual band gap.

2.5.5 References

- [1] H. Lange, G. Wötting, G. Winter, *Angew. Chem.* **1991**, *103*, 1606–1625; *Angew. Chem. Int. Ed. Engl.* **1991**, *30*, 1579–1597.
- [2] A. Zerr, G. Miehe, G. Serghiou, M. Schwarz, E. Kroke, R. Riedel, H. Fueß, P. Kroll, R. Boehler, *Nature* **1999**, *400*, 340–342.
- [3] M. Schwarz, G. Miehe, A. Zerr, E. Kroke, B. T. Poe, H. Fuess, R. Riedel, *Adv. Mater.* **2000**, *12*, 883–887.
- [4] W. Schnick, *Int. J. Inorg. Mater.* **2001**, *3*, 1267–1272.
- [5] R.-J. Xie, N. Hirosaki, T. Suehiro, F.-F. Xu, M. Mitomo, *Chem. Mater.* **2006**, *18*, 5578–5583.
- [6] M. Zeuner, P. J. Schmidt, W. Schnick, *Chem. Mater.* **2009**, *21*, 2467–2473.
- [7] M. Zeuner, F. Hintze, W. Schnick, *Chem. Mater.* **2009**, *21*, 336–342.
- [8] H. Huppertz, W. Schnick, *Acta Crystallogr. Sect. C* **1997**, *53*, 1751–1753.
- [9] H. A. Höpfe, H. Trill, B. D. Mosel, H. Eckert, G. Kotzyba, R. Pöttgen, W. Schnick, *J. Phys. Chem. Solids* **2002**, *63*, 853–859.
- [10] S. Hampshire, in *Materials Science and Technology, Vol. 11* (Eds.: R.W. Cahn, P. Haasen, E.J. Kramer), Wiley-VCH, Weinheim, **1994**.
- [11] L.-O. Nordberg, M. Nygren, P.-O. Käll, Z. Shen, *J. Am. Ceram. Soc.* **1998**, *81*, 1461–1470.
- [12] R. Mueller-Mach, G. Mueller, M. R. Krames, H. A. Höpfe, F. Stadler, W. Schnick, T. Jüstel, P. Schmidt, *Phys. Status Solidi A* **2005**, *202*, 1727–1732.
- [13] T. Jüstel, H. Nikol, C. Ronda, *Angew. Chem.* **1999**, *110*, 3250–3271; *Angew. Chem. Int. Ed.* **1998**, *37*, 3084–3103.
- [14] C. Ronda, *Luminescence: From Theory to Applications*, Wiley-VCH, Weinheim, **2008**.
- [15] W. Schnick, *Phys. Status Solidi RRL* **2009**, *3*, A113–A114.
- [16] R. Mueller-Mach, G. O. Mueller, M. R. Krames, O. B. Shchekin, P. J. Schmidt, H. Bechtel, C.-H. Chen, O. Steigelmann, *Phys. Status Solidi RRL* **2009**, *3*, 215–217.

- [17] T. Schlieper, W. Schnick, *Z. Anorg. Allg. Chem.* **1995**, *621*, 1037–1041.
- [18] T. Schlieper, W. Milius, W. Schnick, *Z. Anorg. Allg. Chem.* **1995**, *621*, 1380–1384.
- [19] H. A. Höpfe, H. Lutz, P. Morys, W. Schnick, A. Seilmeier, *J. Phys. Chem. Solids* **2000**, *61*, 2001–2006.
- [20] H. A. Höpfe, F. Stadler, O. Oeckler, W. Schnick, *Angew. Chem.* **2004**, *116*, 5656–5659; *Angew. Chem. Int. Ed.* **2004**, *43*, 5540–5542.
- [21] O. Oeckler, F. Stadler, T. Rosenthal, W. Schnick, *Solid State Sci.* **2007**, *9*, 205–212.
- [22] F. Stadler, O. Oeckler, H. A. Höpfe, M. H. Möller, R. Pöttgen, B. D. Mosel, P. Schmidt, V. Duppel, A. Simon, W. Schnick, *Chem. Eur. J.* **2006**, *12*, 6984–6990.
- [23] J. A. Kechele, O. Oeckler, F. Stadler, W. Schnick, *Solid State Sci.* **2009**, *11*, 537–543.
- [24] V. Bachmann, C. Ronda, O. Oeckler, W. Schnick, A. Meijerink, *Chem. Mater.* **2009**, *21*, 316–325.
- [25] a) C.-C. Yang, C.-M. Lin, Y.-J. Chen, Y.-T. Wu, S.-R. Chuang, R.-S. Liu, S.-F. Hu, *Appl. Phys. Lett.* **2007**, *90*, 123503–1–3; b) R.-S. Liu, Y.-H. Liu, N. C. Bagkar, S.-F. Hu, *Appl. Phys. Lett.* **2007**, *91*, 061119/1–3; c) Y. Q. Li, A. C. A. Delsing, G. de With, H. T. Hintzen, *Chem. Mater.* **2005**, *17*, 3242–3248; d) Y. Q. Li, G. de With, H. T. Hintzen, *J. Mater. Chem.* **2005**, *15*, 4492–4496; e) B.-G. Yun, Y. Miyamoto, H. Yamamoto, *J. Electrochem. Soc.* **2007**, *154*, J320–J325; f) D. Becker, T. Fiedler, W. Hempel, F. Jermann (Patra Patent Treuhand), PCT Int. Appl., WO2007096333A1, **2007**; g) B.-G. Yun, K. Machida, H. Yamamoto, *J. Ceram. Soc. Jpn.* **2007**, *115*, 619–622; h) V. Bachmann, T. Juestel, A. Meijerink, C. Ronda, P. J. Schmidt, *J. Lumin.* **2006**, *221*, 441–449; i) A. C. A. Delsing, H. T. Hintzen, Y.-Q. Li (Osram Opto Semiconductors GmbH), PCT Int. Appl., WO2004030109A1, **2004**; j) T. Fiedler, F. Jermann (Patra Patent Treuhand), Ger. Offen., DE 102004051395A1, **2006**; k) H. Brunner, T. Fiedler, F. Jermann, J. Strauss, M. Zachau (Patra Patent Treuhand, Osram Opto Semiconductors GmbH), PCT Int. Appl., WO2005031797A2, **2005**; l) T. Fiedler, F. Jermann (Patra Patent Treuhand), PCT. Int. Appl., WO2005030905A1, **2005**; m) H. Brunner, T. Fiedler, F. Jermann, M. Zachau, B. Braune (Osram Opto Semiconductors GmbH, Patra Patent Treuhand), PCT Int. Appl., WO2005030904A1, **2005**; n) H. Brunner, T. Fiedler, F. Jermann, M. Zachau (Patra Patent Treuhand, Osram Opto Semiconductors GmbH), PCT Int. Appl., WO 2005030903A1, **2005**.
- [26] X.-H. He, N. Lian, J.-H. Sun, M.-Y. Guan, *J. Mater. Sci.* **2009**, *44*, 4763–4775.
- [27] M. Mikami, H. Watanabe, K. Uheda, S. Shimooka, Y. Shimomura, T. Kurushima, N. Kijima, *IOP Conf. Ser.: Mater. Sci. Eng.* **2009**, *1*, 012002–012012.

- [28] S. Nakamura, T. Mukai, M. Senoh, *Appl. Phys. Lett.* **1994**, *64*, 1687–1689.
- [29] T. Mukai, S. Nagahama, N. Iwasa, M. Senoh, T. Yamada, *J. Phys.: Condens. Matter* **2001**, *13*, 7089–7098.
- [30] H. A. Höpfe, *Angew. Chem.* **2009**, *121*, 3626–3636; *Angew. Chem. Int. Ed.* **2009**, *48*, 3572–3582.
- [31] S. Shimooka, K. Uheda, M. Mikami, N. Kijima, H. Imura, K. Horibe, PCT Int. Appl., WO088966A1, **2007**.
- [32] M. Mikami, S. Shimooka, K. Uheda, H. Imura, N. Kijima, *Key Eng. Mater.* **2009**, *403*, 11–14.
- [33] W. Schnick, H. Huppertz, R. Lauterbach, *J. Mater. Chem.* **1999**, *9*, 289–296.
- [34] H. Huppertz, *Z. Kristallogr.* **2004**, *219*, 330–338.
- [35] D. Walker, M. A. Carpenter, C. M. Hitch, *Am. Mineral.* **1990**, *75*, 1020–1028.
- [36] D. Walker, *Am. Mineral.* **1991**, *76*, 1092–1100.
- [37] M. C. Burla, M. Camalli, B. Carrozzini, G. L. Casciarano, C. Giacovazzo, G. Polidori, R. Spagna, *J. Appl. Crystallogr.* **2003**, *36*, 1103–1103.
- [38] G. M. Sheldrick, *Acta Crystallogr. Sect. A* **2008**, *64*, 112–122.
- [39] Fullprof. 2k-version 4.40, J. Rodriguez-Carvajal, **2008**.
- [40] L. B. McCusker, F. Liebau, G. Engelhardt, *Pure Appl. Chem.* **2001**, *73*, 381–394.
- [41] P. E. D. Morgan, *J. Mater. Sci.* **1986**, *21*, 4305–4309.
- [42] F. Liebau, *Structural Chemistry of Silicates*, Springer, Berlin, **1985**.
- [43] H.-J. Klein, F. Liebau, *J. Solid State Chem.* **2008**, *181*, 2412–2417.
- [44] R. Hoppe, *Angew. Chem.* **1970**, *82*, 7–16; *Angew. Chem. Int. Ed. Engl.* **1970**, *9*, 25–34.
- [45] a) R. Hoppe, *Angew. Chem.* **1966**, *78*, 52–63; *Angew. Chem. Int. Ed. Engl.* **1966**, *5*, 95–106; b) R. Hoppe, *Z. Naturforsch. A* **1995**, *50*, 555–567; c) C. Weiß, R. Hoppe, *Z. Anorg. Allg. Chem.* **1996**, *622*, 1019–1026.
- [46] MAPLE, Madlung Part of Lattice Energy (Program), Version 4, R. Hübenthal, University of Gießen (Germany), **1993**.
- [47] S. J. Sedlmaier, J. Schmedt auf der Günne, W. Schnick, *Dalton Trans.* **2009**, 4081–4084.
- [48] R. Grün, *Acta Crystallogr. Sect. B* **1979**, *35*, 800–804.
- [49] F. Stadler, W. Schnick, *Z. Anorg. Allg. Chem.* **2006**, *632*, 949–954.

- [50] The term dreier (3er) ring was coined by Liebau and is derived from the German word “drei”, which means three; however, a dreier ring is not a three-membered ring, but a six-membered ring comprising three tetrahedral centers (Si) and three electronegative atoms (N). Similar terms exist for rings comprising four, five, and six tetrahedral centers (and the corresponding number of electronegative atoms), namely vierer (4er), fünfer (5er), and sechser (6er) rings, respectively. (F. Liebau, *Structural Chemistry of Silicates*, Springer, Berlin, **1985**.)
- [51] C. Braun, H. Ehrenberg, T. D. Boyko, A. Moewes, W. Schnick, unpublished results.
- [52] T. L. Barry, *J. Electrochem. Soc.* **1968**, *115*, 1181–1184.
- [53] P. Schmidt, A. Tuecks, J. Meyer, H. Bechtel, D. Wiechert, R. Mueller-Mach, G. Mueller, W. Schnick, Philips Research Europe Aachen (Germany); Proceedings of SPIE–The International Society for Optical Engineering **2007**, 6669 (Seventh International Conference on Solid State Lighting **2007**), 66690P/1–9.
- [54] F. Tran, P. Blaha, *Phys. Rev. Lett.* **2009**, *102*, 226401.
- [55] E. Z. Kurmaev, R. G. Wilks, A. Moewes, L. D. Finkelstein, S. Shamin, J. N. Kunes, *Phys. Rev. B* **2008**, *77*, 165127–165131.
- [56] Y. N. Xu, W. Y. Ching, *Phys. Rev. B* **1995**, *51*, 17379–17389.
- [57] N. Kijima, Y. Shimomura, T. Kurushima, H. Watanabe, S. Shimooka, M. Mikami, K. Uheda, *J. Light Visual Environ.* **2008**, *32*, 202–205.
- [58] K. Uheda, N. Hirosaki, H. Yamamoto, *Phys. Status Solidi A* **2006**, *203*, 2712–2717.
- [59] R.-J. Xie, N. Hirosaki, T. Suehiro, F.-F. Xu, M. Mitomo, *Chem. Mater.* **2006**, *18*, 5578–5583.
- [60] D. C. Rubie, *Phase Transitions* **1999**, *68*, 431–451.
- [61] XPREP, Version 6.12, Siemens Analytical X-ray Instruments Inc., Madison, **1996**.
- [62] J. F. Berar, P. Lelann, *J. Appl. Crystallogr.* **1991**, *24*, 1–5.
- [63] D. L. Decker, *J. Appl. Phys.* **1971**, *42*, 3239–3244.
- [64] J. J. Jia, T. A. Callcott, J. Yurkas, A. W. Ellis, F. J. Himpsel, M. G. Samant, J. Stöhr, D. L. Ederer, J. A. Carlisle, E. A. Hudson, L. J. Terminello, D. K. Shuh, R. C. C. Perera, *Rev. Sci. Instrum.* **1995**, *66*, 1394–1397.
- [65] T. Regier, J. Krochak, T. K. Sham, Y. F. Hu, J. Thompson, R. I. R. Blyth, *Nucl. Instr. Methods Phys. Res. A* **2007**, *582*, 93–95.
- [66] WIEN2k An Augmented Plane Wave+Local Orbitals Program for Calculating Crystal Properties, P. Blaha, K. Schwarz, G. K. H. Madsen, D. Kvasnicka, J. Luitz, , Vienna University of Technology (Austria), Revised Edition, **2008**.

- [67] K. Schwarz, P. Blaha, G. Madsen, *Comput. Phys. Commun.* **2002**, *147*, 71–76.
- [68] K. Schwarz, P. Blaha, *Comput. Mater. Sci.* **2003**, *28*, 259–273.
- [69] J. Perdew, K. Burke, M. Ernzerhof, *Phys. Rev. Lett.* **1996**, *77*, 3865–3868.
- [70] M. O. Krause, J. H. Oliver, *J. Phys. Chem. Ref. Data* **1979**, *8*, 329–338.
- [71] D. A. Goodings, R. Harris, *J. Phys. Pt. Sol. Stat. Phys. C* **1969**, *2*, 1808–1816.
- [72] H. A. Höpfe, PhD-thesis, University of Munich, **2003**.

3. Luminescent Gallium Compounds

3.1 Preface

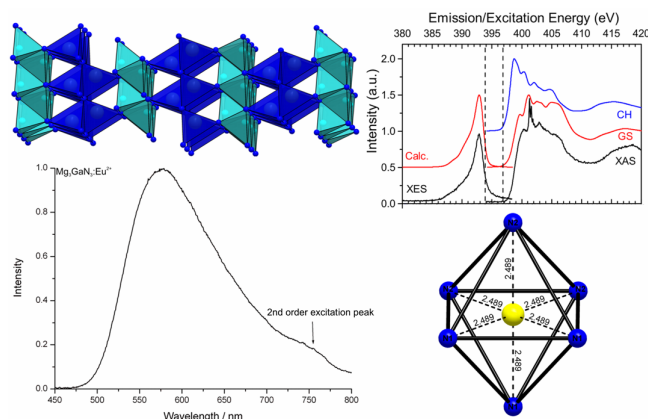
Based on naturally occurring oxosilicates, Si^{4+} can formally be substituted by Al^{3+} leading to various kinds of oxoalumosilicate minerals. Charge balance is usually achieved by insertion of alkali-metal ions in the crystal structure. Both, Si^{4+} and Al^{3+} , prefer a tetrahedral coordination by the anions. Special synthesis strategies in the laboratory allow the formation of nitridoalumosilicates (e.g. $\text{Ba}_2\text{AlSi}_5\text{N}_9$, $\text{SrAlSi}_4\text{N}_7$)^[1,2] or nitridoaluminates (e.g. $\text{Ca}[\text{LiAlN}_2]$).^[3] To balance the higher negative charge from substitution of O^{2-} by N^{3-} , alkaline-earth ions (M^{2+}) are inserted into the crystal structure. In the case of $\text{Ba}_2\text{AlSi}_5\text{N}_9$ and $\text{SrAlSi}_4\text{N}_7$, an intense emission in the orange to red spectral region is observed when doped with small amounts of Eu^{2+} and excited by UV to blue light.^[1,2] This is due to the decreasing difference in electronegativity of Eu^{2+} and the ligands (N instead of O) which equals an increasing nephelauxetic effect. As there is a demand for highly efficient red emitters usable for pc-LED applications, it is desirable to shift the emission signal into the red spectral region. In order to retain the stability of the host lattice (which is a result of the high degree of tetrahedra condensation) it might be favorable to substitute the Si / Al atoms within the tetrahedra by larger cations like Ga^{3+} . As a consequence of longer distances within the tetrahedra, the Eu-ligand distances might contract which means a red-shift of the emission signal. This theoretical consideration was confirmed by *Hintze et al.* in 2012.^[4] The synthesized compound $\text{Ba}_3\text{Ga}_3\text{N}_5:\text{Eu}^{2+}$ is the first example for a luminescent nitridogallate and its emission maximum is situated in the red spectral region ($\lambda_{\text{em}} = 638 \text{ nm}$, FWHM = 85 nm). In the following chapter a new luminescent Ga-N compound is characterized in detail regarding its crystal structure and band gap. Additionally, it is discussed whether this phase represents a nitridogallate in a classical sense or not.

References

- [1] J. A. Kechele, C. Hecht, O. Oeckler, J. Schmedt auf der Günne, P. J. Schmidt, W. Schnick *Chem. Mater.* **2009**, *21*, 1288-1295.
- [2] C. Hecht, F. Stadler, P. J. Schmidt, J. Schmedt auf der Günne, V. Baumann, W. Schnick *Chem. Mater.* **2009**, *21*, 1595-1601.
- [3] P. Pust, S. Pagano, W. Schnick *Eur. J. Inorg. Chem.* **2013**, 1157-1160.
- [4] F. Hintze, F. Hummel, P. J. Schmidt, D. Wiechert, W. Schnick *Chem. Mater.* **2012**, *24*, 402-407.

3.2 Magnesium Double Nitride Mg_3GaN_3 as New Host Lattice for Eu^{2+} -Doping – Synthesis, Structural Studies, Luminescence and Band-Gap Determination

Frauke Hintze, Neil W. Johnson, Markus Seibald, David Muir, Alexander Moewes, and Wolfgang Schnick



published in: *Chem. Mater.* **2013**, (in press); DOI: 10.1021/cm402191d

Copyright © 2013 American Chemical Society

Abstract

The double nitride Mg_3GaN_3 and binary nitride Mg_3N_2 were synthesized from the elements by reaction with NaN_3 in a sodium flux. Reactions were carried out at $760\text{ }^\circ\text{C}$ in welded shut tantalum ampules. Mg_3GaN_3 was obtained as single crystals (space group $R\bar{3}m$ (no. 166), $a = 3.3939(5)$ and $c = 25.854(5)$ Å, $Z = 3$, $R1 = 0.0252$ $wR2 = 0.0616$ for 10 refined parameters, 264 diffraction data). This double nitride consists of an uncharged three-dimensional network of MgN_4 and mixed $(\text{Mg}/\text{Ga})\text{N}_4$ tetrahedra, which share common corners and edges. First-principles density functional theory (DFT) calculations predict Mg_3GaN_3 to have a direct band gap of 3.0 eV, a value supported by soft X-ray spectroscopy measurements at the N K-edge. Eu^{2+} -doped samples show yellow luminescence when irradiated with UV to blue light ($\lambda_{\text{max.}} = 578\text{ nm}$, full width at half maximum (fwhm) = 132 nm). Eu^{2+} -doped samples of Mg_3N_2 also show luminescence at room temperature when excited with ultraviolet (UV) to blue light. The maximum intensity of the emission band is found at 589 nm (fwhm = 145 nm).

Keywords: Gallium Nitride, Double Nitride, Luminescence, Band Gap, Europium

3.2.1 Introduction

Gallium nitride has found broad application in high-performance light-emitting diodes (LEDs), because of its properties as a direct, wide band gap semiconductor.^[1-5] Recently, crystal growth and doping of GaN have been studied thoroughly.^[6-10] In contrast, investigations of the deriving ternary and higher nitridogallates or gallium nitrides have been scarcely pursued so far. Mg was found to be suited for p-doping in GaN or AlGaN thus increasing hole concentration.^[11-13] Mostly, GaN:Mg has been synthesized by MOCVD with bis(cyclopentadienyl) magnesium (Cp_2Mg) as the magnesium source.^[14-16] The influence of such doping on the GaN lattice and its physical properties have been investigated in detail.^[17-20] So-called “heavily doped GaN:Mg” was obtained when the magnesium concentration was $\sim 10^{20} \text{ cm}^{-3}$ and resulting photoluminescence bands at 2.8 eV (443 nm) and 3.2 eV (388 nm) were observed.^[19,21-23]

Binary magnesium nitride (Mg_3N_2) has been known for some time, but has been much less in the focus of applications than GaN.^[24,25] Nevertheless, in the past few years, some interest in Mg_3N_2 has arisen. Its structure in the antibixbyite type was further investigated,^[26,27] and a green photoluminescence was reported in the literature.^[28]

During the past decade, ternary and multinary alkaline-earth nitrides emerged as important host lattices for doping with Eu^{2+} , exhibiting parity-allowed $4f^6(^7F)5d^1 \rightarrow 4f^7(^8S_{7/2})$ transitions resulting in intense broad-band emission. This is due to the fact that these levels lie within the band gap as shown by Dorenbos,^[29,30] for the important phosphor material $\text{M}_2\text{Si}_5\text{N}_8:\text{Eu}^{2+}$.^[31] In order to estimate the performance of a luminescent material in phosphor-converted light-emitting diodes (pc-LEDs) at higher temperatures, band-gap investigations are of special interest. These results allow assessment of the thermal quenching behavior.

Some of the aforementioned nitrides were identified as highly efficient optical luminescence materials and, therefore, are promising candidates for photon conversion.^[32] In this respect, (oxo-)nitridosilicates, nitridoalumosilicates, and (oxo-)nitridoalumosilicates have been intensively investigated.^[33-39] Recent research has also focused on nitridogallates as host lattices for Eu^{2+} doping.^[40] The aforementioned materials are made up of tetrahedra-based anionic substructures, wherein tetrahedra can be connected via common corners or edges, building either isolated polyhedra or one-dimensional (1D), two-dimensional (2D), or three-dimensional (3D) structures.^[39,41,42] Some of these materials are suitable as host lattices for Eu^{2+} , with their emission depending on the coordination of Eu^{2+} by the surrounding anions.

Basically, Eu^{2+} can either substitute other electropositive ions (typically alkaline-earth ions) when the ionic radii are appropriate, or it can occupy interstitial sites.

In this contribution, we report on the investigation of Eu^{2+} -doped Mg_3N_2 as well as the double nitride $\text{Mg}_3\text{GaN}_3\cdot\text{Eu}^{2+}$, with respect to their synthesis, structure elucidation and luminescence. These nitrides represent interesting new host lattices for Eu^{2+} doping. Furthermore, we explore the electronic partial density of states (pDOS) of the latter and quantify its band gap through calculation and experiment.

3.2.2 Experimental Section

Synthesis of Mg_3GaN_3 was carried out in welded shut tantalum ampules (30 mm length, 10 mm diameter, 0.5 mm wall thickness). All manipulations were done under argon atmosphere in a glovebox (Unilab, MBraun, Garching; $\text{O}_2 < 1$ ppm, $\text{H}_2\text{O} < 1$ ppm). Single crystals were obtained from reaction of 0.38 mmol NaN_3 (25.0 mg, Acros, 99%), 0.59 mmol Mg (14.3 mg, Alfa Aesar, 99.9%) and 0.58 mmol Ga (40.4 mg, AluSuisse, 99.999%) in 2.19 mmol sodium flux (50.4 mg, Sigma-Aldrich, 99.95%). For doping, 2 mol% of EuF_3 was added. Ca was introduced into the metallic melt with the initial goal of finding new compounds in the system Ca-Ga-Mg-N. However, in these experiments, calcium has not been incorporated into the final products but did appear to improve crystallinity. Reactions without additional Ca have been unsuccessful so far.

Synthesis of doped Mg_3N_2 was performed analogously in tantalum ampules sealed under inert-gas conditions in argon atmosphere. Single crystals were obtained from reaction of 0.30 mmol NaN_3 (20.2 mg, Acros, 99%), 0.47 mmol Mg (11.4 mg, Alfa Aesar, 99.9%) and 0.5×10^{-3} mmol EuF_3 (1.2 mg, Sigma-Aldrich, 99.99%) as dopant in 2.12 mmol sodium flux (48.7 mg, Sigma-Aldrich, 99.95%). According to energy-dispersive X-ray spectroscopy (EDX) measurements, the addition of strontium and germanium metal was found to improve crystallinity but these atoms were not incorporated into the crystalline product.

Welded shut tantalum ampules were placed into quartz tubings under vacuum to prevent oxidation of the ampules. The respective reaction mixtures were then heated in a tube furnace at a rate of 0.83 °C/min to 760 °C, maintained at that temperature for 48 h, and then cooled to 200 °C at a rate of 0.06 °C/min. Subsequently, the furnace was turned off and the tantalum ampules were opened in a glovebox. The sodium flux was removed from the reaction products by sublimation at 320 °C under vacuum for 10 h.

Scanning electron microscopy (SEM) was performed on a JEOL Model JSM 6500 F microscope equipped with a field-emission gun at an acceleration voltage of 30 kV. Synthesized samples were prepared on adhesive conductive carbon pads and coated with a similarly conductive carbon film. Chemical compositions were confirmed by EDX spectra (using an Oxford Instruments detector), and each spectrum was recorded on an area limited to one crystal face to avoid influence of possible contaminating phases and to verify that additional calcium or strontium and germanium were not incorporated into the crystalline products.

For X-ray diffraction (XRD) and luminescence investigations, single crystals of each compound were sealed in glass capillaries under inert conditions.

Single-crystal XRD data of Mg_3GaN_3 were collected on a Nonius Kappa-CCD diffractometer with graded multilayer X-ray optics and monochromated Mo-K_α radiation ($\lambda = 0.71073 \text{ \AA}$). X-ray diffraction data of Mg_3N_2 single crystals were collected on a STOE IPDS I diffractometer using monochromated Mo-K_α radiation ($\lambda = 0.71073 \text{ \AA}$). Applied absorption corrections were done using WinGX and X-RED.^[43,44] The structures were solved by direct methods implemented in SHELXS-97.^[45,46] Refinement of crystal structures was carried out with anisotropic displacement parameters for all atoms by full-matrix least-squares calculation on F^2 in SHELXL-97.^[46,47] [Further details of the structure investigations are available from the Fachinformationszentrum Karlsruhe, D-76344 Eggenstein Leopoldshafen, Germany (fax: +49-7247-808-666; email: crysdata@fiz.karlsruhe.de) on quoting the depository numbers CSD-425108 (Mg_3GaN_3) and CSD-425109 (Mg_3N_2), respectively.]

N K-edge soft X-ray emission spectroscopy and absorption spectroscopy (XES and XAS, respectively) measurements of Mg_3GaN_3 were performed at the XES endstation of the resonant elastic and inelastic X-ray scattering beamline of the Canadian Light Source located on the University of Saskatchewan campus. The monochromator's resolving power ($E/\Delta E$) was $\sim 1 \times 10^4$, and it was calibrated such that the lowest energy peak in the *h*-BN absorption spectrum appeared at 402.1 eV in the bulk-sensitive total fluorescence yield (TFY) mode. All reported Mg_3GaN_3 absorption measurements were also performed in TFY mode to mitigate the possibility of surface contamination effects. The emission spectrometer, currently undergoing commission, has a theoretical resolving power of 2×10^3 at the N K-edge. It uses diffraction gratings in a Rowland circle geometry as dispersive elements, and is fitted with a microchannel plate detector. XES measurements were calibrated relative to the monochromator using a series of elastic peak measurements. The double nitride sample

consisted of an agglomeration of single crystals, stored under an argon atmosphere prior to being mounted on carbon tape. The exposure to ambient conditions was <10 min.

Density functional theory (DFT) calculations of the electronic structure of Mg_3GaN_3 were performed with the *WIEN2k* software package,^[48] using the Perdew-Burke-Ernzerhoff generalized gradient approximation (PBE-GGA).^[49] The theoretical band gap was calculated with the modified Becke-Johnson (mBJ) exchange-correlation functional,^[50] which has been shown to improve calculated band-gap values for most semiconductors.^[51] Calculations were performed on a $(5 \times 7 \times 12)$ *k*-point mesh with a plane-wave cutoff of -8.0 Ryd.

Luminescence investigations were performed on single crystals placed in glass capillaries (diameter 0.2 mm, Hilgenberg) at room temperature. The capillaries were aligned with a Leitz Epiverts microscope. A Jobin Yvon Traix190 monochromator with 365 nm wavelength was used as excitation source, while a CCD camera (LaVision Dyna Vision) was used to detect the luminescence through a 500 μm slit.

3.2.3 Results and Discussion

The ternary nitride Mg_3GaN_3 was obtained as a colorless to light yellow powder with light yellow crystals having the appearance of hexagonal plates. EDX analyses have confirmed the sum formula. The crystals were not sensitive to moisture and air, even contact with ethanol or acetone had no influence on the compound.

The existence of a ternary nitride with stoichiometric formula Mg_3GaN_3 was claimed earlier by *Verdier et al.*, obtained as a green powder from the reaction of GaN and Mg_3N_2 at 930 °C.^[52] The authors reported nonindexed powder data and postulated an atomic ratio Mg:Ga:N of 3:1:3 but no structural details have been published so far. Here, we were able to obtain this compound as colorless single crystals and to elucidate the crystal structure. Calculated reflection positions and intensities from single-crystal data show accordance to data reported by *Verdier et al.*^[52]

The product of the second reaction route described in the Experimental Section was obtained as a heterogeneous mixture of metallic powder, orange crystals, and colorless cube-shaped crystals. EDX analysis showed the presence of only magnesium and nitrogen in the cube-shaped crystals, while the orange crystals were found to be $\text{Sr}(\text{Mg}_3\text{Ge})\text{N}_4$.^[53]

3.2.3.1 Crystal-Structure Description

The crystal structure of Mg₃GaN₃:Eu²⁺ was solved using single-crystal X-ray diffraction data. The Eu²⁺ content was neglected because of its insignificant contribution to the scattering density. Initially, the solution was carried out in space group *R3m* (no. 160). After examination with PLATON^[54,55] further refinement was performed in space group *R* $\bar{3}$ *m* (no. 166) with $a = 3.3939(5)$ and $c = 25.854(5)$ Å. Crystallographic data for Mg₃GaN₃ are summarized in Table 1.

Table 1. Crystallographic Data for Mg₃GaN₃.

	Mg ₃ GaN ₃
Formula mass (g·mol ⁻¹)	184.68
Temperature/K	293(2)
Crystal system	trigonal
Space group	<i>R</i> 3m (no. 166)
Lattice parameters/Å	$a = 3.3939(5)$ $c = 25.854(5)$
$V/\text{Å}^3$	257.91(7)
Formula units/cell	3
Crystal size/mm ³	0.05 · 0.04 · 0.02
Abs. coefficient μ/mm^{-1}	8.321
$F(000)$	264
Diffractometer	Nonius Kappa-CCD
Radiation, graphite-monochromator	Mo-K α ($\lambda = 0.71073$ Å)
θ range/°	4.73 - 27.48
Measured reflections	275
Independent reflections	102
Observed reflections	100
Refined parameters	10
GOF	1.067
R indices ($F_o^2 \geq 2\sigma(F_o^2)$)	$R1 = 0.0252$; $wR2 = 0.0616$
R indices (all data)	$R1 = 0.0255$; $wR2 = 0.0617$

The atomic coordinates and displacement parameters are listed in Table 2 and 3, while selected bond lengths and angles are shown in Table 4.

Similarly to most Ga-N compounds, the structure of Mg₃GaN₃ is composed of metal centered nitrogen tetrahedra (Figure 1). Two metal sites are present in the crystal structure, whereby one site is occupied by an even number of Mg and Ga atoms, while the other is occupied solely by Mg. The Mg-N and (Mg/Ga)-N distances vary in the range of 1.9815(6)-2.1915(8) Å and, thus, are representative for typical Ga-N or Mg-N distances.^[40,53,56] The

observed bond lengths agree well with the expected sum of the ionic radii, even for the mixed occupied site.^[57-59]

Table 2. Atomic coordinates and equivalent isotropic displacement parameters ($\times 10^4 \text{ pm}^2$) of Mg_3GaN_3 .^[a]

site	Wyckoff Position	x	y	z	U_{eq}
Mg1/Ga1	6c	0	0	0.12999(3)	0.0124(4)
Mg2	6c	0	0	0.29538(7)	0.0092(4)
N1	6c	0	0	0.21474(13)	0.0105(9)
N2	3a	0	0	0	0.0090(11)

[a] Estimated standard deviation (esd) values are shown in parantheses.

Table 3. Anisotropic displacement parameters (in 10^4 pm^2) for Mg_3GaN_3 .^[a]

atom	U_{11}	U_{22}	U_{33}	U_{23}	U_{13}	U_{12}
Mg1/Ga1	0.0081(4)	U_{11}	0.0210(6)	0	0	0.00406(19)
Mg2	0.0080(5)	U_{11}	0.0116(8)	0	0	0.0040(3)

[a] Estimated standard deviation (esd) values are shown in parantheses.

The tetrahedra are connected to each other by common corners and edges, building a 3D network. Both tetrahedra MgN_4 and $(\text{Mg}/\text{Ga})\text{N}_4$ are connected via edges to themselves and via corners to the other kind. Thereby, sheets of MgN_4 and $(\text{Mg}/\text{Ga})\text{N}_4$ tetrahedra are built which are linked to each other via vertices and stacked along [001] (see Figure 1). In their second coordination sphere, each metal atom is coordinated by 12 other metal atoms. The mixed (Mg/Ga) site is surrounded by a cuboctahedron, while the pure Mg site is coordinated with an anticuboctahedron.

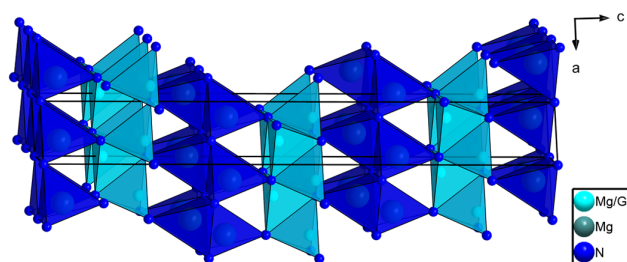


Figure 1. Crystal structure of Mg_3GaN_3 . Unit cell shown in solid black lines. Sheets of $(\text{Mg}/\text{Ga})\text{N}_4$ units (light blue) and MgN_4 tetrahedra (dark blue) are linked via corners to each other and via edges within the sheets.

Nitridogallates that contain magnesium are barely known thus far. The only examples appearing in the literature are $\text{Ca}_2\text{Ga}_3\text{MgN}_5$ and $\text{Sr}(\text{Mg}_2\text{Ga}_2)\text{N}_4$.^[42,53] For both compounds, mixed occupation Mg/Ga on the tetrahedral sites has been reported. These tetrahedra exhibit both corner and edge sharing, forming a network that represents the anionic substructure charge balanced by Ca^{2+} or Sr^{2+} , respectively.

Table 4. Selected bond lengths in Mg₃GaN₃.^[a]

(Mg1/Ga1)-N1	3x	1.9815(6) Å
(Mg1/Ga1)-N2		2.191(4) Å
Mg2-N1	3x	2.1915(8) Å
Mg2-N2		2.085(4) Å

[a] Estimated standard deviation (esd) values are shown in parantheses.

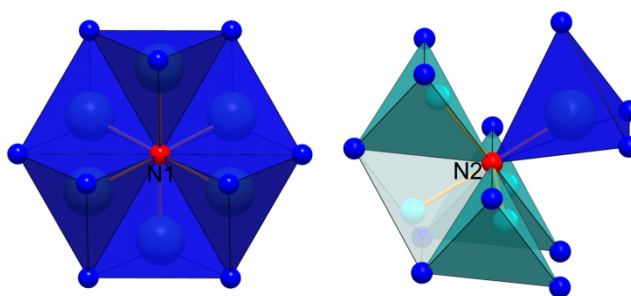
Contrary to this, in the crystal structure of Mg₃GaN₃ there are no further metal sites beside the ones in the uncharged tetrahedron network. Therefore, the atomic ratio (Mg/Ga):N, representing the degree of condensation (κ) is 4:3, which is much higher than the κ value of any other known nitridogallate. According to *Liebau*,^[60] Mg₃GaN₃ can be interpreted as a double nitride of Mg and Ga, rather than a magnesium nitridogallate, as previously assumed.^[52]

Table 5. MAPLE values^[a] for Mg₃GaN₃ and Mg₃N₂ and respective deviation Δ from theoretical values of the constituting nitrides.

Mg ₃ GaN ₃	MAPLE values [kJ mol ⁻¹]	Mg ₃ N ₂	MAPLE values [kJ mol ⁻¹]
Mg	2206 – 2417	Mg	2251
Mg / Ga	3402 – 3588	N	4757 – 4764
N	45289 - 5276	Mg ₃ N ₂	16285
Mg ₃ GaN ₃	26395	3MgSiN ₂ – Si ₃ N ₄ → Mg ₃ N ₂	16265 ^[c]
Mg ₃ N ₂ + GaN → Mg ₃ GaN ₃	26773 ^[b]	Δ	0.11%
Δ	1.41%		

[a] Typical partial MAPLE values [kJ/mol]: Ga³⁺, 4500 - 6000; Mg²⁺, 2100 - 2400; N³⁻, 3000 – 6000.^[34,64-66] [b] Mg₃N₂ data taken from ref 27; GaN data taken from ref 61. [c] MgSiN₂ data taken from ref 62; Si₃N₄ data taken from ref 63.

An alternate structural description of Mg₃GaN₃ can be afforded on the basis of anion-centered polyhedra. There are two distinct nitrogen sites (see Figure 2). N1 is surrounded by six Mg atoms in edge-sharing MgN₄-units in a slightly distorted octahedron, while N2 is coordinated by five metal atoms in a trigonal bipyramidal configuration, belonging to one MgN₄ tetrahedron and four (Mg/Ga)N₄ tetrahedra.

Figure 2. Coordination of N sites in Mg₃GaN₃.

These structural details can be compared to the respective binary nitrides Mg_3N_2 and GaN . In Mg_3N_2 , there are also two N sites,^[27] both of which are 6-fold coordinated, with one of them showing the same hexagonal arrangement of six MgN_4 tetrahedra as N1 in Mg_3GaN_3 . In GaN , regardless of whether hexagonal or cubic modification^[61,67] is realized, nitrogen is coordinated by four GaN_4 units in a tetrahedral arrangement. This arrangement is comparable to the surroundings of N2 in Mg_3GaN_3 , where the 5-fold coordination of the N atom can also be seen as a tetrahedral arrangement of three $(\text{Mg/Ga})\text{N}_4$ and one MgN_4 unit with a further $(\text{Mg/Ga})\text{N}_4$ tetrahedron. The anion-centered polyhedra illustrate the structural relation to the binary nitrides and support the double nitride character of Mg_3GaN_3 . Sr_3GaN_3 is also known to exist, and its structure has been described in the literature. Unlike Mg_3GaN_3 , the strontium compound is composed of Sr^{2+} and isolated trigonal planar $[\text{GaN}_3]^{6-}$ ions.^[68] In contrast, Mg_3BN_3 must be classified as a nitridoborate nitride containing even linear $[\text{BN}_2]^{3-}$ ions and isolated N^{3-} ions besides Mg^{2+} .^[69] The Mg/Ga/N system has been thoroughly studied in the literature.^[11-20] However, only the quaternary Mg-containing nitridogallates $\text{Ca}_2\text{Ga}_3\text{MgN}_5$ and $\text{Sr}(\text{Mg}_2\text{Ga}_2)\text{N}_4$ have been described; no other ternary Mg-Ga-N compounds have been observed at this point.^[42,53]

There are several other double nitrides (e.g., Li_7PN_4) composed of edge-sharing LiN_4 and PN_4 tetrahedra^[70] or phenakite-type BeP_2N_4 containing an uncharged three-dimensional network of all corner-sharing BeN_4 and PN_4 tetrahedra.^[71]

Concerning the degree of condensation (κ), the double nitride Mg_3GaN_3 ($\kappa = 4:3$) is intermediate between that of the binary nitrides Mg_3N_2 ($\kappa = 3:2$) and that of GaN ($\kappa = 1:1$).

The crystal structure of Mg_3N_2 was re-refined on the basis of single-crystal XRD data. The solution and refinement was performed in cubic space group $Ia\bar{3}$ (no. 206) with $a = 9.955(2)$ Å. The refined crystal structure parameters are slightly different from the single-crystal data previously published;^[27] however, they agree well with literature values from powder X-ray investigations on Mg_3N_2 .^[24-26,72] The results of the crystal-structure refinement are listed in the Supporting Information. Mg_3N_2 crystallizes in the antibixbyite type and is constituted of edge-sharing MgN_4 tetrahedra.^[27] To further confirm the refined crystal structures of Mg_3GaN_3 and Mg_3N_2 , Madelung part of lattice energy (MAPLE) calculations were performed on both compounds. The electrostatic consistency was proven by comparison of the MAPLE sum with the sum of constituting nitrides. Moreover, MAPLE values for each atom were compared with known MAPLE values from reference data previously reported.^[34] The results of MAPLE investigations^[34] are listed in Table 5.

3.2.3.2 DFT Calculations and Soft X-ray Spectroscopy of Mg_3GaN_3

Given a well-defined, periodic crystal structure, DFT calculations can be used to predict the electronic properties of a material, to explore the chemical bonding that occurs and further refine its structural parameters. In order to perform DFT calculations on Mg_3GaN_3 (Figure 1), the mixed occupancy on the metal sites must be divided evenly into pure Mg and Ga sites with periodic ordering. Since the unit cell in Figure 1 contains six inequivalent mixed sites, a simple way to achieve this would be to assign 3 of them as Ga atoms and 3 as Mg atoms. There are 10 unique unit cells that can be created in this manner, all of which predict Mg_3GaN_3 to be either a metal or a narrow band gap (<0.2 eV) semiconductor when their electronic structure is calculated. Given the colorless nature of the double nitride crystals, such structures can be safely ruled out.

In a $2 \times 2 \times 1$ supercell, all of the aforementioned inequivalent sites are quadrupled, generating six different sets of four equivalent crystal positions. The total energy of the unit cell is found to decrease when each set of equivalent sites is half-filled with Mg and half-filled with Ga, and the total energy decreases further if each Ga site is only coordinated with one more Ga atom in the second coordination sphere, as shown in Figure 3.

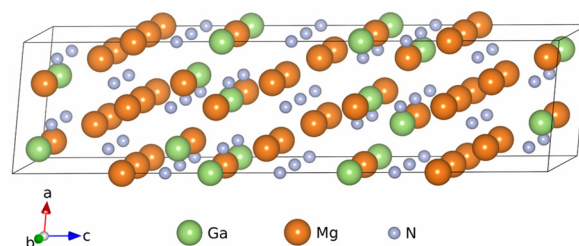


Figure 3. A VESTA^[73] visualization of the energetically favored crystal structure of Mg_3GaN_3 with optimal Mg/Ga ordering and crystal symmetry.

Furthermore, when the electronic structure of this particular configuration is calculated, a band gap compatible with colorless Mg_3GaN_3 crystals is predicted. If this structure is relaxed to minimize internal atomic forces and pressure on the unit cell, the resulting optimized atomic coordinates and lattice constants agree with results of the single-crystal XRD experiment. The calculated band gap is not significantly affected by relaxing the crystal structure.

The calculated DOS is shown in the bottom frame of Figure 4. Typically, calculations using the PBE-GGA exchange-correlation functional are found to underestimate the band gap,

while mBJ calculations provide more appropriate band-gap estimates but have been observed to horizontally contract the surrounding states.^[74] For Mg_3GaN_3 , PBE-GGA calculations returned a band gap of 1.7 eV, while mBJ calculations predicted a more reasonable value of 3.0 eV. To compensate for the shortcomings of both techniques, Figure 4 uses the PBE-GGA calculated DOS but with the conduction states shifted up 1.3 eV to reflect the mBJ band gap.

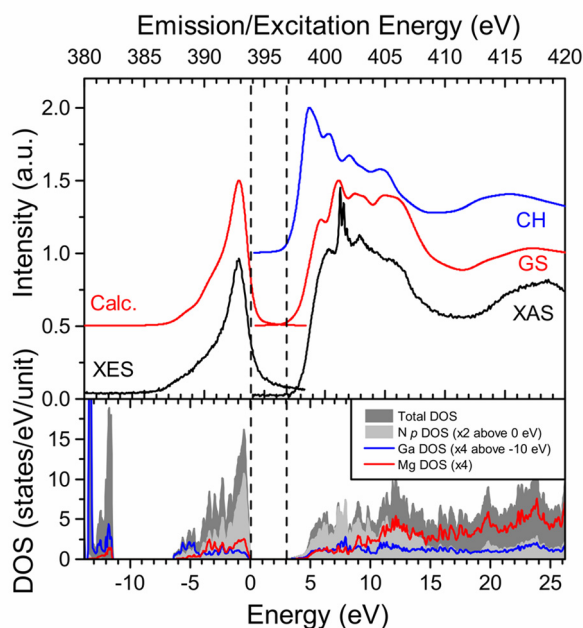


Figure 4. Calculated density of states (DOS) of Mg_3GaN_3 (bottom panel). The total DOS for all atoms is shown in dark gray, $N p$ states are light gray, and total Ga and Mg states are blue and red, respectively. Measured and calculated soft X-ray emission (XES) and absorption spectra (XAS, top panel). Measurements are shown in black, ground state (GS) calculations are red, and the core-hole (CH) absorption spectrum is shown in blue. Dashed lines represent the band-gap edges.

A band of Ga $3d$ states can be found from -15 to -11 eV, relative to the Fermi energy, in which a narrow peak of states at -13.3 eV, composed primarily of Ga $3d$ character is surrounded by hybridized Ga $3d$ and N $2s$ states. The 6.5 eV wide valence band, terminating at the Fermi energy, is dominated by N $2p$ character and contains very little charge associated with Mg or Ga. This suggests that bonding is fairly ionic, with N atoms peeling away some valence electrons from the metal sites. In fact, each Ga site only contributes 0.3 e of charge to the DOS in the valence band, essentially giving them a $3d^{10}$ valency. This could explain the energetic preference for the Mg/Ga ordering in Figure 4. Any other stoichiometric configuration would include more than one Ga-Ga coordination in the second coordination sphere, which would increase the total energy of the cell through d^{10} - d^{10} filled-shell Pauli repulsion.

The conduction band contains relatively few states from 3 eV to 5 eV. N s and p character dominate the conduction band from 5 eV to 15 eV, at which point the N p states begin to recede and N s and Mg states become more prominent.

Examining the ground-state band structure (Figure 5), the weak low-energy conduction states are observed to be the result of a single high-curvature band at the conduction-band minimum. This calculation also reveals that the band gap of Mg_3GaN_3 is direct across the Γ -point.

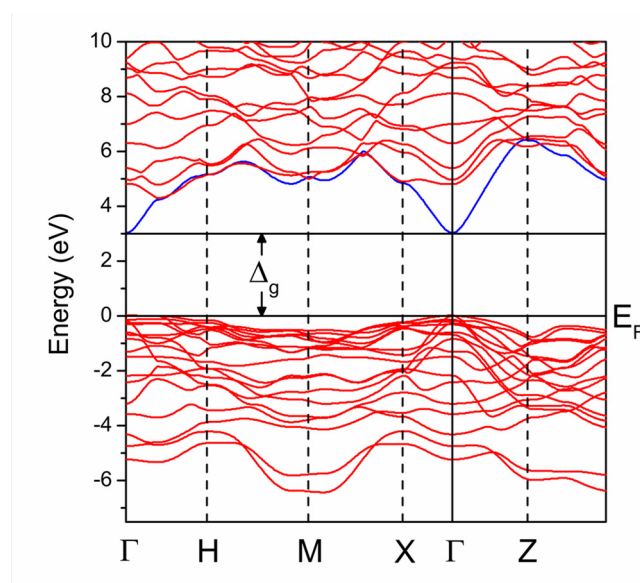


Figure 5. Calculated ground-state band structure of Mg_3GaN_3 . The blue band is responsible for the weak states near the conduction-band minimum. The chosen k -point path is standard for monoclinic unit cells.

XES and XAS offer an indirect probe of the local partial DOS in the valence and conduction bands, respectively. At the N K -edge, these techniques are predominantly sensitive to N p states. The measured N- K_{α} emission and N $1s$ absorption spectra are shown in the top frame of Figure 4 in black.

Significant CH lifetime broadening effects prevent any fine details of the emission spectrum from being resolved. There is a single peak at 392 eV (relative to the N $1s$ core level) with a broad low-energy shoulder. The measured XAS has a 3 eV wide onset, followed by four resolvable features, including an N_2 gas absorption spectrum superimposed on the Mg_3GaN_3 spectrum between 400.5 eV and 402 eV. This gas likely originates from within the material, liberated by irradiation before becoming trapped in the pockets between agglomerated crystals.^[75] Successive XAS scans show an increase in N_2 gas buildup, but no other spectral changes due to radiation damage are observed.

The WIEN2k utility XSPEC, which uses the formalism described in ref 76, is used to estimate ground-state N- K_α emission spectra from the occupied DOS and absorption spectra from the unoccupied DOS. These calculated spectra are shown in the top frame of Figure 4 in red. The calculated XES spectrum agrees well with the measured emission profile, in terms of valence bandwidth and overall shape. All three of the Mg_3GaN_3 absorption features observed in the XAS measurement are re-created in the calculated absorption spectrum at approximately the same energy, as well as a fourth feature that may have been obscured by the N_2 gas signal in the measured XAS. There is a slight disagreement in the relative peak heights between the measurement and calculation, which is likely the result of the N 1s core hole introduced in the course of an XAS measurement. Indeed, in calculations with a core hole present, the relative amplitudes of lower energy features are increased (see blue line in the top panel of Figure 4). However, such calculations almost invariably overestimate the density of CHs and their effects on the electronic structure, placing too much emphasis on the low-energy states and shifting the entire conduction band down in energy. It would be possible to decrease the CH density by further expanding the supercell or introducing fractional core holes, but such calculations are computationally expensive, and the observed CH effect is too small to make this approach worthwhile.

In the region of the valence-band maximum and conduction-band minimum, the measured and calculated spectra are in very good agreement, suggesting experimental confirmation of the predicted 3.0 eV band gap. Furthermore, the excellent overall agreement between the experimental and theoretical soft X-ray spectra lead us to conclude that the structure shown in Figure 3 is the correct choice for Mg_3GaN_3 .

3.2.3.3 Luminescence Investigations

Luminescence investigations were performed on Eu^{2+} -doped single crystals of both compounds. When irradiated with ultraviolet (UV) to blue light, crystals of $\text{Mg}_3\text{GaN}_3:\text{Eu}^{2+}$ show yellowish luminescence at room temperature. The excitation at 365 nm yields an emission band peaking at 578 nm with a lumen equivalent of 132 lm/W and CIE color coordinates of $x = 0.491$ and $y = 0.498$. The full width at half maximum (fwhm) was measured to be 4052 cm^{-1} (132 nm). The emission spectrum (Figure 6) shows a tailing on the right and a second-order excitation peak that occurs due to instrumental reasons. Eu^{2+} -doped samples of Mg_3N_2 were equally investigated under room temperature. An emission band with

a maximum intensity at 589 nm was observed when $\text{Mg}_3\text{N}_2:\text{Eu}^{2+}$ is excited at 365 nm (see Figure 6). $\text{Mg}_3\text{N}_2:\text{Eu}^{2+}$ shows a fwhm of 4056 cm^{-1} (147 nm) with a lumen equivalent of 317 lm/W and CIE color coordinates $x = 0.509$ and $y = 0.480$. An uncommon green luminescence of nondoped Mg_3N_2 powders has been reported in literature.^[28]

In both compounds, it is important to determine where the Eu^{2+} activator ions are located within the crystal structure. In most nitride host lattices, Eu^{2+} is supposed to occupy an alkaline-earth site (e.g., $\text{Ba}_3\text{Ga}_3\text{N}_5:\text{Eu}^{2+}$ and $\text{Sr}_2\text{Si}_5\text{N}_8:\text{Eu}^{2+}$).^[34,40] The ionic radii of 6-fold coordinated alkaline-earth ions Ba^{2+} (1.35 Å), Sr^{2+} (1.18 Å) and Ca^{2+} (1.00 Å) fit that of 6-fold surrounded Eu^{2+} (1.17 Å) although Ba^{2+} is slightly larger and Ca^{2+} is smaller.^[58] Nevertheless, the change of lattice structure caused by this mismatch is often helpful for luminescence, because of influence on bond lengths and the resulting change in energy-level positions. Presumably, the 4-fold coordinated Mg^{2+} site in Mg_3GaN_3 with an ionic radius of 0.57 Å is much too small to be occupied by Eu^{2+} . The mixed occupancy on the metal site can also be ruled out, because it is even smaller than a pure Mg^{2+} site. This leads to the assumption that Eu^{2+} is incorporated on interstitial sites of the crystal structure. In the network of Mg_3GaN_3 , two types of octahedral voids are present (see Figure 7a and 7b). The polyhedra around these voids are linked to themselves through edges and to each other via faces. Both octahedra offer a possible position for Eu^{2+} . Thereby, the positions displayed in yellow color in Figure 7 are suitable for Eu^{2+} , and the observed distances to N atoms of 2.320-2.489 Å are in good agreement with typical distances for Eu-N found in the literature.^[77,78]

Mg_3N_2 crystallizes in an antibixbyite type of structure. In this crystal structure, there are also two different octahedral voids; however, these are edge-sharing in all three spatial directions. Eu^{2+} atoms have been introduced onto these sites in order to verify the occurring Eu-N distances (see Figure 7c and 7d), which range from 2.489 to 2.525 Å. The highest remaining electron density during structure refinement of $\text{Mg}_3\text{N}_2:\text{Eu}^{2+}$ lies on a special site (δa) and is therefore exactly in the center of one of these octahedral voids (see Figure 7d). This could be another hint for Eu^{2+} being located on this site. Due to the low doping level (2 mol% Eu), no refinement of the occupancy of Eu on this position has been possible.

To reassess if the observed luminescence of $\text{Mg}_3\text{GaN}_3:\text{Eu}^{2+}$ and $\text{Mg}_3\text{N}_2:\text{Eu}^{2+}$ could be traced to these voids, known compounds with similar Eu-N distances and coordination numbers have been compared. One example is $\text{Li}_2\text{CaSiN}_4$, where a 6-fold coordinated Ca site was reported with Ca-N distances ranging from 2.489-2.586 Å.^[79] In the doped compound $\text{Li}_2\text{CaSiN}_4:\text{Eu}^{2+}$, it is assumed that Eu^{2+} occupies a Ca^{2+} site. The observed luminescence shows an emission-band maximum at 583-585 nm.^[80] In Eu^{2+} -doped Li- α -SiAlON, the

activator Eu^{2+} is supposed to occupy the Li^+ site.^[81] There, the coordination number is seven and distances to N/O range from 2.052 to 2.767 Å. The reported luminescence varies between 563 and 586 nm, depending on composition and Eu^{2+} concentration. This is in good agreement with the luminescence data of $\text{Mg}_3\text{GaN}_3:\text{Eu}^{2+}$ and $\text{Mg}_3\text{N}_2:\text{Eu}^{2+}$, so we can assume that Eu^{2+} occupies an interstitial position in these two nitride networks. To understand the origin and the quality of luminescence properties, detailed knowledge of the local environment of the activator ion is necessary. Recent investigations focused on determination of Eu contribution in the M sites in $M_2\text{Si}_5\text{N}_8$ (where $M = \text{Ca}, \text{Sr}, \text{Ba}$). With a high concentration of Eu^{2+} , a reliable distribution and a preferred site can be determined based on structural refinement methods and composition investigations.^[82] These investigations give an indication of the average Eu^{2+} contribution, statistically distributed over the entire crystal, but no information of the local structure of the activator can be achieved. Another recent approach to detect interstitial dopants and elucidate local surrounding of the dopant involved scanning transmission electron microscopy (STEM) investigations on β -SiAlON. There, a single dopant ion was detected in the atomic channel of the crystal structure.^[83] This method seems quite promising when the layer thickness is suitable for such measurements and the crystal structure reveals appropriate requirements. Nevertheless, it is still difficult to determine the real location and the amount of activator ions in such host lattices.

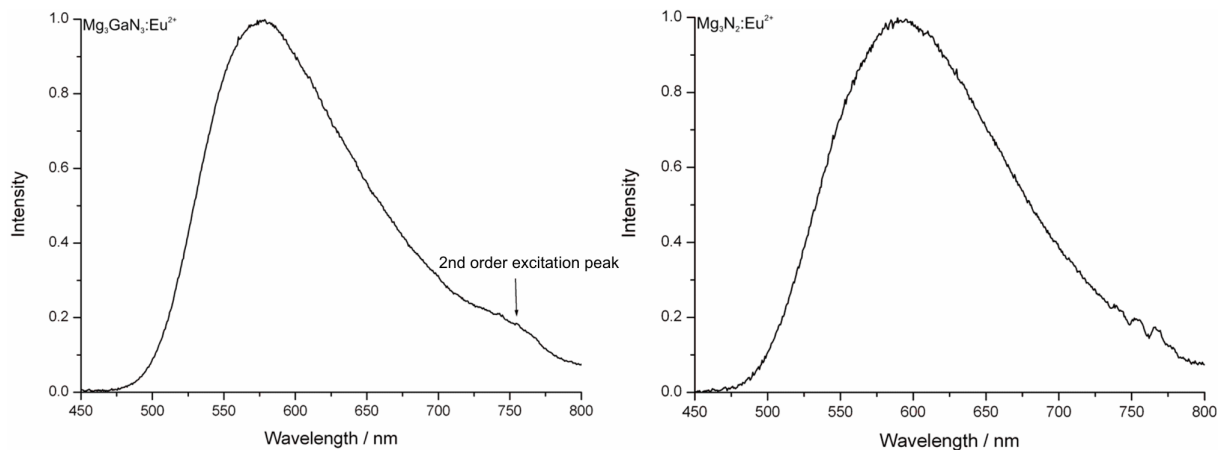


Figure 6. Emission spectra of $\text{Mg}_3\text{GaN}_3:\text{Eu}^{2+}$ (left) and $\text{Mg}_3\text{N}_2:\text{Eu}^{2+}$ (right).

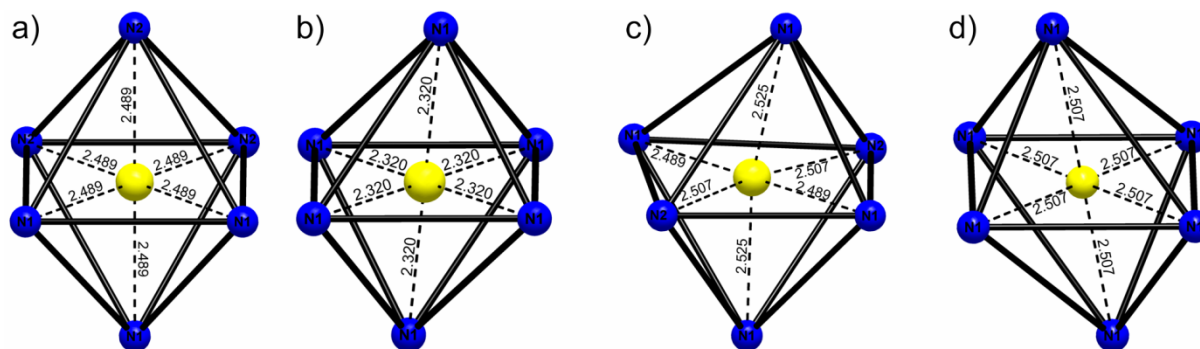


Figure 7. Octahedral voids in the crystal structures of Mg_3GaN_3 (panels a and b) and Mg_3N_2 (panels c and d). The yellow spheres are possible Eu -atom positions, and the resulting distances to coordinating N are given in Å.

3.2.3.4 Conclusion

In this study we present a structural description of Mg_3GaN_3 based on single-crystal X-ray diffraction (XRD) data, which shows a 3D uncharged network of corner- and edge-sharing MgN_4 and mixed $(\text{Mg}/\text{Ga})\text{N}_4$ tetrahedra. Since all metal atoms are part of the tetrahedral network, Mg_3GaN_3 can be classified as a double nitride, in contrast to known nitridogallates, which exhibit an anionic tetrahedra substructure with electropositive counterions such as Sr^{2+} or Ba^{2+} . To our knowledge, the compound Mg_3GaN_3 represents the first known stoichiometrically defined ternary compound in the system $\text{Mg}/\text{Ga}/\text{N}$. It is found to be a semiconductor with a direct band gap of 3.0 eV across the Γ -point. Density functional theory (DFT) calculations suggest a periodic ordering on the metal sites, and the measured soft X-ray spectra confirm these calculations. The band gap of Mg_3GaN_3 (3.0 eV) ranges between that of Mg_3N_2 (2.8 eV)^[84] and GaN (3.02–3.20 eV),^[85] which further emphasizes the double nitride character of Mg_3GaN_3 . Upon doping with Eu^{2+} , the double nitride shows broad-band emission due to $4f^6(^7F)5d^1 \rightarrow 4f^7(^8S_{7/2})$ transitions with maximum intensity at 578 nm after excitation at 365 nm. Because of the structural characteristics of $\text{Mg}_3\text{GaN}_3:\text{Eu}^{2+}$, it is assumed that activator ions are localized in interstitial octahedral voids of the crystal structure.

A similar luminescent binary nitride, $\text{Mg}_3\text{N}_2:\text{Eu}^{2+}$, is also investigated. Structural details are known from the literature and presumably Eu^{2+} also occupies interstitial sites. After excitation with ultraviolet (UV) to blue light, this compound shows luminescence with an emission-band maximum at 589 nm with a full width at half maximum (fwhm) of 4056 cm^{-1} (147 nm).

Both presented nitrides are new host lattices for Eu^{2+} doping and show interesting luminescence properties. The results of this study illustrate the potential of nitrides as host lattices for Eu^{2+} doping once again. It is remarkable that the double nitride Mg_3GaN_3 is the first representative showing luminescence, to the best of our knowledge. Further optimization

of synthesis and the optical properties of these materials must be achieved for them to have possible applications as phosphor materials.

Acknowledgment

The authors gratefully acknowledge financial support by the Fonds der Chemischen Industrie (FCI), Germany; the Natural Sciences and Engineering Research Council of Canada (NSERC); and the Canada Research Chair Program. Calculations utilized Compute Canada's WestGrid HPC consortium. We also thank Thomas Miller and Dr. Peter Mayer for X-ray diffraction data collection, Christian Minke for EDX/SEM investigations (all at LMU Munich, Department of Chemistry), Detlef Wiechert for emission spectra data collection (Lumileds Development Center Aachen) and Teak Boyko (University of Saskatchewan) for advice on soft X-ray measurements and DFT calculations. Research was performed at the REIXS beamline of the Canadian Light Source, which is supported by NSERC, the National Research Council Canada, the Canadian Institutes of Health Research, the Province of Saskatchewan, Western Economic Diversification Canada, and the University of Saskatchewan.

3.2.3.5 References

- [1] S. Nakamura, M. Senoh, N. Iwasa, S. Nagahama, T. Yamada, T. Mukai, *Jpn. J. Appl. Phys.* **1995**, *34*, L1332-L1335.
- [2] S. Nakamura, *Solid State Commun.* **1997**, *102*, 237-248.
- [3] T. Fujii, Y. Gao, R. Sharma, E. L. Hu, S. P. DenBaars, S. Nakamura, *Appl. Phys. Lett.* **2004**, *84*, 855-857.
- [4] S. Nakamura, *Science* **1998**, *281*, 956-961.
- [5] S. Nakamura, S. Pearton, G. Fasol, *The Blue Laser Diode*, Springer Verlag, Berlin, **2000**.
- [6] A. Denis, G. Goglio, G. Demazeau, *Mater. Sci. Eng.* **2006**, *R 50*, 167-194.
- [7] M. Bockowski, *Cryst. Res. Technol.* **2007**, *42*, 1162-1175.
- [8] S. Krukowski, P. Kempisty, P. Strak, *Cryst. Res. Technol.* **2009**, *44*, 1038-1046.
- [9] B. Wang, M. J. Callahan, *Cryst. Growth Des.* **2006**, *6*, 1227-1246.
- [10] R. P. Parikh, R. A. Adomaitis, *J. Cryst. Growth* **2006**, *286*, 259-278.

- [11] T. Onuma, A. Uedono, H. Asamizu, H. Sato, J. F. Kaeding, M. Iza, S. P. DenBaars, S. Nakamura, S. F. Chichibu, *Appl. Phys. Lett.* **2010**, *96*, 091913.
- [12] S. Nakamura, M. Senoh, T. Mukai, *Jpn. J. Appl. Phys.* **1991**, *30*, L1708.
- [13] S. Nakamura, T. Mukai, M. Senoh, N. Iwasa, *Jpn. J. Appl. Phys.* **1992**, *31*, L139.
- [14] C. H. Kuo, S. J. Chang, Y. K. Su, L. W. Wu, J. K. Sheu, C. H. Chen, G. C. Chi, *Jpn. J. Appl. Phys.* **2008**, *41*, L112.
- [15] Y. Nakano, O. Fujishima, T. Kachi, *J. Appl. Phys.* **2004**, *96*, 415-419.
- [16] Z. Chen, N. Fichtenbaum, D. Brown, S. Keller, U. K. Mishra, S. P. DenBaars, S. Nakamura, *J. Electron. Mater.* **2008**, *37*, 546-549.
- [17] Y. Zohta, Y. Iwasaki, S. Nakamura, T. Mukai, *Jpn. J. Appl. Phys.* **2001**, *40*, L423-L425.
- [18] T. Akiyama, D. Ammi, K. Nakamura, T. Ito, *Jpn. J. Appl. Phys.* **2009**, *48*, 110202.
- [19] F. Shahedipour, B. W. Wessels, *Appl. Phys. Lett.* **2000**, *76*, 3011-3013.
- [20] D. Ehrentraut, E. Meißner, M. Bockowski, *Technology of Gallium Nitride Crystal Growth*, Springer, Berlin, Heidelberg, **2010**, Vol. 133.
- [21] M. A. Reshchikov, G.-C. Yi, B. W. Wessels, *Phys. Rev. B* **1999**, *59*, 13176-13183.
- [22] B. Z. Qu, Q. S. Zhu, X. H. Sun, S. K. Wan, Z. G. Wang, H. Nagai, Y. Kawaguchi, K. Hiramatsu, N. Sawaki, *J. Vac. Sci. Technol. A* **2003**, *21*, 838-843.
- [23] U. Kaufmann, M. Kunzer, M. Maier, H. Obloh, A. Ramakrishnan, B. Santic, P. Schlotter, *Appl. Phys. Lett.* **1998**, *72*, 1326-1328.
- [24] M. von Stackelberg, R. Paulus, *Z. Phys. Chem. (Abt. B)* **1933**, *22*, 305-322.
- [25] J. David, Y. Laurent, J. Lang, *Bull. Soc. Fr. Mineral. Cristallogr.* **1971**, *94*, 340-346.
- [26] D. E. Partin, D. J. Williams, M. O'Keefe, *J. Solid State Chem.* **1997**, *132*, 56-59.
- [27] O. Reckeweg, F. J. DiSalvo, *Z. Anorg. Allg. Chem.* **2001**, *627*, 371-377.
- [28] X. Chengshan, A. Yujie, S. Lili, S. Chuanwei, Z. Huizhao, W. Fuxue, Y. Zhaozhu, Q. Lixia, C. Jinhua, L. Hong, *Rare Metal Materials and Engineering* **2007**, *36*, 2020-2022.
- [29] P. Dorenbos, *J. Lumin.* **2003**, *104*, 239-260.
- [30] P. Dorenbos, *ECS J. Solid State Sci. Technol.* **2013**, *2*, R3001-R3011.
- [31] O. M. ten Kate, Z. Zhang, P. Dorenbos, H. T. Hintzen, E. van der Kolk, *J. Solid State Chem.* **2013**, *197*, 209-217.
- [32] H. A. Höpfe, *Angew. Chem.* **2009**, *121*, 3626-3636; *Angew. Chem. Int. Ed.* **2009**, *3648*, 3572-3582.

- [33] Y. Q. Li, N. Hirosaki, R. J. Xie, T. Takeda, M. Mitomo, *J. Solid State Chem.* **2008**, *181*, 3200-3210.
- [34] M. Zeuner, S. Pagano, W. Schnick, *Angew. Chem.* **2011**, *123*, 7898-7920; *Angew. Chem. Int. Ed.* **2011**, *7850*, 7754-7775.
- [35] W. Schnick, *Phys. Status Solidi RRL* **2009**, *3*, A113-A114.
- [36] M. Seibald, O. Oeckler, V. R. Celinski, P. J. Schmidt, A. Tücks, W. Schnick, *Solid State Sci.* **2011**, *13*, 1769-1778.
- [37] J. A. Kechele, C. Hecht, O. Oeckler, J. Schmedt auf der Günne, P. J. Schmidt, W. Schnick, *Chem. Mater.* **2009**, *21*, 1288-1295.
- [38] K. Shioi, N. Hirosaki, R.-J. Xie, T. Takeda, Y. Q. Li, *J. Mater. Sci.* **2010**, *45*, 3198-3203.
- [39] S. Pagano, S. Lupart, M. Zeuner, W. Schnick, *Angew. Chem.* **2009**, *121*, 6453-6456; *Angew. Chem. Int. Ed.* **2009**, *48*, 6335-6338.
- [40] F. Hintze, F. Hummel, P. J. Schmidt, D. Wiechert, W. Schnick, *Chem. Mater.* **2012**, *24*, 402-407.
- [41] S. J. Clarke, F. J. DiSalvo, *Inorg. Chem.* **1997**, *36*, 1143-1148.
- [42] F. Hintze, W. Schnick, *Z. Anorg. Allg. Chem.* **2012**, *638*, 2243-2247.
- [43] L. J. Farrugia, *J. Appl. Crystallogr.* **1999**, *32*, 837-838.
- [44] X-RED 32, 1.03 ed., Darmstadt, **2002**.
- [45] SHELXS, Universität Göttingen, **1997**.
- [46] G. M. Sheldrick, *Acta Crystallogr. Sect. A: Found. Crystallogr.* **2008**, *64*, 112-122.
- [47] SHELXL, Universität Göttingen, **1997**.
- [48] P. Blaha, K. Schwarz, G. K. H. Madsen, D. Kvasnicka, J. Luitz, WIEN2K An Augmented Plane Wave + Local Orbitals Program for Calculating Crystal Properties, Technical University Vienna, **2001**.
- [49] J. P. Perdew, K. Burke, M. Ernzerhof, *Phys. Rev. Lett.* **1996**, *77*, 3865-3868.
- [50] A. D. Becke, E. R. Johnson, *J. Chem. Phys.* **2006**, *124*, 221101.
- [51] F. Tran, P. Blaha, *Phys. Rev. Lett.* **2009**, *102*, 226401.
- [52] P. Verdier, R. Marchand, J. Lang, *C. R. Acad. Sci. Ser. C.* **1970**, *271*, 1002-1004.
- [53] D. G. Park, Y. Dong, F. J. DiSalvo, *Solid State Sci.* **2008**, *10*, 1846-1852.
- [54] A. L. Spek, *Acta Crystallogr. Sect. D: Biol. Crystallogr.* **2009**, *65*, 148-155.
- [55] P. Van Der Sluis, A. L. Spek, *Acta Crystallogr. Sect. A: Found. Crystallogr.* **1990**, *46*, 194-201.
- [56] D. G. Park, Z. A. Gál, F. J. DiSalvo, *J. Alloys Compd.* **2003**, *360*, 85-89.

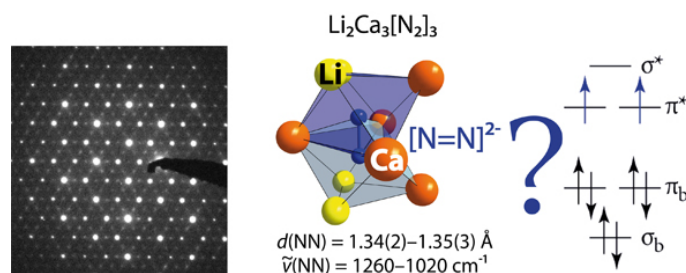
- [57] W. H. Baur, *Crystallogr. Rev.* **1987**, *1*, 59-80.
- [58] R. D. Shannon, *Acta Crystallogr., Sect. A: Found. Crystallogr.* **1976**, *32*, 751-767.
- [59] J. C. Slater, *J. Chem. Phys.* **1964**, *41*, 3199-3204.
- [60] F. Liebau, *Structural Chemistry of Silicates*, Springer, Berlin, **1985**.
- [61] M. Roos, J. Wittrock, G. Meyer, S. Fritz, J. Strähle, *Z. Anorg. Allg. Chem.* **2000**, *626*, 1179-1185.
- [62] M. Wintenberger, F. Tcheou, J. David, J. Lang, *Z. Naturforsch. B* **1980**, *35*, 604-606.
- [63] J. Schneider, F. Frey, N. Johnson, K. Laschke, *Z. Kristallogr.* **1994**, *209*, 328-333.
- [64] H. A. Höpfe, *Doctoral Thesis*, Ludwig-Maximilians-Universität München **2003**.
- [65] K. Köllisch, *Doctoral Thesis*, Ludwig-Maximilians-Universität München **2001**.
- [66] R. Lauterbach, *Doctoral Thesis*, Universität Bayreuth **1999**.
- [67] S. Saib, N. Bouarissa, *Physica B: Condensed Mater.* **2007**, *387*, 377-382.
- [68] D. G. Park, Z. A. Gál, F. J. DiSalvo, *Inorg. Chem.* **2003**, *42*, 1779-1785.
- [69] H. Hiraguchi, H. Hashizume, O. Fukunaga, A. Takenaka, M. Sakata, *J. Appl. Crystallogr.* **1991**, *24*, 286-292.
- [70] W. Schnick, J. Lücke, *J. Solid State Chem.* **1990**, *87*, 101-106.
- [71] F. J. Pucher, S. R. Römer, F. W. Karau, W. Schnick, *Chem. Eur. J.* **2010**, *16*, 7208-7214.
- [72] E. Orhan, S. Jovic, R. Brec, R. Marchand, J. Y. Saillard, *J. Mater. Chem.* **2002**, *12*, 2475-2479.
- [73] K. Momma, F. Izumi, *J. Appl. Crystallogr.* **2011**, *44*, 1272.
- [74] N. W. Johnson, J. A. McLeod, A. Moewes, *J. Phys.: Condens. Matter* **2011**, *23*, 445501.
- [75] C. Braun, S. L. Börger, T. D. Boyko, G. Miehe, H. Ehrenberg, P. Höhn, A. Moewes, W. Schnick, *J. Am. Chem. Soc.* **2011**, *133*, 4307-4315.
- [76] K. Schwarz, A. Neckel, J. Nordgren, *J. Phys. F: Met. Phys.* **1979**, *9*, 2509-2521.
- [77] H. Huppertz, W. Schnick, *Acta Crystallogr., Sect. C: Cryst. Struct. Commun.* **1997**, *53*, 1751-1753.
- [78] M. Zeuner, S. Pagano, P. Matthes, D. Bichler, D. Johrendt, T. Harmening, R. Pöttgen, W. Schnick, *J. Am. Chem. Soc.* **2009**, *131*, 11242-11248.
- [79] M. Zeuner, S. Pagano, S. Hug, P. Pust, S. Schmiechen, C. Scheu, W. Schnick, *Eur. J. Inorg. Chem.* **2010**, *2010*, 4945-4951.
- [80] M. Zeuner, *Doctoral Thesis*, Ludwig-Maximilians-Universität München **2009**.

- [81] R.-J. Xie, N. Hirosaki, M. Mitomo, K. Sakuma, N. Kimura, *Appl. Phys. Lett.* **2006**, *89*, 241103.
- [82] Y.-I. Kim, K. B. Kim, Y.-H. Lee, K.-B. Kim, *J. Nanosci. Nanotechnol.* **2012**, *12*, 3443-3446.
- [83] K. Kimoto, R.-J. Xie, Y. Matsui, K. Ishizuka, N. Hirosaki, *Appl. Phys. Lett.* **2009**, *94*, 041908.
- [84] M. C. Fang, R. A. de Groot, R. J. Bruls, H. T. Hintzen, G. de With, *J. Phys.: Condens. Matter* **1999**, *11*, 4833.
- [85] Y. Duan, L. Qin, L. Shi, G. Tang, H. Shi, *Appl. Phys. Lett.* **2012**, *199*, 022104.

4. Crystal-Structure Investigations of Other Nitride Compounds

4.1 High-Pressure Synthesis and Characterization of $\text{Li}_2\text{Ca}_3[\text{N}_2]_3$ – An Uncommon Metallic Diazenide with $[\text{N}_2]^{2-}$ Ions

Sebastian B. Schneider, Markus Seibald, Volker L. Deringer, Ralf P. Stoffel, Gina M. Friederichs, Henryk Laqua, Viola Duppel, Gunnar Jeschke, Richard Dronskowski, and Wolfgang Schnick



published in: *J. Am. Chem. Soc.* **2013**, *135*, 16668-16679.

Copyright © 2013 American Chemical Society

Abstract

Dinitrogen (N_2) ligation is a common and well-characterized structural motif in bioinorganic synthesis. In solid-state chemistry, on the other hand, homonuclear dinitrogen entities as structural building units proved existence only very recently. High-pressure/high-temperature (HP/HT) syntheses have afforded a number of binary diazenides and pernitrides with $[\text{N}_2]^{2-}$ and $[\text{N}_2]^{4-}$ ions, respectively. Here, we report on the HP/HT synthesis of the first ternary diazenide. $\text{Li}_2\text{Ca}_3[\text{N}_2]_3$ (space group *Pmma*, no. 51, $a = 4.7747(1)$, $b = 13.9792(4)$, $c = 8.0718(4) \text{ \AA}$, $Z = 4$, $wR_p = 0.08109$) was synthesized by controlled thermal decomposition of a stoichiometric mixture of lithium azide and calcium azide in a multianvil device under a pressure of 9 GPa and 1023 K. Powder X-ray diffraction analysis reveals strongly elongated N–N bond lengths of $d_{\text{NN}} = 1.34(2)\text{--}1.35(3) \text{ \AA}$ exceeding those of previously known, binary diazenides. In fact, the refined N–N distances in $\text{Li}_2\text{Ca}_3[\text{N}_2]_3$ would rather suggest the presence of $[\text{N}_2]^{3-}$ radical ions. Also, characteristic features of the N–N stretching vibration occur at lower wavenumbers ($1260\text{--}1020 \text{ cm}^{-1}$) than in the binary phases, and these assignments are supported by first-principles phonon calculations. Ultimately, the true character of the N_2 entity in $\text{Li}_2\text{Ca}_3[\text{N}_2]_3$ is probed by a variety of complementary techniques,

including electron diffraction, electron spin resonance spectroscopy (ESR), magnetic and electric conductivity measurements, as well as density-functional theory calculations (DFT). Unequivocally, the title compound is shown to be metallic containing diazenide $[\text{N}_2]^{2-}$ units according to the formula $(\text{Li}^+)_2(\text{Ca}^{2+})_3([\text{N}_2]^{2-})_3 \cdot (\text{e}^-)_2$.

Keywords: Diazenide, Solid-State Chemistry, Density-Functional Theory (DFT), High-Pressure/High-Temperature, Lithium

4.1.1 Introduction

Among the most important processes in modern chemistry is the conversion of dinitrogen molecules (N_2) into environmentally sustainable intermediates or products. This process is referred to as “nitrogen fixation”. In industry, this process is named after its inventors *Fritz Haber* and *Carl Bosch*, the Haber–Bosch cycle,^[1] which offers rapid access to synthetic fertilizers and has become essential for the nutrition of a large amount of the world population. In nature, this enormously expensive and complex industrial process is replaced by the enzyme nitrogenase, whose crystal structure has been determined only recently.^[2] Nitrogenases can cleave the $\text{N}\equiv\text{N}$ triple bond already at ambient conditions and transform it into ammonia, which however consumes huge amounts of energy (adenosine triphosphate, ATP).^[3,4] Nitrogenase fixes atmospheric dinitrogen through an inimitable class of various metal clusters.^[2,5–9] However, despite detailed knowledge of these structural motifs, a basic mechanism for the biological process still lacks evidence. Hence, the activation and conversion of free N_2 to ammonia including the characterization of a diversity of intermediates with bound dinitrogen is one of the major challenges in bioinorganic and organo-metallic chemistry, to finally unravel nature’s mystery.^[10]

Synthetic nitrogen fixation focuses on the binding, activation and reduction of N_2 on mono-, di- and polynuclear transition metal centers coordinated by capacious steric ligands. Mono- and dinuclear transition metal complexes have long been known to activate dinitrogen in various ways: they enable protonation, reduction, functionalization and even N–N bond cleavage steps. Besides a handful of examples of transition metal complexes with trapped and activated N_2 , up to date only two distinct classes of molybdenum- or tungsten-based model systems have emerged, involving a full set of well-defined intermediates, such as diazenido,

hydrazido, nitrido, imido, amido or amine intermediates, on the way from N_2 to NH_3 . These systems form the basis of the Chatt and the Schrock cycles.^[11,12]

However, true mimicry of the multielectron reduction process still proves difficult because both cycles explain the sequence of reactions involved in biological dinitrogen reduction, on the one hand, but only a low yield catalytic reaction is observed in one of those systems, on the other hand.^[11–23] The monometallic model systems of Chatt and Schrock cycles bind N_2 in an *end-on* manner and therefore lead to only weakly or moderately activated N_2 -intermediates, which might be the crucial factor for the absence of a catalytic reaction. The binding of N_2 in *side-on* manner is usually accessed by homonuclear bimetallic complexes. Common oxidation states for *side-on* bound N_2 when acting as a ligand are 0, $-\text{II}$ or $-\text{IV}$ representing nonactivated dinitrogen(0), diazenido $[\text{N}_2]^{2-}$, or hydrazido $[\text{N}_2]^{4-}$ intermediates. This is not surprising as the dinitrogen ligand is reduced in multiples of two electrons, because each of the two metal atoms contributes either zero, one or two electrons to nitrogen reduction. Odd-electron nitrogen oxidation states, instead, propose radical character and one-electron reduction mechanisms, but have not been observed in Chatt or Schrock cycles so far. However, this potential intermediacy of $[\text{N}_2]^{-}$ or $[\text{N}_2]^{3-}$ radical ions in metal complexes proved existence only very recently in dinuclear nickel, iron and lanthanide complexes, respectively.^[10,24–33] Thereby, $[\text{N}_2]^{-}$ were found to exhibit N–N bond lengths of about 1.13–1.18 Å and N–N stretching frequencies of 1740–1950 cm^{-1} ,^[10,24–26,32,33] whereas the d_{NN} in $[\text{N}_2]^{3-}$ ions was found to be at 1.39–1.41 Å with shifted N–N stretching energies of below 1000 cm^{-1} .^[27–33] To gain final evidence for the presence of such radical anions $[\text{N}_2]^{-}$ or $[\text{N}_2]^{3-}$, electron spin resonance spectroscopy (ESR) revealed clearly visible signals in accordance with simulated spectra indicative of unpaired electrons and supporting the radical formulation of dinitrogen ligation.^[24,27,28] Gauging “weakly” to “highly” activated systems is possible at the hand of N–N bond lengths and corresponding N–N stretching frequencies in spectroscopic studies of bound dinitrogen molecules or ions. For such purpose, reliable crystallographic and spectroscopic data for protonated reference compounds, such as diazene $\text{HN}=\text{NH}$ and hydrazine N_2H_4 , are required to facilitate the classification of even- and odd-electron nitrogen-oxidation states. Surprisingly, given the importance of homonuclear dinitrogen anions in biological and organo-metallic chemistry, it was not before 2001 that such ions have been observed in solid-state chemistry for the first time.^[34–39] Pioneering works by *Kniep* et al. introduced the hitherto unknown compounds Sr_4N_3 ($\equiv \text{Sr}_8\text{N}_4[\text{N}_2]\cdot 2\text{e}^-$), SrN ($\equiv \text{Sr}_8\text{N}_4[\text{N}_2]_2$), SrN_2 and BaN_2 , which are the first so-called diazenides with ionic $[\text{N}_2]^{2-}$ units. The latter show characteristic N–N bond lengths (1.22 Å) and stretching frequencies (1307 cm^{-1} in SrN_2

and 1380 cm^{-1} in SrN), which may be compared to protonated diazene N_2H_2 ($1.21\text{--}1.25\text{ \AA}$, $1400\text{--}1700\text{ cm}^{-1}$).^[34–45] Only five years later, high-pressure/high-temperature (HP/HT) experiments revealed the existence of noble metal compounds with $M\text{N}_2$ stoichiometry ($M = \text{Os, Ir, Pd}$ and Pt) exhibiting ultrahigh hardness with bulk moduli of about $250\text{--}350\text{ GPa}$.^[46–53] Theoretical investigations finally concluded the presence of tetravalent metals and $[\text{N}_2]^{4-}$ anions, with N–N bond lengths (about 1.40 \AA) and stretching frequencies ($700\text{--}1000\text{ cm}^{-1}$) similar to those of hydrazine N_2H_4 ($d_{\text{NN}} = 1.47\text{ \AA}$, $\nu_{\text{NN}} < 1000\text{ cm}^{-1}$).^[46–57] The latter anions are isoelectronic with peroxides $[\text{O}_2]^{2-}$, and so they were dubbed “pernitrides”. In 2012, we were able to extend the compositional range of binary diazenides by subjecting ionic azides to HP/HT conditions in a multianvil device.^[58,59] We succeeded in synthesizing SrN_2 and BaN_2 , as well as the unprecedented (but theoretically predicted) CaN_2 and also Li_2N_2 , the latter one representing the first alkali diazenide.^[58–61] Crystallographic, spectroscopic, and theoretical investigations confirmed the presence of $[\text{N}_2]^{2-}$ anions in these crystal structures.^[58,59] Only very recently, LaN_2 ($\equiv \text{La}^{3+}[\text{N}_2]^{2-}\cdot\text{e}^-$) proved existence in shockwave experiments in accord with theoretical predictions.^[54,62] Again, crystallographic studies showed the presence of diazenide anions with slightly elongated N–N bonds ($1.30\text{--}1.32\text{ \AA}$), possibly due to the metallic character of the crystalline host. In summary, the recent success in identifying diazenides and pernitrides in solid-state chemistry has fuelled various theoretical and synthetic efforts to predict and characterize further compounds containing dinitrogen anions. However, despite the as-mentioned examples, no further representatives of diazenides, pernitrides, or even intermediate dinitrogen ions are known to date in ionic solids.

In this contribution, we present the successful synthesis and structural elucidation of $\text{Li}_2\text{Ca}_3[\text{N}_2]_3$, the first ternary compound with dinitrogen anions. Detailed crystallographic, spectroscopic, and theoretical studies at the respective state-of-the-art support the presence of solely $[\text{N}_2]^{2-}$ anions in the crystal structure. As we demonstrate, the title compound may be seen as the first ternary sub-diazenide with $(\text{Li}^+)_2(\text{Ca}^{2+})_3([\text{N}_2]^{2-})_3\cdot(\text{e}^-)_2$ formulation.

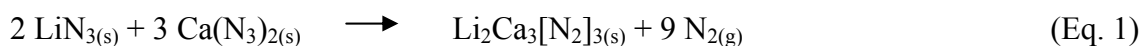
4.1.2 Experimental Section

4.1.2.1 Synthesis of $\text{Li}_2\text{Ca}_3[\text{N}_2]_3$

$\text{Li}_2\text{Ca}_3[\text{N}_2]_3$ was prepared under HP/HT conditions in a modified Walker-type module in combination with a 1000 t press (Voggenreiter, Mainleus, Germany). As pressure medium,

Cr_2O_3 doped (5%) MgO-octahedra (Ceramic Substrates & Components, Isle of Wight, UK) with edge lengths of 18 mm (18/11 assembly) were employed. Eight tungsten carbide cubes (Hawedia, Marklkofen, Germany) with truncation edge lengths of 11 mm compressed the octahedron.

$\text{Li}_2\text{Ca}_3[\text{N}_2]_3$ can be synthesized from two different stoichiometric mixtures of lithium and calcium azides according to equations 1 and 2. For a detailed description of the synthesis of both azides, see Supporting Information.



The corresponding mixtures were carefully ground, filled into a cylindrical boron nitride crucible (Henze BNP GmbH, Kempten, Germany) and sealed with a fitting boron nitride plate. Details of the setup are described in the literature.^[63–67] The assembly was compressed up to 9 GPa at room temperature within 213 min, then heated up to 1023 K in 10 min, kept at this temperature for 20 min, and cooled down to room temperature in 10 min again. Subsequently, the pressure was released over a period of 620 min. The recovered MgO-octahedron was broken apart in a glovebox (Unilab, MBraun, Garching; $\text{O}_2 < 1$ ppm, $\text{H}_2\text{O} < 1$ ppm), and the sample was carefully isolated from the surrounding boron nitride crucible. Besides a golden metallic powder of the title compound (see Figure S1 in the Supporting Information), which is very sensitive to moisture, small amounts of a red, but yet not identified side-phase were obtained.

4.1.2.2 Powder X-ray Diffraction (PXRD)

For powder X-ray diffraction experiments, ground $\text{Li}_2\text{Ca}_3[\text{N}_2]_3$ was loaded into tube capillaries (Hilgenberg, Malsfeld, Germany) with diameters of 0.2–0.3 mm in a glovebox. Data were recorded with a STOE Stadi P powder diffractometer (STOE, Darmstadt, Germany) in Debye–Scherrer geometry using Ge(111) monochromated Cu and Mo $K_{\alpha 1}$ -radiation (1.54056 and 0.7093 Å) with a step size of 0.01° . Data acquisition was done using the STOE software (WinXPOW). The indexing, integration and extraction of the intensities as well as the structure solution and Rietveld refinement were performed with the TOPAS package (see Figure 1).^[68]

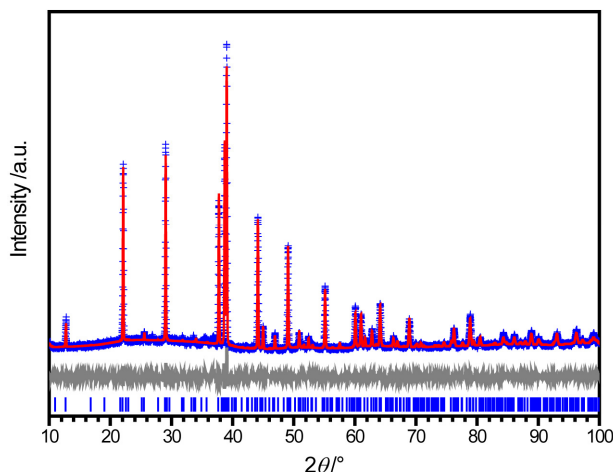


Figure 1. Observed (blue) and calculated (red) powder diffraction pattern (Cu $K_{\alpha 1}$ radiation, 1.54056 Å) and difference profile (gray) of the Rietveld refinement of $\text{Li}_2\text{Ca}_3[\text{N}_2]_3$. Peak positions are marked by vertical blue lines (bottom).

The reflection profiles were determined using the fundamental parameter approach^[69] by convolution of appropriate source emission profiles with axial instrument contributions and crystalline microstructure effects. Preferred orientation of the crystallites was described with a spherical harmonic of fourth order. A search for potential higher symmetry obtained after structure solutions and Rietveld refinements was carried out using the program PLATON.^[70] The relevant crystallographic data for the title compound as well as further details of the data collection are summarized in Tables 1 and S1 in the Supporting Information. Further information of the crystal structure may be obtained from the Fachinformationszentrum Karlsruhe, 76344 Eggenstein-Leopoldshafen, Germany (fax: (49) 7247-808-666; e-mail: crysdata@fiz-karlsruhe.de) on quoting the depository number CSD-426449.

High-temperature *in situ* X-ray powder diffraction data were collected with a STOE Stadi P powder diffractometer (Mo $K_{\alpha 1}$ -radiation (0.7093 Å)) equipped with a computer-controlled STOE resistance graphite furnace. Enclosed in a silica glass capillary under argon, the samples were heated from room temperature to 700 K at a rate of 5 K/min in steps of 25 K (see Figure S2 in the Supporting Information). At each heating step (after holding the temperature for 1 min), a diffraction pattern was recorded with an IP-PSD in the range of $2^\circ \leq 2\theta \leq 80^\circ$. At about 610 K, the sample decomposed spontaneously.

Low-temperature *in situ* X-ray powder diffraction data were collected in intervals of 5 K using a Huber G670 Guinier imaging plate diffractometer (Co $K_{\alpha 1}$ radiation (1.7890 Å)) equipped with a closed cycle He-cryostat. The samples were cooled down from room temperature to 10 K in 5 K/min. At each cooling step (after holding the temperature for

1 minute), a diffraction pattern was recorded in the range of $10^\circ \leq 2\theta \leq 80^\circ$. No phase transition was observed.

Table 1. Refined atomic coordinates and isotropic displacement factors of $\text{Li}_2\text{Ca}_3[\text{N}_2]_3$.^[a]

atom (Wyckoff)	<i>x</i>	<i>y</i>	<i>z</i>	U_{iso} (0.01 \AA^2) ^[b]
Li1 (4g)	0	0.346(2)	0	0.033(9)
Li2 (4h)	0	0.847(3)	$\frac{1}{2}$	0.02(1)
Ca1 (2e)	$\frac{1}{4}$	0	0.697(1)	0.039(3)
Ca2 (2f)	$\frac{1}{4}$	$\frac{1}{2}$	0.195(2)	0.042(4)
Ca3 (4k)	$\frac{1}{4}$	0.1446(5)	0.164(1)	0.055(3)
Ca4 (4k)	$\frac{1}{4}$	0.6435(5)	0.651(1)	0.057(3)
N1 (4k)	$\frac{1}{4}$	0.177(1)	0.7043(9)	0.027(6)
N2 (4k)	$\frac{1}{4}$	0.6656(8)	0.2002(9)	0.048(9)
N3 (4k)	$\frac{1}{4}$	0.048(2)	0.410(4)	0.06(1)
N4 (4k)	$\frac{1}{4}$	0.548(1)	0.91(3)	0.027(7)
N5 (4k)	$\frac{1}{4}$	0.2860(8)	0.343(2)	0.026(5)
N6 (4k)	$\frac{1}{4}$	0.803(1)	0.867(1)	0.04(1)

[a] Space group *Pmma* (no. 51), $a = 4.7747(1)$, $b = 13.9792(4)$, $c = 8.0718(4)$ Å, $Z = 4$; [b] $U_{iso} = B_{eq}/(8 \cdot \pi^2)$.

4.1.2.3 Transmission Electron Microscopy (TEM)

All manipulations for the preparation and transfer of the sample were carried out under argon atmosphere. Data were recorded with a Philips CM30/ST (LaB₆ cathode) at 300 kV. Selected area electron diffraction (SAED) as well as precession electron diffraction patterns (PED) were collected with a GATAN slow-scan CCD camera. Simulations of diffraction patterns were calculated with the EMS program package.^[71] Elemental analysis by EDX was performed with a Si/Li detector (Thermo Fischer, NSS). Tilt series of diffraction patterns were obtained using a double tilt sample holder with maximum tilt angle of $\pm 25^\circ$.

4.1.2.4 Computational Details

Periodic density-functional theory (DFT) computations in the generalized gradient approximation of Perdew, Burke, and Ernzerhof (PBE)^[72] were done using the projector augmented-wave (PAW)^[73] method as implemented in the Vienna *ab initio* Simulation Package (VASP).^[74] The cutoff energy for the plane-wave expansion was set to 500 eV, and the Brillouin zone was sampled on a dense Monkhorst–Pack mesh of reciprocal-space points.^[75] Electronic wave functions (crystal structures) were optimized until the energy difference between two iterative steps fell below 10^{-8} eV/cell (10^{-6} eV/cell), respectively.

Chemical-bonding analyses were performed by computing the crystal orbital Hamilton population (COHP),^[76] which allows to identify bonding and antibonding contributions to the electronic band structure by weighting the off-site projected DOS with the corresponding Hamiltonian matrix elements (hence, negative COHP values denote stabilizing interactions). These computations were done for the previously optimized structures using the TB-LMTO-ASA program,^[77] version 4.7, as in our previous studies of diazenides.^[54,58–60] In this case, the local von Barth–Hedin exchange–correlation functional^[78] had to be employed to ensure convergence.

Vibrational properties such as phonon densities of states were calculated by the *ab initio* force-constant method^[79] as implemented in the FROPHO code^[80] based on forces obtained from VASP.

4.1.2.5 Electron Spin Resonance Spectroscopy (ESR)

ESR measurements were carried out on powdered samples covering a temperature range of 10–525 K. For that, the sample was filled into a quartz Mark tube capillary (diameter: 0.3 mm) and sealed under inert conditions. Low-temperature (ambient temperature to 10 K) continuous-wave (CW) ESR measurements at X-band frequencies were performed on three spectrometers: (a) on a Bruker Elexsys 500 CW ESR spectrometer equipped with a Bruker ER 4122 SHQ resonator with or without an Oxford Helium flow cryostat, (b) on a Bruker Elexsys 580 X-band CW/pulse ESR spectrometer equipped with a Bruker dielectric ENDOR resonator and an Oxford Helium flow cryostat, and (c) on a Magnetech MS 400 miniscope spectrometer equipped with a nitrogen flow cryostat. High-temperature (ambient temperature to 525 K) measurements were carried out on spectrometer (a). All measurements were properly calibrated and referenced to standards as detailed in the Supporting Information.

4.1.2.6 Fourier Transform Infrared Spectroscopy (FTIR)

Fourier transform infrared spectroscopy measurements were carried out on a Bruker FTIR-IS66V-S spectrometer. Spectra of the samples were recorded at ambient conditions between 400 and 4000 cm^{-1} after the samples were diluted in dried KBr pellets under inert conditions.

4.1.2.7 Magnetic and Electric Conductivity Measurements

The magnetic measurements were performed on a Quantum Design MPMS XL5 SQUID magnetometer. Electric resistivity and conductivity were determined from a cold pressed (10 kN) pellet of nonsintered $\text{Li}_2\text{Ca}_3[\text{N}_2]_3$ (diameter: 4.0 mm, thickness: 1.28 mm) using the four-probe method. For the measurement, three batches of previously synthesized $\text{Li}_2\text{Ca}_3[\text{N}_2]_3$ had to be combined due to the small sample amount obtained upon one HP/HT experiment. In addition, each product of synthesis was analyzed separately by means of powder X-ray diffraction to rely on a successful synthesis. The pellet was contacted with four equidistant probes using silver conducting paint. As the compound is very sensitive to moisture, all preparations had to be done in a glove box. A current of 5.0 mA was applied and the potential difference was measured as a function of temperature (3.5–300 K) yielding the resistivity. No superconductivity was observed.

4.1.3 Results and Discussion

4.1.3.1 Unit-Cell Metrics

The unit-cell metrics was analyzed on the basis of powder X-ray diffraction (PXRD) and transmission electron microscopy (TEM) data. The indexing of PXRD patterns suggested a unit cell with hexagonal metrics ($a = 8.06$, $c = 4.76$ Å). From systematic absences, as well as from the integration and extraction of the intensities, a first structural model in space group $P6_3/mcm$ (no. 193) was derived (see Figures S4–S6 in the Supporting Information). However, SAEDs with the hexagonal $[001]_{\text{hex}}$ zone axis of all investigated crystallites significantly differed from simulated ones (see Figure 2). Hereby, the experimental diffraction patterns of $[001]_{\text{hex}}$ zone axes contain additional reflections that suggest a doubling of the unit cell axes a and b . Though simulated diffraction patterns of $[001]_{\text{hex}}$ zone axes of an isomorphic subgroup with $a' = 2a$ and $b' = 2b$ ($P6_3/mcm$, no. 193) would result in the experimentally observed diffraction profile, the simple doubling of the lattice parameters does not fit other zone axes due to a simulated, doubled spot density that is absent in the experimental diffraction patterns. Therefore, a simple doubling of the lattice parameters does not suffice to reconcile experimental and simulated diffraction patterns.

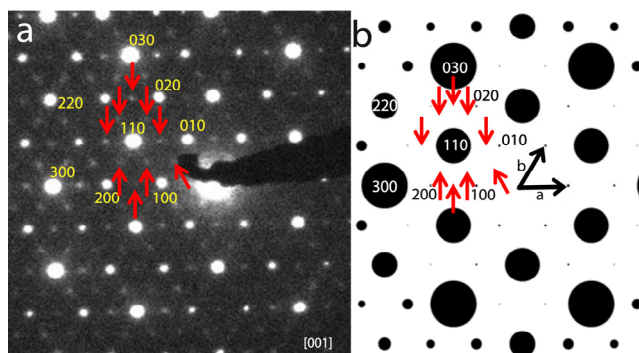


Figure 2. Experimental (a) and simulated (b, hexagonal model with $a = 8.06$, $c = 4.76$ Å) SAED pattern of $[001]_{\text{hex}}$ zone axis of hexagonal “ LiCaN_2 ”. In the experimental SAED pattern, between each indexed spot, there are further residual spots (red arrows). According to the simulated SAED pattern, these additional reflections suggest a doubling of the unit cell according to $a' = 2a$ and $b' = 2b$.

As it was not possible to describe all diffraction patterns with the obtained hexagonal model, reduction of symmetry was done referring to group–subgroup relations. A first *translationsgleich* reduction in symmetry of index 3 (structure model in hexagonal space group $P6_3/mcm$, no. 193) results in the orthorhombic space group $Cmcm$ (no. 63) with $a = 13.96$, $b = 8.06$ and $c = 4.76$ Å. The C -centering, however, still results in an extinction of reflections with $h + k = 2n + 1$, and hence the simulated diffraction pattern of the $[001]$ zone axis in $Cmcm$ is similar to the one of the hexagonal model. Thus, the C -centering has to be omitted and the symmetry further reduced in a second step. This *klassengleich* symmetry reduction of index 2 into space group $Pmma$ (no. 51) finally results in an adequate model. The simulated diffraction pattern of the resulting $[100]_{\text{orth}}$ zone axis (former $[001]$ zone axes in $P6_3/mcm$ and $Cmcm$) matches the experimental reflection profile for the latter model by additional stepwise tilting by 120° around the origin of $[100]_{\text{orth}}$ zone axes quite well (see Figure 3) and indicates a $[100]_{\text{orth}}$ ($= [001]_{\text{hex}}$) stacked 3-fold twin.

The latter, orthorhombic unit-cell metrics is supported by comparison of experimental SAED patterns to simulated ones; zone axes and lattice parameters have been obtained by transformations of the former hexagonal model (see the Supporting Information).

In addition, the theoretical positions of reflections of the as-obtained model are consistent with the experimentally observed positions in the corresponding PXRD patterns, resulting in Pawley-fitted parameters of $a = 4.7747(1)$, $b = 13.9792(4)$ and $c = 8.0718(4)$ Å in space group $Pmma$ (no. 51). Note that as-investigated hexagonal and orthorhombic models mentioned in this section exhibit stoichiometric compositions of “ LiCaN_2 ” diverging from elemental analysis suggesting lithium-deficiency (see the following sections).

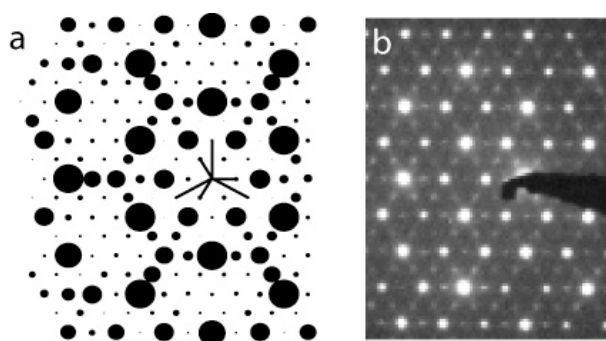


Figure 3. (a) Simulated SAED pattern of 3-fold twin by rotation in orthorhombic space group $Pmma$ (no. 51) obtained after stepwise tilting the simulated $[100]_{\text{orth}}$ pattern by 120° around the origin. (b) Experimental SAED pattern of former hexagonal $[001]_{\text{hex}}$ zone axis matching the diffraction profile of the 3-fold twin.

4.1.3.2 Theoretical Considerations of the Hexagonal Model

The complex nature of the problem at hand called for a complementary quantum-theoretical analysis in search of the structure, and the first computations were performed for the initially assigned, hexagonal model with “ LiCaN_2 ” composition ($P6_3/mcm$, see Supporting Information Figure S4). Surprisingly, at first sight, this structure showed pronounced instability during relaxation: the Hellmann–Feynman forces computed at temperature zero were enough to totally destroy the Li–Ca coordination environment. Moreover, phonon computations characterize this structure as dynamically unstable, proven by the presence of several imaginary eigenmodes (see Figure 4a). To improve this structural model, we applied a multistep procedure that has been described in more detail recently.^[81] First, we applied eigenvectors of the imaginary modes at the Γ point followed by structural optimization, for which the $E(V)$ plot is shown in Figure 4b. This process, labeled (1) in Figure 4b for two distinct eigenmodes, leads to the new $E(V)$ curves shown in green and light blue, respectively. This structural change is accompanied by an energy gain of over 30 kJ/mol, quite impressively. For both of these structures, subsequent energy–volume scans were performed (labeled (2)). Upon compressing the simulated cells, both still showed an inherent instability upon decreasing the unit-cell volume below $\sim 28 \text{ cm}^3 \text{ mol}^{-1}$ (green dots) or $\sim 25 \text{ cm}^3 \text{ mol}^{-1}$, respectively. The most favorable structure, finally, was obtained upon relaxation (labeled (3); dark blue line in Figure 4b) and led to an energy gain of $\sim 55 \text{ kJ/mol}$ as compared to the initial $P6_3/mcm$ guess.

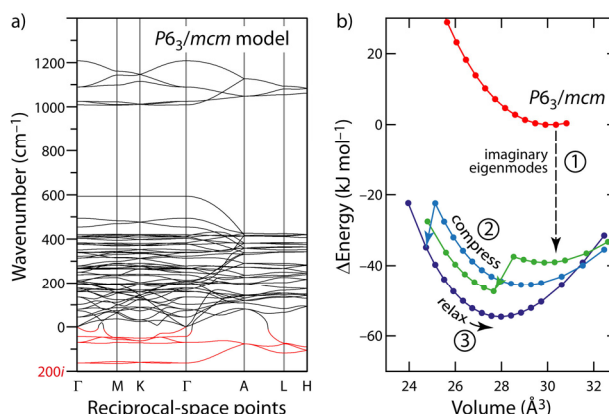


Figure 4. (a) Phonon band structure computed for the hexagonal $P6_3/mcm$ model exhibiting “ LiCaN_2 ” stoichiometry. Several imaginary eigenvalues (highlighted in red), seemingly extending throughout the entire Brillouin zone, are visible. (b) Energy–volume plots for the different structural models of “ LiCaN_2 ”, with arrows describing how one is obtained from the other. Lines connecting data points are only guides to the eye. See text for discussion.

The new theoretical structure with “ LiCaN_2 ” composition was found in space group $Pmma$ (no. 51). It must be noted, however, that the resulting space group equals that of the TEM model (see previous section) only by coincidence, and the reason is as follows. Despite the large energetic stabilization of $\sim 55 \text{ kJ mol}^{-1}$ gained during the optimization procedure that started from the initial model ($P6_3/mcm$, Figure 4b), a simulated diffraction pattern for the optimized “ LiCaN_2 ” model could not be reconciled with the experimental diffractogram. In particular, the computational result so far did not correspond to the revised unit-cell metrics but to those of the initial model, which had been falsified in the sequel. Consequently, what was initially believed to be the “correct” answer from theory (Figure 4b, dark blue curve) had to be discarded in the light of experiment.

On the other hand, the revised structural model derived from TEM (sketched in Figure 5, top), again proved unstable during quantum-chemical relaxation. This led to conclude that the results of the elemental analysis (see the Supporting Information) had to be recalled as the compound obtained from HP/HT experiments might differ in stoichiometry compared to the originally proposed sum formula of LiCaN_2 .

4.1.3.3 Improving the Structural Model

The elemental analysis, albeit with some uncertainty, suggested a Li deficiency with a atomic ratio $\text{Li}:\text{Ca} \approx 0.8:1$ in the title compound, whereas a $\text{Ca}:\text{N}$ ratio of $\sim 1:2$ had been observed. Also, the exclusively Ca-coordinated Li positions in the $Pmma$ structure model (2a and 2d)

were the ones that experienced the most pronounced structural change/instability in the theoretical computations. Hence, it became obvious that the structural model with $\text{Li}:\text{Ca} = 1$ did not suffice because it did not lead to an agreement of experiment and theory.

Indeed, upon removing the Li atoms in question, the stoichiometric composition was changed to $\text{Li}_2\text{Ca}_3[\text{N}_2]_3$, and we again carried out structural optimizations (see Tables S3 and S4 in the Supporting Information), starting from the TEM-based experimental, orthorhombic “ LiCaN_2 ” model in space group $Pmma$ (see Figure 5) but with Li deficiency at $2a$ and $2d$ sites.

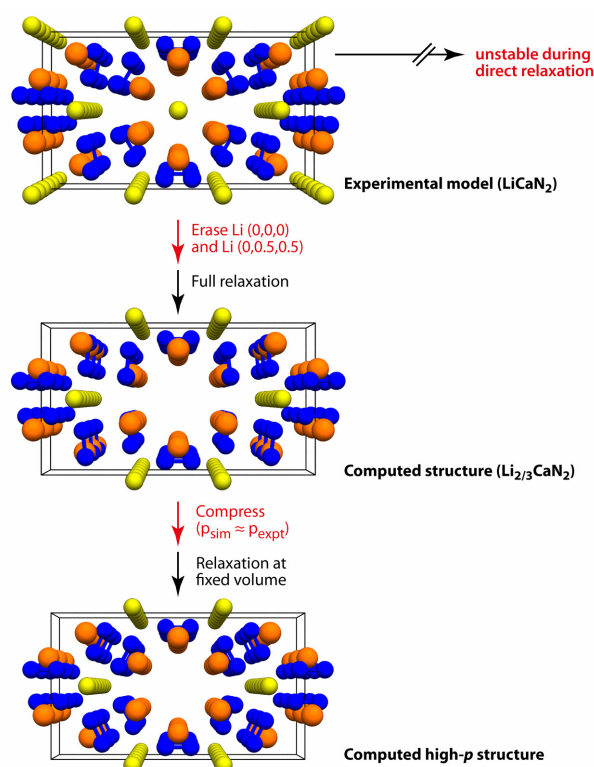


Figure 5. Schematic drawing of the route from the initial experimental, orthorhombic “ LiCaN_2 ” model to the final, Li-deficient model with $\text{Li}_2\text{Ca}_3[\text{N}_2]_3$ stoichiometry, both of which exhibit space group $Pmma$ (no. 51). Cell sizes are not to scale; Li yellow, Ca orange, N blue.

In the absence of external pressure, the structure seemed to be unstable again as indicated by the presence of imaginary phonon modes (albeit less strongly pronounced than in the $P6_3/mcm$ model characterized in Figure 4a). Nonetheless, by decreasing the simulation cell volume, the proposed structure could be stabilized. The imaginary modes disappeared entirely once the simulated pressure increased to ~ 13 GPa and above (see Figure 6), which is close to synthesis conditions (9 GPa).

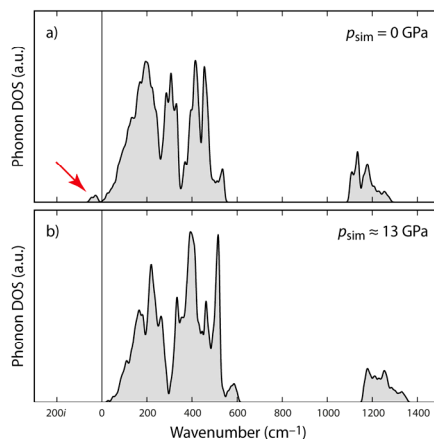


Figure 6. Computed phonon DOS for the final structural model with $\text{Li}_2\text{Ca}_3[\text{N}_2]_3$ stoichiometry without external pressure (a) and at a simulated pressure of approximately 13 GPa (b). In the upper panel, a small number of imaginary eigenmodes are visible as indicated by a red arrow. In the lower panel, these imaginary modes have disappeared, and the structural model proves dynamically stable.

The imaginary eigenmodes at zero pressure might propose further instability of the crystal structure at ambient conditions; however, a collapse of the crystal structure at these conditions seems to be kinetically hindered as $\text{Li}_2\text{Ca}_3[\text{N}_2]_3$ could be analyzed experimentally even after releasing high pressure.

Note that the spot density in simulated diffraction patterns of $\text{Li}_2\text{Ca}_3[\text{N}_2]_3$ (data not shown) is equal to orthorhombic “ LiCaN_2 ” in space group $Pmma$ (no. 51, TEM-based model).

It is only the intensity of the spots that slightly varies due to the lithium depletion of Wyckoff positions $2a$ and $2d$ in “ LiCaN_2 ” resulting in the composition $\text{Li}_2\text{Ca}_3[\text{N}_2]_3$. Thus, the simulated diffraction patterns are also in good agreement with the final crystal structure.

4.1.3.4 Description of the Crystal Structure

$\text{Li}_2\text{Ca}_3[\text{N}_2]_3$ shows a close structural relationship to hexagonal Mn_5Si_3 -type structures ($P6_3/mcm$, no. 193), better known as Nowotny phases.^[82–84]

$\text{Li}_2\text{Ca}_3[\text{N}_2]_3$ contains four pairs of crystallographically independent nitrogen dumbbells exhibiting N–N bond lengths of $d_{\text{NN}} = 1.337(17)–1.353(32)$ Å (see Figure 7 and Table 2). These N–N distances are intermediate to those in experimentally reported diazenides MN_2 ($M = \text{Ca}, \text{Sr}, \text{Ba}$), Li_2N_2 and LaN_2 having distances of about 1.20–1.32 Å,^[58,59,62] and to pernitride $[\text{N}_2]^{4-}$ ions with N–N bond lengths of about 1.40 Å.^[46–54] For $\text{Li}_2\text{Ca}_3[\text{N}_2]_3$, this suggests a $[\text{N}_2]^{3-}$ formulation which would correspond to a radical character of the dinitrogen anion. In more detail, as-obtained N–N distances are in good agreement with corresponding

characteristics of $[\text{N}_2]^{3-}$ ligation observed in already mentioned bimetallic lanthanide complexes ($d_{\text{NN}} = 1.39\text{--}1.41 \text{ \AA}$).^[10,27–31] However, recent theoretical calculations considering hypothetical TiN_2 also support diazenide $[\text{N}_2]^{2-}$ units with N–N bond lengths up to even 1.46 \AA .^[85]

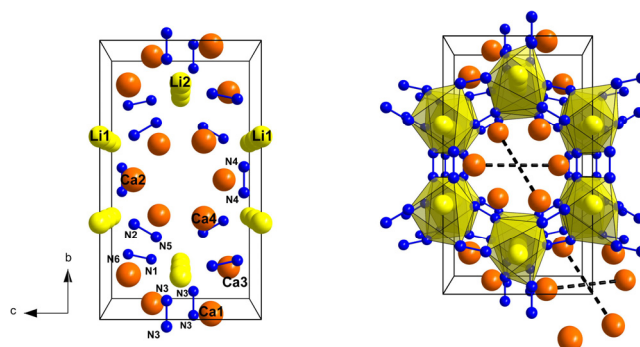


Figure 7. Unit cell of $\text{Li}_2\text{Ca}_3[\text{N}_2]_3$ viewed along $[100]$ as resulting from the final refinement. Polyhedra around Li atoms are marked in yellow; Li yellow, Ca orange, N blue. Dashed lines in the right figure represent Ca–Ca distances in the center of the unit cell with $d_{\text{Ca1–Ca1}} = 5.45(1)$, $d_{\text{Ca2–Ca2}} = 5.47(2)$, $d_{\text{Ca3–Ca3}} = 5.39(1)$, and $d_{\text{Ca4–Ca4}} = 5.267(9) \text{ \AA}$, respectively. For further information see Table S6 in the Supporting Information.

To elucidate the electronic character of the dinitrogen anion, we targeted chemical bonding analysis by means of the crystal orbital Hamiltonian population (COHP) method, as done previously for different diazenide/pernitride compounds.^[54,58–60] Figure 8 shows the well-known electronic „fingerprint” of the dinitrogen entity in the region close to the Fermi level ε_{F} .^[54]

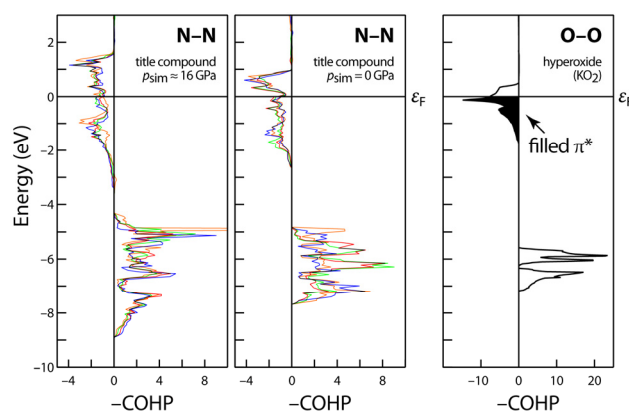
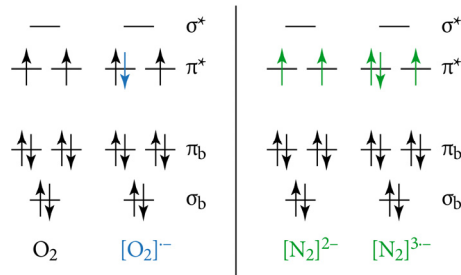


Figure 8. Left and middle: COHP analysis for the 4 $[\text{N}_2]$ entities in $\text{Li}_2\text{Ca}_3[\text{N}_2]_3$ depicted in different arbitrarily chosen colors, computed under pressure of 16 GPa (left) and for the fully relaxed structure at zero pressure (middle), respectively. For the definition of π^* filling, see text. Right: Same but for the $[\text{O}_2]$ entity in potassium hyperoxide KO_2 .

In agreement with Scheme 1, a set of π bonding and π^* antibonding bands may be discerned. The four dinitrogen dumbbells, despite overall similarities, have a unique bonding fingerprint

each (shown in different colors), which is in accord with the experimental observation of several N–N stretching modes in the vibrational spectrum.



Scheme 1. Schematic molecular-orbital diagrams (not drawn to scale) for the species discussed. Electrons in excess of the neutral diatomic ground state are indicated in color.

For a more quantitative analysis, we calculate the “filling” of the π^* orbitals as reflected in the integrated COHPs. (We are aware of difficulties in integrating over an unoccupied area of the band structure; relative comparison is however well permitted). We derive the filling as

$$\left(\int_{\varepsilon_-}^{\varepsilon_F} \text{COHP}(E) dE \right) / \left(\int_{\varepsilon_-}^{\varepsilon_+} \text{COHP}(E) dE \right)$$

where ε_- denotes a suitably chosen lower energy limit (in Figure 8, 4 eV below the Fermi level) and ε_+ is the upper one (2 eV above ε_F). The resulting values of the π^* filling up to the Fermi level are given in Table 2. Note that these values have also been averaged over the four bonds present in equal amounts.

For comparison, an O–O COHP curve has been computed for potassium hyperoxide as a well-characterized representative compound with an anion isoelectronic to $[\text{N}_2]^{3-}$.^[86] Thereby, the calculated filling is 73%, well matching the ideally expected percentage of 75% according to Scheme 1. The individual and averaged electronic character of the four N_2 entities in $\text{Li}_2\text{Ca}_3[\text{N}_2]_3$ are listed in Table 2. Accordingly, with an averaged π^* filling of 57% at zero pressure (53% at 16 GPa) resembling an expected value of 50% for diazenides, the N_2 units in $\text{Li}_2\text{Ca}_3[\text{N}_2]_3$ clearly exhibit different electronic behavior compared to hypothetical $[\text{N}_2]^{3-}$ radical anions.

Taking these theoretical considerations into account, $\text{Li}_2\text{Ca}_3[\text{N}_2]_3$ is conjectured to consist of diazenide $[\text{N}_2]^{2-}$ ions rather than $[\text{N}_2]^{3-}$ radical anions. This assignment is probed by experiment in the next sections.

Table 2. Experimental and computationally optimized N–N bond lengths (in amgstroms) of nitrogen dumbbells in $\text{Li}_2\text{Ca}_3[\text{N}_2]_3$, together with π^* orbital fillings (see text).

$\text{N}_x\text{--N}_y$ ^[a]	1–6	2–5	3–3	4–4	average
exp.	1.342(14)	1.337(17)	1.353(32)	1.348(26)	
calcd. at 0 GPa	1.308	1.308	1.313	1.313	
π^* filling	55%	59%	59%	56%	57%
calcd. at 16 GPa	1.293	1.293	1.291	1.289	
π^* filling	55%	51%	59%	46%	53%

[a] The pairing of six crystallographically independent nitrogen sites (all Wyckoff site $4k$), thereby referring to Table 1, results in four crystallographically independent N_2 entities.

The presence of only diazenide ions in $\text{Li}_2\text{Ca}_3[\text{N}_2]_3$ and the reasonable requirement of singly (doubly) positively charged Li (Ca) ions, respectively, results in a more precise formulation as in $(\text{Li}^+)_2(\text{Ca}^{2+})_3([\text{N}_2]^{2-})_3\cdot(\text{e}^-)_2$, an anion-deficient or vice versa electron-rich structure. As prominent representatives of such compounds, suboxides or subnitrides come to mind.^[87–97] Interestingly, each nitrogen atom of the diazenide entities is octahedrally coordinated by four calcium and two lithium cations. Both octahedra share one common face, which is similar to the Rb_9O_2 -type cluster observed in the rubidium suboxides Rb_9O_2 and Rb_6O (see Figure 9).^[87–90]

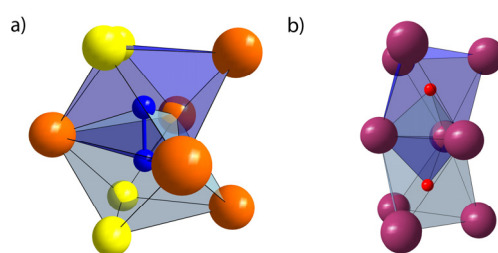


Figure 9. Coordination sphere of diazenide ions in $\text{Li}_2\text{Ca}_3[\text{N}_2]_3$ (a). Thereby each nitrogen atom is octahedrally coordinated by Li^+ and Ca^{2+} . The resulting octahedra share a common face, representing the basic motif of anion coordination in rubidium suboxides Rb_9O_2 and Rb_6O (b); Li yellow, Rb violet, Ca orange, N blue, O red.

These compounds represent oxygen-deficient (or, again, electron-rich) structures. Formally, Rb_9O_2 and Rb_6O can also be written as $(\text{Rb}^+)_9(\text{O}^{2-})_2\cdot(\text{e}^-)_5$ or $(\text{Rb}^+)_6(\text{O}^{2-})\cdot(\text{e}^-)_4$, respectively. As the $[\text{N}_2]^{2-}$ coordination spheres resemble those of the oxygen ions in suboxides and due to potential formulation of $\text{Li}_2\text{Ca}_3[\text{N}_2]_3$ as $(\text{Li}^+)_2(\text{Ca}^{2+})_3([\text{N}_2]^{2-})_3\cdot(\text{e}^-)_2$, the title compound might also constitute the first representative of hitherto unknown ternary subdiazenides. However, as compared to the Rb_9O_2 structure (see Figure 9b), with isolated Rb_9O_2 units in the rubidium-based lattice, the resulting structural motifs of N_2 -coordination in $\text{Li}_2\text{Ca}_3[\text{N}_2]_3$ are exclusively interconnected again by sharing octahedral faces (see Supporting Information Figure S8).

The two independent lithium sites are coordinated by six $[\text{N}_2]^{2-}$ ions in an *end-on* manner, building up a strand of face-sharing octahedra (see Figures 7 and S9 in the Supporting

Information). These strands are interconnected to other ${}^2_{\infty}[\text{Li}(\text{N}_2)_{6/2}]$ -strands via diazenide units. The refined Li–Li distances (see Table S5 in the Supporting Information) match with reported ones.^[59,98–103] Additionally, we compared the obtained Li–N distances with the sum of the ionic radii. Preliminary investigations already resulted in an average radius of one nitrogen atom in a diazenide ion to be 1.27 Å.^[60] According to Shannon,^[104] the ionic radius of 6-fold coordinated Li^+ is 0.76 Å. On the basis of this empirical values, the refined Li–N distances correspond well with the sum of the ionic radii.

Like hexagonal Mn_5Si_3 , $\text{Li}_2\text{Ca}_3[\text{N}_2]_3$ contains structural voids, which due to the orthorhombic metric are located at (0,0,0) and (0,½,½). Many A_5B_3 -type compounds were observed to incorporate nonmetal atoms like B, C, N, O or even metals into these cavities to result in $\text{A}_5\text{B}_3\text{Z}$ -type compounds.^[82] However, a clear tendency for occupying the voids is very hard to predict. Moreover, nonstoichiometric intercalation of Z elements into the cavities is supposed to stabilize A_5B_3 -type structures.^[82] In $\text{Li}_2\text{Ca}_3[\text{N}_2]_3$, the average void diameter is found to be 3.15 Å (see Supporting Information Table S6), which is within the range of those in the aforementioned A_5B_3 compounds and thus formally enables incorporation of further elements into these voids. However, elemental analysis (see the Supporting Information) resulted in no significant stoichiometric atom content other than Li, Ca, and N. In addition, due to electrostatic reasons, the incorporation of cations/metals is supposed to be rather energetically unstable as shown by theoretical consideration finally resulting in $\text{Li}_2\text{Ca}_3[\text{N}_2]_3$ after removing Li atoms of Wyckoff positions $2a$ and $2d$.

4.1.3.5 Infrared Spectroscopy

In bioinorganic chemistry, the valency of dinitrogen anions is routinely assigned according to the N–N bond lengths and their corresponding N–N stretching vibrations upon infrared or Raman spectroscopy. Recently, it has been shown experimentally that the infrared spectra of the diazenides MN_2 ($M=\text{Ca}, \text{Sr}, \text{Ba}$), as well as of Li_2N_2 , exhibit clear features in the range of 1380–1330 cm^{-1} , which had been assigned to the N–N stretching vibration of the diazenide units.^[58,59] Pernitride units as observed in noble metal $M_{\text{NM}}\text{N}_2$ compounds ($M_{\text{NM}} = \text{Os}, \text{Ir}, \text{Pd},$ and Pt) also exhibit distinct features around 800 cm^{-1} , attributed to the stretching of $[\text{N}_2]^{4-}$ units.^[46–54] In addition, radical dinitrogen ions $[\text{N}_2]^{3-}$ have recently been observed, and they show characteristic N–N vibrations at wavenumbers shortly below 1000 cm^{-1} .^[27–31]

For $\text{Li}_2\text{Ca}_3[\text{N}_2]_3$, infrared spectroscopy revealed significant features at 1260, 1100, 1020 and 802 cm^{-1} besides overtones at about 3000 cm^{-1} (see Figure 10). The nitrogen dumbbells in $\text{Li}_2\text{Ca}_3[\text{N}_2]_3$ exhibit bond lengths of $d_{\text{NN}} = 1.34(2)\text{--}1.35(3)\text{ \AA}$, which are intermediate to previous reports for $[\text{N}_2]^{2-}$ and $[\text{N}_2]^{3-}$ ions. In accord with this observation, the wavenumbers of the observed features in the infrared spectrum of $\text{Li}_2\text{Ca}_3[\text{N}_2]_3$ are also intermediate to those of the latter two anions. Thus, the theoretical COHP analysis of the N–N bonding in the title compound (suggesting diazenide $[\text{N}_2]^{2-}$ ions, rather than radicals) despite elongated N–N bond lengths is in good agreement with the vibrational measurements.

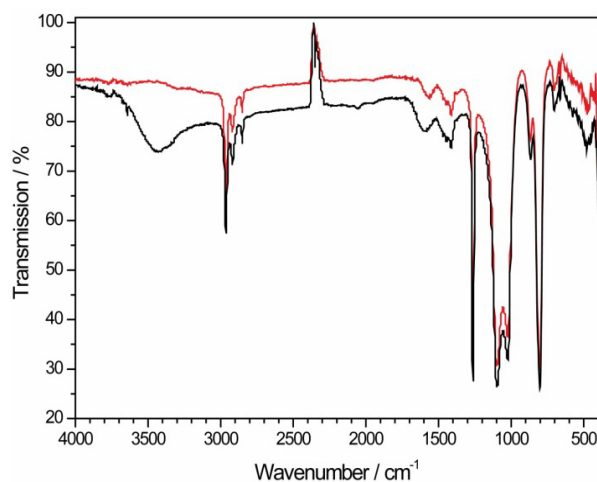


Figure 10. FTIR spectra of $\text{Li}_2\text{Ca}_3[\text{N}_2]_3$ (black) and after exposure to moisture for 5 minutes (red). The absorption features at about 2250 cm^{-1} are artifacts of the spectrometer.

Seeking again a corroboration of experimental findings, we also performed pressure-dependent phonon calculations to assign the vibrational modes from first principles, and also to look at the high-pressure trend in vibrational properties that is much more difficult to determine experimentally.

For the fully optimized (pressure-free) structural model, as well as with simulated pressures of a few GPa applied, the phonon calculations give imaginary vibrational modes (see Figure 11), which indicates dynamical instability already seen in Figure 6a (red arrow). With increasing (simulated) pressure, the imaginary modes disappear, which points toward the structure being stable under pressure. As can further be seen in Figure 11, the theoretical phonon DOS shows a broad signal in the range from 1100 to 1300 cm^{-1} without external pressure applied, which is shifted to higher wavenumbers with increasing pressure due to shorter atomic distances. This part of the spectrum is related to the N–N stretching vibrations of the diazenide ions, and the signals are broadened because of their interaction. The experimentally obtained features at 1260 , 1100 , and 1020 cm^{-1} can be confirmed by the theoretical calculations, albeit caution

must be taken because not all lattice modes are infrared active, and hence the IR spectrum and the computed PDOS may not be compared with each other without care.

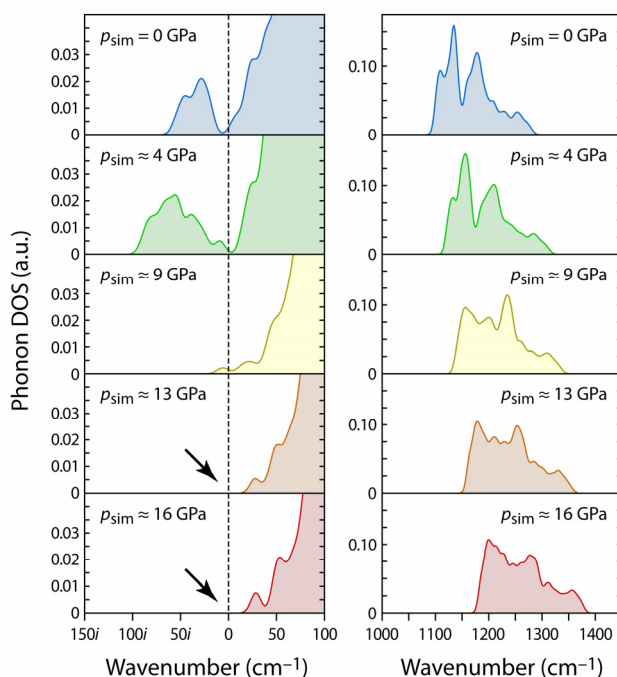


Figure 11. Excerpts from phonon densities of states computed at different simulated pressures, evolving from pressure-free structures (top) to 16 GPa. Note the absence of dynamic instabilities (that would be indicated by complex-valued vibrational modes), which sets in at increased pressure (arrows).

As our calculations reveal, the feature at 800 cm^{-1} cannot be assigned to the N–N stretching vibrations of one of the diazenide units. However, the product of the high-pressure synthesis is always affected with an unknown impurity (see the Experimental Section), which might constitute an oxo- or nitridoborate originating from the BN crucible used. Such compounds exhibit distinct features at wavenumbers $< 1000\text{ cm}^{-1}$ assigned to lattice vibrations of the oxo- or nitridoborate units,^[105–109] and thus might account for the unexplained signal in the IR spectrum of the title compound. A more detailed assignment of observed features in the experimental and theoretical vibrational spectrum to N–N bond lengths can be found in the Supporting Information.

4.1.3.6 Electron Spin Resonance (ESR) Spectroscopy

To settle the character of the nitrogen dumbbells experimentally, we next employed electron spin resonance spectroscopy, which is routinely used for the detection and further analysis of unpaired electrons. As the $[\text{N}_2]^{2-}$ ion is isosteric to molecular oxygen O_2 , it should exhibit paramagnetic behavior (see Scheme 1). However, despite the paramagnetic character, the detection of an ESR-signal for molecular oxygen is hindered due to the enormous zero field splitting of the triplet state, which in general leads to a broadening and therefore makes detection of an ESR signal impossible. On the contrary, $[\text{N}_2]^{3-}$ radical anions are shown to give a very sharp signal as they are isosteric to hyperoxides $[\text{O}_2]^-$ (see Scheme 1).^[27,28] Indeed, ESR measurements of alkali and alkaline-earth hyperoxides resulted in distinct signals at a g -factor ranging from 2.001 to 2.004, close to the g -factor of free electrons (2.0023).^[110,111]

Figure 12a displays the ESR spectrum of $\text{Li}_2\text{Ca}_3[\text{N}_2]_3$, whereas in Figure 12b that of BaN_2 is depicted, the latter serving as diazenide reference. The spectrum of $\text{Li}_2\text{Ca}_3[\text{N}_2]_3$ contains a narrow-line and a broad-line signal at $g_{\text{narrow}} = 2.0052(1)$ and $g_{\text{broad}} = 2.0052(10)$, which would, in principle, be consistent with the presence of free electrons and support a potential $[\text{N}_2]^{3-}$ formulation. However, the ESR spectrum of BaN_2 also consists of a signal at about the g -factor of free electrons contradicting the unambiguous correlation of the signals in the spectrum of $\text{Li}_2\text{Ca}_3[\text{N}_2]_3$ to $[\text{N}_2]^{3-}$ radical anions.

Additionally, we analyzed the spin concentration of the obtained signals in $\text{Li}_2\text{Ca}_3[\text{N}_2]_3$ and BaN_2 and referenced them to common ESR standards. For BaN_2 , the obtained spin concentration of 16.6 mM is far below the expected value of 60.8 M for the biradical $[\text{N}_2]^{2-}$. These data are in good agreement with as-mentioned difficulties in signal detection due to triplet state splitting of paramagnetic diazenide ions. Thus, the visible signal of the HP/HT product is attributed either to impurities in the mmol range or surface defects in BaN_2 evolving unpaired electrons, which then can be detected.

The ratio of double integrals of the broad-line signal of $\text{Li}_2\text{Ca}_3[\text{N}_2]_3$ to the one of the utilized one-electron references is 1:373, suggesting an effective spin concentration in $\text{Li}_2\text{Ca}_3[\text{N}_2]_3$ of 373(60) mM. The spin concentration of the narrow-line signal is only in the 10^{-3} mM range. In any case, a rough estimate indicates that the number of spins is too low for a compound with all or at least one nitrogen dumbbell in a $[\text{N}_2]^{3-}$ radical anion state. Therefore, even considering a 20% uncertainty in determining spin concentration, the observed concentration is much too low for assigning an electronic structure with $[\text{N}_2]^{3-}$ radical anions. Again, the

presence of the signals is presumably due to surface defects or impurities in the sample. Taking all these facts into account, $\text{Li}_2\text{Ca}_3[\text{N}_2]_3$ rather consists of $[\text{N}_2]^{2-}$ ions than $[\text{N}_2]^{3-}$ radical anions, which is in sound agreement with electronic-structure theory (see Figure 8).

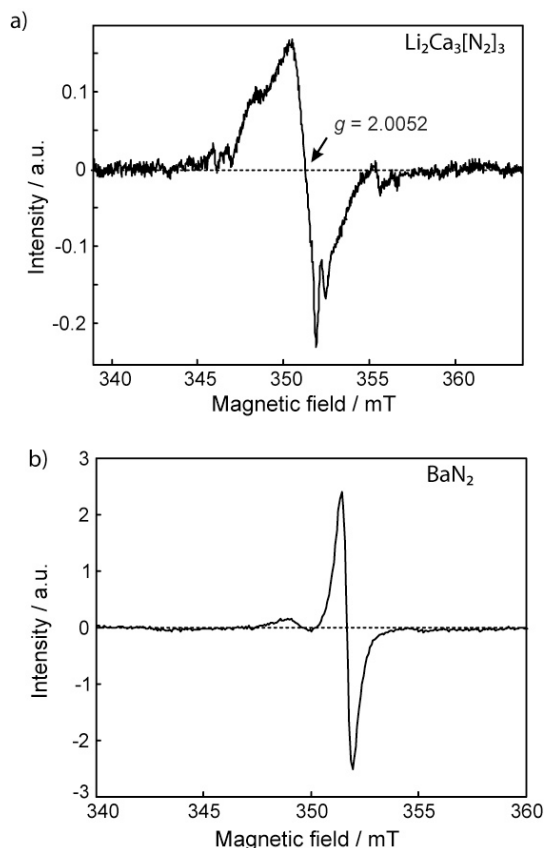


Figure 12. (a) Detail ESR spectrum at ambient temperature after background correction (black). In addition to the narrow-line signal shown here in detail, an overview spectrum (see Supporting Information Figure S3) reveals the presence of a broad-line signal. The g values for the narrow-line and the broad-line signal are 2.0052(1) and 2.0052(10), respectively. The dotted line only serves as guide to the eyes for the zero crossing of the spectrum. (b) ESR spectrum of BaN_2 after background correction recorded at ambient temperature.

4.1.3.7 Magnetic and Electric Conductivity Measurements

Magnetic measurements are supposed to ultimately end speculations on the potential presence of $[\text{N}_2]^{3-}$ radical anions in $\text{Li}_2\text{Ca}_3[\text{N}_2]_3$. If $\text{Li}_2\text{Ca}_3[\text{N}_2]_3$ contained $[\text{N}_2]^{3-}$ radical anions, magnetic characteristics like antiferro- or ferromagnetism would be expected as observed for the isosteric hyperoxides.^[112] However, susceptibility measurements of $\text{Li}_2\text{Ca}_3[\text{N}_2]_3$ at 1 and 0.01 T show nearly temperature-independent (Pauli-paramagnetic) behavior down to low temperatures (see Figure 13a). To rely on this observation especially in the low-temperature region where the susceptibility slightly increases again (see Figure 13a), we also plotted the product of $X_{\text{mol}}T$ versus T (see Figure S11 in the Supporting Information), which resulted in a

continuous increase of $X_{\text{mol}}T$ with increasing temperature indicative for true temperature-independent behavior of the susceptibility. This observation is in good agreement with previous magnetic measurements of again BaN_2 revealing that the dominant magnetic behavior in BaN_2 is also Pauli-paramagnetism.^[39]

As shown in Figure 13b, the resistivity of $\text{Li}_2\text{Ca}_3[\text{N}_2]_3$ decreases with decreasing temperature, as is typical for metals. The resistivity at ambient temperature is found to be $7.23 \cdot 10^{-6} \Omega \text{ m}$, which is in the range of good metallic conduction and qualitatively in accord with electronic-structure computations that predict a finite density of electronic states at the Fermi level (see Figure 8). Again, as-obtained results are in very good agreement with the presence of solely $[\text{N}_2]^{2-}$ ions in $\text{Li}_2\text{Ca}_3[\text{N}_2]_3$.

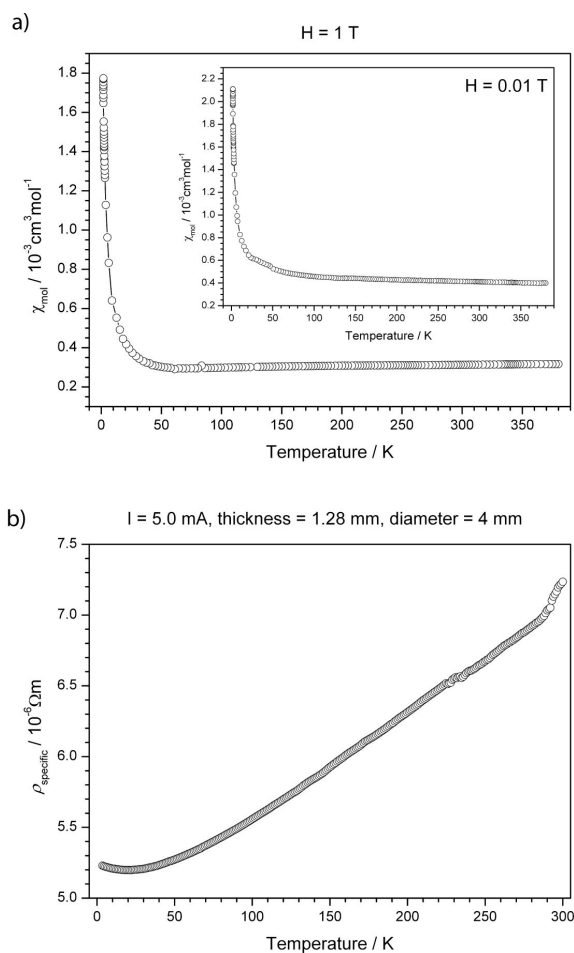


Figure 13. Course of the molar susceptibility of $\text{Li}_2\text{Ca}_3[\text{N}_2]_3$ with temperature (a) at an applied external field of 1 and 0.01 T (insert); specific resistance with temperature upon cooling (b). Error bars are not shown. The lines only serve as guide to the eyes.

4.1.4 Conclusion

We were able to synthesize the first ternary compound with homonuclear dinitrogen entities by thermal decomposition of stoichiometric mixtures of ionic lithium and calcium azides under HP/HT conditions. In contrast to binary diazenides such as Li_2N_2 , MN_2 ($M = \text{Ca}, \text{Sr}$ and Ba), and LaN_2 , the ternary title compound $\text{Li}_2\text{Ca}_3[\text{N}_2]_3$ exhibits pronounced elongation of the N–N bond lengths, which would intuitively contradict the presence of $[\text{N}_2]^{2-}$ ions. In fact, these N–N distances would be better described by $[\text{N}_2]^{3-}$ units, as has been previously observed in metal-organic reference compounds.

Much to the contrary, the true character of the N_2 entity was finally elucidated by complementary use of various analytical methods. Experimental and theoretical studies excluded the presence of $[\text{N}_2]^{3-}$ radical anions, but instead supported the presence of only $[\text{N}_2]^{2-}$ ions in the crystal structure. Therefore, the ionic formulation of $\text{Li}_2\text{Ca}_3[\text{N}_2]_3$ is better described as $(\text{Li}^+)_2(\text{Ca}^{2+})_3([\text{N}_2]^{2-})_3 \cdot (\text{e}^-)_2$.

Interestingly, $\text{Li}_2\text{Ca}_3[\text{N}_2]_3$ exhibits distinct structural motifs with regard to anion coordination that have been observed in Rb_9O_2^- and Rb_6O -type suboxides, which represent anion-deficient (or, depending on perspective, electron-rich) structures. Within this context, the title compound might also be interpreted as the first representative of “sub-diazenides”.

Finally, as compared to the classification of valencies in bound N_2 entities observed in bioinorganic or metal-organic chemistry, their adequate description in solid-state chemistry is hindered due to, for example, potential metallicity in such compounds. However, by the use of a variety of complementary methods as presented, the identification of the true oxidation state in $[\text{N}_2]^x$ -anions remains possible.

Acknowledgment

We would like to thank Prof. Dirk Johrendt (LMU Munich) for providing the equipment for the electric conductivity and SQUID measurements, Prof. Bettina Lotsch for providing the TEM (MPI Stuttgart), Franziska Hummel and Thomas Miller (both LMU Munich) for the low- and high-temperature powder diffraction measurements, Dr. Constantin Hoch (LMU Munich) for helpful discussions concerning the structural analysis, Nicole Dannenbauer (JMU Würzburg) for the FTIR measurements, Andreas Groß and Dr. Malte Drescher (both University Konstanz) for preliminary ESR experiments, as well as Christian Minke (LMU Munich) for solid-state MAS-NMR measurements. Financial support by the Fonds der

Chemischen Industrie (FCI), Deutsche Forschungsgemeinschaft (DFG), project SCHN 377/13-2, and the Max-Planck Society is gratefully acknowledged. V.L.D. is thankful to the Studienstiftung des Deutschen Volkes for a scholarship.

4.1.5 References

- [1] J. R. Jennings, *Catalytic Ammonia Synthesis*, Plenum Press: New York, **1991**.
- [2] F. A. Tezcan, S. L. A. Andrade, B. Schmid, M. Yoshida, J. B. Howard, D. C. Rees, O. Einsle, *Science* **2002**, *297*, 1696.
- [3] B. K. Burgess, D. J. Lowe, *Chem. Rev.* **1996**, *96*, 2983.
- [4] R. A. Alberty, R. N. Goldberg, *Biochemistry* **1992**, *31*, 10610.
- [5] B. K. Burgess, *Chem. Rev.* **1990**, *90*, 1377.
- [6] J. S. Kim, D. C. Rees, *Nature* **1992**, *360*, 553.
- [7] K. M. Lancaster, M. Roemelt, P. Ettenhuber, Y. L. Hu, M. W. Ribbe, F. Neese, U. Bergmann, S. DeBeer, *Science* **2011**, *334*, 974.
- [8] T. Spatzal, M. Aksoyoglu, L. M. Zhang, S. L. A. Andrade, E. Schleicher, S. Weber, D. C. Rees, O. Einsle, *Science* **2011**, *334*, 940.
- [9] R. N. F. Thorneley, D. J. Lowe, *Molybdenum Enzymes*; Wiley:New York, **1985**.
- [10] B. A. MacKay, M. D. Fryzuk, *Chem. Rev.* **2004**, *104*, 385.
- [11] C. J. Pickett, *J. Biol. Inorg. Chem.* **1996**, *1*, 601.
- [12] D. V. Yandulov, R. R. Schrock, *Inorg. Chem.* **2005**, *44*, 1103.
- [13] F. Studt, F. Tuczek, *J. Comput. Chem.* **2006**, *27*, 1278.
- [14] H. Broda, S. Hinrichsen, F. Tuczek, *Coord. Chem. Rev.* **2013**, *257*, 587.
- [15] D. V. Yandulov, R. R. Schrock, *Science* **2003**, *301*, 76.
- [16] D. V. Yandulov, R. R. Schrock, A. L. Rheingold, C. Ceccarelli, W. M. Davis, *Inorg. Chem.* **2003**, *42*, 796.
- [17] V. Ritleng, D. V. Yandulov, W. W. Weare, R. R. Schrock, A. S. Hock, W. M. Davis, *J. Am. Chem. Soc.* **2004**, *126*, 6150.
- [18] R. Römer, C. Gradert, A. Bannwarth, G. Peters, C. Näther, F. Tuczek, *Dalton Trans.* **2011**, 3229.
- [19] K. Klatt, G. Stephan, G. Peters, F. Tuczek, *Inorg. Chem.* **2008**, *47*, 6541.
- [20] G. Stephan, G. Peters, N. Lehnert, C. Habeck, C. Näther, F. Tuczek, *Can. J. Chem.* **2005**, *83*, 385.

- [21] G. Stephan, C. Näther, F. Tuczek, *Acta Cryst. E* **2008**, *64*, M629.
- [22] G. Stephan, C. Näther, C. Sivasankara, F. Tuczek, *Inorg. Chim. Acta* **2008**, *361*, 1008.
- [23] A. Dreher, G. Stephan, F. Tuczek, *Advances in Inorganic Chemistry. Metal Ion Controlled Reactivity*; Elsevier:Amsterdam, 2009.
- [24] S. Pfirrmann, C. Herwig, R. Stöber, B. Ziemer, C. Limberg, *Angew. Chem.* **2009**, *121*, 3407; *Angew. Chem. Int. Ed.* **2009**, *48*, 3357.
- [25] J. M. Smith, R. J. Lachicotte, K. A. Pittard, T. R. Cundari, G. Lukat-Rodgers, K. R. Rodgers, P. L. Holland, *J. Am. Chem. Soc.* **2001**, *123*, 9222.
- [26] J. M. Smith, A. R. Sadique, T. R. Cundari, K. R. Rodgers, G. Lukat-Rodgers, R. J. Lachicotte, C. J. Flaschenriem, J. Vela, P. L. Holland, *J. Am. Chem. Soc.* **2006**, *128*, 756.
- [27] W. J. Evans, M. Fang, G. Zucchi, F. Furche, J. W. Ziller, R. M. Hoekstra, J. I. Zink, *J. Am. Chem. Soc.* **2009**, *131*, 11195.
- [28] M. Fang, J. E. Bates, S. E. Lorenz, D. S. Lee, D. B. Rego, J. W. Ziller, F. Furche, W. J. Evans, *Inorg. Chem.* **2011**, *50*, 1459.
- [29] M. Fang, D. S. Lee, J. W. Ziller, R. J. Doedens, J. E. Bates, F. Furche, W. J. Evans, *J. Am. Chem. Soc.* **2011**, *133*, 3784.
- [30] J. D. Rinehart, M. Fang, W. J. Evans, J. R. Long, *J. Am. Chem. Soc.* **2011**, *133*, 14236.
- [31] J. D. Rinehart, M. Fang, W. J. Evans, J. R. Long, *Nat. Chem.* **2011**, *3*, 538.
- [32] P. J. Chirik, *Nature Chem.* **2009**, *1*, 520.
- [33] W. Kaim, B. Sarkar, *Angew. Chem.* **2009**, *121*, 9573; *Angew. Chem. Int. Ed.* **2009**, *48*, 9409.
- [34] G. Auffermann, Y. Prots, R. Kniep, *Angew. Chem.* **2001**, *113*, 565; *Angew. Chem. Int. Ed.* **2001**, *40*, 547.
- [35] G. Auffermann, Y. Prots, R. Kniep, S. F. Parker, S. M. Bennington, *Chem. Phys. Chem.* **2002**, *9*, 815.
- [36] G. Auffermann, U. Schmidt, B. Bayer, Y. Prots, R. Kniep, *Anal. Bioanal. Chem.* **2002**, *373*, 880.
- [37] G. Auffermann, R. Kniep, W. Bronger, *Z. Anorg. Allg. Chem.* **2006**, *632*, 565.
- [38] Y. Prots, G. Auffermann, M. Tovar, R. Kniep, *Angew. Chem.* **2002**, *114*, 2392; *Angew. Chem. Int. Ed.* **2002**, *41*, 2288.
- [39] G. V. Vajenine, G. Auffermann, Y. Prots, W. Schelle, R. K. Kremer, A. Simon, R. Kniep, *Inorg. Chem.* **2001**, *40*, 4866.

- [40] A. F. Holleman, E. Wiberg, *Lehrbuch der Anorganischen Chemie*, de Gruyter: Berlin-New York, **2007**.
- [41] N. Wiberg, G. Fischer, H. Bachhuber, *Chem. Ber.* **1974**, *107*, 1456.
- [42] V. E. Bondybey, J. W. Nibler, *J. Chem. Phys.* **1973**, *58*, 2125.
- [43] E. J. Blau, B. F. Hochheimer, *J. Chem. Phys.* **1964**, *41*, 1174.
- [44] K. Rosengren, G. C. Pimentel, *J. Chem. Phys.* **1965**, *43*, 507.
- [45] R. Minkwitz, *Z. Anorg. Allg. Chem.* **1975**, *411*, 1.
- [46] E. Gregoryanz, C. Sanloup, M. Somayazulu, J. Badro, G. Fiquet, H.-K. Mao, R. J. Hemely, *Nat. Mater.* **2004**, *3*, 294.
- [47] J. von Appen, M.-W. Lumey, R. Dronskowski, *Angew. Chem.* **2006**, *118*, 4472; *Angew. Chem. Int. Ed.* **2006**, *45*, 4365.
- [48] J. C. Crowhurst, A. F. Goncharov, B. Sadigh, C. L. Evans, P. G. Morrall, J. L. Ferreira, A. J. Nelson, *Science* **2006**, *311*, 1275.
- [49] A. F. Young, J. A. Montoya, C. Sanloup, M. Lazzeri, E. Gregoryanz, S. Scandolo, *Phys. Rev. B* **2006**, *73*, 153102.
- [50] J. A. Montoya, A. D. Hernandez, C. Sanloup, E. Gregoryanz, S. Scandolo, *Appl. Phys. Lett.* **2007**, *90*, 011909.
- [51] J. C. Crowhurst, A. F. Goncharov, B. Sadigh, J. M. Zaug, D. Aberg, Y. Meng, V. B. Prakapenka, *J. Mater. Res.* **2008**, *23*, 1.
- [52] Z. W. Chen, X. J. Guo, Z. Y. Liu, M. Z. Ma, Q. Jing, G. Li, X. Y. Zhang, L. X. Li, Q. Wang, Y. J. Tian, R. P. Liu, *Phys. Rev. B* **2007**, *75*, 054103.
- [53] R. Yu, Q. Zhan, L. C. De Jonghe, *Angew. Chem.* **2007**, *119*, 1154; *Angew. Chem. Int. Ed.* **2007**, *46*, 1136.
- [54] M. Wessel, R. Dronskowski, *J. Am. Chem. Soc.* **2010**, *132*, 2421.
- [55] N. T. Allen, O. Kennard, D. G. Watson, L. Brammer, A. G. Orpen, R. Taylor, *J. Chem. Soc., Perkin Trans.* **1987**, *2*, S1.
- [56] L. E. Sutton, *Tables of Interatomic Distances and Configuration in Molecules and Ions*, Chemical Society Spec. Publ. 11, Chemical Society: London, **1958**.
- [57] P. A. Giguère, I. D. Liu, *J. Chem. Phys.* **1952**, *20*, 136.
- [58] S. B. Schneider, R. Frankovsky, W. Schnick, *Inorg. Chem.* **2012**, *51*, 2366.
- [59] S. B. Schneider, R. Frankovsky, W. Schnick, *Angew. Chem.* **2012**, *124*, 1909; *Angew. Chem. Int. Ed.* **2012**, *51*, 1873.
- [60] M. Wessel, R. Dronskowski, *J. Comput. Chem.* **2010**, *31*, 1613.
- [61] X. Zhang, A. Zunger, G. Trimarchi, *J. Chem. Phys.* **2010**, *133*, 194504.

- [62] O. Tschauner, S. N. Luo, Y. J. Chen, A. McDowell, J. Knight, S. M. Clark, *High Press. Res.* **2013**, *33*, 202.
- [63] D. Walker, M. A. Carpenter, C. M. Hitch, *Am. Mineral.* **1990**, *75*, 1020.
- [64] D. Walker, *Am. Mineral.* **1991**, *76*, 1092.
- [65] H. Huppertz, *Z. Kristallogr.* **2004**, *219*, 330.
- [66] D. C. Rubie, *Phase Transitions* **1999**, *68*, 431.
- [67] N. Kawai, S. Endo, *Rev. Sci. Instrum.* **1970**, *8*, 1178.
- [68] A. A. Coelho, TOPAS-Academic, Version 4.1; Coelho Software: Brisbane, **2007**.
- [69] J. Bergmann, R. Kleeberg, A. Haase, B. Breidenstein, *Mater. Sci. Forum* **2000**, *303*, 347.
- [70] A. L. Spek, *PLATON, A Multipurpose Crystallographic Tool*, v1.07, Utrecht University, Netherlands, **2003**.
- [71] P. A. Stadelmann, *Ultramicroscopy* **1987**, *21*, 131
- [72] J. P. Perdew, K. Burke, M. Ernzerhof, *Phys. Rev. Lett.* **1996**, *77*, 3865–3868.
- [73] P. E. Blöchl, *Phys. Rev. B* **1994**, *50*, 17953.
- [74] (a) G. Kresse, J. Hafner, *Phys. Rev. B* **1993**, *47*, 558. (b) G. Kresse, J. Furthmüller, *Comput. Mater. Sci.* **1996**, *6*, 15. (c) G. Kresse, J. Furthmüller, *Phys. Rev. B* **1996**, *54*, 11169. (d) G. Kresse, D. Joubert, *Phys. Rev. B* **1999**, *59*, 1758.
- [75] H. J. Monkhorst, J. D. Pack, *Phys. Rev. B* **1976**, *13*, 5188.
- [76] R. Dronskowski, P. E. Blöchl, *J. Phys. Chem.* **1993**, *97*, 8617.
- [77] (a) O. K. Andersen, *Phys. Rev. B* **1975**, *12*, 3060. (b) O. K. Andersen, O. Jepsen, *Phys. Rev. Lett.* **1984**, *83*, 2571.
- [78] U. von Barth, L. Hedin, *J. Phys. C: Solid State Phys.* **1972**, *5*, 1629.
- [79] K. Parlinski, Z. Q. Li, Y. Kawazoe, *Phys. Rev. Lett.* **1997**, *78*, 4063.
- [80] A. Togo, F. Oba, I. Tanaka, *Phys. Rev. B* **2008**, *78*, 134106.
- [81] R. P. Stoffel, R. Dronskowski, *Z. Anorg. Allg. Chem.* **2013**, *639*, 1227.
- [82] J. D. Corbett, E. Carcia, A. M. Guloy, W.-M. Hurng, Y.-U. Kwon, E. A. Leon-Escamilla, *Chem. Mater.* **1998**, *10*, 2824.
- [83] B. Aronsson, *Acta Chem. Scand.* **1960**, *14*, 1414.
- [84] H. Schachner, E. Cerwenka, H. Nowotny, *Monatsh. Chem.* **1954**, *85*, 241.
- [85] A. Kulkarni, J. C. Schön, K. Doll, M. Jansen, *Chem. Asian J.* **2013**, *8*, 743.

- [86] The structure was taken from an earlier experimental report in Smith, H. G.; Nicklow, R. M.; Raubenheimer, L. J.; Wilkinson, M. K. *J. Appl. Phys.* **1966**, *37*, 1047, with $d(\text{O}-\text{O}) = 1.25 \text{ \AA}$. Test computations including full relaxation at the GGA level were also performed, giving a quite different $d(\text{O}-\text{O}) = 1.34 \text{ \AA}$. Nonetheless, COHPs computed for the analogous optimized structure lead to a π^* occupation of 74%, which is within one percent of that given in Figure 8 (right) for the experimental structure. We conclude that the relative filling of the π^* orbital does not seem strongly affected by the structural optimization.
- [87] A. Simon, *Z. Anorg. Allg. Chem.* **1977**, *431*, 5.
- [88] A. Simon, H. J. Deiseroth, *Rev. Chim. Miner.* **1976**, *13*, 98.
- [89] A. Simon, *Molecular Clusters of the Main Group Elements*; Wiley-VCH: Weinheim, **2004**.
- [90] A. Simon, *Crystal Structure and Chemical Bonding in Inorganic Chemistry*; North-Holland Publ. Comb., **1975**.
- [91] A. Simon, *Z. Anorg. Allg. Chem.* **1973**, *395*, 301.
- [92] A. Simon, *Z. Anorg. Allg. Chem.* **1977**, *428*, 187.
- [93] K.-R. Tsai, P. Harris, E. Lassette, *J. Phys. Chem.* **1956**, *60*, 338.
- [94] A. Simon, *Struct. Bonding* **1979**, *36*, 81.
- [95] P. Rauch, A. Simon, *Angew. Chem.* **1992**, *104*, 1505; *Angew. Chem., Int. Ed.* **1992**, *31*, 1519.
- [96] G. Snyder, A. Simon, *J. Am. Chem. Soc.* **1995**, *117*, 1996.
- [97] G. Snyder, A. Simon, *Angew. Chem.* **1994**, *106*, 713; *Angew. Chem., Int. Ed.* **1994**, *33*, 689.
- [98] A. Rabenau, H. Schulz, *J. Less Common Met.* **1976**, *50*, 155.
- [99] L. G. Cota, P. De La Mora, *Acta Crystallogr. B* **2005**, *61*, 133.
- [100] D. Fischer, M. Jansen, *Z. Anorg. Chem.* **2003**, *629*, 1934.
- [101] E. Hellner, F. Laves, *Z. Kristallogr.* **1943**, *105*, 134.
- [102] O. Reckeweg, A. Simon, *Z. Naturforsch. B* **2003**, *85*, 1097.
- [103] (a) E. Zintl, G. Z. Brauer, *Elektrochem.* **1935**, *41*, 102; (b) A. Rabenau, H. Schultz, *J. Less-Common Met.* **1976**, *50*, 155; (c) N. E. Brese, M. O'Keeffe, *Structural Bonding*, Springer: Berlin, **1992**.
- [104] R. D. Shannon, *Acta Crystallogr. Sect. A* **1976**, *32*, 751.
- [105] M. Ren, J. H. Lin, Y. Dong, L. Q. Yang, M. Z. Su, L. P. You, *Chem. Mater.* **1999**, *11*, 1576.

- [106] J. P. Laperches, P. Tarte, *Spectrochim. Acta* **1966**, *22*, 1201.
- [107] G. Blasse, G. P. M. van den Heuvel, *Phys. Stat. Sol* **1973**, *19*, 111.
- [108] M. Somer, *Z. Naturforsch.* **1991**, *46b*, 1664.
- [109] R. Kaindl, G. Sohr, H. Huppertz, *Spectrochim. Acta, Part A* **2013**, *116*, 408.
- [110] A. U. Khan, S. D. Mahanti, *J. Chem. Phys.* **1975**, *63*, 2271.
- [111] V. N. Belevskii, I. I. Vol'nov, S. A. Tokareva, *Bull. Acad. Sci. USSR* **1972**, *21*, 1366.
- [112] Zumsteg, A.; Ziegler, M.; Känzig, W.; Bösch, M. *Phys. Cond. Matter* **1974**, *17*, 267.

5. Conclusion and Outlook

Phases with composition $\text{Sr}_{1-x}\text{Ba}_x\text{Si}_2\text{O}_2\text{N}_2:\text{Eu}^{2+}$ show a tendency to form polytypic modifications, but the presence of various real-structure effects does not affect the luminescence properties in a negative way.^[1-3] At first glance, this is an uncommon behavior since significant deviations from an ordered crystal structure, accompanied by local changes of activator-atom surrounding, are supposed to affect the FWHM value due to an increase of inhomogeneous line broadening. For $\text{Sr}_{1-x}\text{Ba}_x\text{Si}_2\text{O}_2\text{N}_2:\text{Eu}^{2+}$ this is not the case, because the stacking faults present have no impact on the Eu^{2+} coordination sphere.^[3] As a consequence, both modifications of $\text{SrSi}_2\text{O}_2\text{N}_2:\text{Eu}^{2+}$ with different stacking sequences exhibit excellent luminescence properties.^[1,4] Till now, $\text{SrSi}_2\text{O}_2\text{N}_2:\text{Eu}^{2+}$ (QE > 90 %) based LEDs are the most efficient green pc-LEDs (LE = 537 lm/W; η_L = 166 lm/W).^[5]

Even an intergrowth structure, as present in $\text{Sr}_{0.25}\text{Ba}_{0.75}\text{Si}_2\text{O}_2\text{N}_2:\text{Eu}^{2+}$, does not necessarily result in a disadvantage.^[2] On the contrary, this compound exhibits the smallest FWHM value (37nm) ever observed for a blue emitting Eu^{2+} -doped nitride material. For improving the luminescence properties of these materials, further strategies might be the selective control of above mentioned real-structure effects during synthesis, optimization of the temperature program due to economical reasons and to change particle morphology from platelets to more sphere-like crystallites. The latter one would lead to a higher efficiency and a closer packing in ceramics. A desired phase within this material class would exhibit an emission wavelength of about 530 nm^[6] (comparable to that of $\text{SrSi}_2\text{O}_2\text{N}_2:\text{Eu}^{2+}$)^[1,4,7] and a FWHM of about 40 nm (comparable to that of $\text{BaSi}_2\text{O}_2\text{N}_2:\text{Eu}^{2+}$)^[4,7]. Such a phase was not yet accessible in high-temperature high-pressure experiments, transforming the crystal structure of $\text{SrSi}_2\text{O}_2\text{N}_2$ ^[1,8] into that of $\text{BaSi}_2\text{O}_2\text{N}_2$ ^[9] by increasing the coordination number according to the “pressure-coordination rule”.^[10] Additionally, unknown $\text{Sr}_{1-x}\text{Ba}_x\text{Si}_2\text{O}_2\text{N}_2:\text{Eu}^{2+}$ modifications might exhibit improved luminescent properties.

Similar investigations are also promising for compounds in the system $\text{Sr}_{1-x}\text{Ca}_x\text{Si}_2\text{O}_2\text{N}_2:\text{Eu}^{2+}$. Here, comparable to $\text{SrSi}_2\text{O}_2\text{N}_2$ and $\text{BaSi}_2\text{O}_2\text{N}_2$,^[1,8,9] the pure phases $\text{SrSi}_2\text{O}_2\text{N}_2$ ^[1,8] and $\text{CaSi}_2\text{O}_2\text{N}_2$ ^[11] are not isotypic which means that no solid-solution series is present. Therefore, surprising luminescence properties of mixed phases might result. However, regarding the different topologies of tetrahedra frameworks in the silicate layers in both phases, less pronounced real-structure effects are expected compared to $\text{Sr}_{1-x}\text{Ba}_x\text{Si}_2\text{O}_2\text{N}_2:\text{Eu}^{2+}$ phases, where the silicate layers are identical in the pure phases.^[1,8,9]

In general, it is still important to search for new phosphors which emit in the green-yellow spectral region, since only a few existing materials are industrially usable for high-power pc-LED applications. Because of the maximum eye sensitivity in this color region, even small changes in the emission behavior of the new compounds might affect e.g. the color rendition in a positive way. Eu^{2+} -doped oxonitridosilicates are currently the most promising material class, regarding the requirements such new phosphors have to fulfill. Due to a high degree of tetrahedra condensation, the silicate substructures are very rigid in these materials. This remarkable stability is the basis for high quantum-efficiency values because lattice vibrations are effectively suppressed. The relative position of 4f and 5d energy levels of Eu^{2+} and the nephelauxetic effect of the ligands O and N lead to the desired emission in the green-yellow spectral region. New compounds may also be synthesized by non-standard synthesis strategies, in order to avoid the formation of thermodynamically controlled products which is often the case for high-temperature solid-state reactions. One example might be the synthesis under ammonothermal conditions. For example, the red phosphor “ $\text{SrAlSiN}_3:\text{Eu}^{2+}$ ” is accessible using this route.^[12] Even though this phosphor can also be synthesized by a common solid-state reaction, *Watanabe* showed that in principle luminescent nitride compounds can be obtained under ammonothermal conditions. Additionally, also lower temperatures are necessary (773 K) compared to the solid-state reaction (> 2000 K). This concept should be transferable also to other / new nitride phosphors.

For the replacement of incandescent lamps and CFLs by warm-white pc-LEDs, efficient red phosphors are needed in addition to the intense green emitters. Nitrido(alumo)silicates like $\text{Ca}_{1-x}\text{Sr}_x\text{AlSiN}_3:\text{Eu}^{2+}$ ^[13] or $\text{Sr}_2\text{Si}_5\text{N}_8:\text{Eu}^{2+}$ ^[14] exhibit emission in the red spectral region due to nephelauxetic effect of N, coordinating the activator ion Eu^{2+} . In order to extend the search for red phosphors to other material classes and retain positive aspects of Eu^{2+} -doped nitridosilicates like high QE value and thermal stability at the same time, nitride compounds with silicate-analogous structures are of great interest. The material class of nitridoaluminates and nitridogallates are promising in this respect, because only a few compounds have been investigated in detail so far and almost nothing is known about their luminescence properties. The main focus is on “narrow-red” phosphors, meaning the minimization of the FWHM value. Thus, a more accurate adjustment of the color temperature becomes possible and the color rendition for a corresponding white pc-LED is improved. Red phosphors, with absorption maximum within the UV to blue spectral range, intrinsically exhibit a large FWHM, since a large Stokes shift, i.e. a strong deformation of the activator surrounding after excitation, favors various f-d transitions for relaxation. As there is an industrial demand for

narrow red phosphors, it is expected that, similar to green phosphors, suitable host lattices will be found and optimized rapidly. A promising strategy is once again to focus on compounds where the activator is coordinated in a highly symmetric way. This reduces inhomogeneous line broadening to a minimum.

Synthesis and exploration of new synthesis routes, material characterization by several analytical methods and evaluation of application possibilities of phosphors will remain a domain of the fundamental research at universities in cooperation with companies in the future. As shown in the past and emphasized in this thesis, a profound comprehension of structure-property relations is the basis for the improvement of phosphor materials until they may reach their marketability. A knowledge transfer between the different phosphor systems (silicates, gallates etc.), i.e. the development of “materials-design concepts”, represents the most challenging part to scientists. At the same time it is the fundamental driving force in the field of phosphor-material research.

References

- [1] M. Seibald, T. Rosenthal, O. Oeckler, C. Maak, A. Tücks, P. J. Schmidt, D. Wiechert, W. Schnick, *Chem. Mater.* **2013**, *25*, 1852-1857.
- [2] M. Seibald, T. Rosenthal, O. Oeckler, F. Fahrnbauer, A. Tücks, P. J. Schmidt, W. Schnick, *Chem. Eur. J.* **2012**, *18*, 13446-13452.
- [3] M. Seibald, O. Oeckler, V. R. Celinski, P. J. Schmidt, A. Tücks, W. Schnick, *Solid State Sci.* **2011**, *13*, 1769-1778.
- [4] V. Bachmann, C. Ronda, O. Oeckler, W. Schnick, A. Meijerink, *Chem. Mater.* **2009**, *21*, 316-325.
- [5] P. Schmidt, A. Tücks, H. Bechtel, D. Wiechert, R. Mueller-Mach, G. Mueller, W. Schnick, *Proc. SPIE-Int. Soc. Opt. Eng.* **2008**, *7058*, 70580L (Eighth International Conference on Solid State Lighting, **2008**).
- [6] J. M. Phillips, M. E. Coltrin, M. H. Crawford, A. J. Fischer, M. R. Krames, R. Mueller-Mach, G. O. Mueller, Y. Ohno, L. E. S. Rohwer, J. A. Simmons, J. Y. Tsao, *Laser & Photon. Rev.* **2007**, *1*, 307-333.
- [7] Y. Q. Li, A. C. A. Delsing, G. de With, H. T. Hintzen, *Chem. Mater.* **2005**, *17*, 3242-3248.

- [8] O. Oeckler, F. Stadler, T. Rosenthal, W. Schnick, *Solid State Sci.* **2007**, *9*, 205-212.
- [9] J. A. Kechele, O. Oeckler, F. Stadler, W. Schnick, *Solid State Sci.* **2009**, *11*, 537-543.
- [10] Unpublished results.
- [11] H. A. Höpfe, F. Stadler, O. Oeckler, W. Schnick, *Angew. Chem.* **2004**, *116*, 5656-5659; *Angew. Chem. Int. Ed.* **2004**, *43*, 5540-5542.
- [12] T. Watanabe, K. Nonaka, J. W. Li, K. Kishida, M. Yoshimura, *J. Ceram. Soc. Jpn.* **2012**, *120*, 500-502.
- [13] H. Watanabe, N. Kijima, *J. Alloys Compd.* **2009**, *475*, 434-439.
- [14] H. A. Höpfe, H. Lutz, P. Morys, W. Schnick, A. Seilmeier, *J. Phys. Chem. Solids* **2000**, *61*, 2001-2006.

6. Summary

1. Highly Efficient pc-LED Phosphors $\text{Sr}_{1-x}\text{Ba}_x\text{Si}_2\text{O}_2\text{N}_2:\text{Eu}^{2+}$ ($0 \leq x \leq 1$) - Crystal Structures and Luminescence Properties Revisited

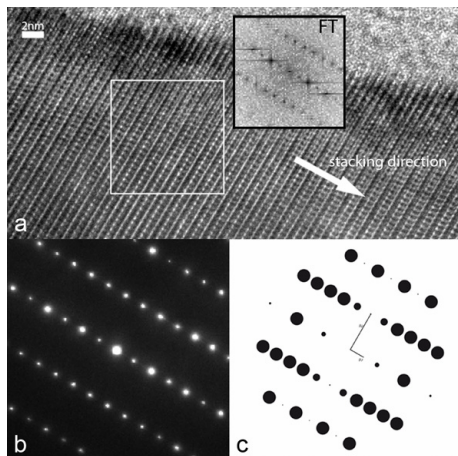
All known $\text{Sr}_{1-x}\text{Ba}_x\text{Si}_2\text{O}_2\text{N}_2:\text{Eu}^{2+}$ ($0 \leq x \leq 1$) phases represent layered oxonitridosilicates with alternately stacked metal-ion and silicate layers. The corresponding structures are compared to each other, elaborating similarities and differences, mainly focusing on the relative orientation of consecutive silicate layers. The impact of various real-structure effects on diffraction patterns is shown and guidelines are worked out to avoid misinterpretation. As the



homogeneity of such samples is strongly related to the synthesis route, a possible reaction mechanism is postulated and possible impurity phases are discussed. Eu-doped $\text{Sr}_{1-x}\text{Ba}_x\text{Si}_2\text{O}_2\text{N}_2:\text{Eu}^{2+}$ ($0 \leq x \leq 1$) samples shown intense luminescence from the blue to the yellow spectral region in dependence of the composition.

2. New Polymorph of the Highly Efficient LED-Phosphor $\text{SrSi}_2\text{O}_2\text{N}_2:\text{Eu}^{2+}$ - Polytypism of a Layered Oxonitridosilicate

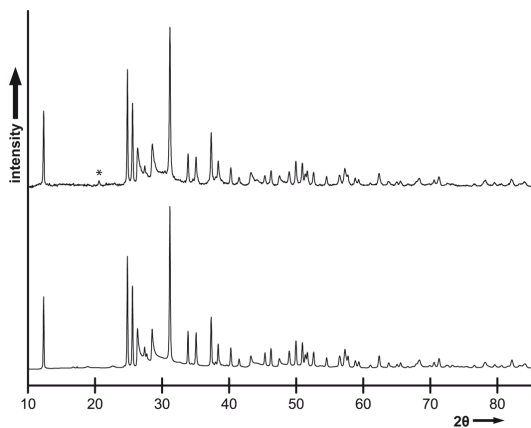
The monoclinic polymorph of $\text{SrSi}_2\text{O}_2\text{N}_2$ was synthesized by a solid-state reaction ($P2_1$, $a = 7.1036(14)$, $b = 14.078(3)$, $c = 7.2833(15)$ Å, $\beta = 95.23(3)^\circ$, $V = 725.3(3)$ Å³). The crystal structure is characterized by an alternating stacking sequence of silicate layers and metal-ion layers. The translation period along the stacking direction is doubled compared to the triclinic



polymorph. The structure model was confirmed by TEM investigations in combination with HRTEM-image simulations. Single-crystal luminescence measurements yielded an emission wavelength of 532 nm (FWHM ~ 2600 cm⁻¹) which is equal to a shift to smaller wavelengths by ~ 5 nm compared to the triclinic polymorph. The monoclinic $\text{SrSi}_2\text{O}_2\text{N}_2:\text{Eu}^{2+}$ polymorph is a very attractive phosphor material for enhancement of color rendition of white-light pc-LEDs.

3. Real Structure and Diffuse Scattering of $\text{Sr}_{0.5}\text{Ba}_{0.5}\text{Si}_2\text{O}_2\text{N}_2:\text{Eu}^{2+}$ - A Highly Efficient Yellow Phosphor for pc-LEDs

$\text{Sr}_{0.5}\text{Ba}_{0.5}\text{Si}_2\text{O}_2\text{N}_2:\text{Eu}^{2+}$ shows intense emission in the yellow spectral range ($\lambda_{\text{em}} \approx 560$ nm). Rietveld refinement reveals the average structure of $\text{Sr}_{0.5}\text{Ba}_{0.5}\text{Si}_2\text{O}_2\text{N}_2:\text{Eu}^{2+}$ ($P1$, $a = 7.2059(2)$, $b = 7.3887(3)$, $c = 7.3340(2)$ Å, $\alpha = 88.524(4)$, $\beta = 84.454(3)$, $\gamma = 75.980(4)^\circ$, $V = 377.07(2)$ Å³) which is isotypic to that of triclinic $\text{SrSi}_2\text{O}_2\text{N}_2:\text{Eu}^{2+}$. The PXRD pattern shows pronounced broad intensity maxima indicative for diffuse scattering from planar defects. In order to elucidate the real structure, PXRD simulations have been calculated based

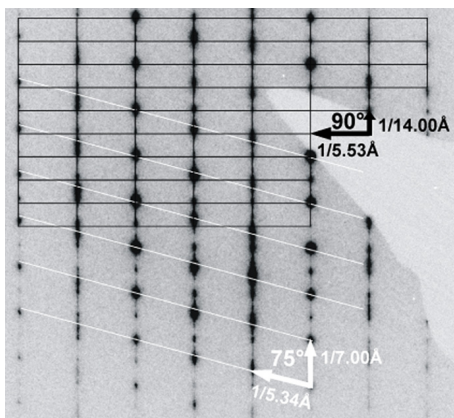


on a disorder model, taking into account all possible metal-atom positions and silicate layer orientations. These simulations show that crystallites of $\text{Sr}_{0.5}\text{Ba}_{0.5}\text{Si}_2\text{O}_2\text{N}_2:\text{Eu}^{2+}$ are built up from small anti-phase domains within larger twin domains. Chromaticity coordinates are almost identical to the most frequently used commercial LED phosphor $\text{YAG}:\text{Ce}^{3+}$ but a significantly

higher luminous efficacy ($\text{LE} = 495$ lm/W) is measured. Therefore, LEDs with this material qualify for applications in e.g. outdoor lighting.

4. Unexpected Luminescence Properties of $\text{Sr}_{0.25}\text{Ba}_{0.75}\text{Si}_2\text{O}_2\text{N}_2:\text{Eu}^{2+}$ - A Narrow Blue Emitting Oxonitridosilicate with Cation Ordering

The crystal structure of $\text{Sr}_{0.25}\text{Ba}_{0.75}\text{Si}_2\text{O}_2\text{N}_2:\text{Eu}^{2+}$ was determined using electron and X-ray diffraction methods ($Pna2_1$, $a = 5.470(2)$, $b = 14.277(3)$, $c = 4.791(1)$ Å and $V = 374.2(2)$ Å³). In crystallites suitable for TEM investigations, intergrowth of nanodomains is present, which

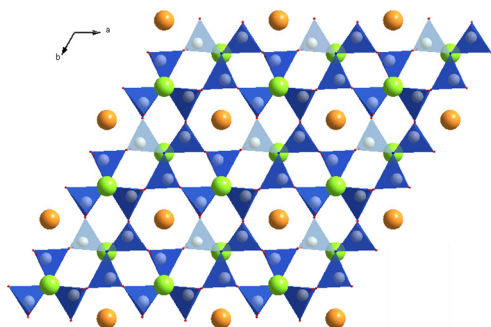


leads to pronounced diffuse scattering. Corrugated metal-atom layers are present in the structure while lattice parameters are similar to those of the $\text{BaSi}_2\text{O}_2\text{N}_2$ -type. HRTEM image simulations indicate cation ordering, which, in combination with the corrugated metal atom layers, explains the unexpected excellent luminescence properties. $\text{Sr}_{0.25}\text{Ba}_{0.75}\text{Si}_2\text{O}_2\text{N}_2:\text{Eu}^{2+}$ shows intense blue emission ($\lambda_{\text{em}} = 472$ nm) and the FWHM of

the emission band (37 nm) corresponds to the smallest value observed for Eu^{2+} -doped blue emitting (oxo)nitridosilicates so far.

5. Material Properties and Structural Characterization of $M_3Si_6O_{12}N_2:Eu^{2+}$ (M=Ba, Sr) - A Comprehensive Study on a Promising Green Phosphor for pc-LEDs

The crystal structure of efficient green phosphor $Ba_{3-x}Sr_xSi_6O_{12}N_2$ ($0 \leq x \leq 1$) was refined on the basis of single-crystal and powder X-ray diffraction data ($Ba_3Si_6O_{12}N_2$, $P\bar{3}$, $a = 7.5218(1) \text{ \AA}$, $c = 6.4684(1) \text{ \AA}$, $V = 316.94(1) \text{ \AA}^3$). The layered oxonitridosilicate consists

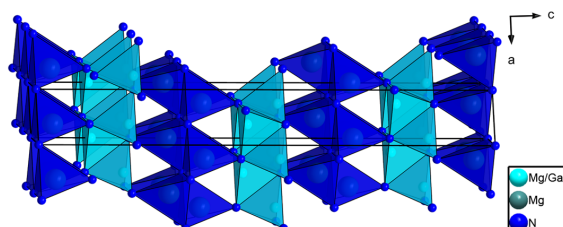


of vertex-sharing SiO_3N -tetrahedra forming 6- and 4er-rings as fundamental building units. High-quality single crystals were the basis for the detailed analysis of structure-property relationships for the mixed phases. The availability of reliable crystallographic data was the basis for further theoretical investigations. The

band gap was measured to be $7.05 \pm 0.25 \text{ eV}$ and therefore agrees well with calculated value of 6.93 eV . $Ba_3Si_6O_{12}N_2:Eu^{2+}$ exhibits excellent luminescence properties ($\lambda \approx 527 \text{ nm}$, $FWHM \approx 65 \text{ nm}$), which provides potential for application in pc-LEDs. For an increasing Sr-ratio a shift of the emission wavelength to lower energies is observed.

6. Magnesium Double Nitride Mg_3GaN_3 as New Host Lattice for Eu^{2+} -Doping - Synthesis, Structural Studies, Luminescence and Band-Gap Determination

The double nitride Mg_3GaN_3 and binary nitride Mg_3N_2 were synthesized from the elements at $760 \text{ }^\circ\text{C}$ in welded shut Ta-ampoules. Mg_3GaN_3 ($R\bar{3}m$, $a = 3.3939(5)$, $c = 25.854(5) \text{ \AA}$, $V = 257.91(7) \text{ \AA}^3$) consists of an electroneutral three-dimensional network of MgN_4 - and mixed $(Mg/Ga)N_4$ -tetrahedra which share common corners and edges. The determination of a structure model for Mg_3GaN_3 was the basis for first-principles DFT calculations. The most challenging part was the precise characterization of the electron density on the mixed

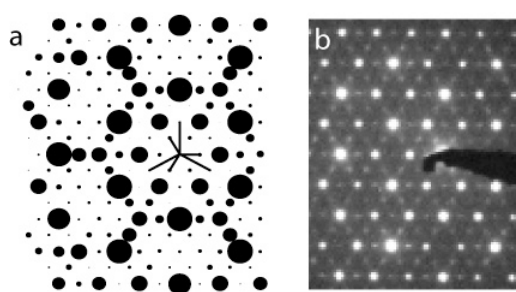


occupied metal site. For Mg_3GaN_3 a direct band gap of 3.0 eV was calculated and confirmed by soft X-ray spectroscopy measurements. As expected, the band gap is between the values for GaN and Mg_3N_2 . $Mg_3GaN_3:Eu^{2+}$ exhibits

yellow luminescence ($\lambda_{max.} = 578 \text{ nm}$, $FWHM = 132 \text{ nm}$), while $Mg_3N_2:Eu^{2+}$ also shows luminescence ($\lambda_{max.} = 589 \text{ nm}$, $FWHM = 145 \text{ nm}$) at room temperature.

7. High-Pressure Synthesis and Characterization of $\text{Li}_2\text{Ca}_3[\text{N}_2]_3$ - An Uncommon Metallic Diazenide with $[\text{N}_2]^{2-}$ Ions

$\text{Li}_2\text{Ca}_3(\text{N}_2)_3$ ($Pmma$, $a = 4.7747(1)$, $b = 13.9792(4)$, $c = 8.0718(4)$ Å, $V = 538.77(3)\text{Å}^3$) is the first representative of a ternary diazenide. The compound was synthesized by controlled thermal decomposition of lithium- and calcium azide mixtures in a multi-anvil press (9 GPa, 1023 K). Due to pseudo-hexagonal metrics, PXRD investigations initially led to incorrect structure models. Especially, SAED simulations significantly differed from experimental ones. Detailed crystallographic analysis, i.e. the stepwise reduction to orthorhombic symmetry (requires threefold twinning), was the basis for a reliable structure model and finally made quantum-theoretical investigations possible. PXRD analysis in correct space group results in



N–N bonds of 1.34(2)-1.35(3) Å exceeding the values of known binary diazenides. Moreover, refined N–N distances rather match reported values for $[\text{N}_2]^{3-}$ radical anions. The true character of the $[\text{N}_2]$ -entity was finally settled by a variety of complementary analyses including electron-

diffraction methods, electron spin resonance spectroscopy (ESR), magnetic and conductivity measurements as well as density-functional theory. $\text{Li}_2\text{Ca}_3[\text{N}_2]_3$ contains solely diazenide $[\text{N}_2]^{2-}$ units and is therefore better described as $(\text{Li}^+)_2(\text{Ca}^{2+})_3([\text{N}_2]^{2-})_3 \cdot (\text{e}^-)_2$.

7. Appendix

7.1 Supporting information for chapter 2.5

Cordula Braun, Markus Seibald, Saskia L. Börger, Oliver Oeckler, Teak D. Boyko, Alexander Moewes, Gerhard Mieke, Andreas Tücks, and Wolfgang Schnick, *Chem. Eur. J.* **2010**, *16*, 9646-9657.

Table S1. Occupied Wyckoff sites, refined atomic coordinates and anisotropic displacement parameters U_{eq} and U_{iso} (in \AA^2) of $\text{Ba}_3\text{Si}_6\text{O}_{12}\text{N}_2$, $\text{Ba}_{2.56}\text{Sr}_{0.44}\text{Si}_6\text{O}_{12}\text{N}_2$ and $\text{Ba}_2\text{SrSi}_6\text{O}_{12}\text{N}_2$ (standard deviation in parentheses).

Compound	Atom	Wyck.	x	y	z	s.o.f.	U_{eq} in \AA^2
$\text{Ba}_3\text{Si}_6\text{O}_{12}\text{N}_2$	Ba1/Sr1	1a	0	0	0	1/0	0.0119(2)
	Ba2/Sr2	2d	1/3	2/3	0.10335(7)	1/0	0.0116(2)
	Si1	6g	0.40651(17)	0.23528(18)	0.38956(17)	1	0.0077(2)
	O1	6g	0.6978(5)	0.0158(4)	0.5907(5)	1	0.0097(6)
	O2	6g	0.6399(5)	0.7006(5)	0.8289(5)	1	0.0108(6)
	N1	2d	1/3	2/3	0.5667(9)	1	0.010(2)
$\text{Ba}_{2.56}\text{Sr}_{0.44}\text{Si}_6\text{O}_{12}\text{N}_2$	Ba1/Sr1	1a	0	0	0	0.673(4)/0.327(4)	0.0183(6)
	Ba2/Sr2	2d	1/3	2/3	0.10448(13)	0.942(8)/0.058(8)	0.0177(3)
	Si1	6g	0.4043(4)	0.2334(3)	0.3866(3)	1	0.0132(8)
	O1	6g	0.6982(8)	0.0165(7)	0.5898(8)	1	0.015(2)
	O2	6g	0.6451(7)	0.7061(8)	0.8322(8)	1	0.018(2)
	N1	2d	1/3	2/3	0.5719(16)	1	0.014(3)
$\text{Ba}_2\text{SrSi}_6\text{O}_{12}\text{N}_2$	Ba1/Sr1	1a	0	0	0	0.360(6)/0.640(6)	0.0106(2)
	Ba2/Sr2	2d	1/3	2/3	0.10524(3)	0.825(7)/0.175(7)	0.01095(6)
	Si1	6g	0.40420(7)	0.23335(7)	0.38535(7)	1	0.0069(2)
	O1	6g	0.6978(2)	0.01838(19)	0.5906(2)	1	0.0100(3)
	O2	6g	0.6482(2)	0.7066(2)	0.8340(2)	1	0.0126(3)
	N1	2d	1/3	2/3	0.5749(4)	1	0.0091(5)

Compound	Atom	U_{11}	U_{22}	U_{33}	U_{12}	$U_{13} = U_{23}$
$\text{Ba}_3\text{Si}_6\text{O}_{12}\text{N}_2$	Ba1/Sr1	0.0093(2)	0.0093(2)	0.0171(3)	0.00466(10)	0
	Ba2/Sr2	0.01170(17)	0.01170(17)	0.0113(2)	0.00585(8)	0
	Si1	0.0064(5)	0.0066(5)	0.0106(5)	0.0036(4)	0
	O1	0.0081(14)	0.0066(14)	0.0131(15)	0.0027(12)	0
	O2	0.0086(14)	0.0111(15)	0.0126(14)	0.0048(12)	0
	N1	0.0086(17)	0.0086(17)	0.012(3)	0.0043(9)	0
$\text{Ba}_{2.56}\text{Sr}_{0.44}\text{Si}_6\text{O}_{12}\text{N}_2$	Ba1/Sr1	0.0149(7)	0.0149(7)	0.0251(9)	0.0075(3)	0
	Ba2/Sr2	0.0174(4)	0.0174(4)	0.0184(5)	0.0087(2)	0
	Si1	0.0104(13)	0.0111(13)	0.0178(13)	0.0051(10)	0
	O1	0.015(3)	0.014(3)	0.019(3)	0.010(3)	0
	O2	0.013(3)	0.024(3)	0.019(3)	0.012(3)	0
	N1	0.013(4)	0.013(4)	0.016(6)	0.007(2)	0
$\text{Ba}_2\text{SrSi}_6\text{O}_{12}\text{N}_2$	Ba1/Sr1	0.00883(12)	0.00883(12)	0.01427(18)	0.00442(6)	0
	Ba2/Sr2	0.01196(7)	0.01196(7)	0.00893(10)	0.00598(4)	0
	Si1	0.0062(2)	0.0066(2)	0.0083(2)	0.00335(17)	0
	O1	0.0110(6)	0.0064(5)	0.0106(6)	0.0030(4)	0
	O2	0.0155(6)	0.0143(6)	0.0099(6)	0.0089(5)	0
	N1	0.0059(6)	0.0059(6)	0.0154(12)	0.0030(3)	0

7.2 Supporting information for chapter 3.2

Frauke Hintze, Neil W. Johnson, Markus Seibald, David Muir, Alexander Moewes, and Wolfgang Schnick, *Chem. Mater.* **2013**, *25*, 4044-4052.

Table S1. Crystallographic Data for Mg₃N₂.

	Mg ₃ N ₂
Formula mass/g·mol ⁻¹	100.95
Temperature/K	293(2)
Crystal system	cubic
Space group	<i>Ia</i> $\bar{3}$ (no. 206)
Lattice parameter/Å	<i>a</i> = 9.9550(11)
V/Å ³	986.56(19)
Formula units/cell	16
Crystal size/mm ³	0.1 · 0.1 · 0.1
Abs. coefficient μ/mm ⁻¹	0.866
<i>F</i> (000)	800
Diffractometer	Stoe IPDS I
Radiation, graphite-monochromator	Mo-K _α (λ = 0.71073 Å)
θ range/°	4.09-29.98
Measured reflections	4724
Independent reflections	243
Observed reflections	205
Refined parameters	18
GOF	1.075
<i>R</i> indices (<i>F</i> _o ² ≥ 2σ(<i>F</i> _o ²))	<i>R</i> 1 = 0.0394, <i>wR</i> 2 = 0.0966
<i>R</i> indices (all data)	<i>R</i> 1 = 0.0476, <i>R</i> 2 = 0.1012

7.3 Supporting information for chapter 4.1

Sebastian B. Schneider, Markus Seibald, Volker L. Deringer, Ralf P. Stoffel, Gina M. Friederichs, Henryk Laqua, Viola Duppel, Gunnar Jeschke, Richard Dronskowski, and Wolfgang Schnick, *J. Am. Chem. Soc.* **2013**, *135*, 16668-16679.

Synthesis of Azides

Lithium azide was obtained by precipitation from its aqueous solution (Sigma-Aldrich, 20 wt% solution in water) by evaporation in vacuum. The product was dried over P_4O_{10} using a vacuum desiccator (24 h). An aqueous solution of calcium azide was obtained from the reaction of $Ca(OH)_2$ with excess of NH_4N_3 (1:4) according to the procedure reported in literature.^[1] First $Ca(OH)_2$ (1.5 g, 20.1 mmol, Sigma-Aldrich, 99.995%) is dissolved in 200 ml of water. Then an excess of NH_4N_3 (4.8 g, 80.5 mmol) is added generating aqueous $Ca(N_3)_2$, NH_3 and H_2O . Ammonia is boiled off and calcium azide is precipitated by evaporating the water. The obtained calcium azide is dried over $CaCl_2$ (Sigma-Aldrich, 99.99%) using a vacuum desiccator (24 h). NH_4N_3 was obtained by the metathesis reaction of NH_4NO_3 (3.99 g, 50 mmol, Sigma-Aldrich, 99.0%) and NaN_3 (3.25 g, 50 mmol, Acros Organics, Geel, Belgium, 99%) in a silica tube at elevated temperatures. By heating from room temperature to 200 °C within 0.5 h, annealing for 12 h and cooling down again to room temperature within 6 h,^[2] NH_4N_3 was precipitated at the cold end of the silica tube separated from $NaNO_3$, which crystallized at the hot end during the reaction.

Each azide was analyzed by means of powder X-ray diffractometry (PXRD) and Fourier transform infrared spectroscopy (FTIR).

Appearance of $Li_2Ca_3[N_2]_3$ powder after HP/HT experiment

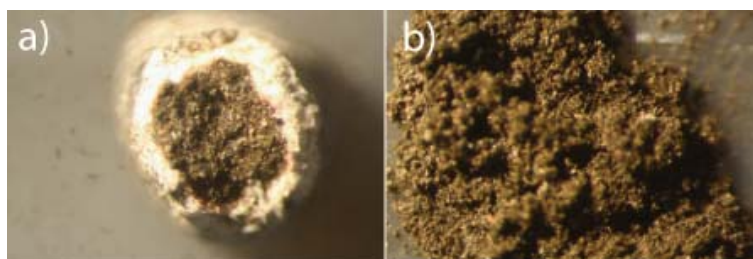


Figure S1. a) $Li_2Ca_3[N_2]_3$ (golden powder) surrounded by the white boron nitride h-BN crucible after HP/HT experiment; b) isolated and ground $Li_2Ca_3[N_2]_3$.

Information about the data collection and selected crystallographic details of the Rietveld refinement of $\text{Li}_2\text{Ca}_3[\text{N}_2]_3$

Table S1. Information about the data collection and selected crystallographic details of the Rietveld refinement of $\text{Li}_2\text{Ca}_3[\text{N}_2]_3$.

Formula	$\text{Li}_2\text{Ca}_3[\text{N}_2]_3$
Synthesis Conditions	9 GPa @ 1023 K
fw /g·mol ⁻¹	218.16
space group	<i>Pmma</i> (no. 51)
cell parameters / Å	$a = 4.7747(1)$ $b = 13.9792(4)$ $c = 8.0718(4)$
V /Å ³	538.77(3)
Z /cell	4
ρ_{calc} /g·cm ⁻³	2.6894(1)
μ_{calc} /mm ⁻¹	26.08(1)
Data Collection	
type of diffractometer	STOE Stadi P
geometry	Debye-Scherrer
radiation, monochromator	Cu- $K_{\alpha 1}$ ($\lambda = 1.54056$ Å), Ge(111)
T /K	298(2)
detector	linear PSD ($\Delta 2\theta = 5^\circ$)
2θ range /°	5–100
number of observed reflections	345
Structure Analysis and Refinement	
method of refinement	fundamental parameter approach ^[3]
program package	TOPAS Academic ^[4]
atomic parameters	32
background function	shifted Chebyshev /16
/parameters	
R indices	GoF(χ^2) = 1.644 $R_p = 0.06168$ $wR_p = 0.08109$

Temperature-dependent *in situ* X-Ray diffraction from 298 to 700K

Figure S2 shows the high-temperature *in situ* X-ray diffraction patterns of $\text{Li}_2\text{Ca}_3[\text{N}_2]_3$ from room temperature to 700 K. At about 610 K $\text{Li}_2\text{Ca}_3[\text{N}_2]_3$ decomposes spontaneously. Thus no further reflections are obtained.

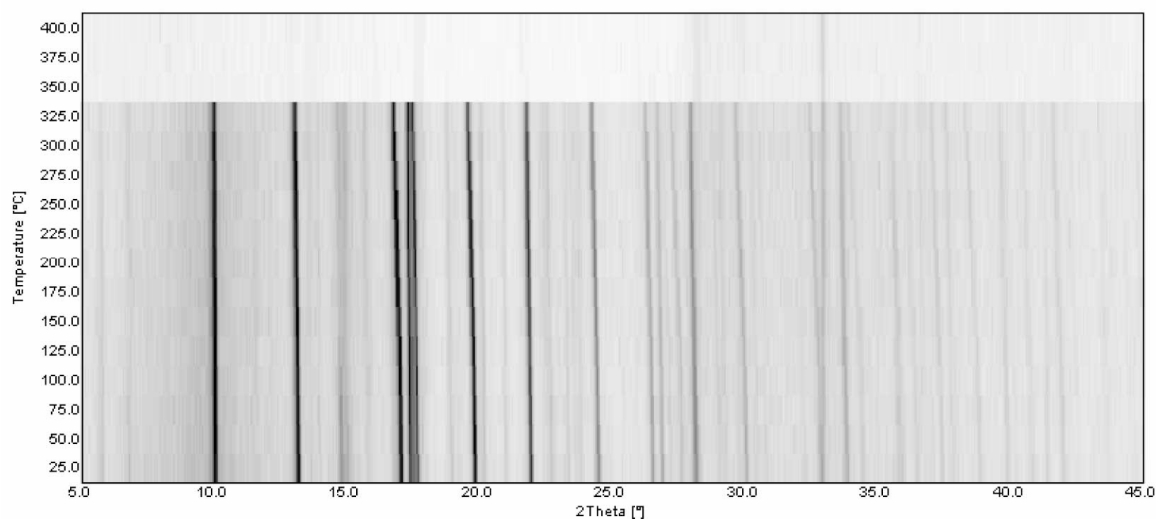


Figure S2. High-temperature *in situ* X-ray diffraction patterns of $\text{Li}_2\text{Ca}_3[\text{N}_2]_3$ (Mo- $K_{\alpha 1}$ -radiation (0.7093 Å)).

Electron Spin Resonance Spectroscopy

A) Further experimental details

Detail spectra of the narrow-line signal in the low- and high-temperature region were measured on spectrometer (a) at 26 dB microwave attenuation (0.5 mW microwave power) with a modulation amplitude of 0.1 mT peak-to-peak, a time constant of 20.48 ms, and a conversion time of 81.92 ms as well as at 20 dB microwave attenuation (2 mW microwave power) with a modulation amplitude of 0.5 mT peak-to-peak, a time constant of 10.24 ms, and a conversion time of 40.96 ms, respectively. The background corrected spectrum was obtained by subtracting the spectrum of the Ar filled capillary (50 scans) from the spectrum of the sample (50 scans) and the subtracting a third-order polynomial background fitted to the first and last 20% of the spectrum (sweep width 25 mT, centered at $g = 2.0023$). The latter background subtraction removes the contribution of the broad-line signal in the measured range. Overview spectra in the low-temperature region of both the broad-line and narrow-line signal were measured at all spectrometers, covering a temperature range between ambient temperature and 10 K in intervals of 20 K. A microwave attenuation of 14 dB (8 mW

microwave power) was found not to lead to signal saturation of either the broad-line or narrow-line signal. Typically 5 scans were measured with a time constant of 10.24 ms and a conversion time of 40.84 ms in a range between 5 and 605 mT, except for spectrometer (c) where a range between 50 and 450 mT and digital smoothing with time constant of 50 ms were used. Overview spectra in the high-temperature region of both the broad-line and narrow-line signal were measured on spectrometer (a) at a microwave attenuation of 14 dB (8 mW microwave power). Depending on signal intensity, either 10 or 40 scans were measured with a time constant of 10.24 ms and a conversion time of 40.84 ms in a range between 4 and 604 mT. Spectra were recorded at 300, 400, 500 and 525 K.

Mn²⁺ centers in magnesium oxide (Aldrich) were used as an intensity reference and TEMPOL (4-Hydroxy-2,2,6,6-tetramethylpiperidin-1-oxyl, Fluka) in deionized water or CuSO₄·5H₂O (Aldrich) were used as a concentration standard. Solid 2,2-Diphenyl-1-picrylhydrazyl (DPPH, Alexis Biochemicals) radical was used as standard ($g = 2.0037$). A quartz Mark tube capillary filled with argon was used as a background standard. Both the sample and background capillaries were placed in 1.5 mm Suprasil tubes (Wilmad), which were in turn placed in 3 mm fused quartz tubes. Spectra measured over the whole range from 4 to 605 mT were analyzed by double integration of the broad line. The very small contribution of the double integral of the narrow line does not exceed other measurement and analysis errors and was neglected. Spectra measured on spectrometer (c) were analyzed by fitting a Voigt derivative line shape and a linear background contribution to the broad line, using home-written Matlab software. Temperature dependence of the sensitivity of spectrometer (a) was calibrated by measurements on the Mn:MgO sample. For analysis of the reference spectra, a Voigt derivative line with fixed Gaussian character of -0.3 and variable amplitude, width, and offset was fitted to the high-field line of the Mn²⁺ sextet, using Bruker Xepr software. The negative Gaussian character may be unphysical, but provided better fits than a purely Lorentzian line. Integral intensity of the absorption spectrum up to a constant factor was computed as the product of amplitude and square width of the derivative absorption signal. Spectra of the concentration standard Tempol and CuSO₄·5H₂O were analyzed by double integration with Xepr.

B) Temperature-dependence of ESR signals from 10 to 525 K

The ESR spectra of $\text{Li}_2\text{Ca}_3[\text{N}_2]_3$ consist of a broad-line component that corresponds to the overwhelming fraction of the observed paramagnetic species and a narrow-line component that corresponds to traces of paramagnetic species of the order of magnitude as it is also found in BaN_2 .

At all temperatures the spectrum of the sample consists of an asymmetric, structured, narrow line with a width of approximately 4.3 mT and of a nearly symmetric, unstructured, broad line with a width of approximately 80 mT. The two lines have comparable amplitude in the usual absorption derivative representation of CW ESR spectra at all temperatures (see Figure S3), which means that the ratio of the numbers of spins contribution to the broad and narrow line, respectively, is about 350:1. The g -value at the zero crossing of the narrow-line spectrum is 2.0052 ± 0.0001 (see Figure 12 in publication); this corresponds to the maximum of the absorption spectrum. The broad line has a similar g -value however, because of the width and of uncertainties of background correction the uncertainty of this g -value is ten times larger. At low temperatures the shape of the broad line changes. At first sight this change is a line narrowing, however, broad wings of the line do persist down to a temperature of 10 K. At $g \sim 4.3$ we observe a background signal (data not shown) that could be traced back to the 1.5 mm Suprasil tube. Therefore, spectra are displayed and analyzed only at fields above 160 mT. Summarizing, the narrow-line component irreversibly changes line width and line shape during a temperature cycle between 300 and 525 K. The broad-line component narrows on decreasing temperature from 300 to 10 K and it broadens on increasing temperature from 300 to 525 K. Throughout the temperature range between 10 and 525 K intensity of the ESR-signals in $\text{Li}_2\text{Ca}_3[\text{N}_2]_3$ corresponds to only a minor fraction of the N_2 species.

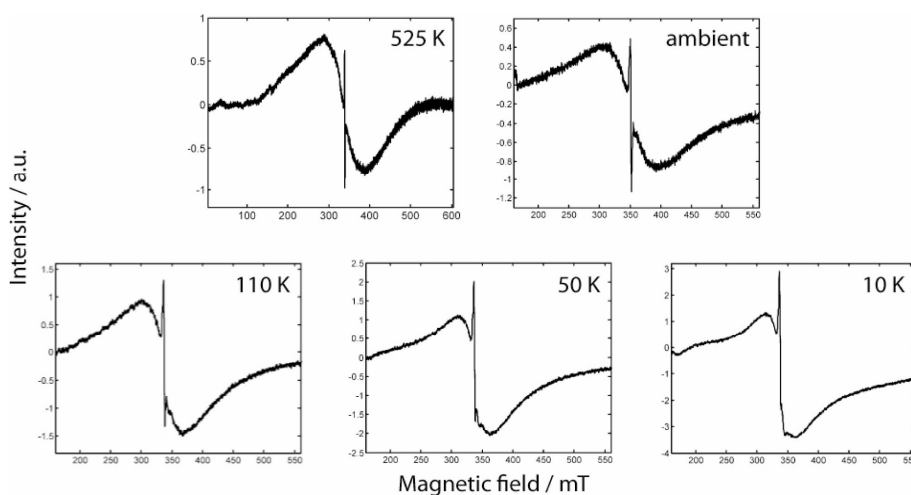


Figure S3. Overview ESR spectra of $\text{Li}_2\text{Ca}_3[\text{N}_2]_3$ at different temperatures after background correction.

Unit-Cell Metrics

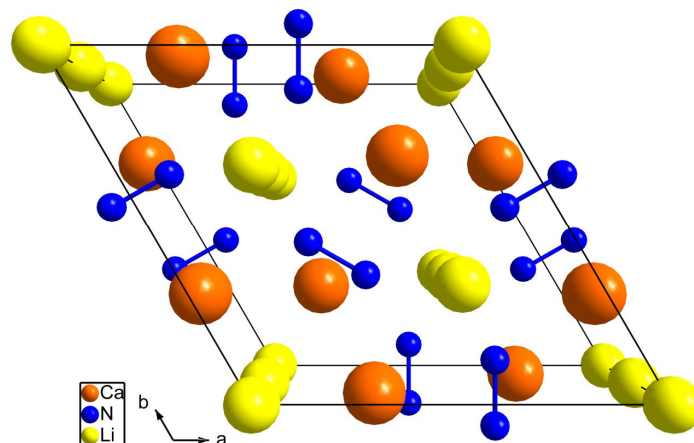


Figure S4. Indexing resulted in a unit cell with hexagonal metrics and $a = 8.0707(7)$ and $c = 4.7630(7)$ Å. The as-depicted structural model was obtained upon structure solution and Rietveld refinement of the PXRD data. “LiCaN₂” crystallizes in $P6_3/mcm$ (no. 193) with $a = 8.0726(2)$ and $c = 4.7755(1)$ Å. The crystallographic data for corresponding atoms are: Li1 at $2b$, Li2 at $4d$, Ca1 at $6g$ with $x = 0.7040(1)$, and N1 at $12j$ with $x = 0.3503(5)$ and $y = 0.4474(5)$.

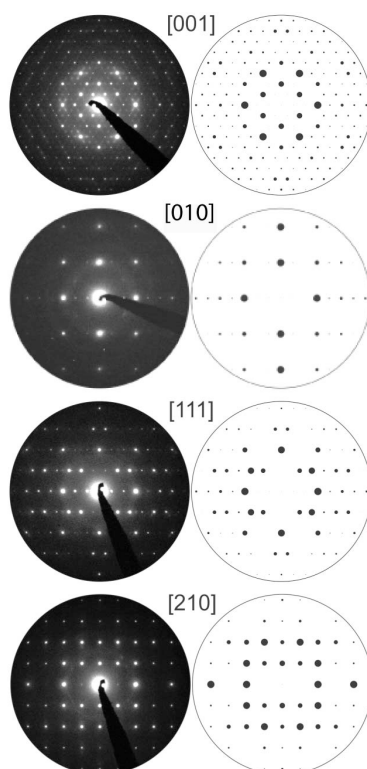


Figure S5. Experimental (black) and simulated (white) SAED patterns of various zone axes for hexagonal “LiCaN₂”.

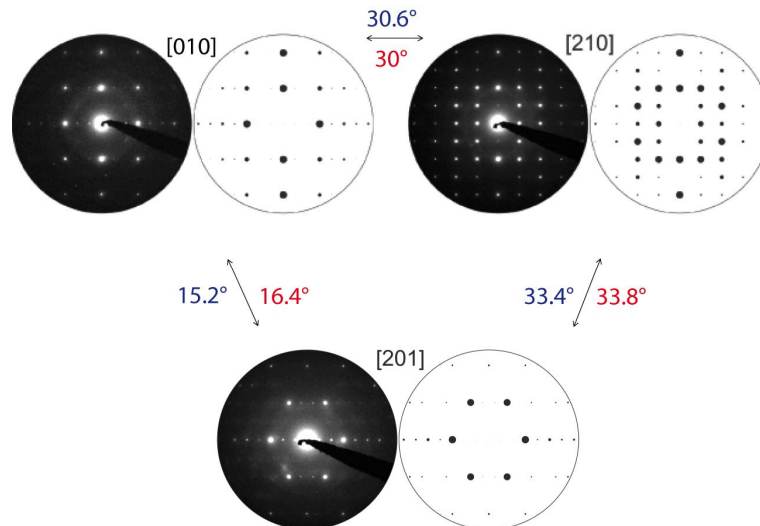


Figure S6. Experimental (black) and simulated (white) SAED patterns of the corresponding zone axes of hexagonal “LiCaN₂”. Experimental tilt angles (blue) between zone axes match calculated ones (red).

Transformation of Lattice Parameters

Transformation of the lattice parameters of the hexagonal starting model ($a = 8.06$ and $c = 4.76$ Å) into the orthorhombic C -centered unit cell are deduced according to the transformation

$$\begin{bmatrix} a \\ b \\ c \end{bmatrix}_{\text{orthC}} = P \begin{bmatrix} a \\ b \\ c \end{bmatrix}_{\text{hex}} \quad (1)$$

with $P = \begin{bmatrix} 2 & 1 & 0 \\ 0 & 1 & 0 \\ 0 & 0 & 1 \end{bmatrix}$. The final orthorhombic P -centered lattice parameters ($a = 4.76$, $b = 13.96$ and $c = 8.06$ Å) are obtained by the further transformation according to

$$\begin{bmatrix} a \\ b \\ c \end{bmatrix}_{\text{orthP}} = \begin{bmatrix} 0 & 0 & 1 \\ 1 & 0 & 0 \\ 0 & 1 & 0 \end{bmatrix} \begin{bmatrix} a \\ b \\ c \end{bmatrix}_{\text{orthC}} \quad (2)$$

Transformation of Zone Axes

The corresponding zone axes of the obtained *C*-centered intermediate as well as of the final *P*-centered orthorhombic threefold twin are deduced referring to the *International Tables for Crystallography: Volume A*. According to the transformation

$$\begin{bmatrix} U \\ V \\ W \end{bmatrix}_{\text{orth}C} = Q \begin{bmatrix} U \\ V \\ W \end{bmatrix}_{\text{hex}} \quad (3)$$

with $Q = P^{-1} = \begin{bmatrix} 1 & -1 & 0 \\ 2 & 2 & 0 \\ 0 & 1 & 0 \\ 0 & 0 & 1 \end{bmatrix}$, the zone axes of the *C*-centered orthorhombic model are obtained. A second transformation referring to

$$\begin{bmatrix} U \\ V \\ W \end{bmatrix}_{\text{orth}P} = \begin{bmatrix} 0 & 0 & 1 \\ 1 & 0 & 0 \\ 0 & 1 & 0 \end{bmatrix} \begin{bmatrix} U \\ V \\ W \end{bmatrix}_{\text{orth}C} \quad (4)$$

finally results in the zone axes for the model in space group *Pmma* (no. 51). In Table S2 corresponding related zone axes are listed.

Table S2. Relation between transformed hexagonal, orthorhombic *C*-centered and *P*-centered zone axes.

Hexagonal zone axes (<i>P6₃/mcm</i> , no. 193)	<i>C</i> -centered orthorhombic zone axes (<i>Cmcm</i> , no. 63)	<i>P</i> -centered orthorhombic zone axes (<i>Pmma</i> , no. 51)
[100]	[100]	[010]
[010]	[-120]	[0-12]
[001]	[001]	[100]
[210]	[120]	[012]
[111]	[011]	[101]

To confirm the orthorhombic unit-cell metrics in space group *Pmma* (no. 51), diffraction patterns of the former hexagonal model are transformed first into orthorhombic *C*-centered (*Cmcm*) and then into *P*-centered (*Pmma*) nomination. As-obtained simulated patterns are finally compared to experimental diffraction patterns of the corresponding zone axes and are still in good agreement with each other (see Figure S7) supporting the symmetry reduction to an orthorhombic threefold twin.

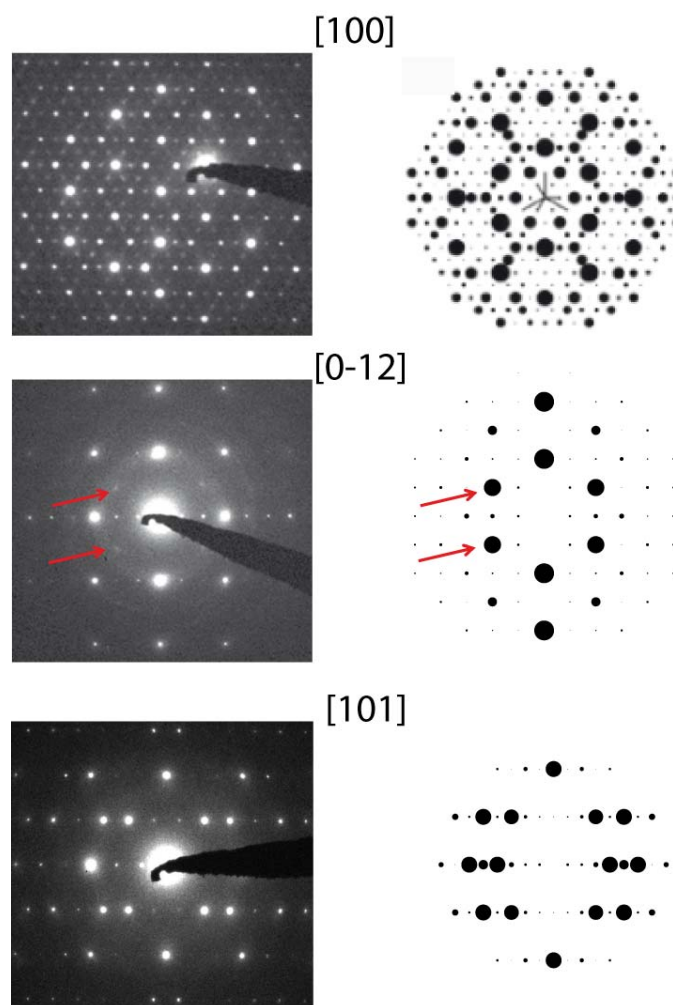


Figure S7. Experimental (black) and simulated (white) SAED patterns of various zone axes for orthorhombic “LiCaN₂” in space group *Pmma* (no. 51).

Elemental Analysis

Energy dispersive X-ray spectroscopy (EDX) confirmed the presence of only calcium and nitrogen/oxygen as lithium can not be detected. Oxygen is supposed to originate from hydrolysis of Li₂Ca₃[N₂]₃ due to the transfer of the sample holder into the microscope. EDX spectra were obtained with a SM-6500F scanning electron microscope (JEOL, Germany). A quantitative analysis of lithium, calcium, nitrogen and oxygen under inert conditions by the Mikroanalytisches Labor Pascher (Remagen, Germany) resulted in Li 7.0, Ca 49.4, N 35.9 and O 3.2 mass-%. EDX measurements of non-hydrolyzed crystallites could be obtained via transmission electron microscopy. Hereby, an averaged ratio of Ca:N of about 1:1.8 besides only traces of oxygen was obtained (measured atomic-%: Ca 32.8, N 64.1 and O 3.0; expected ideal atomic% without lithium: Ca 33.33, N 66.67 and O 0.0). TEM-EDX measurements are in good agreement with obtained results of quantitative analysis, the latter

one resulting an Li:Ca:N ratio of about 0.8:1:2.1 if the presence of oxygen is excluded. Note that if the mass percentages of the individual atoms Li, Ca, N and O are added, 100% are not reached. This is due to the fact that only the corresponding elements have been investigated. However, other heavier elements are not present as TEM-EDX does only result in Ca, N and only traces of O. Therefore, within the fact that the HP/HT product is always affected by an unknown (red) side phase and due to the fact the experiments are done in boron nitride crucibles, the residual mass is supposed to be constituted of e.g. boron originating from oxo- or nitridoborate formation (see FTIR section).

The presence of hydrogen was excluded by ^1H solid-state magic-angle spinning nuclear magnetic resonance spectroscopy (MAS-NMR) as no distinct signal was obtained upon measurements (data not shown).

Concluding, the initial hexagonal and/or orthorhombic models of “ LiCaN_2 ” concerning the Li:Ca ratio as elemental analysis has proven that the true crystal structure has to be a lithium deficient one.

Improving the Structural Model

Table S3. Atomic coordinates for $\text{Li}_2\text{Ca}_3[\text{N}_2]_3$ for the fully relaxed structural model (at zero external pressure), obtained from density-functional theory as described in the Article. Computed cell parameters: $a = 4.9269 \text{ \AA}$; $b = 14.3732 \text{ \AA}$; $c = 7.9656 \text{ \AA}$.

atom (Wyckoff) ^[a]	atom ^[b]	transformation of coordinates	x	y	z
Li1 (4g)	Li41	$\frac{1}{2}, y, 0$	$\frac{1}{2}$	0.351	0
	Li42	$\frac{1}{2}, y, 0$	$\frac{1}{2}$	0.649	0
	Li43	$0, y, 0$	0	0.351	0
	Li44	$0, y, 0$	0	0.649	0
Li2 (4h)	Li37	$\frac{1}{2}, y, \frac{1}{2}$	$\frac{1}{2}$	0.851	$\frac{1}{2}$
	Li38	$0, y, \frac{1}{2}$	0	0.851	$\frac{1}{2}$
	Li39	$\frac{1}{2}, y, \frac{1}{2}$	$\frac{1}{2}$	0.149	$\frac{1}{2}$
	Li40	$0, y, \frac{1}{2}$	0	0.149	$\frac{1}{2}$
Ca1 (2e)	Ca28	$\frac{1}{4}, 0, z$	$\frac{1}{4}$	0	0.6927
	Ca33	$\frac{3}{4}, 0, z$	$\frac{3}{4}$	0	0.3073
Ca2 (2f)	Ca27	$\frac{3}{4}, \frac{1}{2}, z$	$\frac{3}{4}$	$\frac{1}{2}$	0.8074
	Ca34	$\frac{1}{4}, \frac{1}{2}, z$	$\frac{1}{4}$	$\frac{1}{2}$	0.1926
Ca3 (4k)	Ca25	$\frac{3}{4}, y, z$	$\frac{3}{4}$	0.1653	0.8455
	Ca26	$\frac{3}{4}, y, z$	$\frac{3}{4}$	0.8347	0.8455
	Ca35	$\frac{1}{4}, y, z$	$\frac{1}{4}$	0.8347	0.1545
	Ca36	$\frac{1}{4}, y, z$	$\frac{1}{4}$	0.1653	0.1545
Ca4 (4k)	Ca29	$\frac{1}{4}, y, z$	$\frac{1}{4}$	0.3347	0.6546
	Ca30	$\frac{1}{4}, y, z$	$\frac{1}{4}$	0.6653	0.6546
	Ca31	$\frac{3}{4}, y, z$	$\frac{3}{4}$	0.6653	0.3454
	Ca32	$\frac{3}{4}, y, z$	$\frac{3}{4}$	0.3347	0.3454
N1 (4k)	N7	$\frac{1}{4}, y, z$	$\frac{1}{4}$	0.1702	0.6984
	N8	$\frac{1}{4}, y, z$	$\frac{1}{4}$	0.8298	0.6984
	N17	$\frac{3}{4}, y, z$	$\frac{3}{4}$	0.8298	0.3016
	N18	$\frac{3}{4}, y, z$	$\frac{3}{4}$	0.1702	0.3016
N2 (4k)	N5	$\frac{3}{4}, y, z$	$\frac{3}{4}$	0.3298	0.8016
	N6	$\frac{3}{4}, y, z$	$\frac{3}{4}$	0.6702	0.8016
	N19	$\frac{1}{4}, y, z$	$\frac{1}{4}$	0.3298	0.1984
	N20	$\frac{1}{4}, y, z$	$\frac{1}{4}$	0.6702	0.1984
N3 (4k)	N11	$\frac{3}{4}, y, z$	$\frac{3}{4}$	0.9543	0.612
	N12	$\frac{3}{4}, y, z$	$\frac{3}{4}$	0.0457	0.612
	N13	$\frac{1}{4}, y, z$	$\frac{1}{4}$	0.0457	0.388
	N14	$\frac{1}{4}, y, z$	$\frac{1}{4}$	0.9543	0.388
N4 (4k)	N1	$\frac{1}{4}, y, z$	$\frac{1}{4}$	0.4543	0.89
	N2	$\frac{1}{4}, y, z$	$\frac{1}{4}$	0.5457	0.89
	N23	$\frac{3}{4}, y, z$	$\frac{3}{4}$	0.5457	0.11
	N24	$\frac{3}{4}, y, z$	$\frac{3}{4}$	0.4543	0.11
N5 (4k)	N9	$\frac{3}{4}, y, z$	$\frac{3}{4}$	0.3201	0.638
	N10	$\frac{3}{4}, y, z$	$\frac{3}{4}$	0.6799	0.638
	N15	$\frac{1}{4}, y, z$	$\frac{1}{4}$	0.6799	0.362
	N16	$\frac{1}{4}, y, z$	$\frac{1}{4}$	0.3201	0.362
N6 (4k)	N3	$\frac{1}{4}, y, z$	$\frac{1}{4}$	0.8202	0.8616
	N4	$\frac{1}{4}, y, z$	$\frac{1}{4}$	0.1798	0.8616
	N21	$\frac{3}{4}, y, z$	$\frac{3}{4}$	0.1798	0.1384
	N22	$\frac{3}{4}, y, z$	$\frac{3}{4}$	0.8202	0.1384

[a] Related to the refined model in *Pmma* (no. 51) according to Table 1. [b] New atomic site labels as obtained from program output in *P1* (no. 1).

Table S4. Atomic coordinates for $\text{Li}_2\text{Ca}_3[\text{N}_2]_3$ calculated at a simulated pressure of approx. 9 GPa. Computed cell parameters: $a = 4.6177 \text{ \AA}$; $b = 13.6960 \text{ \AA}$; $c = 7.8911 \text{ \AA}$.

atom (Wyckoff) ^[a]	atom ^[b]	transformation of coordinates	x	y	z
Li1 (4g)	Li41	$\frac{1}{2}, \underline{y}, 0$	$\frac{1}{2}$	0.333	0
	Li42	$\frac{1}{2}, y, 0$	$\frac{1}{2}$	0.667	0
	Li43	$0, \underline{y}, 0$	0	0.333	0
	Li44	$0, y, 0$	0	0.667	0
Li2 (4h)	Li37	$\frac{1}{2}, y, \frac{1}{2}$	$\frac{1}{2}$	0.833	$\frac{1}{2}$
	Li38	$0, \underline{y}, \frac{1}{2}$	0	0.833	$\frac{1}{2}$
	Li39	$\frac{1}{2}, y, \frac{1}{2}$	$\frac{1}{2}$	0.167	$\frac{1}{2}$
	Li40	$0, y, \frac{1}{2}$	0	0.167	$\frac{1}{2}$
Ca1 (2e)	Ca28	$\frac{1}{4}, 0, \underline{z}$	$\frac{1}{4}$	0	0.6888
	Ca33	$\frac{3}{4}, 0, \underline{z}$	$\frac{3}{4}$	0	0.3112
Ca2 (2f)	Ca27	$\frac{3}{4}, \frac{1}{2}, \underline{z}$	$\frac{3}{4}$	$\frac{1}{2}$	0.8124
	Ca34	$\frac{1}{4}, \frac{1}{2}, \underline{z}$	$\frac{1}{4}$	$\frac{1}{2}$	0.1876
Ca3 (4k)	Ca25	$\frac{3}{4}, \underline{y}, \underline{z}$	$\frac{3}{4}$	0.1569	0.8440
	Ca26	$\frac{3}{4}, y, \underline{z}$	$\frac{3}{4}$	0.8431	0.8440
	Ca35	$\frac{1}{4}, y, \underline{z}$	$\frac{1}{4}$	0.8431	0.1560
	Ca36	$\frac{1}{4}, \underline{y}, \underline{z}$	$\frac{1}{4}$	0.1569	0.1560
Ca4 (4k)	Ca29	$\frac{1}{4}, y, \underline{z}$	$\frac{1}{4}$	0.3441	0.6568
	Ca30	$\frac{1}{4}, \underline{y}, \underline{z}$	$\frac{1}{4}$	0.6559	0.6568
	Ca31	$\frac{3}{4}, \underline{y}, \underline{z}$	$\frac{3}{4}$	0.6559	0.3432
	Ca32	$\frac{3}{4}, y, \underline{z}$	$\frac{3}{4}$	0.3441	0.3432
N1 (4k)	N7	$\frac{1}{4}, \underline{y}, \underline{z}$	$\frac{1}{4}$	0.1752	0.7246
	N8	$\frac{1}{4}, y, \underline{z}$	$\frac{1}{4}$	0.8248	0.7246
	N17	$\frac{3}{4}, y, \underline{z}$	$\frac{3}{4}$	0.8248	0.2754
	N18	$\frac{3}{4}, \underline{y}, \underline{z}$	$\frac{3}{4}$	0.1752	0.2754
N2 (4k)	N5	$\frac{3}{4}, y, \underline{z}$	$\frac{3}{4}$	0.3262	0.7711
	N6	$\frac{3}{4}, \underline{y}, \underline{z}$	$\frac{3}{4}$	0.6738	0.7711
	N19	$\frac{1}{4}, y, \underline{z}$	$\frac{1}{4}$	0.3262	0.2289
	N20	$\frac{1}{4}, \underline{y}, \underline{z}$	$\frac{1}{4}$	0.6738	0.2289
N3 (4k)	N11	$\frac{3}{4}, y, \underline{z}$	$\frac{3}{4}$	0.9527	0.606
	N12	$\frac{3}{4}, \underline{y}, \underline{z}$	$\frac{3}{4}$	0.0473	0.606
	N13	$\frac{1}{4}, \underline{y}, \underline{z}$	$\frac{1}{4}$	0.0473	0.394
	N14	$\frac{1}{4}, y, \underline{z}$	$\frac{1}{4}$	0.9527	0.394
N4 (4k)	N1	$\frac{1}{4}, y, \underline{z}$	$\frac{1}{4}$	0.4525	0.89
	N2	$\frac{1}{4}, \underline{y}, \underline{z}$	$\frac{1}{4}$	0.5475	0.89
	N23	$\frac{3}{4}, \underline{y}, \underline{z}$	$\frac{3}{4}$	0.5475	0.11
	N24	$\frac{3}{4}, y, \underline{z}$	$\frac{3}{4}$	0.4525	0.11
N5 (4k)	N9	$\frac{3}{4}, \underline{y}, \underline{z}$	$\frac{3}{4}$	0.2800	0.627
	N10	$\frac{3}{4}, y, \underline{z}$	$\frac{3}{4}$	0.7200	0.627
	N15	$\frac{1}{4}, y, \underline{z}$	$\frac{1}{4}$	0.7200	0.373
	N16	$\frac{1}{4}, \underline{y}, \underline{z}$	$\frac{1}{4}$	0.2800	0.373
N6 (4k)	N3	$\frac{1}{4}, \underline{y}, \underline{z}$	$\frac{1}{4}$	0.7830	0.8725
	N4	$\frac{1}{4}, y, \underline{z}$	$\frac{1}{4}$	0.2170	0.8725
	N21	$\frac{3}{4}, y, \underline{z}$	$\frac{3}{4}$	0.2170	0.1275
	N22	$\frac{3}{4}, \underline{y}, \underline{z}$	$\frac{3}{4}$	0.7830	0.1275

[a] Related to the refined model in *Pmma* (no. 51) according to Table 1. [b] New atomic site labels as obtained from calculation in *P1* (no. 1).

Description of the Crystal Structure

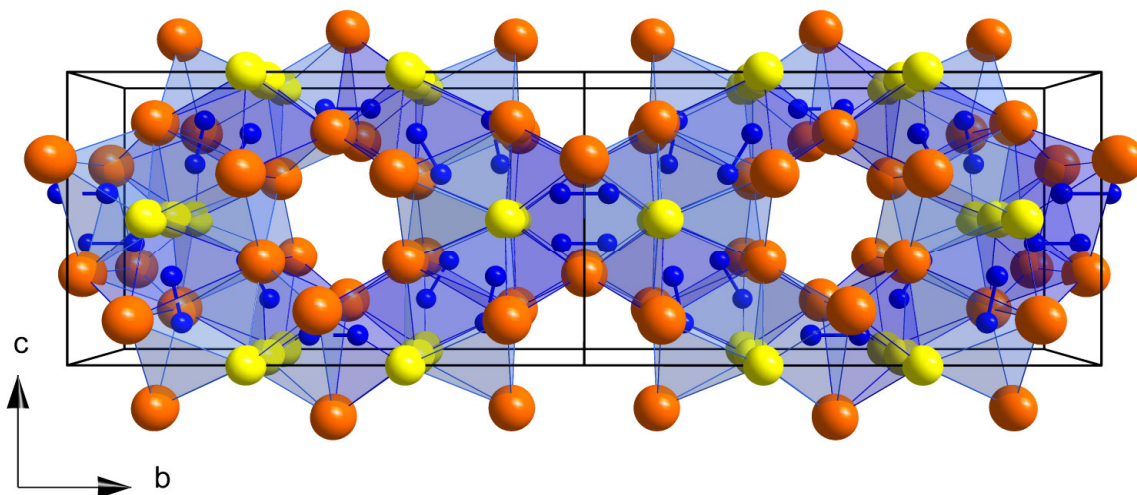


Figure S8. Coordination of the $[\text{N}_2]^{2-}$ ions in $\text{Li}_2\text{Ca}_3[\text{N}_2]_3$ (*Pmma*, no. 51); Li yellow, Ca orange, N blue. Each crystallographically independent nitrogen site is coordinated by two Li and four Ca atoms.

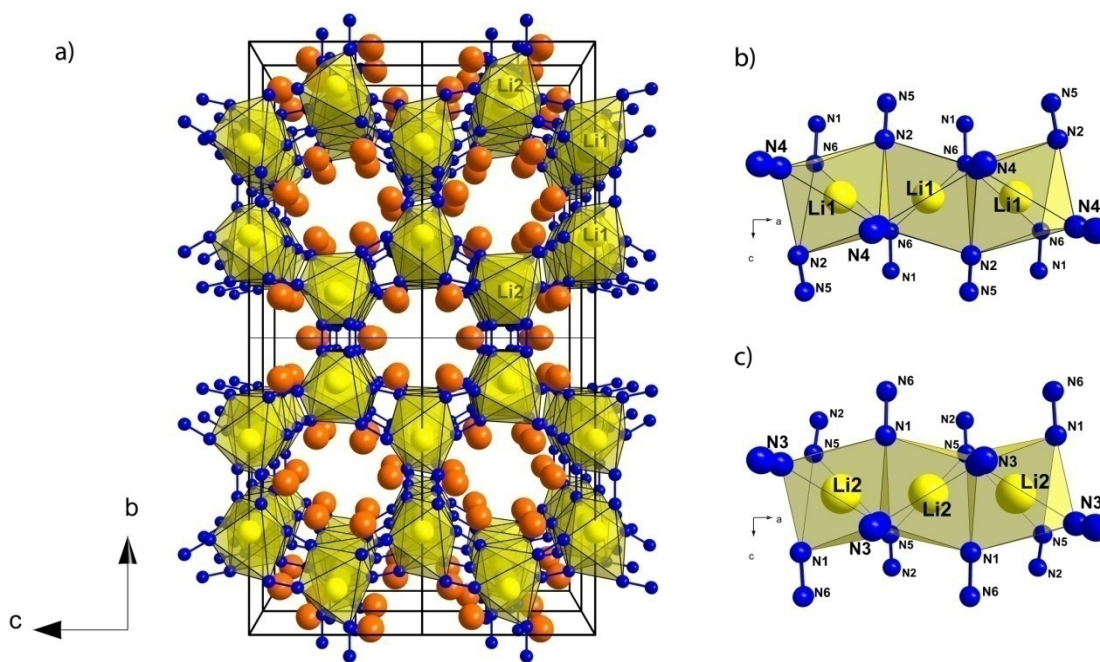


Figure S9. Coordination of the two independent lithium sites in $\text{Li}_2\text{Ca}_3[\text{N}_2]_3$ (*Pmma*, no. 51); Li yellow, Ca orange, N blue. The refined Li–Li distances match with reported values in literature.

Table S5. Refined interatomic distances in $\text{Li}_2\text{Ca}_3[\text{N}_2]_3$ (*Pmma*, no. 51).

atom pair	distance / Å	atom pair	distance / Å
Li1–Li1	2.387(1)	Ca1–Ca3	3.324(7)
Li2–Li2	2.387(1)	Ca1–Ca1	3.97(1)
Li1–N2	2.063(9)	Ca1–Ca3	4.28(1)
Li1–N4	2.015(6)	Ca1–Ca3	4.75(1)
Li1–N6	2.03(9)	Ca1–Ca1	4.7747(1)
Li2–N3	2.63(3)	Ca1–Ca4	4.997(7)
Li2–N1	2.0226(3)	Ca1–Ca1	5.45(1)
Li2–N5	2.063(9)	Ca2–Ca4	3.356(7)
Ca1–Li2	2.92(3)	Ca2–Ca2	3.95(2)
Ca1–Li2	4.46(2)	Ca2–Ca4	4.19(1)
Ca1–Li1	5.55(2)	Ca2–Ca2	4.7747(1)
Ca2–Li1	2.9(2)	Ca2–Ca4	4.83(2)
Ca2–Li1	4.46(1)	Ca2–Ca3	4.974(7)
Ca2–Li2	5.57(4)	Ca2–Ca2	5.47(2)
Ca3–Li2	2.964(9)	Ca3–Ca1	3.324(7)
Ca3–Li1	3.33(2)	Ca3–Ca3	3.57(1)
Ca3–Li2	4.493(6)	Ca3–Ca3	4.04(1)
Ca3–Li1	4.74(2)	Ca3–Ca4	4.086(9)
Ca3–Li2	5.11(3)	Ca3–Ca1	4.28(1)
Ca3–Li2	5.494(9)	Ca3–Ca1	4.75(1)
Ca4–Li1	3.063(9)	Ca3–Ca3	4.7747(1)
Ca4–Li2	3.32(4)	Ca3–Ca4	4.92(1)
Ca4–Li1	4.559(6)	Ca3–Ca2	4.974(7)
Ca4–Li2	4.73(3)	Ca3–Ca4	5.09(1)
Ca4–Li1	5.16(2)	Ca3–Ca3	5.39(1)
Ca4–Li1	5.391(9)	Ca3–Ca3	5.92(1)
Ca1–N3	2.409(3)	Ca4–Ca2	3.356(8)
Ca1–N1	2.47(2)	Ca4–Ca4	3.412(9)
Ca1–N3	2.63(1)	Ca4–Ca4	4.01(1)
Ca2–N2	2.31(1)	Ca4–Ca3	4.086(9)
Ca2–N4	2.4(2)	Ca4–Ca2	4.19(1)
Ca2–N4	2.62(8)	Ca4–Ca4	4.7747(1)
Ca3–N3	2.34(3)	Ca4–Ca2	4.83(2)
Ca3–N5	2.45(1)	Ca4–Ca3	4.92(1)
Ca3–N6	2.511(6)	Ca4–Ca1	4.997(7)
Ca3–N6	2.51(1)	Ca4–Ca3	5.09(1)
Ca3–N1	2.65(6)	Ca4–Ca4	5.267(9)
Ca3–N2	2.67(1)		
Ca4–N4	2.5(2)		
Ca4–N1	2.55(2)		
Ca4–N5	2.583(5)		
Ca4–N5	2.67(2)		

Due to the voids in the crystal structure of $\text{Li}_2\text{Ca}_3[\text{N}_2]_3$, the calcium ions are not reliably coordinated if the Ca–X (X = Li, N) distance is set to a minimum of 2.9 Å (see Figure S9). Hereby, each Ca^{2+} is coordinated by three *side-on* bound and two axial $[\text{N}_2]^{2-}$ ions in an *end-on* manner, which results in a coordination number of 8. The as-obtained Ca–N distances are also compared to the sum of their ionic radii. Eight-fold coordinated Ca^{2+} exhibits an averaged radius of 1.12 Å.⁵ Thus again the Ca–N distances correspond well with their ionic sum. Increasing the coordination sphere to a maximum of about 3.8 Å, then each calcium ion is coordinated by 4 diazenide $[\text{N}_2]^{2-}$ units in *side-on* mode and four additional lithium atoms, resulting in a coordination number of 14.

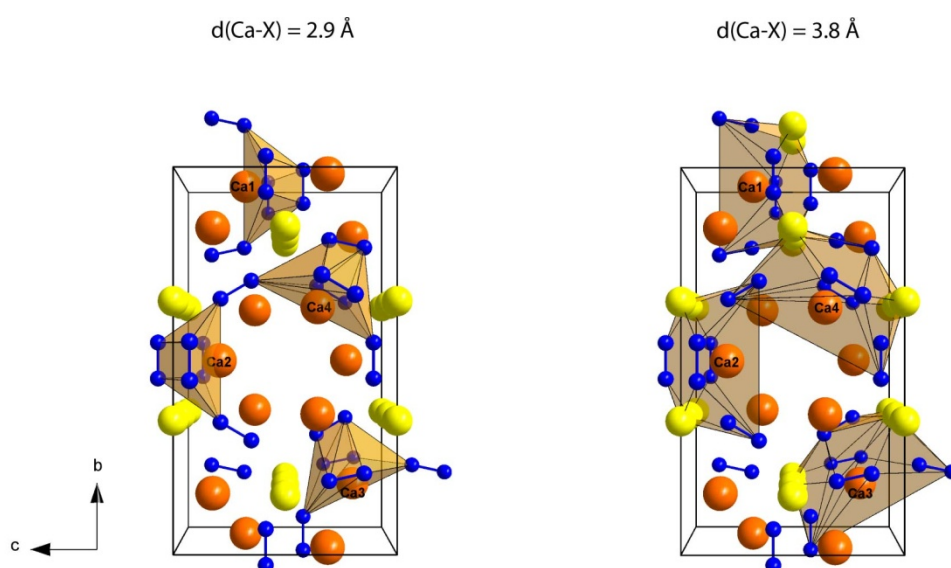


Figure S10. Coordination of the calcium sites in $\text{Li}_2\text{Ca}_3[\text{N}_2]_3$; Li yellow, Ca orange, N blue. The search for coordination polyhedra up to maximum Ca–X distance (X = Li, N) of 2.9 Å results in solely anion-coordinated calcium ions. Thereby, the calcium ions are coordinated by three $[\text{N}_2]^{2-}$ in *side-on* manner and two axial *end-on* coordinated nitrogen dumb-bells. If the Ca–X distance is further increased, the coordination of the calcium ions changes significantly. Up to a maximum Ca–X distance of 3.8 Å each calcium ion is coordinated by four diazenide units in *side-on* mode and four additional lithium atoms, resulting in an coordination number of 14 (or $5(x2) + 4$).

Calculation of Averaged Void-Diameter

To obtain the final void-diameter, the radius of $\text{Ca}^{2+}_{\text{CN}=8}$ (1.12 Å)^[5] has to be subtracted twice from the averaged distance of adverse located Ca^{2+} ions (5.385 Å) resulting in 3.15 Å in diameter for the actual size of the cavities.

Table S6. Refined distances in Ca–Ca pairs in $\text{Li}_2\text{Ca}_3[\text{N}_2]_3$ necessary to calculate the averaged Ca–Ca distance.

atom pair	distance / Å
2xCa1–Ca1	5.45(1)
1xCa2–Ca2	5.47(2)
4xCa3–Ca3	5.39(1)
2xCa4–Ca4	5.267(9)
averaged value = 5.385 Å	

Fourier Transform Infrared Spectroscopy

To relate the observed features to the corresponding nitrogen dumb-bells, the Wyckoff sites of each nitrogen atom as well as their pairing in combination with the N–N bond lengths have to be taken into account. Each nitrogen atom in $\text{Li}_2\text{Ca}_3[\text{N}_2]_3$ occupies the same site at $4k$ (see Table 1), but due to the pairing of nitrogen atoms the occurrence of corresponding nitrogen dumb-bells differs (see Table 2 and Figure 7). Hereby, the pairs of $\text{N}_1\text{--}\text{N}_6$ and $\text{N}_2\text{--}\text{N}_5$ appear twice often than $\text{N}_3\text{--}\text{N}_3$ and $\text{N}_4\text{--}\text{N}_4$, implying an idealized intensity ratio of observed features of 2:2:1:1, respectively. As already mentioned, the feature at 800 cm^{-1} is not attributed to the N–N stretching vibrations of the diazenide ions. The remaining three visible features in the low-energy region show slight differences in intensity, which might be related to the frequency of occurring N–N-pairs in $\text{Li}_2\text{Ca}_3[\text{N}_2]_3$. The two more intense features at 1260 and 1100 cm^{-1} indicate shorter N–N bond lengths, which is in good agreement with the crystallographic data, as the two more frequent $\text{N}_1\text{--}\text{N}_6$ - and $\text{N}_2\text{--}\text{N}_5$ -pairs exhibit the shortest bond lengths (see Table 2). The less intense feature at 1020 cm^{-1} is therefore attributed to one of the longer and less frequent N–N-pairs. The missing feature for the fourth N–N stretching vibration might be covered by the broad appearance of the two-peak feature of 1100 and 1020 cm^{-1} , especially if compared to the very sharp signal at 1260 cm^{-1} .

Magnetic and Electric Conductivity Measurements

As the molar susceptibility slightly increases at decreasing temperatures starting at about 50 K , we plotted the product $X_{\text{mol}}T$ versus T . Hereby, truly temperature-independent behavior is observed if the corresponding run of the curve linearly decreases with decreasing

temperature (see Figure S11). To check the presence of ferromagnetic impurities, we also plotted the field-dependence of μ/μ_B at different temperatures (see Figure S12). As no hysteresis is observed, no ferromagnetic impurities have been present during measurement.

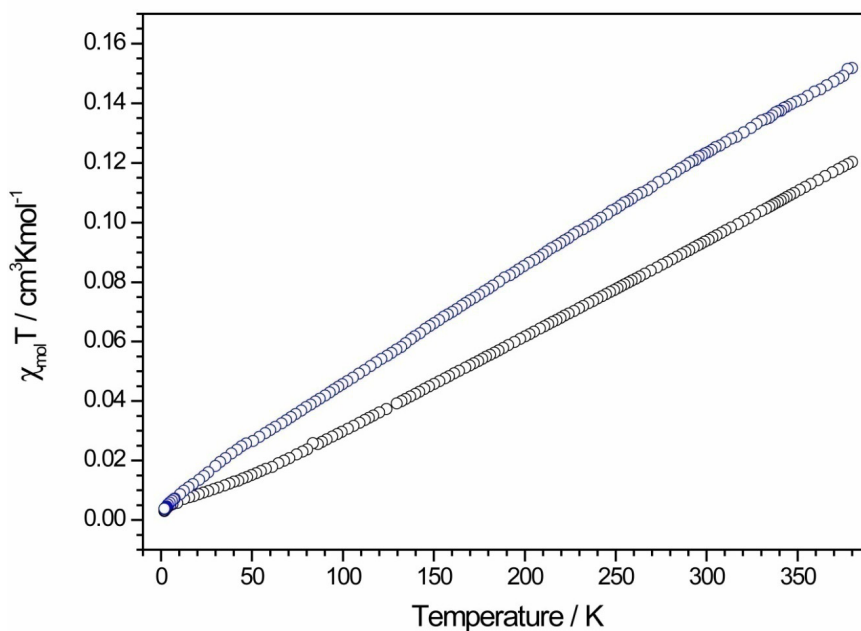


Figure S11. Temperature-dependence of the product $X_{\text{mol}}T$. $X_{\text{mol}}T$ increases linearly indicative for temperature-independent, metallic behavior. Blue: susceptibility measured at 0.01 T; black at 1T.

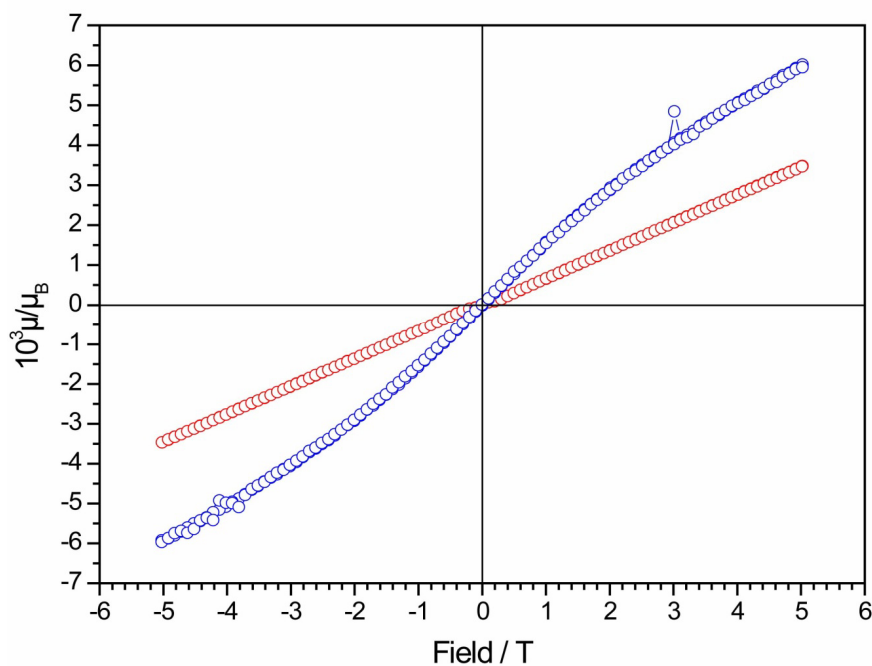


Figure S12. Field-dependence of μ/μ_B . As no hysteresis is observed, no ferromagnetic impurities are present in the sample chamber. Blue: magnetization measured at 1.8 K; red at 300 K.

References

- [1] H. D. Fair, R. F. Walker, *Energetic Materials Vol. 1: Physics and Chemistry of the Inorganic Azides*; Plenum Press: New York, **1977**.
- [2] W. J. Frierson, *Inorg. Synth.* **1946**, 8, 136.
- [3] J. Bergmann, R. Kleeberg, A. Haase, B. Breidenstein, *Mater. Sci. Forum* **2000**, 303, 347.
- [4] A. A. Coelho, TOPAS-Academic, Version 4.1; Coelho Software: Brisbane, 2007.
- [5] R. D. Shannon, *Acta Crystallogr. Sect. A* **1976**, 32, 751.

8. Publications

All results compiled in this thesis were published in scientific journals according to the below-mentioned list. Publications and patents which are not included in this work, as well as talks and poster presentations at scientific conferences, are summarized separately.

A Published as part of this thesis:

1. **High-Pressure Synthesis and Characterization of $\text{Li}_2\text{Ca}_3[\text{N}_2]_3$ - An Uncommon Metallic Diazenide with $[\text{N}_2]^{2-}$ Ions**

Sebastian B. Schneider, Markus Seibald, Volker L. Deringer, Ralf P. Stoffel, Gina M. Friederichs, Henryk Laqua, Viola Duppel, Gunnar Jeschke, Richard Dronskowski, and Wolfgang Schnick

J. Am. Chem. Soc. **2013**, *135*, 16668-16679.

For this publication, SAED patterns of $\text{Li}_2\text{Ca}_3[\text{N}_2]_3$ were analyzed by Markus Seibald. This includes the identification of a threefold twin by rotation instead of hexagonal metrics, simulation of SAED patterns and identification of zone axes for the final structure model in space group $Pm\bar{m}a$. Markus Seibald also revised the manuscript. Writing the manuscript main part, synthesis of the sample, literature screening, PXRD investigations, analysis of IR data, unit-cell and atom-coordinates transformation due to symmetry reduction, image editing, and interpretation of magnetic- and conductivity measurements was done by Sebastian B. Schneider. TEM investigation and parts of the data analysis was carried out by Viola Duppel. Gina M. Friederichs measured magnetic- and conductivity data. ESR investigations and data analyses were accomplished by Henryk Laqua and Gunnar Jeschke. All theoretical investigations, including the creation of Figures, were done by the group of Richard Dronskowski (Ralf P. Stoffel, Volker L. Deringer).

2. **Highly Efficient pc-LED Phosphors $\text{Sr}_{1-x}\text{Ba}_x\text{Si}_2\text{O}_7\text{N}_2:\text{Eu}^{2+}$ ($0 \leq x \leq 1$) - Crystal Structures and Luminescence Properties Revisited**

Markus Seibald, Tobias Rosenthal, Oliver Oeckler, and Wolfgang Schnick

Crit. Rev. Solid State Mater. Sci. **2014**, (accepted).

For this review article, writing the manuscript main part, literature screening and image editing was done by Markus Seibald. Tobias Rosenthal and Oliver Oeckler revised the manuscript and added text parts and images, especially in reference to TEM investigations. Figure 6 results from an idea of Markus Seibald and Philipp Pust while the photograph was done by Philipp Pust and editing by Markus Seibald. TOC of the manuscript was a collaboration of Markus Seibald, Tobias Rosenthal and Oliver Oeckler.

3. **Magnesium Double Nitride Mg_3GaN_3 as New Host Lattice for Eu^{2+} -Doping - Synthesis, Structural Studies, Luminescence and Band-Gap Determination**

Frauke Hintze, Neil W. Johnson, Markus Seibald, David Muir, Alexander Moewes, and Wolfgang Schnick

Chem. Mater. **2013**, 25, 4044-4052.

In this contribution, the crystal structure of Mg_3GaN_3 was determined by Markus Seibald and Frauke Hintze. Writing the manuscript main part, synthesis of the samples, literature screening, MAPLE calculations, and localization of vacancies for Eu^{2+} in the crystal structure were also done by Frauke Hintze. Synchrotron experiments and analysis of these data were done by Neil W. Johnson and David Muir in the group of Alexander Moewes. Detlef Wiechert and Peter J. Schmidt investigated the luminescence properties in the LDC Aachen.

4. **A New Polymorph of the Highly Efficient LED-Phosphor $\text{SrSi}_2\text{O}_2\text{N}_2:\text{Eu}^{2+}$ - Polytypism of a Layered Oxonitridosilicate**

Markus Seibald, Tobias Rosenthal, Oliver Oeckler, Christian Maak, Andreas Tücks, Peter J. Schmidt, Detlef Wiechert, and Wolfgang Schnick

Chem. Mater. **2013**, 25, 1852-1857.

For this publication, writing the manuscript main part, literature screening, SEM analysis, Rietveld refinement, single-crystal structure elucidation, sample preparation for TEM with assistance of Tobias Rosenthal and Christian Maak, SAED analysis and simulation, HRTEM image simulation, interpretation of luminescence measurements, and image editing was done by Markus Seibald. TEM investigations themselves were performed by Tobias Rosenthal, who assisted with their interpretation and also

revised the manuscript. Oliver Oeckler improved the single-crystal structure refinement and contributed to data analysis and discussion. The $\text{SrSi}_2\text{O}_2\text{N}_2:\text{Eu}^{2+}$ sample was synthesized by Andreas Tücks. Luminescence investigations were done in the LDC Aachen by Andreas Tücks, Peter J. Schmid and Detlef Wiechert.

5. **Unexpected Luminescence Properties of $\text{Sr}_{0.25}\text{Ba}_{0.75}\text{Si}_2\text{O}_2\text{N}_2:\text{Eu}^{2+}$ - A Narrow Blue Emitting Oxonitridosilicate with Cation Ordering**

Markus Seibald, Tobias Rosenthal, Oliver Oeckler, Felix Fahrnbauer, Andreas Tücks, Peter J. Schmidt, and Wolfgang Schnick

Chem. Eur. J. **2012**, *18*, 13446-13452.

For this article, writing the manuscript main part, literature screening, SEM analysis, single-crystal structure determination, analysis of reciprocal lattice sections, interpretation of luminescence measurements, and image editing was done by Markus Seibald. TEM investigations were performed by Tobias Rosenthal, who also contributed to the manuscript text. In a close collaboration, Markus Seibald, Felix Fahrnbauer, and Tobias Rosenthal analyzed and interpreted SAED patterns and HRTEM images. They improved HRTEM image simulations for Titan 80-300 TEM with field-emission gun installed at the LMU. With the help of Oliver Oeckler results from HRTEM simulations were transferred to the single-crystal structure elucidation. Luminescence investigations were done in the LDC Aachen by Andreas Tücks and Peter J. Schmidt.

6. **Real Structure and Diffuse Scattering of $\text{Sr}_{0.5}\text{Ba}_{0.5}\text{Si}_2\text{O}_2\text{N}_2:\text{Eu}^{2+}$ - A Highly Efficient Yellow Phosphor for pc-LEDs**

Markus Seibald, Oliver Oeckler, Vinicius R. Celinski, Peter J. Schmidt, Andreas Tücks, and Wolfgang Schnick

Solid State Sci. **2011**, *13*, 1769-1778.

For this publication, writing the manuscript main part, SEM analysis, Rietveld refinement, SAED analysis and simulation, simulation of diffuse scattering in PXRD pattern / SAED images, and image editing was done by Markus Seibald. TEM investigations were performed by Markus Döblinger. Oliver Oeckler improved the Rietveld refinement and contributed to the disorder model and revised the manuscript.

The sample was synthesized by Andreas Tücks. Luminescence investigations and interpretation of measured values were done in the LDC Aachen by Andreas Tücks and Peter J. Schmidt.

7. **Material Properties and Structural Characterization of $M_3Si_6O_{12}N_2:Eu^{2+}$ (M = Ba, Sr) - A Comprehensive Study on a Promising Green Phosphor for pc-LEDs**

Cordula Braun, Markus Seibald, Saskia L. Börger, Oliver Oeckler, Teak D. Boyko, Alexander Moewes, Gerhard Miehe, Andreas Tücks, and Wolfgang Schnick
Chem. Eur. J. **2010**, *16*, 9646-9657.

For this contribution, writing the manuscript parts (also compilation of the tables) concerning single-crystal structure determination for the solid-solution series, synthesis of all single crystals including structure refinement, MAPLE calculations, and the correlation of the emission-band shift to changes in the crystal structure was done by Markus Seibald. Oliver Oeckler discussed the results with the other authors and revised the manuscript. Synchrotron experiments and analysis of these data were done by Teak D. Boyko and Alexander Moewes. Andreas Tücks investigated the luminescence properties in the LDC Aachen.

B Other publications:

- 1. Aperiodic CrSc Multilayer Mirrors for Attosecond Water Window Pulses**
Alexander Guggenmos, Roman Rauhut, Michael Hofstetter, Samira Hertrich, Bert Nickel, Jürgen Schmidt, Eric M. Gullikson, Markus Seibald, Wolfgang Schnick, and Ulf Kleineberg
Opt. Express **2013**, *21*, 21728-21740.
- 2. Asymmetric Fluorodinitromethyl Derivatives of 2,2,2-trinitroethyl N-(2,2,2-trinitroethyl)carbamate**
Thomas M. Klapötke, Burkhard Krumm, Richard Moll, Sebastian F. Rest, Wolfgang Schnick, and Markus Seibald
J. Fluor. Chem. **2013**, *156*, 253-261.
- 3. Ambiguities in the Structure Determination of Antimony Tellurides Arising from Almost Homometric Structure Models and Stacking Disorder**
Matthias N. Schneider, Markus Seibald, Patrick Lagally, and Oliver Oeckler
J. Appl. Crystallogr. **2010**, *43*, 1012-1020.
- 4. A New Series of Long-Range Ordered Metastable Phases in the System M-Sb-Te (M = Ge, Ag)**
Matthias N. Schneider, Markus Seibald, and Oliver Oeckler
Dalton Trans. **2009**, *11*, 2004-2011.
- 5. Salts and Ionic Liquids of Resonance Stabilized Amides**
Harald Brand, Joern Martens, Peter Mayer, Axel Schulz, Markus Seibald, and Thomas Soller
Chem. Asian J. **2009**, *4*, 1588-1603.

C Patents

Mn-Activated Hexafluorosilicates for LED Applications

Volker Weiler, Peter J. Schmidt, Wolfgang Schnick, Markus A. Seibald

PCT Int. Appl. **2013**, WO 2013088313, A1, 26pp, Koninklijke Philips Electronics NV, Philips Intellectual Property & Standards GmbH, Germany

D Conference contributions:

1. **Weißblaue GeSCHICHTEN – Erleuchtung aus Bayern (talk)**

Markus Seibald, Tobias Rosenthal, Oliver Oeckler, Wolfgang Schnick

Hemdsärmelkolloquium, Freiburg, 7.-9. März 2013.

2. **Unerwartete Lumineszenz-Eigenschaften von $\text{Sr}_{1-x}\text{Ba}_x\text{Si}_2\text{O}_2\text{N}_2:\text{Eu}^{2+}$ (poster)**

Markus Seibald, Tobias Rosenthal, Oliver Oeckler, Wolfgang Schnick

16. Vortragstagung der Fachgruppe Festkörperchemie und Materialforschung der Gesellschaft Deutscher Chemiker, Darmstadt, 17.-19. September 2012.

3. **Broadband multilayer mirror and diffractive optics for attosecond pulse shaping in the 280-500 eV photon energy range (poster)**

Alexander Guggenmos, Michael Hofstetter, Roman Rauhut, Christian Späth, S. Hertrich, Bert Nickel, S. Yang, Eric M. Gullikson, Jürgen Schmidt, Markus Seibald, Wolfgang Schnick, Ferenc Krausz, Ulf Kleineberg

XVIIIth International Conference on Ultrafast Phenomena, Lausanne, 8.-13. Juli 2012.

4. **Strukturaufklärung an lumineszierendem $\text{Sr}_{1-x}\text{Ba}_x\text{Si}_2\text{O}_2\text{N}_2:\text{Eu}^{2+}$ durch Kombination von TEM- und Röntgen- Methoden (talk)**

Tobias Rosenthal, Markus Seibald, Oliver Oeckler

Festkörperchemie-Seminar, Hirschegg, 7.-10. Juni 2012.

5. **Synthesis and Analysis – Strategies for New Phosphor Materials (poster)**

Frauke Hintze, Markus Seibald, Philipp Pust, Sebastian Schmiechen, Wolfgang Schnick

Phosphor Global Summit, Scottsdale (AZ), 20.-22. März 2012.

6. **Nitride Phosphor Materials – Research, Application and Pertinence (poster)**
Sebastian Schmiechen, Frauke Hintze, Markus Seibald, Philipp Pust, Wolfgang Schnick
Phosphor Global Summit, Scottsdale (AZ), 20.-22. März 2012.
7. **Real structure of $\text{Sr}_{1-x}\text{Ba}_x\text{Si}_2\text{O}_2\text{N}_2:\text{Eu}^{2+}$ ($0.5 < x < 0.8$) phosphors by TEM and XRD (poster)**
Oliver Oeckler, Tobias Rosenthal, Markus Seibald, Wolfgang Schnick
22nd Congress and General Assembly of the International Union of Crystallography, Madrid (Spain), 22.-30. August 2011.
8. **Diffuse Streuung und Domänenstruktur von $\text{Sr}_{0.47}\text{Ba}_{0.53}\text{Si}_2\text{O}_2\text{N}_2$ (poster)**
Markus Seibald, Oliver Oeckler, Wolfgang Schnick
15. Vortragstagung der Fachgruppe Festkörperchemie und Materialforschung der Gesellschaft Deutscher Chemiker, Berlin, 20.-22. September 2010.
9. **Real-structure effects of luminescent layered oxonitridosilicates (talk)**
Oliver Oeckler, Markus Seibald, Juliane A. Kechele, Florian Stadler, Tobias Rosenthal, Hans Koss, Wolfgang Schnick
26th European Crystallographic Meeting, Darmstadt, 29. August-2. September 2010.
10. **Geordnete Unordnung in SiONen (talk)**
Markus Seibald, Oliver Oeckler, Vinicius R. Celinski, Wolfgang Schnick
Festkörperchemie-Seminar Hirschegg, Hirschegg, 3.-6. Juni 2010.
11. **Metastabile Überstrukturphasen im System Ge-Sb-Te (poster)**
Matthias N. Schneider, Markus Seibald, Oliver Oeckler
14. Vortragstagung der Wöhler-Vereinigung, Garching, 8.-10 Oktober 2008.

E CSD numbers

Crystallographic data (cif file) of investigated compounds can be obtained from the Fachinformationszentrum Karlsruhe, 76344 Eggenstein-Leopoldshafen, Germany (fax, (+49)7247-808-666; e-mail, crysdata@fiz-karlsruhe.de) by quoting the corresponding depository number.

$\text{Ba}_3\text{Si}_6\text{O}_{12}\text{N}_2$	CSD-421322
$\text{Ba}_{2.56}\text{Sr}_{0.44}\text{Si}_6\text{O}_{12}\text{N}_2$	CSD-421324
$\text{Ba}_2\text{SrSi}_6\text{O}_{12}\text{N}_2$	CSD-421323
$\text{SrSi}_2\text{O}_2\text{N}_2$	CSD-425649
$\text{Sr}_{0.5}\text{Ba}_{0.5}\text{Si}_2\text{O}_2\text{N}_2$	CSD-422238
$\text{Sr}_{0.25}\text{Ba}_{0.75}\text{Si}_2\text{O}_2\text{N}_2$	CSD-424289
Mg_3GaN_3	CSD-425108
$\text{Li}_2\text{Ca}_3[\text{N}_2]_3$	CSD-426449